THE GRAVITATIONAL WAVE SIGNATURE OF STELLAR COLLAPSE AND DYNAMICS OF COMPACT STARS

Thesis submitted for the degree of
"Doctor Philosophiæ"

16 October 2009

CANDIDATE

Ernazar B. Abdikamalov

SUPERVISORS

John Miller and Luciano Rezzolla

International School for Advanced Studies
Via Beirut 2-4, 34151 Trieste, Italy.
E-mail: *abdik@sissa.it*

Abstract

This thesis is devoted to the study of the gravitational wave (GW) signature of stellar collapse and the dynamical behavior compact stars. The thesis consists of two parts. In the first one, we study the dynamics of the phase-transition-induced collapse of neutron stars (NSs) and the accretion-induced collapse of white dwarfs (WDs) as well as the associated GW emission. The second part is concerned with the study of the effects of general relativity on the magnetosphere of oscillating NSs.

An increase in the central density of a NS may trigger a phase transition from hadronic matter to deconfined quark matter in the core, causing it to collapse to a more compact hybrid-star configuration. We present a study of this, using general relativistic hydrodynamics simulations with a simplified equation of state and considering the case of supersonic phase transition. We confirm that the emitted GW spectrum is dominated by the fundamental quasi-radial and quadrupolar pulsation modes. We observe a nonlinear mode resonance which substantially enhances the emission in some cases. We explain the damping mechanisms operating and estimate the detectability of the GWs.

In massive accreting oxygen-neon WDs, their core material may in several circumstances experience rapid electron captures leading to collapse of the WD to a protoneutron star and collapse-driven supernova (SN) explosion. This process is called accretion-induced collapse (AIC) and represents a path alternative to thermonuclear disruption of accreting WDs in Type Ia SNe. An AIC-driven SN explosion is expected to be weak and of short duration, making it hard to detect by electromagnetic means alone. Neutrino and GW observations may provide crucial information necessary to reveal a potential AIC event. Motivated by the need for systematic predictions of the GW signature of AIC, we present results from an extensive set of general-relativistic simulations of AIC using a microphysical finite-temperature equation of state and an approximate treatment of deleptonization during collapse. Investigating a set of 114 progenitor models with wide range of rotational configurations, temperatures and central densities, we extend previous Newtonian studies and confirm that the GW signal of core bounce is of generic morphology known as Type III in the literature. We show that the emitted GWs contain enough information that can be used to constrain the progenitor and postbounce rotation. We discuss the detectability of the emitted GW signal. Rapidly rotating models form massive quasi-Keplerian accretion disks in the early postbounce phase. The disk mass is sensitive to the precollapse rotation and it can be as massive as $\sim 0.8 M_\odot$ in rapidly differentially rotating models, while slowly and/or uniformly rotating models have much smaller disks. We find strong evidence that a subset of rapidly rotating models reaches sufficiently rapid rotation to develop a high- and low-$T/|W|$ dynamical instabilities.

Just as a rotating magnetised NS has material pulled away from its surface to populate a magnetosphere, a similar process can occur as a result of NS pulsations rather than rotation. This is of interest in connection with the overall study of NS oscillation modes but with a particular focus on the situation for magnetars. Following a previous Newtonian analysis of the production of a force-free magnetosphere in this way Timokhin et al. [418], we present here a corresponding general-relativistic analysis. We give a derivation of the general relativistic Maxwell equations for small-amplitude arbitrary oscillations of a non-rotating NS with a generic magnetic field and show that these can be solved analytically under the assumption of low current density in the magnetosphere. We apply our formalism to toroidal oscillations of a NS with a dipole magnetic field and calculate the resulting energy losses. We find that in general relativity the energy loss from the NS is significantly smaller than suggested by the Newtonian treatment.

Collaborations

The research presented in this thesis was mainly conducted at SISSA – the International School for Advanced Studies – between November 2005 and October 2009. This thesis is the result of author's own work, as well as the outcome of scientific collaborations mentioned below, except where explicit reference is made to the results of others.

It is based on the following research papers published in refereed journals:

Chapter 3:

E. B. Abdikamalov, H. Dimmelmeier, L. Rezzolla and J. Miller
Relativistic simulations of the phase-transition-induced collapse of neutron stars
Mon. Not. Roy. Astron. Soc., 393:52, 2009

Chapter 4:

E. B. Abdikamalov, C. D. Ott, L. Rezzolla, L. Dessart, H. Dimmelmeier, A. Marek and H.-T. Janka
Axisymmetric General Relativistic Simulations of the Accretion-Induced Collapse of White Dwarfs
Phys. Rev. D, 2009 (submitted)

Chapter 5:

E. B. Abdikamalov, B. Ahmedov and J. Miller
The magnetosphere of oscillating neutron stars in general relativity.
Mon. Not. Roy. Astron. Soc., 395:443, 2009

Acknowledgements

Writing this thesis and conducting the research behind it would have been impossible without the help of a number of people. First and foremost, I would like to thank my family for their love and continuous support, without which I would never been able not only to finish, but even to start the PhD.

I am deeply indebted to my PhD advisors, John Miller and Luciano Rezzolla for guiding my first steps in science, their constant help and continuous support during these years. Special thanks to Luciano also for hosting me at the Albert Einstein Institute in Berlin, where I spent a large part of my PhD time.

I cannot thank enough my closest collaborators and friends Harald Dimmelmeier and Christian Ott, working with whom has been really pleasant and exciting. Harry taught me how to work with the numerical codes that I have used for most of the research behind this thesis. From Christian I have learned a lot about stellar collapse physics. I thank him also for his many invaluable advices. I am also very grateful to my thesis examiners, Ewald Müller and Attilio Ferrari, for reviewing this manuscript and for their useful suggestions and comments.

I have benefited a lot from regular or occasional but always fruitful discussions with a number of people, besides those already mentioned. Although I run the risk of forgetting some of them – I apologise for that in advance – I will try to name them here and express my gratitude: Bobomurat Ahmedov, Marcos Ansorg, Juan Barranco, Michal Bejger, Alessandro Bressan, Pablo Cerdá-Durán, Monica Colpi, Luc Dessart, Alessandro Drago, Joachim Frieben, Filippo Galeazzi, Kostas Glampedakis, Thomas Janka, Stafano Liberati, Matthias Liebendörfer, Andreas Marek, Bernhard Müller, Ewald Müller, Frank Löffler, Pawel Haensel, Stephan Rosswog, Nikolaos Stergioulas, Aaryn Tonita, Shin Yoshida, Leszek Zdunik and Burkhard Zink.

SISSA has provided a nice environment for conducting my research over the last four years. I thank all of my colleagues and friends for contributing to that.

Last, but definitely not least, I wish to thank my friends for all the fun we had together. You all made feel at home in Trieste and in Berlin during these 4 unforgettable years. I hope we will have many chances to be together in the future.

Contents

Chapter 1

Introduction

1.1 Stellar evolution and collapse

During most of their lifetime, stars are in a quasi-equilibrium state in which their self-gravity is balanced by the pressure of the stellar matter and, in some cases, also radiation pressure. However, at some points in their evolution, this equilibrium can be violated by a decrease of pressure support in the inner core at the end of a core-burning phase and/or as a result of interactions with a binary companion. This triggers gradual contraction of the stellar core. Depending on the type of star, this contraction evolves in different ways: in some cases, it can lead to a rapid collapse of the core, either resulting in a new, more compact, equilibrium configuration, or proceeding as a continuing collapse giving rise to a black hole (BH). In some cases, such stellar collapse results in a spectacular explosion, in an event observationally identified as a supernova and/or a gamma-ray burst. Below we give an overview of some relevant aspects of stellar evolution and stellar collapse.

Normal luminous stars form from local condensations of galactic gas, which contract under their own self-gravity and eventually reach sufficiently high central densities and temperatures to ignite self-sustained nuclear reactions in the core. Small contracting gas clouds with masses $\lesssim 0.08 M_\odot$ never reach the conditions necessary for having self-sustained nuclear reactions and becoming a normal star, but instead end up as *brown dwarfs* (or *planets* if they are orbiting round a larger object). More massive clouds, which do reach the necessary conditions, start their life as a star by burning hydrogen into helium in the core, with the energy released by the hydrogen fusion producing the temperature and pressure gradients necessary for sustaining them against contraction under their own self-gravity.

Normal stars spend most of their lifetime in this core-hydrogen-burning phase, known as the *main-sequence* phase. Most of the luminous stars in the sky, including our Sun, are in this phase. Eventually, however, they exhaust the available hydrogen fuel in the core and there is then no longer a central energy source able to sustain the equilibrium. This leads to core contraction under self-gravity, while the outer regions expand, causing the star to swell up in size and become a giant or supergiant. The core contraction increases the core density and temperature, which may become sufficiently high to initiate the burning of helium into carbon in such a way that a new equilibrium state is reached. If helium burning is ignited, this too finishes after some time, and the process of core contraction and envelope expansion is then repeated. Stars less massive than $\sim 7 M_\odot$ cease their normal evolution at the end of core hydrogen or helium burning, because their cores never become dense enough and hot enough to ignite further nuclear reactions. During their later evolution, these stars lose most of their outer material by means of *stellar winds* and may be seen as *planetary nebulae*. The core ends up as a *white dwarf* (WD), supported by electron degeneracy pressure, with its composition consisting mainly of either helium or carbon/oxygen depending on the stage at which the core nuclear burning terminated.

For stars with initial masses in the range $7M_\odot \lesssim M \lesssim 10M_\odot$, the core contraction after helium burning leads to densities and temperatures high enough for the ignition of carbon burning, with most of the core material then being converted into oxygen and neon. Stars with masses close to $7M_\odot$, again have extensive mass-loss via stellar winds and end up as WDs, but now composed of mainly of oxygen and neon rather than carbon and oxygen as before [334]. In slightly more massive stars, with $M \lesssim 10M_\odot$, continuing nuclear burning in a shell surrounding the core, after the end of central carbon burning, keeps increasing the core mass until eventually inverse beta decay becomes energetically favourable, reducing the number of partially-degenerate electrons there and hence reducing their pressure support, leading to core-collapse. The collapsing core quickly separates into a subsonically contracting *inner* part and a supersonically infalling *outer* part. The infall of the inner core first accelerates but is then abruptly halted by the stiffening of the stellar matter when the central density reaches around nuclear-matter density $\rho_{\rm nuc}$ ($\approx 3\times10^{14}\,{\rm g\,cm^{-3}}$). The bouncing inner core then collides with still-infalling outer material, launching a shock wave. While passing through the core, the shock quickly loses most of its kinetic energy through photo-dissociation of nuclei, becoming a stalled accretion shock. However, continuous energy deposition by neutrinos emitted from the collapsed core – now a proto-neutron star (PNS) – then successfully revives the shock, which eventually reaches the stellar surface, leading to expulsion of the outer regions in a supernova explosion. This type of supernova is known as an *electron-capture supernova* [207, 202]. The PNS core subsequently cools to become a standard neutron star (NS).

A star with mass in the range $10M_\odot \lesssim M \lesssim 80M_\odot$ evolves through all of the stages of core nuclear burning up to iron-group nuclei. Stellar nucleosynthesis, which begins with hydrogen burning, proceeds at successively higher temperatures and densities through helium, carbon, neon, oxygen and silicon burning. Silicon burning at about 3×10^9 K leads to a star with a central core of iron-group nuclei surrounded by concentric shells containing silicon, oxygen, neon, carbon, helium and hydrogen (for a recent review on massive star evolution, see, e.g., [448]). Since nuclear fusion beyond iron is endothermic, no further fusion in the core can then take place, and there is a gradual contraction of the central core when silicon burning ends. The photodisintegration of iron-group nuclei through collisions with energetic photons present at high temperatures, as well as inverse beta decay, then reduce the pressure support in the core, triggering rapid collapse. Here again the inner core collapses to a PNS, sending out a shock wave. The shock loses its kinetic energy by photodissociating heavy nuclei, becoming a stalled accretion shock. The subsequent evolution of the shock depends crucially on the mass and rotation of the star.

In a slowly or non-rotating $M \lesssim 25M_\odot$ star, the shock wave is believed to be successfully revived by energy deposition by neutrinos, possibly with the help of convection in the post-shock region that enhances the neutrino energy deposition [254]. The shock reaches the surface, leading to a supernova explosion. The remnant core again emerges as a NS. In more massive non-rotating stars, the shock has to propagate out through a larger amount of matter and hence loses more energy, and neutrino energy deposition is thought to be unable to revive the shock. In this case, the continued accretion of matter onto the PNS increases its mass above the stability limit on a timescale of ~ 1 s, and the star collapses to a BH.

Rotation is thought to have a twofold effect on the explosion of massive stars. On one hand, in rotating stars, in addition to the energy deposition by neutrinos, the collapsed core interacts with the shock front also through magnetic field lines. The rapid rotation of the collapsed core and slow rotation of the shock front leads to stretching of the magnetic field lines that connect the shock front and the PNS. This stretching exerts additional pressure on the shock front, facilitating its outward propagation (e.g., [79]). On the other hand, rotation tends to damp the convective motion in the postshock region, which may lead to smaller amount of energy deposition by neutrinos. Further research is needed in this direction to better understand the effects of rotation.

The evolution of stars more massive than $\sim 80M_\odot$, which are believed to have existed in the early Universe, is poorly understood at the moment, and is beyond the scope of the discussion here. The interested

reader is referred to, e.g., a recent review by Woosley et al. [448].

We point out that the exact values of the stellar masses that mark the boundaries between different evolutionary paths (such as those leading to WDs, NSs or BHs) depends on the details of a specific evolutionary scenario, such as the initial metallicity and possible tidal interaction with a binary companion (e.g., [321, 448]). Moreover, they depend sensitively on the treatment of poorly understood processes such as the mixing of the stellar material, rotation, magnetic fields, and the formation of stellar winds (e.g.,[448]). In depth discussion of stellar evolution can be found in the textbooks by Clayton [100], Kippenhahn & Weigert [206] and Padmanabhan [321].

Having discussed some relevant aspects of the evolution of luminous stars, we now turn our attention to the evolution of compact stars – WDs and NSs – which, as we mentioned above, are products of the evolution of luminous stars.

Unlike luminous stars, compact stars are supported against self-gravity by the quantum degeneracy pressure of their constituent particles: While WDs are supported by the pressure of degenerate electrons, NSs are supported by degenerate nucleons and/or quarks (e.g., [370, 82]). Once formed and if isolated, these objects are essentially stable during most of their lifetime. However, if they are accreting matter from a binary companion, or if they are spinning down due to emission of electromagnetic and/or gravitational waves, their state may change over time. Accretion generally leads to an increase of the mass and angular momentum of the accreting star, while spin-down is associated with the reduction of the centrifugal support, making the NS becoming gradually more compact.

For accreting WD, the mass of the WD may reach the Chandrasekhar mass limit, at which point the pressure of the degenerate electrons can no longer support the star against its self-gravity[1]. This leads to contraction of the WD, leading either to thermonuclear explosion, or to collapse to a PNS. The main factor determining which route the WD follows is thought to be its composition.

Since carbon-oxygen WDs consist predominantly of elements, which are far from the peak of the nuclear binding energy curve, compression and heating soon lead to ignition of explosive thermonuclear fusion of the carbon at the WD center, resulting in complete disruption of WD, leaving no remnant[2]. Such thermonuclear supernovae (type Ia supernovae), depending on the type of their host galaxies, tend to be less prevalent than core-collapse supernovae [86], but are often more than ten times as luminous. The knowledge of their luminosities has enabled them to be used as distance indicators at high redshift. Such distance measurements have lead to the revolutionary discovery that the expansion of the Universe is accelerating [326, 346].

In a massive accreting oxygen-neon WDs approaching the Chandrasekhar mass limit, inverse beta decay becomes energetically favourable when the density reaches a value of $\sim 10^{9.7}$ g cm^{-3} [297, 415, 416]. This leads to quick reduction in the number of electrons, resulting in decreased pressure support and initiating collapse of the WD. Similarly to the collapse of oxygen-neon cores in normal stars, the WD collapses to a PNS, while the outer core material undergoes a delayed neutrino-driven supernova-like explosion. This is called accretion-induced collapse (AIC) of WDs.

One of mysteries of NSs is the structure of their cores above the nuclear matter density $\rho_{\rm nuc}$. For $\rho \lesssim \rho_{\rm nuc}$, the constituents of dense matter are well known (neutrons, protons and electrons). However, for $\rho \gtrsim \rho_{\rm nuc}$, the predictions of different plausible theories diverge with increasing density. The structure of matter at $5-10\rho_{\rm nuc}$, i.e., at densities characteristic for the centre of massive NSs, is not well known. Some theories of dense matter predict a strong softening of the EoS at $\rho \gtrsim 2\rho_{\rm nuc}$, caused by the appearance of

[1]We point out that the rotation increases the Chandrasekhar mass due to centrifugal support. Uniformly rotating WDs have ~ 5 % larger effective Chandrasekhar mass, while differentially rotating ones can be as massive as $\sim 3M_\odot$, limited above only by the onset of the non-axisymmetric rotational instabilities [96, 97, 153].

[2]Note that, if the accretion rate onto carbon-oxygen WD is very high, possibly $\dot{M} \gtrsim 10^{-6} M_\odot$ yr^{-1}, then the carbon burning may be ignited not at the WD centre, but in its envelope. In this case, the flame propagates inward to the centre, converting the carbon-oxygen WD into an oxygen-neon one [361].

hyperons or different phases of matter, such as pion or kaon condensates, or deconfined quark matter (for a review, see [439, 171, 181]). The prediction of observable signatures of the presence of exotic phases in the dense cores of NSs is therefore crucial for testing physical theories of hadronic matter at extreme densities.

The gradual increases of the central density of NSs either due to mass accretion or due to spin-down may lead to a phase transition of the core matter. The phase transition is generally accompanied by the softening of the EoS at high densities which results in a reduction of the pressure support in the NS core. This pressure reduction disturbs the equilibrium of the star and triggers a collapse leading either to resettling into a more compact state or, if the NS is close to the maximum mass limit, to formation of a BH. This process is called phase-transition-induced collapse (PTIC) of NSs.

In the next section, we will discuss the concept of gravitational waves, and show that stellar collapse can be a strong source for them.

1.2 Stellar collapse and gravitational radiation

Einstein put forward his discovery of wavelike vacuum solutions in general relativity (GR) in 1916, soon after establishing his new theory of gravity [135, 136, 137]. However, the physical existence of these *gravitational wave* (GW) solutions was disputed for a long time. Even Eddington thought for a long time that these solutions of the linearised Einstein equations were a mere coordinate effect and were propagating with the "speed of thought" rather than with the speed of light [133], but finally this clarified and GWs were commonly accepted as being physical. Although GWs have not yet been observed directly, there is strong indirect observational evidence supporting their existence from timing measurements of binary pulsars [440].

Unlike electromagnetic radiation, which represents oscillations of electromagnetic fields traveling though spacetime, GWs are oscillations of the spacetime fabric itself. In addition to this fundamental difference, there are other important features where electromagnetic and gravitational radiation differ (e.g., [249]). While electromagnetic waves produced by astrophysical sources are easily absorbed or scattered along the line of propagation by, e.g., the interstellar medium or the Earth's atmosphere, GWs travel nearly unperturbed due to their extremely weak interaction with any matter. The interaction of electromagnetic waves with matter is also responsible for the fact the they retain information predominantly about the thermodynamic state of the emitting outer layers of the source. Moreover, since their wavelength is typically much smaller than the spatial dimensions of the source, they represent local pictures of the emitting object. In contrast to them, GWs have wavelengths comparable to the size of their sources, and they carry information about the global coherent bulk motion of the emitting object. In other words, the content of information carried by electromagnetic waves and GWs coming to us from an astrophysical source are complementary to each other. Observing GWs from relativistic astrophysical sources such as, e.g., rotating NSs, coalescing binary BHs and NSs, or rotational stellar collapse will provide new insights into the dynamics as well as physics and astrophysics of their sources. Furthermore, just as radio astronomy revolutionized the astronomy and astrophysics in the second half of 20th century, GW astronomy could similarly open a new window onto the Universe in the near future.

We now give a rough estimate of the GW amplitude h to be expected from an astrophysical source. The amplitude h measures the average deviation of the actual spacetime away from flat spacetime in a region far from the source, and it can be represented as a "relative strain" of the GW in a spacetime. This strain causes a time dependent change Δl in the distance l between two test particles at a detector site (e.g., [249]):

$$h = \frac{2\Delta l}{l} \,. \tag{1.1}$$

Similarly to electromagnetic waves, gravitational radiation can be expanded into multipoles, where the mass

density plays the role of electric charge density in electromagnetic radiation. Similarly to the absence of electric monopole in electromagnetic radiation due to charge conservation, the corresponding "gravitational" mass monopole in gravitational radiation vanishes owing to mass conservation. Moreover, the time derivatives of the gravitational equivalent for the electric and magnetic dipole moments also vanish, as these moments correspond to linear and angular momenta, which are conserved for an isolated sources (e.g., [272]). Hence, the lowest and leading order of gravitational radiation should be produced by a time-varying mass quadrupole moment. At this order, the wave amplitude is proportional to the second time derivative of the mass quadrupole moment Q divided by the distance to the source R:

$$h \sim \frac{G}{c^4}\frac{\ddot{Q}}{R}\,, \tag{1.2}$$

where c is the speed of light and G is the gravitational constant. In order to obtain a rough estimate of the amplitude of GWs from a source like a collapsing star, we approximate the quadrupole moment Q by

$$Q \sim ML^2\,, \tag{1.3}$$

where M is the mass of the source and L is its characteristic size. For a system in which the constituent masses move from one side of the system to the other in an average time T, the second time derivative of quadrupole moment can be approximated as

$$\ddot{Q} \sim \frac{2ML^2}{T^2} \sim 4MV^2\,, \tag{1.4}$$

where V is the average internal velocity of the source. From this we get an estimate for the GW amplitude:

$$h \sim \frac{4GMV^2}{c^4R}\,. \tag{1.5}$$

Expressions (1.4)-(1.5) show that the amplitude of GWs is severely suppressed by the coefficient $G/c^4 \sim 10^{-49}$ and that the variation of the mass quadrupole can be considerable only for very *large masses* moving at *relativistic speed*. Clearly, these conditions cannot be reached by sources in terrestial laboratories, but can easily be met by astrophysical phenomena such as stellar collapse of or to NSs, which therefore becomes one of the most promising sources of gravitational radiation.

In stellar collapse (such as collapse of degenerate stellar cores, WDs and NSs) most of the gravitational binding energy released during the infall which does not go to neutrino emission will be transferred into radial motion. For a non-rotating object, motion along the radial coordinate does not involve change in the quadrupole moment, hence non-rotating collapse does not emit GWs. In rotating collapse, however, even purely radial motion *does* imply change in quadrupole moment of the star, hence accelerated collapse *does* produce gravitational radiation. In this case, the energy radiated away in GWs due to quadrupole motion has a maximum of $\sim 10^{-7}M_\odot c^2$ (see, e.g., [310, 466, 123, 111, 3, 1]). This then translates into a GW amplitude of $h \sim 10^{-23}$ at a distance of 15 Mpc. The frequency of the radiation will be in the so-called high frequency band ranging from 100 to 1000 Hz, which corresponds to the typical timescales of the oscillatory motion in PNSs. A signal from the coalescence of two BHs of several solar masses is predicted to be in the same frequency scale, but its amplitude would be a few orders of magnitude larger [144], since the BHs are much more compact and the nonsphericity of such a system is much greater. Nevertheless, GW emission from stellar collapse of the types mentioned above is one of the most promising sources for ground-based detectors.

There are two classes of detectors which are capable of measuring such a small length differences caused by gravitational waves from stellar collapse: *resonant mass* and *interferometric* detectors. Resonant mass

detectors use massive bars or spheres tuned to a rather narrow frequency band, where their sensitivity is quite high. This type of detector goes back to a prototype by Joseph Weber built in the 1960s. Several of these detector projects are currently operating in various countries. However, due to their narrow bandwidth they are not ideal for detecting the GW burst signal from stellar core collapse, because that will not be a clean signal but rather a superposition of many frequencies, which will probably vary significantly with each stellar collapse event.

The most promising observational tools available at present or in the near future for detecting GWs from stellar collapse are ground-based interferometers, several of which are operational at present on sites in the USA (the LIGO detectors), Italy (the Italian-French collaboration VIRGO), Germany (the joint German-UK project GEO600), Japan (the TAMA project), and Australia (the AIGO project). Each of these detectors consists of four massive mirror test masses on two perpendicular arms suspended on vibration-isolated supports to damp seismic noise. The change of the separation between the masses can be measured to rather high precision by a laser, which is split to run through optical cavities in the two interferometer arms and is reflected by the mirror masses. When a GW passes through the detector, not only can its amplitude (which translates into a displacement of the mirrors) be measured as long as the detector is sensitive enough, but also its polarization can be determined by two or more detectors. It has been estimated that the GW signal from a Galactic stellar collapse of the types mentioned above is within range of detectability [310, 466, 123, 111, 3, 1]). As advanced detectors with improved sensitivity (like advanced LIGO) will become operational in the near future, the prospects of detection will grow considerably. Such observations could provide information for testing our current understanding of stellar evolution and stellar collapse, as well as significantly extending our knowledge about the detailed physics involved. More specifically, prospective GW astronomy with stellar collapse could extend our knowledge in the following areas:

(i) There is an intriguing prospect of extracting some information about the poorly known properties of the EoS of $\rho \gtrsim \rho_{\rm nuc}$ nuclear matter from observation of the GW signal produced in rotating stellar collapse. In collapse of degenerate stellar cores and WDs to NSs as well as PTIC of NSs, the collapsing object does not come to rest immediately when it reaches the new quasi-equilibrium state. Instead, it overshoots this configuration and settles down to this after a series of ring-down oscillations. The frequencies of these oscillations, which are imprinted in the GW signal, depend on the properties of the high-density nuclear matter. Hence, extraction of the oscillation frequencies from the GW signal could, in principle, be used to put some constraints on the properties of $\rho \gtrsim \rho_{\rm nuc}$ matter (see, e.g., [40, 120] and references therein).

(ii) The detection rate of GW signals from stellar collapse of a given type would give a measure of its occurrence rate. The knowledge of the event rate, in turn, is of fundamental importance in many areas of astrophysics and cosmology. For example, estimates of the population of AIC and type Ia supernova progenitors depend sensitively on the treatment of the poorly understood *common envelope phase*, in which the WD orbits around the companion star inside the envelope of the latter (e.g., [459]). Therefore, knowledge of the event rate could put some constraints on the models of the common envelope phase.

(iii) GWs emited in stellar collapse contain information about the progenitor of the collapsed stars. For example, AIC of WDs is believed to occur in binary systems of either double WDs or of a WD and a normal star. The extraction of rotation of the collapsing WD from the GW signal could, in some cases, shed some light on the of the precollapse conditions in accreting white dwarfs.

(iv) The explosion mechanism of massive stars is not yet fully understood. Although the delayed neutrino mechanism seems to be a main explosion mechanism operating in slowly rotating stars, the importance of a number of other processes which could also play a role in explosions (e.g., [254]) remains to be explored. Moreover, the explosion mechanism in rotating stars is not well understood at present. The detection of GW signal could shed some light on the explosion mechanism (for a recent review on this, see [316]).

The prime aim of the work presented here is to study the dynamics of accretion-induced collapse of WDs and PTIC of NSs as well as the associated GW emission. Our study is based on axisymmetric hydro-

dynamics simulations in general relativity. The latter is necessary for accurately modelling the dynamics and GW emission. We perform parameter studies by considering collapse simulations for a large set of models and explore the dependence of the collapse dynamics and GW emission on as many uncertain and free parameters are possible. These parameters include the rotation and compactness of the progenitor, the stiffness of the $\rho \gtrsim \rho_{\rm nuc}$ matter, etc. We also discuss the inversion problem, i.e., the problem of extracting information about the parameters of the collapsing system from the features of the emitted GW signal. Finally, where possible we discuss astrophysical implications of our results, even those not necessarily related to the emission of GWs.

1.3 The magnetosphere of oscillating neutron stars

The traces of NS oscillations can be imprinted not only in the emitted GW signal, but also in the electromagnetic radiation [320, 424, 66, 51, 125, 131]. The latter again can contain information about the EoS of high-density matter in the NS core. We present work on this as a second topic of this thesis.

Study of gamma-ray flare activity in Soft Gamma-Ray Repeaters (SGRs) [444, 437] – which are thought to be the very highly magnetised NSs known as magnetars – have revealed that their spectrum manifests a number of quasi-periodic oscillations (QPOs) with frequencies in the range from a few tens of Hz up to a few hundred Hz [197, 394, 436]. The giant flares in these objects are thought to be powered by global reconfigurations of the magnetic field and it has been suggested that this might excite global seismic pulsations of the magnetar crust [411, 412, 369, 131]. There is presently substantial evidence that the observed SGR QPOs are caused by NS pulsations [167, 362, 226, 383, 384]. However, there remain a great deal of uncertainty about how stellar surface motion gets transformed into the observed features of the radiation [393, 394, 421]. To make progress with this, it is necessary to develop a better understanding of the processes happening in the magnetospheres of oscillating NSs.

Standard pulsars typically have magnetic fields of around 10^{12} G while magnetars may have fields of up to $10^{14} - 10^{15}$ G near to the surface. Rotation of a magnetized star generates an electric field $E^{\rm rot} \sim \frac{\Omega R}{c} B$, where B is the magnetic field strength, c is the speed of light, Ω is the angular velocity, and R is the radius of the star. Depending on the rotation velocity and the magnetic field strength, the electric field at the surface may be as strong as 10^{10} V cm^{-1} and have a longitudinal component (parallel to B) which can be able to pull charged particles away from the stellar surface and accelerate them up to ultra-relativistic velocities. This result led Goldreich & Julian [173] to suggest that a rotating NS with a sufficiently strong magnetic field should be surrounded by a magnetosphere filled with charge-separated plasma which screens the accelerating electric field and thus hinders further outflow of charged particles from the stellar surface [395, 354] (a detailed discussion of of pulsar models can be found in textbooks [267, 44, 45]).

Timokhin, Bisnovatyi-Kogan & Spruit (2000) [418] showed that an oscillating magnetized NS should also have a magnetosphere filled with charge-separated plasma, even if it is not rotating, since the vacuum electric field induced by the oscillations would have a large radial component which can be of the same order as the rotationally-induced electric fields. Against this background, [418] developed a formalism extending the basic aspects of the standard pulsar model to the situation for a non-rotating magnetized NS undergoing arbitrary oscillations. [418] applied their formalism to toroidal oscillations of a NS with a dipole magnetic field (toroidal oscillations are thought to be particularly relevant for magnetar QPO phenomena), and calculated the electromagnetic field and charge density in the magnetosphere. They estimated the energy losses due to plasma outflow caused by some of these modes, and found that the energy losses are strongly affected by the magnetospheric plasma.

The aim of the work on this presented here is to give a general relativistic reworking of the model of [418] so as to investigate the effects of the changes with respect to the Newtonian treatment.

1.4 Organization of this thesis

This thesis is structured as follows:

In Chapter 2 we give an overview of the methods used. In Section 2.1 we give an introduction to the Einstein equations in the Arnowitt-Deser-Misner $\{3+1\}$ formalism. This section is also devoted to the discussion of the conformally flat (CFC) approximation of GR, which was used for the simulations presented in this work. In Section 2.2, we discuss the GR system of hydrodynamic conservation equations. The numerical implementation of the hydrodynamics and metric equations is discussed in Section 2.3. We discuss the quadrupole formula for the extraction of GW, which we use in our calculations, in Section 2.3.8.

In Chapter 3 we present our work on the phase-transition-induced collapse of NSs. In Section 3.3 we introduce the initial models investigated. In Section 3.5 we discuss the results of our simulations, and we conclude with a summary in Section 3.6.

In Chapter 4 we presented the results of simulations of the AIC of WDs. In Sec. 4.2, we describe the numerical methods employed for generation of our 2D rotational-equilibrium precollapse WD models and the parameter space of WD structure and rotational configuration investigated. We go on to discuss the overall AIC dynamics in the collapse and bounce phase as well as the associated GW emission in Secs. 4.3 and4.4. In Sec. 4.6 we conclude with a summary.

Chapter 5 is devoted to the discussion of our work the magnetosphere of oscillating NSs. In Section 5.2 we derive the quasi-stationary Maxwell equations in Schwarzschild spacetime. In Sections 5.3-5.4 we solve analytically the Maxwell equations for arbitrary NS oscillations with a generic magnetic field configuration and consider the case of purely toroidal oscillations of a NS with a dipole magnetic field. In Sec. 5.5 we calculate the energy losses due to plasma outflow caused by the toroidal oscillations and discuss the role of the GR effects. The summary of the results is given in Sec. 5.6.

This thesis is summarized in Chapter 6, particularly focusing on future directions for continuing and extending the work presented here.

1.5 Conventions and Units

The unit system used in the sections that discuss numerical relativity and general relativistic hydrodynamics is fixed by taking $c = G = M_\odot$, where c is the speed of light, G is the Newtonian gravitational constant and $M_\odot$ is the mass of the Sun. All sections discussing numerical results and all sections related to astrophysics are kept in standard cgs units. Greek indices are taken to run from 0 to 3, while Latin indices run from 1 to 3. We abbreviate, where convenient, the partial derivative $\partial/\partial x^i$ using $,i$ or ∂_i and the covariant derivative ∇_i using $;i$. Repeated indices are summed over according to the Einstein summation convention. The signature of the metric is assumed to be $(-,+,+,+)$. Four-vectors v^μ are called timelike if $v_\mu v^\mu < 0$, and space-like if $v_\mu v^\mu > 0$. We use $g_{\mu\nu}$ as the four-metric, while γ_{ij} is used for the spatial three-metric.

Chapter 2

Methodology

2.1 The Einstein field equations in $\{3+1\}$ formalism

In Einstein's Theory of General Relativity, the gravity manifests itself as a curvature of four-dimensional spacetime (one temporal, three spatial dimensions). The gravity described by curvature is created in a non-linear way by the mass-energy of matter or by gravity itself and changes when the energy-momentum (including rest-mass energy, kinetic energy, electro-magnetic field energy etc.) changes. This curvature completely governs the motion of mass-energy in the absence of other forces, such as strong, electromagnetic and weak interactions. In contrast to Newtonian theory where gravitational action is instantaneous, changes in the "gravitational field" propagate in vacuum at the finite speed of light.

GR is described by differential geometry in which the spacetime is treated as a four-dimensional manifold $\mathcal{M}$ on which a metric $g_{\mu\nu}$ (and its inverse $g^{\mu\nu}$) is defined. One can then introduce an invariant line element measuring the physical distance between two infinitesimally separated spacetime events:

$$ds^2 = g_{\mu\nu} dx^\mu dx^\nu \,, \tag{2.1}$$

where the dx^α are the components of the separation vector $\boldsymbol{dx}$ between the two events. The Einstein equations relate the spacetime curvature – specified in the Einstein's tensor $G_{\mu\nu}$ – with the energy-momentum tensor $T_{\mu\nu}$ of the mass mass-energy distribution in the spacetime:

$$G_{\mu\nu} \equiv R_{\mu\nu} - \frac{1}{2} g_{\mu\nu} R = \frac{8\pi G}{c^4} T_{\mu\nu} \,, \tag{2.2}$$

where $R = R^\alpha_\alpha$ is the Ricci scalar, $R_{\mu\nu} = R^\alpha_{\mu\alpha\nu}$ is the Ricci tensor and $R^\alpha_{\mu\beta\nu}$ is the Riemann curvature tensor. The latter is obtained from the connection coefficients, the *Christoffel symbols* $\Gamma^\sigma_{\mu\nu}$:

$$R^\sigma_{\mu\rho\nu} \equiv \Gamma^\sigma_{\mu\nu,\rho} - \Gamma^\sigma_{\mu\rho,\nu} + \Gamma^\sigma_{\tau\rho}\Gamma^\tau_{\mu\nu} - \Gamma^\sigma_{\tau\nu}\Gamma^\tau_{\mu\rho} \,, \tag{2.3}$$

where the quantities $\Gamma^\sigma_{\mu\nu}$ are defined in terms of the metric as:

$$\Gamma^\sigma_{\mu\rho} \equiv \frac{1}{2} g^{\sigma\tau} \left(g_{\rho\tau,\mu} + g_{\mu\tau,\rho} - g_{\mu\rho,\tau} \right) \,. \tag{2.4}$$

Note that the forms of equations (2.2)-(2.3) are covariant, that is, they are independent of the choice of coordinates. In GR, all coordinate systems and frames of reference are treated on an equal footing. However, in order to solve these equations numerically, one has to adopt an appropriate coordinate system. Unlike to Special Relativity and Newtonian theory, the concept of a global inertial frame is not valid in GR.

In spite of their seeming simplicity, the Einstein equations (2.2) represent a complicated set of 10 coupled non-linear partial differential equations ($G_{\mu\nu}$ is a symmemtric tensor). The Einstein equations have analytical solutions only in the case of simplified and idealized physical configurations (e.g., static spherically-symmetric solution by Schwarzschild, stationary axi-symmetric solution of Kerr and Friedmann-Lamaitre-Robertson-Walker solution of a homogeneous, isotropically expanding or contracting universe. A thorough discussion of exact solutions can be found in, e.g., [272, 244]). In most of astrophysically interesting scenarios it is necessary to solve the Einsteins equations numerically.

2.1.1 The Arnowitt-Deser-Misner $\{3+1\}$ formalism

In numerical relativity, the Einstein equations are most commonly formulated as an initial-value evolution problem. A formalism of this type, known as the ADM formalism, was introduced by Arnowitt, Deser and Misner [17, 458], based on the $\{3+1\}$ splitting of spacetime by Lichnerowics [227]. In the following, we will only outline the most essential aspects of the ADM formalism. A much more thorough derivation and discussion may be found, for example, in York's seminal article from 1979 [458], in the review article by Baumgarte and Shapiro [34] and in the textbook by Alcubierre [10]. Parts of the following discussion have already appeared in similar form in the dissertations of Baiotti [20], Dimmelmeier [116] and Ott [310].

The ADM $\{3+1\}$ formalism is based on splitting the four-dimensional spacetime manifold $\mathcal{M}$ into a continuous sequence of non-intersecting three-dimensional spacelike hypersurfaces (slices) Σ_t. Each of these t-parametrized time slices Σ_t encompasses the entire three-dimensional space. Such a decomposition separates "space" from "time", taking a step backwards from the elegance of the Einstein's original covariant formulations, but enabling GR to be viewed as a more appropriate dynamical field theory. In doing so, we have defined a Cauchy problem, that is, if the appropriate initial data on some slice Σ_t and boundary conditions for all other $\Sigma_{t'>t}$ are specified, then the time evolution of the initial data is determined (see, e.g., [433]).

We define a future-directed timelike unit vector $\boldsymbol{n}$ orthonormal to the slices Σ_t: $\boldsymbol{n} = -\alpha\nabla t$, where α is the *lapse function* that determines how much *proper* time elapses between timeslices along the normal vector $\boldsymbol{n}$. Furthermore, we introduce a coordinate basis for the entire spacetime manifold $\mathcal{M}$:

$$\left\{\boldsymbol{e}_{(\mu)}\right\} = \left\{\boldsymbol{e}_{(0)}, \boldsymbol{e}_{(t)}\right\} \,, \tag{2.5}$$

where $\boldsymbol{e}_{(i)}$ is a purely spatial vector and is tangent to the slices Σ_t at any point (i.e., orthogonal to the unit-normal $\boldsymbol{n}$). In these coordinates, an event $\boldsymbol{x}$ has components $x^\mu = (t, x^i)$. The invariant line element connecting two events x^μ and x'^μ on infinitesimally separated slices Σ_t and Σ_{t+dt} is then given by

$$ds^2 = -\left(d\hat{t}\right)^2 + \left(d\hat{x}\right)^2 \,, \tag{2.6}$$

where $d\hat{t}$ and $d\hat{x}$ are the changes in physical time and physical distance, respectively. From the above definition of the lapse, one can obtain the following relation

$$d\hat{t} = \alpha dt \,. \tag{2.7}$$

The spatial location of an observer momentarily at rest in Σ_t with coordinates x^i can generally be related to the spatial locations x'^i at Σ_{t+dt} via $x'^i = x^i - \beta^i dt$, where β^i is an arbirary spatial vector, tangent to Σ_t. In the original coordinate labeling, we get the following relation:

$$d\hat{x}^i = dx^i + \beta^i dt \,. \tag{2.8}$$

where dx^i is the coordinate distance and β^i represents the coordinate *shift*. Hence, the shift vector β^i determines by how much spatial coordinates are shifted with respect to normal observer between timeslices.

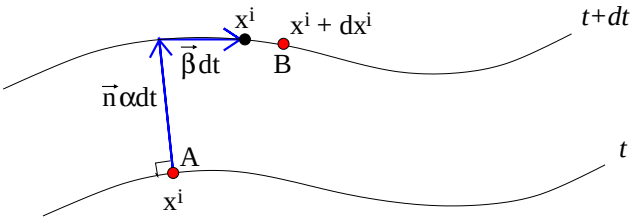

Figure 2.1: Schematic representation of the $\{3+1\}$ foliation of spacetime. Spacelike slices Σ_t are connected by local unit normal vectors n^μ along which time is evolved at rate α. The change of coordinate labels are expressed by the coordinate shift vector β^i. The figure is taken from Shapiro's review paper from 2005 [371].

Using the above choice of $\left\{\mathbf{e}_{(\mu)}\right\}$ and the definitions of α and β^i, we can write the coordinate representation of the timelike contravariant unit vector n^μ normal to Σ_t:

$$n^\mu = \left(\frac{1}{\alpha}, -\frac{\beta^i}{\alpha}\right) . \tag{2.9}$$

Due to arbitrariness of the shifts β^i, the world line of a general observer does not need to be normal to Σ_t. Instead, its tangent is given by the timelike unit vector

$$t^\mu = \alpha n^\mu + \beta^\mu . \tag{2.10}$$

Figure 2.1 schematically depicts the geometrical interpretation of the foliation, lapse and shift.
The general line element (2.1) can now be decomposed in $\{3+1\}$ manner:

$$ds^2 = g_{\mu\nu}dx^\mu dx^n u \equiv -\alpha^2 dt^2 + \gamma_{ij}(dx^i + \beta^i dt)(dx^j + \beta^j dt) , \tag{2.11}$$

where γ_{ij} is the 3-metric that represents the spatial part of the 4-metric: $\gamma_{ij} = g_{ij}$. The 4-metric now takes the following form:

$$g_{\mu\nu} = \begin{pmatrix} -\alpha^2 + \beta_i\beta^i & \beta_i \\ \beta_j & \gamma_{ij} \end{pmatrix} , \tag{2.12}$$

where $\beta_i = \gamma_{ij}\beta^j$ and the inverse metric writes

$$g^{\mu\nu} = \begin{pmatrix} -\alpha^{-2} & -\alpha^{-2}\beta^i \\ -\alpha^{-2}\beta^j & \gamma^{ij} - \alpha^{-2}\beta^i\beta^j \end{pmatrix} . \tag{2.13}$$

In order to project a general four-dimensional vector and a tensor that reside on $\mathcal{M}$ onto Σ_t, one has to use the projection tensor

$$\perp^\mu_\nu = g^\mu_\nu + n^\mu n_\nu , \tag{2.14}$$

which is orthogonal to $\mathbf{n}$: $\perp \cdot \mathbf{n} = 0$.

2.1.2 Eulerian observers, Eulerian 3-velocities, physical 3-velocities

We now introduce the concept of *Eulerian* observers (see, e.g., [458, 34, 10]). Eulerian observers are at rest in the slice Σ_t, have four-velocities parallel to $\boldsymbol{n}$ and have $\boldsymbol{n}$ as their 3-velocity. For future reference in the

section on GR hydrodynamics (§2.2), we define the 3-velocity of a fluid (or anything else) as measured by an Eulerian observer:

$$v^i = \frac{\perp^i_p u^\rho}{-\boldsymbol{n}\cdot\boldsymbol{u}} = \frac{u^i}{\alpha u^0} - n^i = \frac{u^i}{W} + \frac{\beta^i}{\alpha}\,, \tag{2.15}$$

where the fluid 4-velocity $\boldsymbol{u}$ is defined as $u^\mu = dx^\mu/d\hat{t}$ with $\hat{t}$ being the physical (or proper) time. We have used equation (2.9) and the condition $n_\mu n^\mu = -1$ to write $\boldsymbol{n}\cdot\boldsymbol{u} = \alpha u^0$, where αu^0 is the Lorentz factor W satisfying

$$W = \frac{1}{\sqrt{1 - v^i v_i}}\,. \tag{2.16}$$

Other quantities which will be useful in a later section (§2.2) are the covariant components of the Eulerian coordinate 3-velocity

$$v_i = \frac{\perp^\rho_i}{-\boldsymbol{n}\cdot\boldsymbol{u}} = \frac{u^i}{W}\,. \tag{2.17}$$

In general coordinate bases in GR, the magnitude of the Eulerian 3-velocity vector is limited by the speed of light, but its components, in general, are not. A simple example that demonstrates this is Minkowski spacetime in spherical coordinates where $ds^2 = -dt^2 + dr^2 + r^2(d\theta^2 + \sin^2\theta d\phi^2)$ and $\vec{v} = [v^r, v^\theta, v^\phi]^{\rm T}$. In these coordinates, the angular velocity components may become arbitrarily large for $r \to 0$. It is then useful to define a *physical velocity* as the 3-velocity $\hat{v}^i$ measured by an Eulerian observer in a local orthonormal coordinate system which can be introduced at any point on the spacelike hypersurface Σ [272]. Each of the components of this $\hat{v}^i$ are limited by the speed of light and thus $\hat{v}^i\hat{v}_i < c$ as well. To obtain $\hat{v}^i$, one calculates a transformation tensor A^{ij} to diagonalize the 3-metric γ_{ij}. The physical velocity components are then given by

$$\hat{v}^i = \hat{v}_i = \sqrt{\hat{\gamma}_{ij}} A^{ij} v_j\,, \tag{2.18}$$

where $\hat{\gamma}_{ij}$ is the diagonalized 3-metric and no summation over the index i is carried out here.

2.1.3 Extrinsic curvature and the ADM equations

It is clear that the decomposition of Einstein's equations into a $\{3+1\}$ form will require expressing the four-dimensional Riemann tensor $R^\alpha_{\mu\beta\nu}$ in terms of its three dimensional counterpart. It is also clear, however, that the latter cannot contain all of the relevant information because it is a purely spatial object (and can be computed from spatial derivatives of the spatial metric alone), while $R^\alpha_{\mu\beta\nu}$ is the spacetime object which also contains time-derivatives of the four-dimensional metric. This missing information is expressed by a tensor called the *extrinsic curvature*, which describes how the spacelike hypersurface Σ_t is embedded in the spacetime $\mathcal{M}$ (see, e.g., York [458], Baumgarte & Shapiro [34], and Alcubierre [10]). The extrinsic curvature can be defined as

$$K_{ij} \equiv -\frac{1}{2}\mathcal{L}_{\boldsymbol{n}}\gamma_{ij} = \gamma^l_i\gamma^k_j n_{(l;k)}\,, \tag{2.19}$$

where $\mathcal{L}_{\boldsymbol{n}}$ is the *Lie derivative* along the unit-normal vector $\boldsymbol{n}$ on Σ_t[1]. The semicolon denotes covariant differentiation ($x_{;i} = \nabla_\mu x^i$) with respect to the 3-metric γ_{ij} and the round brackets around $(l;k)$ denote symmetrization in l and k. The Lie derivative may be thought of as the geometric generalization of the partial time derivative ∂_t and its definition is derived from the properties of parallel transport on general curved

[1]The Lie derivative of a general tensor $T^{a_1,\ldots,a_n}_{b_1,\ldots,b_m}$ along a vector $\boldsymbol{w}$ is defined (in component notation) as (see, e.g., [184, 433, 368])

$$\mathcal{L}_{\boldsymbol{w}} T^{a_1,\ldots,a_n}_{b_1,\ldots,b_m} = w^r T^{a_1,\ldots,a_n}_{b_1,\ldots,b_m;r} - \sum_{i=1}^{n} T^{a_1,\ldots,r,\ldots,a_n}_{b_1,\ldots,b_m} w^{a_i}_{;r} + \sum_{i=1}^{n} T^{a_1,\ldots,a_n}_{b_1,\ldots,r,\ldots,b_m} w^r_{;b_i}\,. \tag{2.20}$$

manifolds. An introduction to the Lie derivative and its geometric meaning can be found, for example, in [433, 368].

In York's form of the ADM equations [458], the Einstein equations (2.2) are rewritten as a first-order in time and second-order in space system of partial differential hyperbolic *evolution equations* and a set of four elliptic *constraint equations*. The evolved variables are the 3-metric γ_{ij} and the extrinsic curvature K_{ij}:

$$\left(\frac{\partial}{\partial t} - \mathcal{L}_\beta\right)\gamma_{ij} = -2\alpha K_{ij}\,, \tag{2.21}$$

$$\left(\frac{\partial}{\partial t} - \mathcal{L}_\beta\right)K_{ij} = -\alpha_{;ij} + \alpha\big[R_{ij} + KK_{ij} - 2K_{im}K^m_j - 8\pi\left(S_{ij} - \frac{1}{2}\gamma_{ij}S\right) - 4\pi\rho_{\rm ADM}\gamma_{ij}\big]\,, \tag{2.22}$$

where R_{ij} is the 3-Ricci tensor, $K \equiv \gamma^{ij}K_{ij}$ is the trace of the extrinsic curvature, $\rho_{\rm ADM} \equiv n_\mu n_\nu T^{\mu\nu}$ is the total energy density as measured by an Eulerian observer, and $S_{ij} \equiv \gamma_{i\mu}\gamma j\nu T^{\mu\nu}$ is the projection of the stress-energy tensor onto ${\Sigma_t}^2$.

Equation (2.21) most clearly illustrates the above interpretation of the extrinsic curvature as the "time derivative" of the 3-metric. However, when switched from slice Σ_t to Σ_{t+dt}, it may still differ by an arbitrarily coordinate shift. This is expressed by the Lie derivative along β. Intuitively, equation (2.22) represents the "acceleration" of γ_{ij}, that is, the time variation of the time variation of the 3-metric.

In addition to the above evolution equations for the 3-metric and the extrinsic curvature, the ADM decomposition yields four elliptic constraint equation (the *constraints*) that must be satisfied on each spacelike hypersurface. The constraints are related to the conservation of energy and momentum[3]. The Hamiltonian constraint equation is

$$R + K^2 - K_{ij}K^{ij} - 16\pi\rho_{\rm ADM} = 0\,, \tag{2.23}$$

where R is the 3-Ricci scalar. The three momentum constraints are given by

$$K^{ij}_{;j} - \gamma^{ij}K_{;j} - 8\pi S^i = 0\,, \tag{2.24}$$

where $D^i \equiv -\gamma^{i\mu}n^\nu T_{\mu\nu}$ is the momentum density as seen by an Eulerian observer.

It can be shown that if the constraint equations are satisfied initially at $t = 0$, they should also be satisfied at $t > 0$ [156]. This statement, however, holds only in the idealized continuum case [458, 98, 99, 155]. In a discretized scheme, numerical errors such as round-off, truncation and discretization errors lead to violation of the constraints, and, if the numerical scheme is unstable, these errors can become arbitrarily large. Therefore, in order to solve the $\{3+1\}$ evolution equations numerically, one must have some discretization of the equations that would guarantee that the discretized constraint equations remain satisfied to sufficient accuracy during the time-evolution.

In practice, one can take three different approaches to the problem of choosing which set of equations to solve numerically. The first approach is know as *free evolution* in which one starts with a solution of the constraint equations as initial data, and later advances in time by solving all of the evolution equations for γ_{ij} and K_{ij}. The constraints are then monitored only to see how much they are violated during the

[2]Note that Arnowitt et al. (1962) originally derived these equations in terms of the conjugate momenta π_{ij} instead of the extrinsic curvature.

[3]Energy and momentum, in general, can only be measured locally by observers and hence cannot be defined unambiguously in GR unless special conditions are met (see, e.g., the extensive discussion in Misner, Thorne & Wheeler [272]). In an asymptotically flat spacetime - a spacetime in which the curvature vanishes at large distances from some region so that at large distances the geometry becomes essentially that of a Minkowski spacetime - it is possible to define a total energy and total angular momentum [272, 285]

evolution, which gives a rough idea of the accuracy of the simulation. Alternatively, we can choose to solve some or all of the constraint equations at each time step for a specific subset of the components of the metric and extrinsic curvature, and evolve the remaining components using the evolution equations. This second approach is known as *constrained evolution.*

Constrained evolution is in fact well suited for situations which possess a high degree of symmetry, like spherical symmetry, but is much harder to use in the case of fully three-dimensional systems. Moreover, the mathematical properties of a constrained scheme are much more difficult to analyze in the sense of studying the well-posedness of the system of equations [10]. And finally, since the constraints involve elliptic equations, a constrained scheme is also more expensive and slower to solve numerically in three dimensions than a free evolution scheme.

In the numerical simulations presented in this work, we choose the third alternative known as *constrained metric evolution.* In this approach, we choose an extra condition on the spatial metric tensor, namely the conformal flatness condition (CFC) [196], and impose this condition during the time evolution, thus simplifying considerably the equations to be solved. Imposing this extra condition on the metric is not, in principle, equivalent to the Einstein field equations, and the results of such simulations should be regarded as approximations even in the continuum limit. However, comparison of simulations performed in the CFC approximation with the ones in full GR have revealed that the CFC approximation is of excellent quality for spacetimes that does not deviate too much from spherical symmetry. In particular, for spacetimes of any relativistic stars, even those with high degree of compactness and rapid rotation, the CFC approximation yields results which are practically identical to those of full GR calculations [310, 311, 312]. Therefore, the use of CFC approximation in our simulations is well justified. In the following section, we shall discuss the CFC metric equations in more detail.

2.1.4 Conformally flat approximation to general relativity

In the CFC approximation to general relativity, which was introduced by Isenberg [196] and first used by Wilson et al. [441], the ADM spatial 3-metric is replaced by the conformally flat 3-metric:

$$\gamma_{ij} = \phi^4 \eta_{ij} \tag{2.25}$$

where η_{ij} is the flat-space metric, hence $\eta_{ij} = \delta_{ij}$ in Cartesian coordinates and $\eta_{ij} = \mathrm{diag}(1, r^2, r^2 \sin^2\theta)$ in spherical coordinates. The condition expressed in (2.25) is called conformally flatness condition (CFC). ϕ is the conformal factor and it appears in its fourth power in equation (2.25) due to a convention that simplifies the ADM equations (introduced in Section 2.1.3). We now fix the coordinates by imposing the so-called maximal slicing gauge condition on the lapse function (which translates into a condition for the trace of the extrinsic curvature $K = K^i_i = 0$). With this choice of gauge, the Hamiltonian and the momentum constraints decouple and the ADM equations in the CFC approximation reduce to the following set of equations [441]:

$$\hat{\Delta}\phi = -2\pi\phi^5 \left(\rho h W^2 - p + \frac{K_{ij}K^{ij}}{16\pi} \right) , \tag{2.26}$$

$$\hat{\Delta}(\alpha\phi) = 2\pi\alpha\phi^5 \left(\rho h (3W^3 - 2) + 5\frac{7K_{ij}K^{ij}}{16\pi} \right) , \tag{2.27}$$

$$\hat{\Delta}\beta^i = 16\pi\alpha\phi^4 S^i + 2\phi^{10} K^{ij} \hat{\nabla}_j \left(\frac{\alpha}{\phi^6} \right) - \frac{1}{3}\hat{\nabla}^i \hat{\nabla}_k \beta^k , \tag{2.28}$$

where $\hat{\nabla}$ and $\hat{\Delta}$ are the flat-space Nabla and Laplace operators, respectively. We point out that approximating GR with the CFC implies that the time derivatives of the trace-free part of γ_{ij}, i.e., the off-diagonal

components, have to vanish, leading to the following condition for the components of the extrinsic curvature tensor

$$K_{ij} = \frac{1}{2\alpha}\left(\nabla_i\beta_j + \nabla_j\beta_i - \frac{2}{3}\gamma_{ij}\nabla_k\beta^k\right) , \tag{2.29}$$

where ∇ is the covariant derivative with respect to γ_{ij}.

The CFC metric equations (2.26)-(2.28) are five Poisson-like equations for the metric components ϕ, α, and β. However, while a system of genuine Poisson equation is linear and its equations are independent of each other, each of the metric equations of the system (2.26)-(2.28) couple to each other via their right hand sides, and, in the case of the equations for β^i, couple additionally via the operator $\hat{\Delta}$ acting on β^i. The equations are dominated by the source terms involving the hydrodynamic quantities ρ, p, and v^i, whereas the nonlinear coupling through the other, purely metric, source terms only becomes important for strong gravity.

By approximating the three-metric by a conformally flat one, the complexity of solving the full set of Einstein evolution and constraint equations is reduced to solving five not explicitly time-dependent equations. On each time slice, the metric is solely determined by the instantaneous hydrodynamic state, i.e., the distribution of matter and its momentum in space. Compared to the general system of evolution and metric equations, the number of terms involving time derivatives is reduced significantly. Therefore, the CFC approximation allows for more stable numerical evolution schemes. In the simulations using CFC, no severe problems with numerical instabilities were encountered [119].

However, the original formulation of the CFC metric equations (2.26)-(2.28) proposed by Wilson et al. [441] suffers from a mathematical non-uniqueness problem when the configurations become too compact. Such a situation is encountered, for example, in the case of the collapse of a stellar core or a (proto-) neutron star to a black hole even before the formations of the apparent horizon. This issue has in the past been prohibitive for successfully applying such a formulation to numerical simulations of astrophysical problems involving very compact objects like black holes. Recently, Cordero-Carrión et al. [107] proposed a reformulations of the original CFC metric equations (2.26)-(2.28) that has the fundamental property of overcoming the local non-uniqueness problem. In the formulation of [107], the original CFC metric equations (2.26)-(2.28) are rewritten by introducing an auxiliary vector field W^i:

$$\hat{\Delta}\phi = -2\pi\phi^5\left(\rho h W^2 - p\right) - \phi^{-7}\frac{\hat{K}_{ij}\hat{K}^{ij}}{8} , \tag{2.30}$$

$$\hat{\Delta}(\alpha\phi) = 2\pi\alpha\phi^5\left[\rho h(3W^3 - 2) + 5p\right] + \alpha\phi^{-7}\frac{7\hat{K}_{ij}\hat{K}^{ij}}{8} , \tag{2.31}$$

$$\hat{\Delta}\beta^i = 2\hat{\nabla}_j\left(2\alpha\phi^{-6}\hat{K}^{ij}\right) - \frac{1}{3}\hat{\nabla}^i\hat{\nabla}_k\beta^k , \tag{2.32}$$

$$\hat{\Delta}W^i = 8\pi\phi^{10}\rho h W^2 v^i - \frac{1}{3}\hat{\nabla}^i\hat{\nabla}_k W^k , \tag{2.33}$$

where we have introduced the flat space extrinsic curvature $\hat{K}_{ij}$:

$$\hat{K}_{ij} = \hat{\nabla}_i W_j + \hat{\nabla}_j W_i - \frac{2}{3}\hat{\gamma}_{ij}\hat{\nabla}_k W^k , \tag{2.34}$$

which relates to the regular extrinsic curvature through the relations $\hat{K}_{ij} = \phi^2 K_{ij}$ and $\hat{K}^{ij} = \phi^{10}K^{ij}$. All of the simulations presented in this work were performed using this new formulations of the CFC metric equation.

CFC is equivalent to GR in spherical symmetry and, in general, the conformal flatness of the spatial metric implies the absence of any gravitational waves in such spacetimes. Due to this, in 2 and 3 dimensions a CFC spacetime is often regarded as GR minus the dynamical degrees of freedom of the gravitational field

that correspond to the gravitational wave content[4] [457]. However, this statement does not characterize the CFC in general: even stationary spacetimes that do not contain gravitational waves can be conformally non-flat. Famous examples are Kerr black holes [163] and rotating neutron stars in equilibrium [105]. Nevertheless, as mentioned above (section 2.1.3), the CFC approximation is of excellent quality for the spacetimes of relativistic stars [310, 311, 312].

2.2 General-relativistic hydrodynamics

This section is devoted to the description of the general-relativistic hydrodynamics equations governing the dynamics of a single compressible fluid. *Hydrodynamics* concerns itself with the study of the motion of fluids (liquids or gases). Since the phenomena considered in hydrodynamics are macroscopic, a fluid is regarded as a continuum medium. This means that any small volume element in the fluid is always supposed to be so large that it still contains huge number of physical fluid particles. In the the work presented in this dissertation, we neglect fluid bulk and shear viscosities, microscopic heat transfer and magnetic fields, hence we consider a single ideal fluid with zero magnetic field strength.

The mathematical description of the state of a moving ideal fluid of a given chemical composition is effected by means of functions which give the distribution of the fluid velocity $\boldsymbol{v} = \boldsymbol{v}(x^i, t)$ and of any two thermodynamic quantities pertaining to the fluid, for example, the pressure p and the density ρ. As is well known, for a given chemical composition, all of the thermodynamic quantities are determined by the values of any two of them, together with the equation of state (EoS) [218]. Hence, if we are given five quantities – namely the three components of the velocity $\boldsymbol{v}$, the pressure p and the density ρ – the state of the moving fluid is completely determined. The full set of hydrodynamics equations represents a non-linear system of hyperbolic equations derived from the conservation laws of matter, momentum and energy. Due to their nonlinear nature, the hydrodynamics equations allow for discontinuities of arbitrary magnitude in their solution (that generically develop even from smooth initial data) and special care must be taken in their numerical solution.

2.2.1 Flux-conservative formulation

In our discussion of the general-relativistic hydrodynamics equations, we focus on the flux-conservative formalism in the framework of the ADM $\{3+1\}$ splitting of GR which was first derived at the Universitat de Valencia by the group of Jose M. Ibáñez (therefore this formulation is often called as the *Valencia formulation*)) [257, 194, 350, 26]. We choose the frame of reference in which an Eulerian observer is at rest in a space-like hypersurface Σ_t. For a discussion of different formulations and an overview of GR hydrodynamics, the interested reader is referred, e.g., to the extensive review by Font [150].

As we shall see later, the flux-conservative formalism takes advantage of the hyperbolic and conservative character of the GR hydrodynamics equations and in this way allows for numerical schemes based on the characteristic information of the hyperbolic system. Such high-resolution shock-capturing (HRSC) schemes (also called Godunov-type methods [172]) are widely used in classical fluid dynamics (see, e.g., [225]) and their incorporation into general-relativistic hydrodynamics provides better resolution of physical discontinuities in the fluid flow than is possible with most of the other non-HRSC schemes [258, 148]. The Valencia formulation has been implemented in a number of modern general-relativistic codes, including, among others, MAHC/GRAstro [148, 149], CoCoNuT [117, 119], Whisky/Whisky2D [20, 21, 205], M. Shibata's code [374], and the Nada code [278].

[4] In axisymmetry, the gravitational field has one dynamical degree of freedom and it corresponds to gravitational waves. In 3D it has two. York [458, 457] has shown that the dynamical degrees of freedom of the gravitational field can be identified with parts of the conformally-related spatial metric and the transverse-traceless part of the conformally-related extrinsic curvature.

We begin with the definition of a few key quantities. The baryonic rest-mass density ρ is given by

$$\rho = m_u n_{\rm B} \tag{2.35}$$

where m_u is the atomic mass unit and $n_{\rm B}$ is the number density of baryons. The specific enthalpy h is defined as

$$h = 1 + \epsilon + \frac{p}{\rho}\,, \tag{2.36}$$

where ϵ is the specific internal energy of the fluid, and p is the fluid pressure as given by the general equation of state (EoS)

$$p = p\left(\rho, \epsilon, X_i\right)\,. \tag{2.37}$$

Here X_i is a quantity that specifies the mass fraction of each fluid species. Note that the chosen set of independent variables for the EoS $\{\rho, \epsilon, X_i\}$ is not unique and most finite-temperature nuclear equations of state are given in terms of the fluid temperature rather than of its internal energy (see, e.g., [222, 372, 373]).

The GR hydrodynamics equations in a covariant form consist of the local conservation laws of the rest-mass-current density $J^\mu = \rho u_\mu$ and the stress-energy tensor $T^{\mu\nu}$:

$$J^\mu_{\ ;\mu} = 0\,, \tag{2.38}$$

$$T^{\mu\nu}_{\ \ ;\mu} = 0\,, \tag{2.39}$$

where $_{;\mu} = \nabla_\mu$ is the covariant derivative with respect to the 4-metric $g_{\mu\nu}$. The stress-energy tensor of an ideal-fliud is given by

$$T^{\mu\nu} = \rho h u^\mu u^\mu + p g^{\mu\nu}\,. \tag{2.40}$$

The GR hydrodynamics equations (2.38) and (2.39) can now be recast as

$$\frac{1}{\sqrt{-g}}\left(\sqrt{-g}J^\mu\right)_{,\mu} = 0\,, \tag{2.41}$$

$$\frac{1}{\sqrt{-g}}\left(\sqrt{-g}T^{\mu\nu}\right)_{,\mu} = -\Gamma^\nu_{\mu\lambda}T^{\mu\lambda}\,, \tag{2.42}$$

where we have made use of the covariant divergence formula [217],

$$\nabla_\alpha a^\alpha = a^\alpha_{\ ;\alpha} = \frac{1}{\sqrt{-g}}\left(\sqrt{-g}a^\alpha\right)_{,\alpha}\,, \tag{2.43}$$

where a^α is a contravariant vector, ∇_α is the covariant derivative with respect to the 4-metric $g_{\mu\nu}$ and $\sqrt{-g} = \alpha\sqrt{\gamma}$, while $g = \det\left(g_{\mu\nu}\right)$ and $\gamma = \det\left(\gamma_{\mu\nu}\right)$.

In order to rewrite equations (2.41)-(2.42) in a flux-conservative form, we follow Banyuls et al. [26] and define a set of *conserved* variables in terms of the *primitive* variables ρ, ϵ and v^i:

$$D = J^\mu n_\mu = \alpha\rho u^0 = \rho W\,, \qquad (\text{rest}-\text{mass density}) \tag{2.44}$$

$$S^i = \perp^i_\nu T^{\mu\nu} n_\nu = \rho h W^2 v^i\,, \qquad (\text{momentum density}) \tag{2.45}$$

$$\tau = T^{\mu\nu}n_\mu n_\nu - J^\mu n_\mu = \rho h W^2 - p - D\,, (\text{total energy density}) \tag{2.46}$$

where we have made use of the time-like unit-normal vector n^μ and the projection operator $\perp^\mu_\nu$ onto the spatial 3-hypersurfaces introduced in §2.1.1. The equations of GR hydrodynamics can now be written as a first order hyperbolic system of conservation laws:

$$\frac{1}{\sqrt{-g}}\left(\left(\sqrt{\gamma}\mathbf{U}\right)_{,0} + \left(\sqrt{\gamma}\,\mathbf{F}^i\right)_{,i}\right) = \boldsymbol{s}\,, \tag{2.47}$$

where $\mathbf{U}$ is the state vector:

$$\mathbf{U} = (D, S_i, \tau)^T \ , \tag{2.48}$$

$\mathbf{F}^i$ is the flux vector:

$$\mathbf{F}^i = \begin{pmatrix} (\alpha v^i - \beta^i) D \\ (\alpha v^i - \beta^i) S_j + \alpha p \delta^i_j \\ (\alpha v^i - \beta^i) \tau + \alpha p v^i \end{pmatrix} , \tag{2.49}$$

and s^i is the source vector:

$$\boldsymbol{S} = \begin{pmatrix} 0 \\ T^{\mu\nu} \left(g_{\nu j, \mu} + \Gamma^\delta_{\mu\nu} g_{\delta j} \right) \\ \alpha \left(T^{\mu 0} \frac{1}{\alpha} \alpha_{,\mu} - T^{\mu\nu} \Gamma^0_{\mu\nu} \right) \end{pmatrix} . \tag{2.50}$$

Note that while the state vector $\mathbf{U}$ of the conserved variables is updated in time, the knowledge of the primitive variables (ρ, ϵ, v^i) is required for the calculation of the flux term $\mathbf{F}^i$ and for the computation of the characteristic fields and speeds discussed below. Hence, it is necessary to *recover* the primitive variables (ρ, ϵ, v^i) from the conserved ones after *each* timestep. In contrast to the Newtonian case, these variables cannot be obtained in closed functional form in GR and must by recovered using a numerical root-finding procedure, as discussed in more detail in Section 2.3.6.

Equations (2.47) form a system of hyperbolic *balance* laws [225] that reduce to conservation laws if $\boldsymbol{S} = 0$, i.e. in flat spacetime. For this reason, equations (2.47) are referred to as flux-conservative. Since the right-hand side source vector $\boldsymbol{S}$ does not contain derivatives of the conserved variables in $\mathbf{U}$, it is numerically stable to first solve the homogeneous equations and then apply the source term in an operator-split manner or through the Method of Lines [225].

2.2.2 Special relativistic and Newtonian limits

In special relativity the geometry of spacetime is flat, hence the general metric $g_{\mu\nu}$ reduces to the Minkowski case ($g_{\mu\nu} = \eta_{\mu\nu} = \mathrm{diag}(-1, 1, 1, 1)$) and the source vector in (2.47) vanishes in Cartesian coordinates, while the state vector $\mathbf{U}$ remains unchanged. For an extensive review of numerical methods for special relativistic hydrodynamics, the interested reader is referred to Martí & Müller [258].

In order to obtain the Newtonian limit (Newtonian gravity, $v \ll 1$) of the GR state vector (2.48), one has to expand the Lorentz factor W in v^2,

$$W = 1 + \frac{1}{2} v^2 + \mathcal{O}(v^4) \ , \tag{2.51}$$

and neglect terms of order $\mathcal{O}(v^4)$. Moreover, in the limit of small v we have $\rho \gg \frac{1}{2}\rho v^2$ [218], hence,

$$D = \rho W \overset{\text{Newt.}}{\longrightarrow} \rho \ . \tag{2.52}$$

Analogously,

$$S^i = \rho h W^2 v^i = \rho \left(1 + \epsilon + \frac{p}{\rho} \right) W^2 v^i \overset{\text{Newt.}}{\longrightarrow} \rho v^i \ , \tag{2.53}$$

and, using the assumption that in the non-relativistic limit, $\frac{1}{2}\rho v^2 \gg v^2(\rho\epsilon + p)$ [218],

$$\tau = \rho h W^2 - p - D \overset{\text{Newt.}}{\longrightarrow} \rho\epsilon + \frac{1}{2}\rho v^2 \tag{2.54}$$

Note that the energy equation (2.54) requires expansion to second order in v^2 to get the Newtonian limit.

The Newtonian hydrodynamics equations in Cartesian coordinates are then

$$\rho_{,t} + \left(\rho v^i\right)_{,i} = 0 \,, \tag{2.55}$$

$$\left(\rho v_j\right)_{,t} + \left(\rho v_j v^i + p\delta^i_j\right)_{,i} = \rho g_j \,, \tag{2.56}$$

$$\left(\rho\epsilon + \frac{1}{2}\rho v^2\right)_{,t} + \left[\left(\rho\epsilon + \frac{1}{2}v^2 + p\right)v^i\right]_{,i} = \rho g_i v^i \,, \tag{2.57}$$

$$\tag{2.58}$$

where $g_i = -\phi_{,i}$ is the Newtonian free-fall gravitational acceleration and ϕ is the Newtonian gravitational potential.

2.2.3 Godunov-type methods and the characteristic structure of the GR hydrodynamics equations

The general relativistic hydrodynamics equations for the evolution of an ideal fluid represent a highly non-linear problem. In general, non-linear hyperbolic systems have the property that allows for weak solutions, i.e., classical solutions in smooth regions which are separated by a finite number of discontinuities such as shocks or contact discontinuities. Even an initially smooth density, velocity and energy distribution can evolve into shocks after some time, if it is governed by such nonlinear hyperbolic equations. For example, in massive star core-collapse and accretion-induced collapse of white dwarfs, in which the initial distributions of the density, velocity and internal energy are smooth, core bounce will result in the formation of a shock wave, which then propagates through the envelope of the star.

On the other hand, in numerical approaches based on finite difference or finite volume methods, hydrodynamics quantities are represented as discrete data. As a result, even a smooth data is treated as a sequence of pieces of piecewise constant data, which exhibit jumps of finite size at the computational-cell interfaces in any non-trivial case. In his groundbreaking work from 1959 [172], Godunov realized that each cell-interface discontinuity may be viewed as a local Riemann problem, which can be solved exactly [225, 258]. Since the solution of the local Riemann problems are themselves solutions of the conservation laws, a series of such local solutions on a discrete grid constitutes a global solution of the conservation equations for the discrete initial data.

The Riemann problem for the hydrodynamics equations (and, more generally, for any hyperbolic system) is an initial-value problem with initial conditions (in one spatial dimension)

$$\mathbf{U}(x, t=0) = \begin{cases} \mathbf{U}_L & \text{if } x < a \,, \\ \mathbf{U}_R & \text{if } x > a \,, \end{cases} \tag{2.59}$$

where $\mathbf{U}_L$ and $\mathbf{U}_R$ are constant state vectors representing left (L) and right (R) states with respect to an interface at point a, respectively. The exact solution of the above Riemann problem in ideal hydrodynamics is generally represented in terms of three elementary waves: a forward propagating non-linear shock wave, a contact discontinuity, and a non-linear backward propagating rarefaction wave[5]. In the shock wave all of the state variables are discontinuous, in the rarefaction wave all variables are continuous, but change with time in self-similar fashion, while the contact discontinuity carries a jump in density, whereas the other variables are continuous.

[5] Actually, the possible types of waves present in the solution of Riemann problem depend crucially on the closure condition, i.e., on the EoS [423]. For the EoSs usually considered in GR numerical simulations, though, only shocks, contact discontinuities and rarefaction waves appear, and so we will restrict our discussion only to these cases.

The three waves are associated with the *characteristic fields*, the eigenvectors of the three 5×5 Jacobi matrices of the GR hydrodynamics equations (2.47)

$$\mathbf{B}^i = \frac{\partial\left(\sqrt{\gamma}\mathbf{F}^i\right)}{\partial\left(\sqrt{\gamma}\mathbf{U}\right)} = \frac{\partial\left(\mathbf{F}^i\right)}{\partial\left(\mathbf{U}\right)} \,, \tag{2.60}$$

where the index i corresponds to the spatial dimensions. Each of the three Jacobi matrices $\mathbf{B}^i$ has 5 eigenvalues and three of them are unique [26]

$$\lambda_0^i = \alpha v^i - \beta^i \quad (3-\text{fold degenerate}) \,, \tag{2.61}$$

$$\lambda_\pm^i = \frac{\alpha}{1-v^2c_s^2}\left\{v^i(1-c_s^2) \pm \sqrt{c_s^2(1-v^2)\left[\gamma^{ij}(1-v^2c_s^2) - v^iv^j(1-c_s^2)\right]}\right\} - \beta^i \,, \tag{2.62}$$

where c_s is the local speed of sound.

Due to the hyperbolic nature of the hydrodynamics equations, the physical information of the system is carried by the three characteristic waves (*characteristics*) at the *characteristic speeds*, corresponding to the three unique eigenvalues of the Jacobi matrices. In fact, in order to solve the Riemann problem exactly, it is necessary to know only the characteristic speeds and the initial left and right states (see [423, 225, 172, 258]). On the other hand, in practice and in particular in multi-dimensional simulations, the exact solution of the Riemann problem becomes too computationally demanding. To cope with this fact, it is often sufficient in numerics to solve the Riemann problem approximately. As discussed in detail in Section 2.3.3, the numerical solution of the Riemann problem can be accomplished in a fast and easy way. Modern numerical methods for hydrodynamic flows often rely on approximate Riemann solvers. The solutions obtained in that way are for practical purposes almost as good as the approaches based on solution of the full non-linear Riemann problem [126].

Godunov's original scheme used piecewise-constant states as initial data for the Riemann problems at cell interfaces and hence was only first-order accurate in space. As discussed in more detail in Section 2.3.5, more modern Godunov-type schemes use interpolation procedures to reconstruct a higher-order approximation to the physical data at cell interfaces.

2.3 Numerical methods: the CoCoNuT code

In this section, we give an overview of the numerical methods and tools that used in the simulations presented in this dissertation. This includes a discussion of the CoCoNuT code [117, 119] and an initial data solver for equilibrium configurations of rotating stars [180, 209, 104, 389, 390]. Our discussion of the CoCoNuT code below is based on Harald Dimmelmeier's PhD dissertation [116] and on the papers by Dimmelmeier et al. [117, 119].

CoCoNuT is a general relativistic hydrodynamics code with dynamical CFC space-time evolution. This numerical code is mainly aimed at the study of astrophysical scenarios in which GR can play an important role, such as the collapse of rapidly rotating stellar cores and the evolution of neutron stars. CoCoNuT was originally developed as two-dimensional axisymmetric code by Harald Dimmelmeier at the Max-Planck Institute for Astrophysics (Garching bei München, Germany) as part of his PhD thesis [116]. It was then extended to three dimensions in collaboration with Jérŏme Novak from the LUTH laboratory at the Observatoire de Paris (Meudon, France) [119] and to include magnetohydrodynamics by Pable Cerdá-Durán from the Max-Planck Institute for Astrophysics [94].

2.3.1 Finite difference grid and boundary conditions

In computational fluid dynamics, and especially in numerical relativity, the choice of the coordinates and their suitability for the geometry of a given problem is of crucial importance. Since the early attempts at making axisymmetric simulations of ideal fluid in general relativity over 20 years ago, the issue of coordinate problems has always been a challenge. At those times, due to insufficient computer power, it was unfeasible to use a three-dimensional Cartesian grid to make simulations of axisymmetric problems. But even if this is now possible with modern computers, Cartesian coordinates are not well adapted for axisymmetric or nearly spherically symmetric geometries and they do not exploit the existence of a rotational symmetry to reduce the dimensionality of the problem to two dimensions.

For axisymmetric problems, both cylindrical and polar coordinates are suitable. However, these coordinate systems share a common disadvantage: The rotation axis $\theta = 0$ in polar coordinates and coordinate origin at $r = 0$ in both coordinate systems are distinguished from the other coordinate points. Often the equations contain terms involving geometrical quantities such as $\hat{\gamma}^{22} = r^{-1}$, which become infinite at the origin, or $\hat{\gamma}^{33} = r^{-1}\sin^{-1}\theta$, which become infinite at the axis. Thus, the reduction of the problem from three to two dimensions is paid for by having to deal with coordinate singularities at certain points. This coordinate pathologies prevented early axisymmetric relativistic ADM codes providing long-term stability (e.g., [143, 356]). Attempts to solve the axisymmetric problem are nowadays made by using the two- dimensional "cartoon" method [9], or by going towards three dimensions in Cartesian coordinates either using a uniform grid or by mesh-refinement techniques (e.g., [42]), or by using multi-block or multi-patch methods (e.g., [465]), now that larger and faster computers are available.

Still, the geometry of the polar coordinates is the most suitable one for simulations of axisymmetric objects. These coordinates are used in the CoCoNuT code. We assume axial symmetry with respect to the rotation axis in all of the simulations presented here. However, note that the code is not restricted to axisymmetry, and it can be used for simulations also in three dimensions.

We further assume symmetry with respect to the equatorial plane $\theta = \pi/2$. Therefore, θ spans the interval between 0 and $\pi/2$. The angular grid consisting of n_θ zones is equally spaced, with θ_j denoting the coordinates of the cell centers in the angular direction ($1 \leq j \leq n_\theta$). The n_r radial zones (zone centers located at r_i) are logarithmically spaced. Each computational cell (r_i, θ_j) is bounded by interfaces at $r_{i-\frac{1}{2}}$, $r_{i+\frac{1}{2}}$, $\theta_{j-\frac{1}{2}}$, and $\theta_{j+\frac{1}{2}}$, respectively. The angular size of a zone is $\Delta\theta = \frac{1}{2}\pi/n_\theta$, while the radial size is given by $\Delta r_i = r_{i+\frac{1}{2}} - r_{i-\frac{1}{2}}$. The radial size of the three innermost cells is enlarged in order to ease the timestep restriction; for $i > 3$, $\Delta r_{i+1}/\Delta r_i = \text{const}$. Note that $r_{\frac{1}{2}} = 0$ is the origin, and $r_{n_r+\frac{1}{2}} = R$ defines the outer boundary of the grid. The rotation axis coincides with $\theta_{\frac{1}{2}} = 0$, and $\theta_{n_\theta+\frac{1}{2}} = \frac{1}{2}\pi$ denotes the equatorial plane.

Due to the symmetry conditions stated above, only one quadrant of the actual spacetime domain is evolved. As a consequence, the symmetry conditions are imposed for both hydrodynamic and metric quantities at the center ($r = 0$), the rotation axis ($\theta = 0$), and the equatorial plane ($\theta = \pi/2$). Quantities are assumed to be either symmetric or antisymmetric across a boundary. These two options are combined in the following notation for a quantity $q_{i,j}$:

$$q_{-\frac{1}{2},j} = \pm\, q_{\frac{1}{2},j}, \tag{2.63}$$

$$q_{i,n_\theta+\frac{1}{2}} = \pm\, q_{i,n_\theta-\frac{1}{2}}, \tag{2.64}$$

$$q_{i,-\frac{1}{2}} = \pm\, q_{i,\frac{1}{2}}, \tag{2.65}$$

where

$$\pm = \begin{cases} + & \text{symmetric,} \\ - & \text{antisymmetric.} \end{cases} \tag{2.66}$$

The symmetry conditions for the scalar quantities ρ, ϵ, ϕ and α are straightforward. Like their Newtonian counterparts ρ, ϵ and Φ they have to be continuous across all boundaries. Thus, the scalar quantities are assumed to be symmetric (+) with respect to all boundaries. Contrary to Newtonian hydrodynamics, the symmetry conditions for the vector quantities are nontrivial, as they occur both in covariant and contravariant form. By defining "physical" velocities (the same can be done for the shift vector components β^i),

$$v_r \equiv \sqrt{v_1 v^1} = \phi^{-2} v_1 = \phi^2 v^1, \tag{2.67}$$

$$v_\theta \equiv \sqrt{v_2 v^2} = \phi^{-2} r^{-1} v_2 = \phi^2 r v^2, \tag{2.68}$$

$$v_\varphi \equiv \sqrt{v_3 v^3} = \phi^{-2} r^{-1} \sin^{-1}\theta v_3 = \phi^2 r \sin\theta v^3, \tag{2.69}$$

which are bounded by the speed of light ($0 \leq |v_r|, |v_\theta|, |v_\varphi| \leq 1$), we can specify the symmetry conditions from Newtonian hydrodynamics. Keeping in mind the symmetry behavior of the geometrical terms in the three-metric components γ_{ij} and γ^{ij}, the symmetry conditions for the "physical velocity vector" and the shift vector are:

	v_r	v_θ	v_φ	β^1	β^2	β^3
center	$-$	$-$	$-$	$-$	$+$	$+$
pole	$+$	$-$	$-$	$+$	$-$	$+$
equator	$+$	$-$	$+$	$+$	$-$	$+$

Here we demand that (i) all velocities have to vanish at the center (no mass flow across the center), that (ii) the meridional velocity v_θ is zero along the rotation axis and in the equatorial plane (no mass flow across these boundaries), and (iii) the azimuthal velocity v_φ is zero along the rotation axis. Hence, these entries are set to ($-$), while all others, where the velocities are continuous, are set to (+). The shift vector components β^i are treated similarly to the contravariant three-velocity vector v^i, as the shift vector corresponds to a "coordinate velocity".

At the outer radial boundary, the hydrodynamic quantities are extrapolated from the interior to the boundary zones. The metric equations are solved using spectral methods, in which the boundary conditions are imposed at spatial infinity, as discussed in detail in Section 2.3.2.

2.3.2 Einstein field equations and spectral methods

The most common approach to numerically solving the Einstein equations is by means of finite differences (see [10, 223] and references therein). However, it is well known that spectral methods [175, 85] are far more accurate than finite differences for smooth solutions (i.e, they are best for initial data without discontinuities), and are particularly well suited to solving elliptic and parabolic equations. Good results can be obtained also for hyperbolic equations, as long as no discontinuities appear in the solution. The basic principle underlying spectral methods is the representation of a given function $f(x)$ by its coefficients in a complete basis of orthonormal functions: sines and cosines (Fourier expansion) or a family of orthogonal polynomials (e.g. Chebyshev polynomials $T_i(x)$ or Legendre polynomials). In practice, of course, only a *finite* set of coefficients is used and one approximates f by the truncated series $f(x) \simeq \sum_{i=0}^{n} c_i T_i(x)$ of such functions. The use of spectral methods results in a very high accuracy, since the error made by this truncation decreases like e^{-n} for smooth functions (exponential convergence). Moreover, in order to achieve a comparable accuracy in the representation of functions and their derivatives, the finite difference grid generally needs many more points than the spectral one. For example, when considering the representation of some function like $\exp(-x^2)$ on the interval $[0, 1]$, spectral methods using Chebyshev polynomials need ~ 30 coefficients to reach machine double precision (10^{-16}) for the representation of the function and 10^{-13} for the representation of its first derivative. For comparison, a third order scheme based on finite differences needs $\sim 10^5$ points to achieve the same accuracy.

In an astrophysical context spectral methods made possible the study of subtle phenomena such as the development of physical instabilities leading to gravitational collapse [61]. In the last few years, spectral methods have been successfully employed by the *Meudon group* [263] in a number of relativistic astrophysics scenarios [62], among them the gravitational collapse of a neutron star to a black hole, the infall phase of a tri-axial stellar core in a core collapse supernova (extracting the gravitational waves emitted in such process), the construction of equilibrium configurations of rapidly rotating neutron stars with magnetic fields, and the tidal interaction of a star with a massive black hole. To carry out these numerical simulations the group has developed a fully object-oriented library called LORENE [242] to implement spectral methods in spherical coordinates. Spectral methods are now employed in numerical relativity by other groups as well [151, 329, 130].

On the other hand, robust finite difference schemes for solving hyperbolic systems of conservation (and balance) laws, such as the Euler equations of fluid dynamics, have been known for a long time and have been employed successfully in computational fluid dynamics (see e.g. [423] and references therein). In particular, the high-resolution shock-capturing schemes (e.g., [225, 423]) have shown their advantages over other types of method even when dealing with relativistic flows with highly ultrarelativistic fluid speeds, as discussed in detail in Section 2.3.3.

From the above considerations, it seems a promising strategy, in the case of relativistic problems where coupled systems of elliptic (for CFC field) and hyperbolic (the hydrodynamics) equations must be solved, to use spectral methods for the former and HRSC schemes for the latter (where solutions may be discontinuous). The efficiency of such a hybrid approach was demonstrated extensively by Dimmelmeier et al. [119], who implemented this in the COCONUT code, which is used for simulations presented in this work. Such an approach is best suited for formulations of the Einstein equations which favor the appearance of elliptic equations against hyperbolic equations, i.e. either approximations such as CFC [196, 441, 107] (the approximation which we adopt in the simulations presented in this work), higher-order post-Newtonian extensions [91], or *exact* formulations as recently proposed by [63, 366]. Note that the combined approach put forward by Dimmelmeier et al. [119] was first used in one-dimensional core collapse simulations in the framework of a tensor-scalar theory of gravitation by Novak et al. [300]. Such a hybrid scheme has recently been developed and used for simulations of the coalescence of black hole and neutron star binaries [130].

Spectral methods

The basic principle of spectral methods has been presented in Section 2.3.2. Let us now describe some details of the implementation in the case of 3D functions in spherical coordinates. The interested reader can refer to [62, 177] for further details. A function f can be decomposed as follows:

$$f(\xi,\theta,\varphi) = \sum_{k=0}^{\hat{n}_\varphi} \sum_{j=0}^{\hat{n}_\theta} \sum_{i=0}^{\hat{n}_r} c_{ijk} T_i(\xi) Y_j^k(\theta,\varphi), \tag{2.70}$$

where $Y_j^k(\theta,\varphi)$ are spherical harmonics and ξ is linked with the radial coordinate r, as given below. One of the advantages of spectral methods is that they allow spatial derivatives to be computed more easily. If f is represented by its coefficients c_{ijk}, it is easy to obtain the coefficients of e.g. $\partial f/\partial r$, Δf (or the result of any linear differential operator applied to f) thanks to the properties of Chebyshev polynomials or spherical harmonics. For instance, to compute the coefficients of the radial derivative of f, we make use of the following recursion formula og Chebyshev polynomials:

$$\frac{dT_{n+1}(x)}{dx} = 2(n+1)T_n(x) + \frac{n+1}{n-1}\frac{dT_{n-1}(x)}{dx} \quad \forall n > 1. \tag{2.71}$$

A grid is still needed for two reasons: firstly, to calculate these coefficients through the computation of integrals, and secondly to evaluate non-linear operators (e.g. $\nabla f \times \nabla f$), using the values of the functions at grid points (in physical space). The spectral grid points, called collocation points, are situated at $(\hat{r}_i, \hat{\theta}_j, \hat{\varphi}_k)$, where i, j, k run from 1 to $\hat{n}_r, \hat{n}_\theta, \hat{n}_\varphi$, respectively. They are the nodes of a Gauss–Lobato quadrature used to compute the integrals giving the spectral coefficients. The use of Fast Fourier Transforms (FFT) for the angular part requires equally spaced points in the angular directions, whereas a fast Chebyshev transform (also making use of FFT) requires that the radial grid points correspond, in ξ, to the zeros of $T_{\hat{n}_r}$. Note that in our simulations each of the domains contains the same number of radial and angular collocation points.

In order to be able to cover the entire space ($r \in [0, +\infty]$) and to handle coordinate singularities at the origin ($r = 0$), CoCoNuT uses several grid *domains*:

- a core extending from $r = 0$ to r_d, where $r = \alpha\xi$, with $\xi \in [0, 1]$ and α is a constant (CoCoNuT uses either only even Chebyshev polynomials $T_{2i}(\xi)$, or only odd polynomials $T_{2i+1}(\xi)$);
- an arbitrary number (including zero) of shells bounded by the inner radius $r_{\mathrm{d}\,i}$ and outer radius $r_{\mathrm{d}\,i+1}$, where r is set to $\alpha_i\xi + \beta_i$ with $\xi \in [-1, 1]$ and α_i and β_i are constants that depend on the shell number i;
- a compactified external domain spanning from the outer boundary of the finite difference grid at r_fd to radial infinity, where $r = 1/[\alpha_\mathrm{c}(\xi + 1)]$, with $\xi \in [-1, 1]$ and α_c is a constant.

Moreover, the ratio f_d between the outer boundary radii of two consecutive domains is assumed to be a constant, which gives the relation

$$f_\mathrm{d} = \left(\frac{r_\mathrm{fd}}{r_\mathrm{d}}\right)^{1/(n_\mathrm{d}-2)}, \tag{2.72}$$

where n_d is the number of domains. Therefore, for a given choice of n_d and the radius of the nucleus r_d, the setup of the spectral grid is completely specified:

$$\begin{aligned} r_{\mathrm{d}\,1} &= r_\mathrm{d}, \\ &\vdots \\ r_{\mathrm{d}\,i} &= f_\mathrm{d} \times r_{\mathrm{d}\,i-1}, \\ &\vdots \\ r_{\mathrm{d}\,n_\mathrm{d}-1} &= r_\mathrm{fd}, \\ r_{\mathrm{d}\,n_\mathrm{d}} &= \infty. \end{aligned} \tag{2.73}$$

The setup of the spectral and finite difference grids for a sample stellar iron core collapse model is illustrated in Fig. 2.2 for $\hat{n}_r = 33$ grid points per spectral radial domain and $n_r = 200$ finite difference grid points. Note the logarithmic radial spacing of the finite difference grid in the central parts of the star (upper panel). While the finite difference grid ends at the finite radius r_fd (with the exception of four ghost zones, which are needed for the hydrodynamic reconstruction scheme; see Section 2.3.5), the outermost radially compactified 6th domain of the spectral grid covers the entire space to radial infinity (lower panel). The finite difference grid does not change during the time-evolution, while the boundaries $r_{\mathrm{d}i}$ of the spectral radial domains (and thus the radial collocation points) can change adaptively during the evolution. Note that the spectral radial collocation points, which correspond to the roots of the Chebyshev polynomials, are more densely populated near the domain boundaries.

Communication between spectral and finite difference grids

Passing information from the spectral grid to the finite difference grid is technically very easy. Knowing the spectral coefficients of a function, this step simply requires the evaluation of the sum (2.70) at the finite

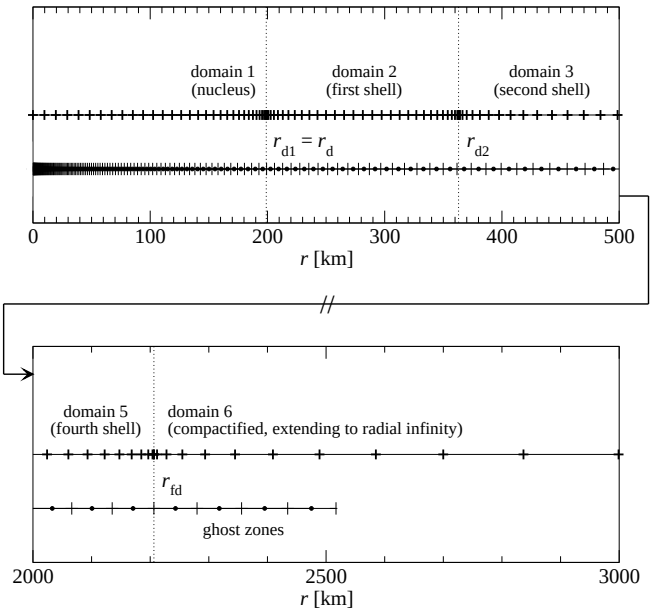

Figure 2.2: Radial setup of the initial spectral grid (collocation points are marked by plus symbols) and the time-independent finite difference grid (cell centers are marked by filled circles, separated by cell interfaces shown by vertical dashes) for a sample iron core collapse simulation of [119]. The upper panel shows the innermost $500\ \mathrm{km}$ containing the nucleus (ending at $r_\mathrm{d} \approx 200\ \mathrm{km}$), the first shell, and a part of the second shell of the spectral grid. In the lower panel a part of the last regular shell (which is confined by the outer boundary of the finite difference grid at $r_\mathrm{fd} \approx 2200\ \mathrm{km}$) and the beginning of the compactified domain of the spectral grid are plotted. The domain boundaries are indicated by vertical dotted lines. This figure is taken from [119].

difference grid points. However, this method has a drawback of being computationally too expensive [119]. For example, in 3D the time spent on this can even be larger than the time spent by the spectral elliptic solver [119]. Going from the finite difference grid to the spectral grid requires an interpolation, taking special care to avoid Gibbs phenomena that can appear in the spectral representation of discontinuous functions[6]. The matter terms entering in the sources of the gravitational field equations can be discontinuous when a shock forms. Thus, it is necessary to smooth or filter out high frequencies that would otherwise spoil the spectral representation. This introduces a numerical error in the fields that should remain within the overall error of the code. The important point to notice here is that an accurate description does not need be achieved in the spectral representation of the sources (the hydrodynamic quantities are well described on the finite difference grid), but only in that of the metric functions, which are always continuous, as well as their first derivatives.

COCONUT interpolates from the finite difference grid to the spectral grid using a one-dimensional algorithm and intermediate grids. First, it performs an interpolation in the r-direction, then in the θ-direction and finally in the φ-direction. We can choose between piecewise linear and parabolic interpolations, and a scheme that globally minimizes the norm of the second derivative of the interpolated function [300]. The filtering of spectral coefficients is performed *a posteriori* by removing the coefficients corresponding to higher frequencies. For example, in the radial direction, this is done by canceling the c_{ijk} in Eq. (2.70) for i larger than a given threshold. In practice, the best results were found when canceling the last third

[6] In mathematics, the Gibbs phenomenon, named after the American physicist J. Willard Gibbs, is the peculiar manner in which the Fourier series of a piecewise continuously differentiable periodic function f behaves at a jump discontinuity: the nth partial sum of the Fourier series has large oscillations near the jump, which might increase the maximum of the partial sum above that of the function itself. The overshoot does not die out as the frequency increases, but approaches a finite limit.

of the radial coefficients [119]. This can be linked with the so-called "two-thirds rule" used for spectral computations of quadratically nonlinear equations [35]. Nevertheless, a different (higher) threshold would also give good results, in the sense that there are no high-frequency terms arising during the metric iteration.

Spectral elliptic solver

In order to formalize the metric equations (2.30)-(2.33), we define a vector of unknowns

$$\hat{u} = u^p = (\phi, \alpha\phi, \beta^1, \beta^2, \beta^3). \tag{2.74}$$

Then the CFC metric equations (2.30)-(2.33) can be written as

$$\hat{f}(\hat{u}) = f^q(u^p) = 0, \tag{2.75}$$

with $\hat{f} = f^q$ denoting the vector of the five metric equations for $\hat{u}$ ($p, q = 1, \ldots, 5$). In the spectral metric solver, the metric equations are evaluated at collocation points $(\hat{r}_i, \hat{\theta}_j, \hat{\varphi}_k)$ on the spectral grid. Thus, when discretized, Eq. (2.75) transforms into the following coupled nonlinear system of equations of dimension $5 \times \hat{n}_r \times \hat{n}_\theta \times \hat{n}_\varphi$:

$$\hat{\boldsymbol{f}}(\hat{\boldsymbol{u}}) = \hat{f}_{i,j,k}(\hat{u}_{l,m,n}) = f^q_{i,j,k}(u^p_{l,m,n}) = 0, \tag{2.76}$$

with the vector of discretized equations $\hat{\boldsymbol{f}} = \hat{f}_{i,j,k} = f^q_{i,j,k}$ for the unknowns $\hat{\boldsymbol{u}} = \hat{u}_{l,m,n} = u^p_{l,m,n}$. For this system we have to find the roots. Note that, in general, each discretized metric equation $f^q_{i,j,k}$ couples both to the other metric equations through the five unknowns (indices p), and to other (neighboring) cell locations on the grid (indices l, m, n).

The spectral metric solver is based on iterative methods, where the new value for the metric $\hat{\boldsymbol{u}}^{s+1}$ is computed from the value at the current iteration s by adding an increment $\Delta\hat{\boldsymbol{u}}^s$ which is weighted with a relaxation factor f_r. The tolerance measure which we use to control convergence of the iteration is the maximum increment of the solution vector on the grid on which the iteration is executed, i.e.

$$\Delta\hat{u}^s_{\max} = \max\left(\Delta\hat{\boldsymbol{u}}^s\right) = \max\left(\Delta u^{p\,s}_{i,j,k}\right). \tag{2.77}$$

The spectral solver exploits the fact that the metric equations (2.30)-(2.33) can be written in the form of a system of nonlinear coupled equations with a Laplace operator on the left-hand side. A common method for solving such kinds of equation is to keep the right-hand side fixed, solve each of the resulting decoupled linear Poisson equations and iterate until the convergence criterion (2.77) is fulfilled. The spectral solver is built from routines of the publicly available LORENE library [242] and uses spectral methods to solve the scalar and vector Poisson equations [176].

Before every computation of the spacetime metric, the hydrodynamic and metric fields are interpolated from the finite difference grid to the spectral grid by the methods detailed above. All three-dimensional functions are decomposed into Chebyshev polynomials $T_n(r)$ and spherical harmonics $Y^m_l(\theta, \varphi)$ in each domain. Furthermore, the metric equations (2.30)-(2.33) are rewritten in order to gain accuracy according to the following transformations. The scalar metric functions ϕ and α have the same type of asymptotic behavior near spatial infinity, $\phi|_{r\to\infty} \sim 1 + \Delta\phi(r)$, $\alpha|_{r\to\infty} \sim 1 + \Delta\alpha(r)$, with $\Delta\phi(r)$ and $\Delta\alpha(r)$ approaching 0 as $r \to \infty$. Therefore, to obtain a more precise numerical description of the (usually small) deviations of ϕ and α from unity, the equations are solved for the logarithm of ϕ and $\alpha\phi$, imposing that $\ln\phi$ and $\ln(\alpha\phi)$ approach zero at spatial infinity. The vector Poisson equation for the shift vector β^i is not decomposed into single scalar components, but instead the entire linear vector Poisson equation is solved, including the $\frac{1}{3}\hat{\nabla}^i\hat{\nabla}_k$ operator on the left hand side.

During each iteration a spectral representation of the solution of the linear scalar and vector Poisson equations associated with the system (2.30)-(2.33) is obtained. The Laplace operator is inverted (i.e. the

linear Poisson equation is solved) in the following way: For a given pair of indices l and m of $Y_l^m(\theta, \varphi)$, the linear scalar Poisson equation reduces to an ordinary differential equation in r. The action of the differential operator

$$\frac{\partial^2}{\partial r^2} + \frac{2}{r}\frac{\partial}{\partial r} - \frac{l(l+1)}{r^2} \tag{2.78}$$

on each multipolar component (l and m) of a scalar function corresponds to a matrix multiplication in the Chebyshev coefficient space. The corresponding matrix is inverted to get a particular solution in each domain, which is then combined with the homogeneous solutions (r^l and $1/r^l$, for a given l) to satisfy the regularity and boundary conditions. The matrix has a small size (about 30×30) and can be put into a banded form, due to the properties of the Chebyshev polynomials, which allows fast inversion. For more details about this procedure, and how the vector Poisson equation is treated, the reader is referred to [176]. Note that in order to solve the shift vector equation, β^i is decomposed into Cartesian components defined on the spherical polar grid [176].

The spatial differentials in the source terms on the right hand sides of the metric equations are obtained by spectral methods. When using ~ 30 collocation points, very high precision ($\sim 10^{-13}$) can be achieved in the evaluation of these derivatives. Another advantage of the spectral metric solver is that a compactified radial coordinate $u = 1/r$ enables us to solve for the entire space, and to impose exact boundary conditions at spatial infinity, $u = 0$. This both ensures asymptotic flatness and fully accounts for the effects of the source terms in the metric equations with noncompact support. Due to the direct solution of the vector Poisson equation for the shift vector β^i, it converges to the correct solution in all of the investigated models [119]. Furthermore, convergence can be achieved with the maximum possible relaxation factor, $f_\mathrm{r} = 1$, starting from the flat metric as the initial estimate.

There is an additional computational cost due to the communication between the finite difference and the spectral grids. As shown by [119], these computational costs may actually become a dominant part when calculating the metric. The interpolation methods also have to be chosen carefully to obtain the desired accuracy. Furthermore, spectral methods may suffer from Gibbs phenomena if the source terms of the Poisson-like equations contain discontinuities. For the particular type of simulations which we are aiming at, discontinuities are present (bounce shock front, discontinuity at the transition from the stellar matter distribution to the artificial atmosphere at the boundary of the star). This can result in high-frequency spurious oscillations of the metric solution, if too few radial domains are used, or if the boundaries of the spectral domains are not chosen properly. As mentioned before, a simple way to reduce the oscillations is to filter out part of the high-frequency spectral coefficients.

2.3.3 High-resolution shock-capturing method

Whereas Section 2.2.3 was devoted to an introduction to the general relativistic Riemann problem and the spectral decomposition of the Jacobi matrices, we will now apply these concepts to discussing numerical algorithms for solving the evolution equations.

Many modern computational codes which simulate gas/fluid dynamics exploit Godunov type methods. In such codes, the evolution equations for the hydrodynamics are discretized in finite volumes, which are bounded by cell interfaces. The hydrodynamic quantities at the cell centers represent the corresponding average value within the cell. An interpolation method is used to construct values at cell interfaces from these cell centered mean quantities. From these reconstructed quantities, the numerical fluxes through the cell boundaries are computed, which then, together with the source terms, determine the time evolution of the cell averaged quantities. The evolution is propagated forward in time by solving local Riemann problems at each cell interface. The maximum numerical time step is limited by the criterion that waves propagating from neighboring cells must not interfere with one another, i.e., that characteristics originating from the cell

interfaces do not cross within one timestep.

A numerical implementation based on the solution of local Riemann problems is called high-resolution shock-capturing (HRSC) scheme. The fact that HRSC schemes are based on (exactly or approximately) solving discontinuous Riemann problems results in the ability to capture shocks accurately and resolve them within only a few grid points. Additionally, such methods guarantee, when written in conservation form, the convergence of the numerical solution to the physical solution of the problem, and the correct propagation speeds of discontinuities.

The solution of the local Riemann problem depends on the fluxes of density, momentum, and energy which cross the cell interface. Therefore, it is important to numerically approximate these fluxes as accurately as possible. First we have to specify how the values of the hydrodynamics quantities at the left (L) and right (L) side of the cell interfaces[7],

$$q^{\mathrm{L}}_{i-\frac{1}{2},j}, \quad q^{\mathrm{R}}_{i+\frac{1}{2},j}, \qquad \text{in } r\text{–direction}\,, \tag{2.79}$$

$$q^{\mathrm{L}}_{i,j-\frac{1}{2}}, \quad q^{\mathrm{R}}_{i,j+\frac{1}{2}}, \qquad \text{in } \theta-\text{direction}\,, \tag{2.80}$$

are reconstructed from the corresponding cell averages $q_{i,j}$, which are defined at cell centers. Note that all components of the state vector (2.44)-(2.46) and the primitive variables have to be reconstructed at the interfaces.

The simplest way of reconstructing is to assume constant functions within a zone, which means that the zone interface values are set to the values $q_{i,j}$ at the cell cell centers. This piecewise constant reconstruction, which is first order accurate in space, was originally proposed by Godunov in 1959 [172] in the development of his exact solver. Higher order reconstruction methods were gradually introduced, including second order accurate MUSCL (monotonic upstream schemes for conservation laws [429]), or third order accurate PHM (piecewise hyperbolic methods) and PPM (piecewise parabolic methods [102]) and their respective derivatives [225], as discussed in more detail in Sec. 2.3.5. As demonstrated in the following section, we can obtain the numerical flux from the reconstructed values of the interfaces, together with the characteristic information from the Riemann problem. As expressed in the conservation equations (2.47), any change in a state variable is completely determined by the flux through the cell boundaries (and additional sources). This is reflected by this numerical scheme, and owing to this property the HRSC methods are called *flux conservative*.

Once the fluxes of density, momentum and energy accross cell boundaries are computed, the time update of system (2.47) from t^n to t^{n+1} is performed according to the following conservative algorithm:

$$\boldsymbol{U}^{n+1}_{i,j} = \boldsymbol{U}^{n}_{i,j} - \frac{\Delta t}{\Delta r_i}(\boldsymbol{F}^{r}_{i+1/2,j} - \boldsymbol{F}^{r}_{i-1/2,j}) - \frac{\Delta t}{\Delta \theta}(\boldsymbol{F}^{\theta}_{i,j+1/2} - \boldsymbol{F}^{\theta}_{i,j-1/2}) + \Delta t\, \boldsymbol{S}_{i,j}.$$

The time update of the state-vector $\boldsymbol{U}$ is done simultaneously in both spatial directions using a method of lines in combination with a second-order (in time) conservative Runge–Kutta scheme. Time derivatives of all metric quantities (ϕ, α, and β^i) are required to compute the Christoffel symbols, and hence the source term $\boldsymbol{S}$. As the equations for the metric in the CFC approximation do not provide explicit expressions for the time derivatives of these quantities, we approximate them numerically by discretized derivatives using values from the two time slices Σ_{t^n} and $\Sigma_{t^{n-1}}$, e.g.

$$\left(\frac{\partial \phi}{\partial t}\right)^{n}_{i,j} = \frac{\phi^{n}_{i,j} - \phi^{n-1}_{i,j}}{\Delta t^{n-1}}. \tag{2.81}$$

[7]The discussion of numerical methods for hydrodynamics equations presented here is restricted to the case of two spatial dimensions r and θ. The extension to three dimensions is straightforward.

Finally, as mentioned in Sect. 2.2.1, for the hydrodynamics update we need to recover the primitive variables (ρ, v_i, ϵ) from the conserved ones (D, S_i, τ). Since the relation between these two sets is only given implicitely, we have to resort to a Newton-Raphson iterative method. This procedure is discussed in Sect. 2.3.6.

2.3.4 Approximate Riemann solvers

In conservative codes, which are based on HRSC schemes for finite volume methods, the wave structure of the system is used to compute the numerical fluxes through the interfaces and to solve the exact or approximate Riemann problem. There are numerous ways for constructing the approximate numerical fluxes (like Roe, HLLE, Shu Osher's ENO solvers, etc., for an overview see [423]) which all involve characteristic information for the structure of the Riemann problem. In the simulations presented in this work, we have chosen to adopt the numerical flux introduced by Donat & Marquina [126], which is called *Marquina flux* formula for short. The Marquina flux formula was implemented in the CoCoNuT code by Dimmelmeier et al. [117].

Like many flux construction methods, this method involves the averaging of state variables left and right of the interface. The characteristic information is contained in a term called numerical viscosity. This viscosity term is a result of the characteristic information of the hyperbolic system of conservation laws, and automatically adds as much viscosity to the evolution scheme as necessary.

The Marquina flux is based upon Roe's formulation of the numerical flux [349] (which is introduced below), and has improved features where the Roe flux produces pathological behavior [126].

- **Roe flux formula**:

  In this formula, the numerical flux at cell interfaces in r- and θ-direction is represneted as the average of the reconstructed fluxes left ($\mathbf{F}^{\mathrm{L}}$) and right ($\mathbf{F}^{\mathrm{R}}$) of the interface as well as the numerical viscosity term:

$$\mathbf{F}^1 = \frac{1}{2}\left(\mathbf{F}^{1,\mathrm{R}} + \mathbf{F}^{1,\mathrm{L}} - \sum_{k=1}^{5} \tilde{\mathbf{r}}^1 |\tilde{\lambda}_k^1| \tilde{\alpha}_l^1\right) , \tag{2.82}$$

$$\mathbf{F}^2 = \frac{1}{2}\left(\mathbf{F}^{2,\mathrm{R}} + \mathbf{F}^{2,\mathrm{L}} - \sum_{k=1}^{5} \tilde{\mathbf{r}}^2 |\tilde{\lambda}_k^2| \tilde{\alpha}_l^2\right) . \tag{2.83}$$

  The quantities with a tilde depend on the "Roe average", which is a function of f of the left and right values of the state vector $\mathbf{F}^0$ at the interface.

  The $\tilde{\lambda}_k^l$ in equations (2.82)-(2.83) are the five eigenvalues (2.61)-(2.62) of the Jacobi matrices, and $\tilde{\mathbf{r}}_k^l$ are the five right eigenvectors. The superscript $l = 1,\ 2$ denotes the r- and θ-detections, respectively. The fluxes in the r- and θ-directions are defined at the corresponding interfaces:

$$\mathbf{F}^1 = \mathbf{F}^1_{i+\frac{1}{2},j}\left(\mathbf{F}^{0\ \mathrm{L}}_{i+\frac{1}{2},j}, \mathbf{F}^{0\ \mathrm{R}}_{i+\frac{1}{2},j}\right) , \quad \mathbf{F}^2 = \mathbf{F}^2_{i+\frac{1}{2},j}\left(\mathbf{F}^{0\ \mathrm{L}}_{i,j+\frac{1}{2}}, \mathbf{F}^{0\ \mathrm{R}}_{i,j+\frac{1}{2}}\right) , \tag{2.84}$$

  The quantities $\tilde{\alpha}_k^l$ are called wave strengths and are defined implicitly via relations

$$\mathbf{F}^{0\ \mathrm{R}} - \mathbf{F}^{0\ \mathrm{L}} = \sum_{k=1}^{5} \tilde{\mathrm{r}}^1 \tilde{\alpha}_l^1 , \quad \mathbf{F}^{0\ \mathrm{R}} - \mathbf{F}^{0\ \mathrm{L}} = \sum_{k=1}^{5} \tilde{\mathrm{r}}^1 \tilde{\alpha}_l^1 . \tag{2.85}$$

  For a locally linear hyperbolic system, the Jacobi matrices are constant. For such a system, the matrix of right eigenvectors can be inverted: $\mathbf{L} = \mathbf{R}^{-1}$. Owing to this property of the Riemann problem, the wave strengths can be obtained as

$$\tilde{\alpha}_l^1 = \tilde{\mathbf{l}}_l^1 \left(\mathbf{F}^{0\ \mathrm{R}} - \mathbf{F}^{0\ \mathrm{L}}\right) , \quad \tilde{\alpha}_2^1 = \tilde{\mathbf{l}}_l^2 \left(\mathbf{F}^{0\ \mathrm{R}} - \mathbf{F}^{0\ \mathrm{L}}\right) , \tag{2.86}$$

and therefore can be calculated analytically in a straightforward way.

- **Marquina flux formula**:

  The Marquina flux formula has a structure that is similar to Roe's flux formula (2.82)-(2.83), but differs in the numerical viscosity term: The latter is not "Roe averaged" for the left and right states, but is determined separately for the left and right states:

$$\mathbf{F}^1 = \frac{1}{2}\left[\mathbf{F}^{1\,\mathrm{R}} + \mathbf{F}^{1\,\mathrm{L}} - \sum_{k=1}^{5}\left(\tilde{\mathbf{r}}^{1\,\mathrm{R}}|\tilde{\lambda}^1_k|_{\max}\tilde{\alpha}^{1\,\mathrm{R}}_l - \tilde{\mathbf{r}}^{1\,\mathrm{L}}|\tilde{\lambda}^1_k|_{\max}\tilde{\alpha}^{1\,\mathrm{R}}_l\right)\right], \tag{2.87}$$

$$\mathbf{F}^2 = \frac{1}{2}\left[\mathbf{F}^{2\,\mathrm{R}} + \mathbf{F}^{2\,\mathrm{L}} - \sum_{k=1}^{5}\left(\tilde{\mathbf{r}}^{2\,\mathrm{R}}|\tilde{\lambda}^2_k|_{\max}\tilde{\alpha}^{2\,\mathrm{R}}_l - \tilde{\mathbf{r}}^{2\,\mathrm{L}}|\tilde{\lambda}^2_k|_{\max}\tilde{\alpha}^{2\,\mathrm{R}}_l\right)\right], \tag{2.88}$$

  where the $|\tilde{\lambda}^l_k|_{\max}$ is the maximum of the right and left reconstructed values of $\tilde{\lambda}^l_k$.

  Again assuming that the system is linear and thus the Jacobi matrices are constant, we can invert the matrix of right eigenvectors. We define the wave strengths as

$$\tilde{\alpha}^{1\,\mathrm{L}}_l = \tilde{\mathbf{l}}^{1\,\mathrm{L}}_k\mathbf{F}^{0\,\mathrm{L}}, \quad \tilde{\alpha}^{1\,\mathrm{R}}_l = \tilde{\mathbf{l}}^{1\,\mathrm{R}}_k\mathbf{F}^{0\,\mathrm{R}}, \quad \tilde{\alpha}^{2\,\mathrm{L}}_l = \tilde{\mathbf{l}}^{2\,\mathrm{L}}_k\mathbf{F}^{0\,\mathrm{L}}, \quad \tilde{\alpha}^{2\,\mathrm{R}}_l = \tilde{\mathbf{l}}^{2\,\mathrm{E}}_k\mathbf{F}^{0\,\mathrm{R}}, \tag{2.89}$$

  and recast the flux formula into

$$\mathbf{F}^1 = \frac{1}{2}\left(\mathbf{F}^{1\,\mathrm{R}} + \mathbf{F}^{1\,\mathrm{L}} - \Delta\mathbf{q}^1\right), \tag{2.90}$$

$$\mathbf{F}^2 = \frac{1}{2}\left(\mathbf{F}^{2\,\mathrm{R}} + \mathbf{F}^{2\,\mathrm{L}} - \Delta\mathbf{q}^2\right), \tag{2.91}$$

  where the numerical viscosity vector $\Delta\mathbf{q}^{\mathrm{l}}$ can be expressed as the difference of the products of the right eigenvector matrix, the diagonal eigenvalue matrix, the left eigenvector matrix, and the state vector, evaluated on the right and left of the interfaces:

$$\Delta\mathbf{q}^l = \mathbf{q}^{l,\,\mathrm{R}} - \mathbf{q}^{l,\,\mathrm{L}} = \mathbf{R}^{l\,\mathrm{R}}|\Lambda^{l\,\mathrm{R}}|\mathbf{L}^{l\,\mathrm{R}}\mathbf{F}^{0\,\mathrm{R}} - \mathbf{R}^{l\,\mathrm{L}}|\Lambda^{l\,\mathrm{L}}|\mathbf{L}^{l\,\mathrm{L}}\mathbf{F}^{0\,\mathrm{L}}. \tag{2.92}$$

  Using these equations, the numerical Marquina flux terms can be calculated in a straight-forward and computationally inexpensive way.

We want to close our discussion of approximate Riemann solvers with a short remark on the justification of the use of such solvers. In Section 2.2.3 we have pointed out the fact that the hydrodynamics equations are non-linear. However, the approximate Marquina Riemann solver is based on the assumption that the Jacobi matrices are locally constant. This assumption does not neglect the nonlinearity of the hydrodynamics equations in a discretization scheme, where the solution of any analytic equation is approximated by a locally linear function. Indeed, as suggested by Donat and Marquina [126], the discretization of analytic equations and the reconstruction at the cell interfaces already lead to some local loss of nonlinear information, so that the use of an approximate Riemann solver instead of an exact one will probably not have a significant impact on the accuracy of the numerical solution. The advantage of approximate Riemann solvers is in their much lower computational cost and this is decisive for choosing this method in the calculations of the numerical flux.

2.3.5 Reconstruction

Since the Riemann problem is formulated in terms of the primitive variables at the cell interfaces, they have to be constructed at each cell interface and each time-step using their cell average values. In a consistent and stable numerical hydrodynamics scheme, the reconstruction procedure of the cell-interface data must not violate the the conservative property of the scheme and must not introduce spurious oscillations. In the late 1950's, Godunov [172] showed that any linear[8] reconstruction method of higher than first-order accuracy will generally introduce spurious oscillations. Therefore, in his original scheme he used piecewise-constant reconstruction which, in a 1D case, is given by

$$q^{\text{first}}(x) = \bar{q}_i, \quad x \in \left[x_{i-1/2}, x_{i+1/2}\right] \ , \tag{2.93}$$

and which is the only conservative first-order reconstruction method.

In order to construct a scheme that is globally higher than first-order accurate for smooth flow and drops to first order only near discontinuities, reconstruction should be carried out with at least second-order accuracy. Besides Godunov reconstruction, COCONUT implements second-order MUSCL reconstruction schemes with a minmod and MC slope limiter [224] and the piecewise-parabolic reconstruction method (PPM) [102]. We will briefly describe these methods in the following, simplified to one spatial dimension and constant grid spacing. A generalization is straightforward. We point out that in all the calculations presented in this work, we have used PPM reconstruction, which provides a superior numerical accuracy.

Slope limited TVD

A straightforward conservative second-order reconstruction method is given in terms of a slope Δ_i by

$$q^{\text{second}}(x) = \bar{q}_i + \frac{x - x_i}{x_{\text{i}+1/2} - x_{\text{i}-1/2}}\Delta_i, \quad x \in \left[x_{\text{i}-1/2}, x_{\text{i}+1/2}\right] \ . \tag{2.94}$$

However, the above inevitably leads to spurious oscillations near extrema where both q and q' change abruptly [423, 225]. In other words, (2.94) does not preserve monotonicity and may lead to an unphysical increase in the total variation (TV) of the discretized function q. A TV-diminishing (TVD) scheme that retains second-order accuracy in smooth parts of q can be constructed by introducing a slope limiter function $\sigma_i(\bar{q}_{i-1}, \bar{q}_i, \bar{q}_{\text{i}+1})$ and writing

$$q(x) = \bar{q}_i + \frac{x - x_i}{x_{\text{i}+1/2} - x_{\text{i}-1/2}}\sigma_i, \quad x \in \left[x_{\text{i}-1/2}, x_{\text{i}+1/2}\right] \ . \tag{2.95}$$

At discontinuities, $\sigma_i = 0$ and the piecewise-constant reconstruction is recovered. Away from discontinuities, the second order form 2.94 is obtained. The simplest though most diffusive slope is given by the *minmod* limiter,

$$\sigma_i = \text{minmod}(\bar{q}_i - \bar{q}_{i-1}, \bar{q}_{i+1} - \bar{q}_i) \ , \tag{2.96}$$

where the minmod function of two arguments is defined by

$$\text{minmod}(a,b) = \begin{cases} a & \text{if } |a| < |b| \text{ and } ab > 0 \ . \\ b & \text{if } |b| < |a| \text{ and } ab > 0 \ . \\ 0 & \text{if } ab \leq 0 \ . \end{cases} \tag{2.97}$$

[8] Here the linearity refers to the independence of the the reconstruction methods on the data to be reconstructed.

Hence, the minmod limiter compares the magnitude of the upwind slope $(\bar{q}_i - \bar{q}_{i-1})$ with that of the downwind slope $(\bar{q}_{i+1} - \bar{q}_i)$ and picks the one that is smaller in magnitude, or, in the case of a local extremum where the two slopes have different signs, returns 0.

Van Leer's monotonized centered (MC) limiter [428, 429] provides considerably sharper resolution of discontinuities while still preserving the TVD property. It is defined by a minmod function of three arguments (defined analogously to (2.97)),

$$\sigma_i = \text{minmod}\left(\frac{1}{2}(\bar{q}_{i+1} - \bar{q}_i),\ 2(\bar{q}_i - \bar{q}_{i-1}),\ 2(\bar{q}_{i+1} - \bar{q}_i)\right) . \tag{2.98}$$

Piecewise parabolic method

The piecewise-parabolic method (PPM) as introduced by Colella and Woodward [102] and first applied to relativistic flows by Martí and Müller [258], is a composite reconstruction method that provides third-order accuracy in space. In the following, we present only the simplified variant of the original method implemented in CoCoNuT that is specialized for the case of an evenly-spaced grid. The fundamental idea behind PPM is to construct an interpolating parabola $a(x)$ in each computational cell $x_{i-1/2} < x < x_{i+1/2}$ such that no new artificial extrema appear in the interpolated function and such that its integral averages coincide with the known cell averages q_i (at timestep n)

$$\frac{1}{\Delta x}\int_{x_{i-1/2}}^{x_{i+1/2}} a(x)dx = \bar{q}_i . \tag{2.99}$$

The three coefficients of the parabola are determined by imposing condition (2.99) and by demanding that the parabola pass through the points $(x_{i-1/2},\ a_{i-1/2})$ and $(x_{i+1/2},\ a_{i+1/2})$. The interface values $a^- = a_{i-1/2}$ and $a^+ = a_{i+1/2}$ are found by demanding: (i) that they do not fall outside the ranges $[q_{i-1},\ q_i]$, $[q_i, q_{i+1}]$ for a^- and a^+ , respectively; (ii) that in smooth parts of q, $a^-_{i+1} = a^+ \equiv q_{i+1/2}$; and (iii) that $a(x)$ is monotonic in each cell. The first step in order to find a^+ and a^- is to consider the indefinite integral $I(x) = \int_x a(\xi)d\xi$ whose values are known at the cell interfaces:

$$I(x_{i+1/2}) = I_{i+1/2} = \sum_{k<1} \bar{q}_k \Delta x . \tag{2.100}$$

To find $q_{i+1/2}$, the above quartic polynomial is interpolated through the points $(x_{i+r+1/2}, I_{i+r+1/2})$, $r = 0,\ \pm 1,\ \pm 2$, which, after some algebra [102], yields from its differentiation:

$$a_i^+ = q_{i+1/2} = \frac{1}{2}(\bar{q}_{i+1} + \bar{q}_i) + \frac{1}{6}(\delta_m \bar{q}_i - \delta_m \bar{q}_{i+1}) , \tag{2.101}$$

where

$$\delta_m \bar{q}_i = \begin{cases} \min(|\delta\bar{q}_i|,\ 2|\bar{q}_{i+1} - \bar{q}_i|,\ 2|\bar{q}_i - \bar{q}_{i-1}|)\text{sign}(\delta\bar{q}_i) & \text{if } (\bar{q}_{i+1} - \bar{q}_i)(\bar{q}_i - \bar{q}_{i-1}) > 0 , \\ 0 & \text{otherwise} , \end{cases} \tag{2.102}$$

and

$$\delta\bar{q}_i = \frac{1}{2}(\bar{q}_{i+1} - \bar{q}_{i-1}) . \tag{2.103}$$

Analogously, a_i^- can be determined and the interpolating parabola is then

$$a(x) = a_i^- + x\left((a_i^+ - a_i^-) + 6\left[\bar{q}_i - \frac{1}{2}(a_i^+ - a_i^-)\right](1 - x)\right) . \tag{2.104}$$

At this point, the left and right states at the interfaces $i+1/2$ (and analogously at $i-1/2$) are set equal to the interpolated values,

$$q_i^+ = q_{i+1}^- = q_{i+1/2} \,. \tag{2.105}$$

This reconstruction will be oscillatory near discontinuities. Monotonicity is enforced by the replacement [102]:

$$q_i^+ = q_i^- = \bar{q}_i \qquad \text{if } (q_i^+ - \bar{q}_i)(\bar{q}_i - q_i^-) \le 0 \,, \tag{2.106}$$

$$q_i^- = 3\bar{q}_i - 2q_i^+ \qquad \text{if } (q_i^+ - \bar{q}_i)\left(\bar{q}_i - \frac{1}{2}(q_i^- + q_i^+)\right) > \frac{1}{6}(q_i^+ + q_i^-)^2 \,,$$

$$q_i^+ = 3\bar{q}_i - 2q_i^+ \qquad \text{if } (q_i^+ - \bar{q}_i)\left(\bar{q}_i - \frac{1}{2}(q_i^- + q_i^+)\right) < \frac{1}{6}(q_i^+ + q_i^-)^2 \,, \tag{2.107}$$

Two optional steps can be applied: Firstly, one may *steepen* discontinuities. This is to ensure sharp profiles and is only applied to contact discontinuities (i.e., discontinuities in ρ and continuous in v and p). The steepening procedure replaces the cell interface values of the density with

$$\rho_i^- = \rho_o^-(1-\eta) + \left(\bar{\rho}_{i-1} + \frac{1}{2}\delta_m\rho_{i-1}\right)\eta \,, \tag{2.108}$$

$$\rho_i^+ = \rho_o^+(1-\eta) + \left(\bar{\rho}_{i+1} + \frac{1}{2}\delta_m\rho_{i+1}\right)\eta \tag{2.109}$$

Here η is defined as

$$\eta = \max(0,\ \min(1,\ \eta_1(\bar{\eta} - \eta_2)), \tag{2.110}$$

where η_1 and η_2 are constants and

$$\delta_m\bar{\eta} = \begin{cases} \frac{\bar{\rho}_{i+2} - \bar{\rho}_{i+2} + 4\delta\bar{\rho}_i}{12\delta\bar{\rho}_i} & \text{if } \begin{cases} \delta^2\bar{\rho}_{i+1}\delta^2\bar{\rho}_{i-1} < 0 \,, \\ |(\bar{\rho}_{i+1} - \bar{\rho}_{i-1})| - \epsilon_{\rm PPM}\min(|\bar{\rho}_{i+1}|,\ |\bar{\rho}_{i-1}|) > 0 \,, \end{cases} \\ 0 & \text{otherwise} \,, \end{cases} \tag{2.111}$$

with $\epsilon_{\rm PPM}$ being another constant and

$$\delta^2\bar{\rho}_i = \frac{\bar{\rho}_{i+1} - 2\bar{\rho}_i + \bar{\rho}_{i-1}}{\Delta x^2} \,. \tag{2.112}$$

In addition to the above rules, $\rho^\pm$ are only modified if

$$K\frac{|\delta\bar{\rho}_i|}{\min(\bar{\rho}_{i+1},\ \bar{\rho}_{i-1}} \ge \frac{|\delta\bar{p}_i|}{\min(\bar{p}_{i+1},\ \bar{p}_{i-1}} \,, \tag{2.113}$$

where $\bar{p}_i$ is the cell average of the pressure in cell i. The above ensures that the discontinuity is predominantly a contact discontinuity. K is another positive parameter.

The second additional step that may be performed before monotonicity enforcement is the flattening of the zone structure near strong shocks. This adds simple dissipation to all reconstructed variables, is always active in CoCoNuT and avoids postshock oscillations:

$$q_i^\pm = \nu_i q_i^\pm + (1-\nu_i)\bar{q}_i \,, \tag{2.114}$$

where

$$\nu_i = \begin{cases} \max\left[0,\ 1-\max\left(0,\ \omega_2\left(\frac{\bar{p}_{i+1}-\bar{p}_{i-1}}{\bar{p}_{i+2}-\bar{p}_{i-2}}\right)\right)\right] & \text{if } \omega_0 \min(\bar{p}_{i-1},\ \bar{p}_{i+1}) < \bar{p}_{i+1}-\bar{p}_{i-1} \\ & \text{and } \bar{v}^X_{i-1}-\bar{v}^X_{i+1}>0\,, \\ 1 & \text{otherwise}\,, \end{cases} \tag{2.115}$$

and ω_0, ω_1 and ω_2 are constants. The implementation of PPM in CoCoNuT has seven tunable parameters whose default values are takes from Colella and Woodward [102].

2.3.6 Recovery of the primitive variables

As discussed in 2.3.3, the HRSC schemes for the solution of the GR hydrodynamics equations relies on the knowledge of the primitive variables (ρ, ϵ, v^i) at the cell interfaces for the computation of the fluxes through the cell boundaries. While there exists is a simple analytic conversion from the primitive to the conserved variables (specified by equations 2.44-2.44), there is no such trivial general relation for transforming back to the primitive variables. Instead they must be recovered by a numerical root-finding technique. For an overview on different methods, the reader is referred to, e.g., [258]. The CoCoNuT code uses a Newton-Raphson type iteration scheme that operates on the pressure. This scheme works for a general form of the EoS $p = p(\rho, \epsilon)$ and also for EoSs of the type $p = p(\rho, \epsilon, \{X_i\})$, if the dependence of p on the compositional variables X_i is much weaker than that on ρ and ϵ. The iteration scheme proceeds as follows.

First, the conserved variables are *undensitized*: $D = \gamma^{-1/2}\hat{D}$, $S^i = \gamma^{-1/2}\hat{S}^i$, and $\tau = \gamma^{-1/2}\hat{\tau}$. An initial guess for the pressure $\bar{p}$ is given from the previous step and the root of the function

$$f = \bar{p} - p(\bar{\rho}, \epsilon)\,, \tag{2.116}$$

is sought, where the approximate density and specific internal energy are given by

$$\bar{\rho} = \frac{D}{\tau+\bar{p}+D}\sqrt{(\tau+\bar{p}+D)^2-S^2}\,, \tag{2.117}$$

$$\bar{W} = \frac{\tau+\bar{p}+D}{\sqrt{(\tau+\bar{p}+D)^2-S^2}}\,, \tag{2.118}$$

$$\bar{\epsilon} = D^{-1}\left(\sqrt{(\tau+\bar{p}+D)^2-S^2}-\bar{p}\bar{W}-D\right)\,, \tag{2.119}$$

where $S^2 = S^i S_i$. The derivative of f is given by

$$f' = 1 - \frac{\partial p}{\partial \rho}\frac{\partial \rho}{\partial \bar{p}} - \frac{\partial p}{\partial \epsilon}\frac{\partial \epsilon}{\partial \bar{p}}\,, \tag{2.120}$$

where $\frac{\partial p}{\partial \rho}$ and $\frac{\partial p}{\partial \epsilon}$ must be provided by the EoS routines, and

$$\frac{\partial \rho}{\partial \bar{p}} = \frac{DS^2}{\sqrt{(\tau+\bar{p}+D)^2-S^2}(\tau+\bar{p}+D)^2}\,, \tag{2.121}$$

$$\frac{\partial \epsilon}{\partial \bar{p}} = \frac{\bar{p}S^2}{\rho\left[(\tau+\bar{p}+D)^2-S^2\right](\tau+\bar{p}+D)}\,. \tag{2.122}$$

Once the pressure is known to sufficient precision, the other variables are obtained straightforwardly. For a polytropic EoS, the procedure is simpler and one iterates over $\bar{p}\bar{W}$:

$$f = \bar{\rho}\bar{W} - D\,, \tag{2.123}$$

where $\bar{\rho}$ is the variable solved for. The pressure, specific internal energy and enthalpy $\bar{h}$ are set from the EoS and the Lorentz factor is found from

$$\bar{W} = \sqrt{1 + \frac{S^2}{(D\bar{h})^2}} \,. \tag{2.124}$$

The derivative is given by

$$f' = \bar{W} - 2\frac{\bar{\rho}S^2\bar{h}'}{\bar{W}D^2\bar{h}^3} \,, \tag{2.125}$$

where

$$\bar{h}' = \bar{\rho}^{-1}\frac{\partial p}{\partial \rho} \,. \tag{2.126}$$

2.3.7 Atmosphere treatment

One common problem of many hydrodynamic codes is their inability to handle regions where the density is zero (or very small compared with the typical densities in the system). However, polytropic density distributions in stellar models have the property that the density has a very sharp drop at the boundary of the star; this fall-off actually defines the stellar surface. For spherically symmetric stars, this rapid drop in density does not result in numerical problems as the exterior boundary of the grid can always be put at a radius where the density is sufficiently large to be properly handled by the numerical scheme.

On the other hand, in multidimensional simulations, particularly for rapidly rotating matter configurations, the deformed stellar surface does not coincide with a coordinate line of the computational grid. For rapidly rotating neutron stars in equilibrium, the axis ratio (i.e., the ratio between polar and equatorial radius) can be as low as 0.7 [209, 389]. Putting the boundary of the computational grid at a fixed radius within the star would cut off a large portion of the star in the vicinity of the equator. Defining the boundary of the grid at the maximum grid radius (which is outside the stellar matter) will also not help, as in those parts of the grid the density is zero, and the hydrodynamics scheme is destined to fail.

As a remedy for this we introduce a low density atmosphere outside the stellar matter distribution. An atmosphere will be assumed in all regions where the density ρ is below a threshold of some fraction $f_{\mathrm{atm\ thr}}$ of the maximum density of the initial matter distribution:

$$\rho_{\mathrm{atm\ thr}} = f_{\mathrm{atm\ thr}}\rho_{\mathrm{max\ ini}} \,. \tag{2.127}$$

The density ρ_{atm} of the atmosphere is again a fraction f_{atm} of $\rho_{\mathrm{atm\ thr}}$ (which gives additional flexibility by e.g. setting the atmosphere density to a lower value than the threshold density, which defines the stellar surface):

$$\rho_{\mathrm{atm}} = f_{\mathrm{atm}}\rho_{\mathrm{atm\ thr}} \,. \tag{2.128}$$

This atmosphere is not only set up initially, but also reset after each evolution step in the simulations. This ensures that the region covered by the atmosphere adapts automatically to the collapse dynamics, as the "shape" of the matter distribution may always change during the evolution.

2.3.8 Gravitational wave extraction

Linearized theory

General relativity describe gravitational waves as ripples in the curvature of spacetime, which propagate in vacuum at the speed of light. Similarly to water waves on the sea, the concept of gravitational wave requires the concept of an idealized smooth, unperturbed background on which the waves propagate. Contrary to

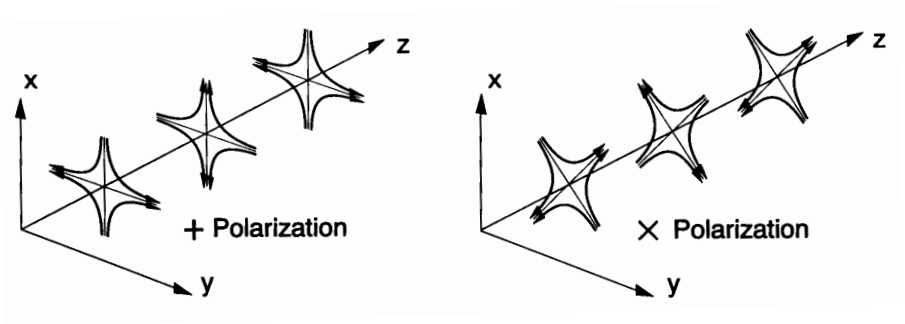

Figure 2.3: The lines of force associated with the two polarizations of a gravitational wave. Figure is taken from [145].

water waves, however, the gravitational waves are not associated with the motion of a material medium, they are ripples of the spacetime itself.

In the following, we give a brief introduction to linearized GR and gravitational wave generation in the weak-field and slow-motion limit by nearly-Newtonian matter sources and with the standard quadrupole formula. For a much more detailed discussion, the reader is referred to the standard textbook by Misner, Thorne & Wheeler [272], to the recent comprehensive textbook by Maggiore [249], the review by Flanagan and Hughes [145] and the numerous articles by Thorne [413, 414].

Once the gravitational waves leave their source ("near zone"), they are generally in regions where their wavelengths λ are very small compared to the curvature radius R of the background spacetime through which they propagate. The fact R is large is simply a restatement of the fact that gravitational field is weak. One can then introduce nearly a Minkowski metric so that

$$g_{\mu\nu} = \eta_{\mu\nu} + h_{\mu\nu} \ , \quad |h_{\mu\nu}| \ll 1 \ , \tag{2.129}$$

where $h_{\mu\nu}$ contains quasistatic contributions and any possible gravitational waves from astrophysical sources. Hereafter we focus only on the wave contributions to $h_{\mu\nu}$ and ignore the quasistatic contributions. We shall generally only summarize most of the results, with little derivation[9].

Gravitational waves are completely described by two dimensionless amplitudes, h_+ and $h_\times$, which correspond to the amplitudes of the two wave polarizations. For waves propagating in the z-direction, h_+ and $h_\times$ are functions only of $t - z/c$. If we introduce polarization tensors $\mathbf{e}_+$ and $\mathbf{e}_\times$ such that

$$\mathbf{e}_+ \equiv \vec{e}_x \otimes \vec{e}_x - \vec{e}_y \otimes \vec{e}_y \ , \quad \mathbf{e}_\times \equiv \vec{e}_x \otimes \vec{e}_x + \vec{e}_y \otimes \vec{e}_y \ , \tag{2.130}$$

where $\vec{e}_x$ and $\vec{e}_y$ are Cartesian unit vectors and $\otimes$ is the outer product, the gravitational wave strain can be written as

$$h_{ij}^{TT} = h_+ \mathbf{e}_+ + h_\times \mathbf{e}_\times \ . \tag{2.131}$$

This is a symmetric spatial tensor that is traceless and transverse to the propagation direction (no z-component). Gravitational waves act tidally, stretching and squeezing space and thus any object that they pass through. Figure 2.3 shows two polarizations of a gravitational wave and their associated lines of force.

The above h_{ij}^{TT} is an analog of the vector potential of electrodynamics in the Lorentz gauge. There one has in the vacuum

$$A_0 = 0 \ , \quad A_{i,i} = 0 \ , \quad \Box A_i = 0 \ , \tag{2.132}$$

[9]Full details of the theory of gravitational waves are given, for example, by [272, 249].

where the last equation comes from Maxwell's field equations in this gauge. Here we have

$$h^{TT}_{o\mu} = 0 \,, \quad h^{TT}_{jk,k} = 0 \,, \quad \Box h^{TT}_{jk} = 0 \,, \tag{2.133}$$

together with the trace-free condition. The last equation comes from the vacuum Einstein field equations in this gauge. The coordinate system in which Eqs. (2.133) are valid is called the *TT gauge* in GR, standing for *transverse-traceless gauge*. In the presence of matter, the Einstein field equations in the same gauge read

$$\Box h^{TT}_{jk} = -\frac{16\pi G}{c^4} T_{jk} \,, \tag{2.134}$$

where T_{jk} is the energy-momentum tensor of matter source (e.g., [272]).

Generation of gravitational waves - quadrupole radiation

The time-retarded solution of the inhomogeneous wave equation (2.134) is found in a way analogous to that in electromagnetic theory via the convolution of the inhomogeneity in equation (2.134) with a time-retarded Green's function which gives

$$h^{TT}_{ij}(t,\vec{x}) = \left[\frac{4G}{c^4} \int \frac{T_{ij}\left(t - |\vec{x} - \vec{x'}|/c, \vec{x'}\right)}{|\vec{x} - \vec{x'}|} d^3x' \right]^{TT} \tag{2.135}$$

We now consider a source of finite stress-energy tensor T_{ij} whose center is located at the origin of the coordinate system. Let $|\vec{x}|$ be the distance from the observer to the source. The source is taken to conform to the weak-field limit ($\frac{G}{c^2}\frac{M}{R} \ll 1$, where R is the radius of the source) and to the slow-motion approximation ($|\vec{v}| \ll c$). In these limits, an expansion in powers of $\vec{x'}/|\vec{x'}|$ gives in the lowest order the so-called *quadrupole formula*

$$h^{TT}_{ij}(t,\vec{x}) = \left[\frac{2}{c^4}\frac{G}{|\vec{x}|} \ddot{I}\left(t - |\vec{x}|/c\right) \right]^{\mathrm{TT}} \,, \tag{2.136}$$

with $\ddot{I}$ being the second time derivative of the mass quadrupole moment

$$I_{ij} = \int \rho x_i x_j d^3x \,. \tag{2.137}$$

To make the right hand side of equation (2.136) match the gauge conditions of the transverse-traceless gauge, we define the *reduced mass quadrupole moment*

$$\text{Ŧ}_{ij} \equiv I_{ij} - \frac{1}{3}\delta_{ij} I^k_k \tag{2.138}$$

and the projector

$$P_{jklm} \equiv P_{jl}P_{km} - \frac{1}{2}P_{jk}P_{lm} \quad \text{with} \quad P_{\mathrm{ij}} = \delta_{ij} - \frac{x_i x_j}{|\vec{x}|^2} \,. \tag{2.139}$$

Finally, we can write what is called the *standard quadrupole formula* (SQF):

$$h^{TT}_{jk}(t,\vec{x}) = \frac{2}{c^4}\frac{G}{|\vec{x}|} P_{jklm} \text{Ŧ}_{lm}(t - |\vec{x}|/c) \,. \tag{2.140}$$

Higher-order radiation is strongly suppressed by powers of $1/c$ (see, e.g., [272, 52]) and will not be considered here. Importantly, note the source-independent $1/|\vec{x}|$ fall-off behavior of the quadrupole wave strain. The quadrupole part of the total energy radiated in gravitational waves is given by [272]

$$E_{\mathrm{GW}} = \frac{1}{5}\frac{G}{c^5} \int_{-\infty}^{\infty} \dddot{\text{Ŧ}}_{ij} \dddot{\text{Ŧ}}_{ij} \, dt \tag{2.141}$$

The definition of the reduced mass quadrupole moment reveals that spherically symmetric configurations cannot emit gravitational radiation: their mass quadrupole moment is a scalar multiplied by the unit tensor. Hence, $\ddot{I}$ will be zero, and, if spherical symmetry is maintained, will remain so.

Numerical gravitational wave extraction

In simulations numerically evolving the full $\{3+1\}$ Einstein equations, the gravitational wave information is present in the curvature variables. Instead of trying to estimate the gravitational wave emission from the matter energy-momentum based on approximate formulae such as the SQF (2.140), it is more natural and – in principle – much more accurate to extract the gravitational waves *directly* from the *spacetime*. Ideally, such a treatment should also be gauge invariant. Over the past decades, a number of approaches have been proposed in the literature [461, 277, 6, 4, 5, 382, 381, 37, 291, 293, 18], including the radiation gauge approach, and using the Newman-Penrose formalism or the Zerilli-Moncrief formalism. However, in the CFC approximation of GR, the gravitational wave degrees of freedom are suppressed, hence one cannot extract gravitational waves from the curvature variables. Instead, in the work presented here, the gravitational waves are extracted using the standard quadrupole formula (2.140).

Using the SQF (2.140) to extract gravitational wave information from a general relativistic simulation must be done with great care and the SQF has a number of issues and drawbacks:

- The SQF describes the gravitational wave generation by nearly Newtonian, slowly moving object as seen by a distant observer. SQF represents fully developed and linear gravitational waves traveling in the distant wave zone. From classical electrodynamics one knows that electromagnetic waves do not acquire their asymptotic shape immediately after emission. The same holds for gravitational waves, with the additional complication that not only is their shape not wavelike and linear, but also they interact non-linearly with the curvature near to their source due to the non-linearity of GR.

- The SQF relies on coordinate quantities that are not covariant and gauge invariant. A change of coordinates (different choice of lapse and/or shift vector) will affect the results and there is no unique definition for the mass quadrupole tensor in full general relativity. However, for pulsating neutron star models, Balbinski et al. [24] found that the Newtonian quadrupole approximation gives good results for neutron stars with moderate compactness of $(GM)/(c^2R) \lesssim 0.04$. Recently, Shibata and Sekiguchi [375] have compared their implementation of the SQF to the gauge-invariant Zerilli-Moncrief method (see [461, 277, 6]) for extracting gravitational waves from oscillating neutron stars. Remarkably, they found very good qualitative agreement between the two methods. In particular, they found very good agreement of the wave phase and amplitude modulation but the SQF appeared to underestimate the magnitude of the wave amplitude typically by $\sim 20\%$.

- The SQF contains second time derivatives of the mass quadrupole tensor components. Two time derivatives are numerically cumbersome. Finn & Evans [147] and, independently, Blanchet and collaborators [52] have derived quadrupole radiation formulae in which one or even both time derivatives are eliminated by means of the (Newtonian) Euler equations.

Despite these issues and problems, we resort to the SQF (equations (2.135) through (2.141) for extracting gravitational waves from the matter motion in our general relativistic simulations. The quadrupole formalism gives a direct estimate for the gravitational waves emitted by an accelerated mass distribution as seen by an asymptotic observer. For the relatively weak-field ($\frac{G}{c^2}\frac{M}{R} \sim 0.1$), relatively slow-motion ($v \sim 0.1 - 0.2c$) situation encountered in stellar core collapse, wave estimates by the quadrupole approximation may actually be more reliable that conceptually and technically more involved methods for wave extraction directly from curvature variables [310].

Throughout this section we will use standard cgs units, and hence retain all factors of c and G. The numerical code used to extract gravitational waves from our simulation data based on the formulae presented in this section was written by H. Dimmelmeier [119].

Standard quadrupole formula in COCONUT

We start with the reduced mass quadrupole tensor defined by

$$\mathcal{I}_{jk} = \int \rho \left(x^j x^k - \frac{1}{3}\delta^{jk} x_i x^i \right) d^3x \; . \tag{2.142}$$

Note that we assume the weak-field, slow motion linear limit and thus raise and lower induces with $\eta_{ij} = \mathrm{diag}(1,\ 1,\ 1)$ making the difference between "upper" and "lower" indeces irrelevant. As motivated by Dimmelmeier et al. [118, 116] and Shibata and Sekiguchi [375], we replace the Newtonian rest-mass density ρ with $\bar{D} = \sqrt{\gamma} W$. Here W is the Lorentz factor and ρW is densitized, because (1) the actual evolved variable is $\sqrt{\gamma}\rho W$ (see equation 2.47) and (2) because the volume element in the above integral becomes an approximate natural volume element (see, e.g., [272]) with this choice.

We first recast the standard quadrupole formula (SQF) introduced above in a slightly different form:

$$h_{jk}^{TT}(t,\ \vec{x}) = \frac{2}{c^2}\frac{G}{R}\left[\frac{d^2}{dt^2}\mathcal{I}_{jk}(t - R/c) \right]^{TT} \; , \tag{2.143}$$

where R is the distance from the source to the observer and TT stands for transverse-traceless. Following Finn and Evans [147] and Blanchet et al. [52], we now make use of the continuity equation,

$$\hat{D}_{,t} + (\hat{D} v^i)_{,i} = 0 \; , \tag{2.144}$$

to eliminate one of the time derivatives from (2.143), arriving at the *first moment of momentum density* formula for the first time derivative of the mass quadrupole tensor:

$$\frac{d}{dt}\mathcal{I}_{ij} = \int \hat{D} \left[v^i x^j + v^j x^i - \frac{2}{3}\delta^{ij}(v^k x^k) \right] d^3x \; . \tag{2.145}$$

For writing our the gravitational wave amplitudes in terms of the two possible polarizations of gravitational waves, h_+ and $h_\times$, we choose a source-local spherical coordinate frame $(r,\ \theta,\ \phi)$ with normalized basis vectors. The unit polarization tensors (2.131) in this basis are

$$\boldsymbol{e}_+ = \boldsymbol{e}_\theta \otimes \boldsymbol{e}_\theta - \boldsymbol{e}_\varphi \otimes e_\varphi \; , \tag{2.146}$$

$$\boldsymbol{e}_\times = \boldsymbol{e}_\theta \otimes \boldsymbol{e}_\varphi + \boldsymbol{e}_\varphi \otimes e_\theta \; , \tag{2.147}$$

and the two dimensionless gravitational wave strains have the particularly simple form

$$h_+ = \frac{G}{c^4}\frac{1}{D}\left(\ddot{\mathcal{I}}_{\theta\theta} - \ddot{\mathcal{I}}_{\phi\phi} \right) \; , \tag{2.148}$$

$$h_\times = \frac{G}{c^4}\frac{2}{D}\ddot{\mathcal{I}}_{\theta\phi} \; , \tag{2.149}$$

where we use the dot convention for time derivatives for simplicity of notation. An observer located on the polar axis of the source ($\theta = 0,\ \phi = 0$) then sees

$$h_+^p = \frac{G}{c^4}\frac{1}{D}\left(\ddot{\mathcal{I}}_{xx} - \ddot{\mathcal{I}}_{yy} \right) \; , \tag{2.150}$$

$$h_\times^p = \frac{G}{c^4}\frac{2}{D}\ddot{\mathcal{I}}_{xy} \; , \tag{2.151}$$

and an observer in the equatorial plane ($\theta = \pi/2, \phi = 0$) sees

$$h^e_+ = \frac{G}{c^4}\frac{1}{D}\left(\ddot{\mathcal{I}}_{zz} - \ddot{\mathcal{I}}_{yy}\right) , \tag{2.152}$$

$$h^e_\times = \frac{G}{c^4}\frac{2}{D}\ddot{\mathcal{I}}_{yz} . \tag{2.153}$$

where $\mathcal{I}_{xx}$, $\mathcal{I}_{yy}$, $\mathcal{I}_{zz}$, $\mathcal{I}_{xy}$ and $\mathcal{I}_{yz}$ are Cartesian components of $\mathcal{I}$. Note that, in axisymmetry, h^p_+, $h^p_\times$ and h^e_+ all vanish, leaving only $h_+ = h^e_+$. The total energy emitted in quadrupole gravitational waves is computed using formula (2.141).

The first moment of momentum density (2.145) recasting of the SQF greatly reduces the numerical noise in the extracted wave signal (see, e.g., [116]). We compute the single remaining time derivative via finite differences in a postprocessing step. Finn and Evans [147] and Blanchet et al. [52] went a step further and additionally applied the Newtonian equation of momentum conservation which led to the *stress formula* variant of the QDF that does not contain any time derivatives, but has terms involving derivatives of the Newtonian gravitational potential Φ

$$\mathcal{I}_{ij} = \int \hat{D}\left[2v^i v^j - x^i\Phi_{,j} - x^j\Phi_{,i} - \frac{2}{3}\delta^{ij}(v^k v^k - x^k\Phi_{,k}\right] d^3x . \tag{2.154}$$

The stress formula is widely used in Newtonian source simulations, but because of the ambiguity concerning the definition of a Newtonian potential in terms of GR field variables, we have decided not to use the stress formula in our GR calculations (see also the discussion in [117]).

Characteristic strain

In order to assess the prospects for detection by current and planned interferometric detectors, we calculate characteristic quantities for the GW signal following [413]. Performing a Fourier transform of the dimensionless GW strain h,

$$\hat{h} = \int_{-\infty}^{\infty} e^{2\pi i f t} h\, dt , \tag{2.155}$$

we can, following [414], compute the (detector dependent) integrated characteristic frequency

$$f_{\rm c} = \left(\int_0^\infty \frac{\langle\hat{h}^2\rangle}{S_h} f\, df\right)\left(\int_0^\infty \frac{\langle\hat{h}^2\rangle}{S_h} df\right)^{-1}, \tag{2.156}$$

and the dimensionless integrated characteristic strain

$$h_{\rm c} = \left(3\int_0^\infty \frac{S_{h\,{\rm c}}}{S_h}\langle\hat{h}^2\rangle f\, df\right)^{1/2}, \tag{2.157}$$

where S_h is the power spectral density of the detector and $S_{h\,{\rm c}} = S_h(f_{\rm c})$. We approximate the average $\langle\hat{h}^2\rangle$ over randomly distributed angles by $\hat{h}^2$, assuming optimal orientation of the detector. From Eqs. (2.156, 2.157) the optimal single-detector signal-to-noise ratio (SNR) can be calculated as $h_{\rm c}/[h_{\rm rms}(f_{\rm c})]$, where $h_{\rm rms} = \sqrt{f S_h}$ is the value of the rms strain noise for the detector. Note that the definition of the SNR given here is a factor of $\sqrt{3/2}$ larger than that given by [144]. This difference is due to the different ways of performing the angular averaging chosen by [414] and [144].

2.3.9 Initial Equilibrium Model Solver

Rotation violates spherical symmetry and initial models in *rotational equilibrium* are oblate spheroids, or in the case of extreme rotation, oblate quasi-toroids. The initial equlibrium models used in our simulations are obtained using Hachisu's self-consistent field (SCF) method [180] which is an iterative method for solving the hydrostatic equilibrium equations for rotating polytropic matter distributions. The SCF methods was extended to GR by Komatsu, Eriguchi & Hachisu [209], and was further improved by Cook et al. [104] and Stergioulas [389, 390, 301]. For a review of rotating stars in GR and the computation of rotational equilibrium models, the interested reader is referred to the Living Reviews in Relativity article by N. Stergioulas [391]. Here we will only delineate the most basic and salient aspects of the Komatsu-Eriguchi-Hachisu scheme. Additional information and numerical details can be found in the above references.

The three basic assumptions are that the considered spacetime is axisymmetric, stationary and asymptotically flat. Stationarity implies that there exists a timelike Killing vector field t^α (see, e.g., [272]). Axisymmetry implies that there exists a spacelike Killing vector field ϕ^α in the symmetry direction. Asymptotic flatness guarantees that $t^\alpha t_\alpha \to -1$, $\phi^\alpha \phi_\alpha \to +\infty$ and $t^\alpha \phi_\alpha \to 0$ at spatial infinity. The two Killing vectors commute [88] and it is possible and convenient to choose coordinates in which t^α and ϕ^α are basis vectors. If, in addition, the rotating flow is strictly circular, all 2-surfaces orthogonal to the two Killing vector fields can be described by the remaining two coordinates x^1 and x^2 [89]. In isotropic coordinates, the 2-surfaces spanned by $x^1 = r$ and $x^2 = \theta$ are conformally flat and the line element can be written as

$$ds^2 = -e^{2\hat{\nu}}dt^2 + e^{2\hat{\alpha}}(dr^2 + r^2 d\theta^2) + e^{2\hat{\beta}} r^2 \sin^2\theta (d\varphi - \omega dt)^2, \tag{2.158}$$

with the metric potentials $\hat{\nu}$, $\hat{\alpha}$, $\hat{\beta}$ and ω.

The rotating matter is assumed to be a non-magnetic neutral perfect fluid with a stress-energy tensor as defined by equation (2.40). The only nonvanishing three-velocity component is v^3, the velocity of the fluid as measured by a local ZAMO (zero angular momentum observer). Thus, the Lorentz factor is given by $W = 1/\sqrt{1 - v_3 v^3}$. With the definitions $u^0 = We^{-\hat{\nu}}$, and $u^3 = \Omega W e^{-\hat{\nu}}$, where Ω is the angular velocity of the fluid as measured from infinity, the four-velocity is given by

$$u^\mu = We^{-\hat{\nu}}(1, 0, 0, \Omega). \tag{2.159}$$

Thus, one gets for the φ-component of the three-velocity:

$$v^3 = \frac{u^3}{u^0 e^{\hat{\nu}}} - \frac{\omega}{e^{\hat{\nu}}} = e^{-\hat{\nu}}(\Omega - \omega), \tag{2.160}$$

$$v_3 = e^{2\hat{\beta} - \hat{\nu}} r^2 \sin^2\theta (\Omega - \omega), \tag{2.161}$$

$$v_\varphi \equiv \sqrt{v_3 v^3} = e^{\hat{\beta} - \hat{\nu}} r \sin\theta (\Omega - \omega). \tag{2.162}$$

Here v_φ is the proper rotation velocity with respect to the ZAMO. The specific angular momentum of the fluid $j \equiv u^0 u_3$ is given by

$$j = W^2 e^{2(\hat{\beta} - \hat{\nu})} r^2 \sin^2\theta (\Omega - \omega) = \frac{v_3 v^3}{(1 - v_3 v^3)(\Omega - \omega)}. \tag{2.163}$$

Using the Einstein equations one can derive the equation of hydrostatic equilibrium for an axisymmetric mass distribution rotating with the angular velocity $\Omega = \Omega(r)$ (e.g., [391]):

$$\frac{\nabla P}{\rho h} + \nabla\hat{\nu} - \frac{v_\varphi}{1 - v_\varphi^2}\nabla v_\varphi + j\nabla\Omega = 0. \tag{2.164}$$

For barotropes, where p depends only on ρ the integrability of Eq. (2.164) requires that j is a function of Ω only. One can now integrate the equation of hydrostatic equilibrium (2.164) to obtain

$$\ln h + \hat{\nu} + \frac{1}{2}\ln(1 - v_\varphi^2) - \int j \, d\Omega = \text{const} \,, \tag{2.165}$$

where h is the enthalpy and the four-metric components $\hat{\alpha}$, $\gamma = \hat{\beta} + \hat{\nu}$, $\delta = \hat{\nu} - \hat{\beta}$ and ω are given by the four coupled partial differential equations [209]

$$\Delta\left(\delta e^{\gamma/2}\right) = S_\delta, \tag{2.166}$$

$$\left(\Delta + \frac{1}{r}\partial_r - \frac{\mu}{r^2}\partial_\mu\right)\gamma e^{\gamma/2} = S_\gamma, \tag{2.167}$$

$$\left(\Delta + \frac{2}{r}\partial_r - \frac{2\mu}{r^2}\partial_\mu\right)\omega e^{(\gamma-2\delta)/2} = S_\omega, \tag{2.168}$$

$$\partial_\mu \hat{\alpha} = S_{\hat{\alpha}}, \tag{2.169}$$

where Δ is the Laplacian and $\mu \equiv \cos\theta$. The source terms S_δ, S_γ, S_ω, and $S_{\hat{\alpha}}$ depend in general on all four metric functions. In order to solve this system of equations the first three PDEs are converted into integral equations using Green's functions which in turn are expanded in Legendre polynomials. In discretized form, these equations are iterated until convergence is obtained. During each iteration, the discretized equation (2.169) for $\hat{\alpha}$ is integrated.

Chapter 3

Phase-transition-induced collapse of neutron stars

3.1 Introduction

The existence of compact stellar objects partially or totally consisting of matter in a deconfined quark phase was already predicted long ago [59, 198, 443]. Such stars are thought likely to originate as a result of the conversion of purely hadronic matter in the interior of a neutron star (NS) into a deconfined quark matter phase when the density exceeds a certain threshold (for a review see, e.g., [439, 171]). We focus here on cases where the conversion occurs only in the core of the NS, while the outer parts remain unchanged. The theory of dense nuclear matter predicts that such compact stars [hereafter we will use the term "hybrid quark star" (HQS) when referring to these objects] would generally be more compact than the progenitor standard NS, and their equilibrium radii would be smaller by up to 20%. The potential energy W released by the phase transition is expected to be of order

$$\Delta W \sim \frac{M^2}{R}\frac{\Delta R}{R} \sim 10^{52}\,\mathrm{erg},$$

where R and M are the typical radius and mass of the NS, respectively, and ΔR is the decrease in radius.

A first-order phase transition is expected to be the most interesting case as far as the dynamics and structure of the star are concerned. Such a transition would proceed by the conversion of initially metastable hadronic matter in the core into the new deconfined quark phase [462, 463]. The metastable phase could be formed as the central density of the NS increases due to mass accretion, spin-down or cooling. This could happen soon after the birth of the NS in a supernova or it could occur for an old NS accreting from a binary companion. The first of these channels is likely to give the higher event rate but the second is also interesting. In the widely accepted scenario for the formation of millisecond pulsars, where an old NS is spun up by accretion from a binary companion, the amount of spin-up would be directly related to the amount of mass accreted [73], meaning that there would be a population of rapidly rotating NSs with rather high mass (and hence high central densities). Recent observational data seems to confirm that a significant proportion of millisecond pulsars do indeed tend to be high-mass objects [152] which would then be candidates for undergoing (or having undergone) a phase-transition-induced collapse of the type which we are discussing here. While some significant proportion of the potential energy release given by Eq. (3.1) would probably go into neutrino emission, a significant proportion might also go into pulsations of the newly-formed HQS, if the conversion process to the new phase is rapid enough, and this could be an interesting source of gravitational waves (GWs; see [256, 271, 233]). If detected, these GW signals, and in particular the identification of quasi-normal mode frequencies in their spectrum, could help to constrain

the properties of matter at the high densities encountered here. For non-rotating cold NSs with various compositions, the related theory of asteroseismology has already been formulated in recent years [13, 208, 40].

A problem for making any detailed studies of phase-transition-induced collapse is that the description of the physics of the phase transition remains very uncertain and controversial (for a recent review see, [192]). Drago et al. [128] discussed possible modes of burning of hadronic matter into quark matter in the framework of relativistic hydrodynamics using a microphysical equation of state (EoS). They found that the conversion process always corresponds to a deflagration and never to a detonation[1]. They also argued that hydrodynamical instabilities can develop at the burning front. They estimated the corresponding increase in the propagation velocity of the phase transition and noticed that, although the increase is significant, it is not sufficient to transform the deflagration into a detonation in essentially all realistic scenarios. On the other hand, Bhattacharyya et al. [49] considered the transition as being a two-step process, in which the hadronic matter is first converted to two-flavour u and d quark matter, which then subsequently transforms into strange quark matter (u, d and s quarks) in a second step. They used the relativistic hydrodynamic equations to calculate the propagation velocity of the first front and found that, in this first stage, a detonation wave develops in the hadronic matter. After this front passes through, leaving behind two-flavour matter, a second front is generated which transforms the two-flavour matter to three-flavour matter via weak interactions. The timescale for the second conversion is $\sim 100\,\mathrm{s}$, while that for the first step is about $1\,\mathrm{ms}$.

Against this background, Lin et al. [233] (hereafter referred to as LCCS) carried out a first study of GW emission by a phase-transition-induced collapse of a rotating NS to a HQS, using a very simplified model for the microphysics and treating the phase transition as occurring instantaneously. On the basis of 3D calculations using Newtonian gravity and hydrodynamics, they obtained waveforms of the emitted GWs for several collapse models, and found that the typical predicted dimensionless GW strain h ranged from 3 to 15×10^{-23} for a source at a distance of $10\,\mathrm{Mpc}$. The corresponding energy E_{gw} carried away by the GWs was found to be between 0.3 and $2.8 \times 10^{51}\,\mathrm{ergs}$. They also determined the modes of stellar pulsation excited by the collapse and showed that the spectrum of the emitted GWs was dominated by the fundamental quasi-radial and quadrupolar pulsation modes of the final star. They suggested that the damping of the stellar pulsations observed in their calculations was due to the production of shock waves leading to the development of differential rotation, which proceeds on a timescale of about $5\,\mathrm{ms}$ for typical collapse models.

The study by LCCS treated the conversion process as being instantaneous, and this was mimicked by replacing, at the initial time, the EoS describing the hadronic nuclear matter in the core (with which the initial equilibrium model had been built) by one describing a central zone of deconfined quarks surrounded by a region of mixed phase. The material outward of this remained in the original hadronic phase. In a first-order phase transition that proceeds via a detonation, the conversion front propagates supersonically with respect to the matter ahead of it. The sound speed in the stellar interior typically has a value of the order of 0.3 to $0.5\,c$. Assuming that the quark-matter core has a radius of about $R \sim 5\,\mathrm{km}$, a rough estimate for the timescale of a supersonic conversion gives $\tau \sim R/v \sim 0.05\,\mathrm{ms}$. Clearly, this value is not much smaller than the dynamical timescale of a NS and so one does not know, a priori, the impact that the properties of the conversion would have for the subsequent stellar dynamics taking place on similar timescales. Therefore, one should first check how the dynamics of the star after the phase transition would depend on the finite propagation velocity of the front, and we do this here.

[1]Detonation is a process of combustion in which a supersonic shock wave is propagated through a fluid due to an energy release in a reaction zone. It is the more powerful of the two general classes of combustion, the other one being deflagration. In a detonation, the shock compresses the material thus increasing the temperature to the point of ignition. The ignited material burns behind the shock and releases energy that supports the shock propagation. This self-sustained detonation wave is different from a deflagration, which propagates at a subsonic rate (i.e., slower than the sound speed in the material itself; e.g., [218]).

LCCS represented the hadronic matter by means of a polytropic EoS, initially having an adiabatic index $\gamma = 2$. When the phase transition was triggered (by changing the EoS in the central regions, reducing the pressure support), they also replaced the original hadronic EoS by a softer ideal-gas type of EoS (with γ then ranging from 1.95 to 1.75 depending on the model), which artificially lowered the pressure *outside* the deconfined quark matter core as well [see their Eq. (44)]. The lowering of the adiabatic index also in the outer regions leads to an increased release of gravitational binding energy and is hard to motivate on physical grounds.

Although the study by LCCS was an important step forward, it was clearly using an extremely simplified model for the physics of the NS matter and of the phase transition (as well as not including emission processes other than GW emission) and one must question how closely it represents such processes occurring in real NSs. Since the full problem is complex and involves some input physics which is very incompletely known at present, the only way to make progress at this stage is, indeed, to work in terms of simplified models but making improvements where possible. The strategy of the work presented here is to take the work of LCCS as a starting point and then to take some steps forward in the direction of including further aspects. In particular, the effects of general relativity certainly play an important role in such studies: for instance, the total rest mass of a typical Newtonian NS may be almost twice as large as that of its counterpart in GR with the same central density and the same EoS. The impact of GR is even more pronounced if the star is near to the maximum mass limit. Therefore, one expects the Newtonian and GR descriptions of NS collapse to differ significantly, thus necessitating a proper treatment of the GR effects.

In this study we extend the previous work of LCCS in a number of ways: (i) we take into account the effects of GR; (ii) we modify the EoS of the stellar matter only in regions which undergo the phase transition and take care to avoid introducing spurious convection; (iii) we consider a larger set of physical models for different values of the stellar parameters and different properties of the stellar matter; (iv) we study the effect of introducing a finite timescale for the initial phase transformation which destabilises the core rather than treating it as occurring instantaneously. Our model for the HQS is based on that of LCCS. The numerical hydrodynamics simulations are here performed in axisymmetry using the conformal flatness approximation to GR. While our model remains extremely simplified, we believe that these modifications do represent valid and significant steps forward. We feel, however, that we should caution against making further elaborate extensions of the hydrodynamics (e.g. to 3D GR hydrodynamics or GR magneto-hydrodynamics) until such time as one has the possibility of including a greatly improved treatment of the microphysics and emission processes so that the models come closer to those of real NSs.

The rest of this chapter is organized as follows: In Section 3.2 we summarize the numerical methods used, while in Section 3.3 we introduce the models investigated. In Section 3.4 we validate our code by performing a comparison with the Newtonian models of LCCS. In Section 3.5 we discuss the results of our simulations of GR models and their dependence on the various parameters, and in Section 3.6 we conclude with a summary. In Appendix A we examine the impact on the collapse dynamics of considering a finite timescale for the initial phase transformation, and in Appendix B we present our method for determining the damping times for the emitted gravitational radiation waveforms.

3.2 Summary of numerical methods

This section provides a brief summary of numerical method employed for the simulations presented in this chapter. More detailed discussion can be found in Chapter 2 of this dissertation.

We construct our initial rotating NS equilibrium models using a variant of the self-consistent field method described in [209] (KEH hereafter), as implemented in the code RNS [389]. This code solves the GR hydro-stationarity equations for rotating matter distributions whose pressure obeys an EoS given by a polytropic relation (see equation 3.1 below). The resulting equilibrium models, which we choose to be

rotating uniformly, are taken as initial data for the evolution code.

The time-dependent numerical simulations were performed with the CoCoNuT code [117, 118, 119]. The code solves the GR field equations for a curved spacetime in the $3+1$ split under the assumption of the conformal flatness condition (CFC) for the three-metric (see Section 2.3.2). To numerically solve the elliptic CFC metric equations we utilise an iterative nonlinear solver based on spectral methods (see Section 2.3.2). The hydrodynamics equations are formulated in conservation form, and are evolved with high-resolution shock-capturing schemes on a finite-difference grid (Section 2.3.3). The CoCoNuT code uses Eulerian spherical polar coordinates $\{r, \theta, \phi\}$; the simulations presented in this chapter are performed assuming axisymmetry with respect to the rotation axis and equatorial symmetry. The finite-difference grid consists of 200 radial grid points and 40 angular grid points, which are equidistantly spaced. A small part of the grid, which initially corresponds to 60 radial gridpoints, covers an artificial low-density atmosphere, extending beyond the stellar surface, whose rest-mass density is 10^{-17} of the initial central rest-mass density of the NS. We also note that tests with different grid resolutions were performed to check that the regular grid resolution specified above is appropriate for our simulations. A check on the relative violation in the conservation of total rest mass, ADM mass and total angular momentum showed that each of these quantities is conserved to within $1\ \%$ during the entire evolution time.

Since the calculation of the spacetime metric is computationally expensive, it is updated only once every 25 hydrodynamic timesteps during the evolution and is extrapolated in between. The suitability of this procedure has been tested and discussed in detail in Dimmelmeier et al [117]. The GWs emitted by the collapsing NS are computed using the Newtonian quadrupole formula in its first time-integrated form (Section 2.3.8).

3.3 Stellar models and treatment of the phase transition

3.3.1 Initial neutron star model

Following LCCS, we compute the initial equilibrium NS model before the phase transition using a polytropic EoS,

$$P = K\rho^{\gamma}, \tag{3.1}$$

where K and γ are constants. We choose $\gamma = 2$ and $K = 100$ (in units where $M_{\odot} = 1$) for all of the GR initial models considered in the present study. On the initial timeslice, we also need to specify the specific internal energy ϵ. For a polytropic EoS, the thermodynamically consistent ϵ is given by

$$\epsilon = \frac{K}{\gamma - 1}\rho^{\gamma-1}. \tag{3.2}$$

3.3.2 Hybrid quark star model

Due to the complexity of the fundamental theory of strong interactions, all theoretical studies of quark matter in compact stars are based on phenomenological models. The MIT bag model EoS, which has been used extensively for this (for a review see, e.g. [439, 171]), is based on the following assumptions: (i) quarks appear in colour neutral clusters confined to a finite region of space, the volume of which is limited by the negative pressure of the QCD vacuum; (ii) within this region, interactions between the quarks are weak and can be treated using low-order perturbation theory in the coupling constant. These two assumptions allow the two main features of QCD to be modelled, namely colour confinement and asymptotic freedom. The parameters of the bag model are the bag constant B, the masses of the quarks and the running coupling constant α_s, whose value at the scale relevant for typical quark chemical potentials is $\alpha_s \in [0.4, 0.6]$ [41].

At the moment there is no general consensus about the value of B. Fits to the spectrum of light hadrons give $B^{1/4} \approx 145$ MeV [110], while the adjustment of B with hadronic structure functions suggests $B^{1/4} \sim 170$ MeV [386]. On the other hand, lattice QCD calculations predict values up to $B^{1/4} \sim 190$ MeV [364]. Hereafter, and following LCCS, we take $B^{1/4} = 170$ MeV.

The masses of the u and d quarks are of the order of a few MeV [182] and can therefore be mostly neglected, whereas the mass of the s quark is much larger, its value being in the range $m_s \in [80, 155]$ MeV. Nevertheless, including this mass for the s quark, rather than taking it to be massless, would decrease the pressure by only a few percent [8]. We do not expect that this would change our results qualitatively, and so we neglect it in our study. We also neglect the residual interaction between the quarks and approximate their temperature as being zero. The EoS of the MIT bag model for massless and non-interacting quarks at zero temperature is given by

$$P_{\rm q} = \frac{1}{3}(e - 4B), \tag{3.3}$$

where e is the total energy density.

A fundamental problem appears to arise in using the hydrodynamic equations of Section 3.2 to describe the quark medium since the quarks are being treated as having zero rest mass. The quantity e represents only the internal energy density of the quarks and contains no rest-mass contribution. Rest mass appears as a fluid quantity, within this picture, only when the quarks become confined. Nevertheless, the continuity equation [the first equation of the system of the hydrodynamic equations (2.47)] remains well-defined if thought of in terms of baryon number (which *is* defined for the quark medium) rather than in terms of rest mass. In order to have a unified treatment for the quark matter and the hadronic matter (which is necessary since we have transformation between the two), one can define a quantity $\rho = n_{\rm b} m_{\rm b}$ in the quark medium (where $n_{\rm b}$ is the baryon number density and $m_{\rm b}$ is the rest mass per baryon in the hadronic medium) and then formally split the internal energy density of the quark medium into two parts, writing $e = \rho + \rho\epsilon$ as usual but bearing in mind that the first term on the right hand side represents just a part of the internal energy density in the quark phase. If one does this, it is easy to show that the treatment of the hydrodynamics goes through unchanged in a consistent way, using this ρ and ϵ.

For the normal hadron matter, during the evolution we use an ideal-gas type of EoS

$$P_{\rm h} = (\gamma - 1)\rho\epsilon. \tag{3.4}$$

However, in contrast to LCCS, we do not reduce the adiabatic index γ from its initial value of 2, because we see no physical mechanism which could be responsible for a global reduction of pressure in the *hadronic* matter phase. Consequently, in our GR models the collapse is caused solely by the pressure change due to the introduction of *quark* matter in the core of the NS.

As first shown by [169, 170], if the surface tension between the phases is not too large, relaxing the condition of local electrical neutrality would allow for the possibility of having coexistence between the two phases within a certain range of densities. In a region where this applied, one would then have many inter-mixed microscopic zones of the lower-density hadronic matter and of the higher-density quark matter. Each zone would have a net electric charge but with the mixture being electrically neutral on average and with the volume fraction occupied by the higher-density phase growing from 0 at the lower-density boundary of the mixed phase $\rho_{\rm hm}$ up to 1 at the upper-density boundary $\rho_{\rm qm}$.

The value of the lower threshold density $\rho_{\rm hm}$, above which free quarks start to appear, is rather uncertain. From simple geometrical considerations, nucleons should begin to touch at $\rho \sim (4\pi r_{\rm nuc}^2/3)$, which for the characteristic nucleon radius $r_{\rm nuc} \sim 1$ fm gives a few times nuclear saturation density, $\rho_{\rm nuc} = 2.7 \times 10^{14}$ g cm^{-3} [168]. For densities above this, one expects that the boundaries of particles like p, n, Σ^-, Λ and K^- would dissolve and that quarks would start to populate free states outside the hadrons [439]. The value of the upper threshold density $\rho_{\rm qm}$, marking the boundary between the mixed phase and the pure

Table 3.1: Summary of the set of initial models: p is the rotation period of the NS, M_0 is the total rest mass, M is the gravitational mass, T is the rotational mass energy, W is the gravitational binding energy, $\rho_{\rm c,i}$ is the central rest-mass density and $r_{\rm e}/r_{\rm p}$ is the ratio of the equatorial and polar radii. Note that the initial models A5, B4 and C3 are identical. Model N is one of the Newtonian initial models used by LCCS.

Model	p [ms]	M_0 [$M_\odot$]	M [$M_\odot$]	$\rho_{\rm c,i}$ [$10^{14}\,{\rm g\,cm^{-3}}$]	$r_{\rm e}/r_{\rm p}$	$T/\lvert W\rvert$ [%]
A1	1.00	1.98	1.81	11.25	0.635	8.44
A2	1.20	1.85	1.70	11.25	0.785	5.30
A3	1.40	1.80	1.65	11.25	0.847	3.75
A4	1.60	1.77	1.62	11.25	0.885	2.80
A5	1.80	1.75	1.60	11.25	0.910	2.18
A6	2.00	1.73	1.59	11.25	0.928	1.74
A7	2.99	1.70	1.57	11.25	0.968	0.76
A8	5.98	1.69	1.55	11.25	0.992	0.50
B1	1.30	1.75	1.62	8.42	0.746	6.32
B2	1.40	1.75	1.61	9.48	0.815	4.57
B3	1.60	1.75	1.61	10.63	0.878	2.98
B4	1.80	1.75	1.60	11.25	0.910	2.18
B5	2.00	1.75	1.60	11.80	0.931	1.66
B6	2.98	1.75	1.60	12.86	0.972	0.66
C1	1.80	1.65	1.53	8.74	0.882	2.89
C2	1.80	1.70	1.57	9.88	0.897	2.51
C3	1.80	1.75	1.60	11.25	0.910	2.18
C4	1.80	1.80	1.65	13.70	0.927	1.75
N	1.20	2.20	1.89	9.34	0.695	7.71

deconfined quark matter phase, is also uncertain (and is model dependent) but it is very probably in the range $4-10\,\rho_{\rm nuc}$.

According to this picture, a hybrid star would then be composed of either two or three parts: (i) a *pure hadronic* matter phase for $\rho < \rho_{\rm hm}$, (ii) a *mixed* phase of the confined-deconfined matter for $\rho_{\rm hm} < \rho < \rho_{\rm qm}$, and (iii) a *pure quark* matter phase for $\rho > \rho_{\rm qm}$ (this might or might not be present in practice, depending on the maximum density reached).

In this work, we follow LCCS in adopting the picture outlined above and we also follow their prescription in formulating the EoS for the HQS matter:

$$P = \begin{cases} P_{\rm h} & \text{for } \rho < \rho_{\rm hm}, \\ \alpha P_{\rm q} + (1-\alpha) P_{\rm h} & \text{for } \rho_{\rm hm} \leq \rho \leq \rho_{\rm qm}, \\ P_{\rm q} & \text{for } \rho_{\rm qm} < \rho, \end{cases} \tag{3.5}$$

where

$$\alpha = 1 - \left(\frac{\rho_{\rm qm} - \rho}{\rho_{\rm qm} - \rho_{\rm hm}} \right)^{\delta} \tag{3.6}$$

is a factor quantifying the contribution of each of the components of the mixed phase to the total pressure. As stated above, we take $P_{\rm q}$ to be given by the MIT bag model (3.3), while $P_{\rm h}$ is calculated using the ideal-gas EoS (3.4). The parameter δ is introduced in order to control the quark matter contribution to the pressure in the mixed phase: with larger δ, the contribution from $P_{\rm q}$ increases. For $\delta = 1$ we recover the EoS of LCCS. We again emphasize that, in contrast to LCCS, we do not reduce the effective adiabatic index of the nuclear matter in our GR models, but rather keep it at its initial value $\gamma = 2$ during the evolution.

For our GR models we define the transition density $\rho_{\rm hm}$ from the pure hadronic matter phase to the mixed phase to be where $P_{\rm q}$ vanishes, similarly to LCCS (although they were identifying energy density

and rest-mass density within their Newtonian regime). This corresponds to $\rho_{\rm hm} = 6.97 \times 10^{14}\,{\rm g\,cm^{-3}} = 2.58\,\rho_{\rm nuc}$ for $B^{1/4} = 170\,{\rm MeV}$ and $\rho_{\rm nuc} = 2.7 \times 10^{14}\,{\rm g\,cm^{-3}}$. Following LCCS, we set $\rho_{\rm qm} = 9\,\rho_{\rm nuc}$ in our simulations (corresponding to $24.3 \times 10^{14}\,{\rm g\,cm^{-3}}$ for our value of $\rho_{\rm nuc}$), but this is just a rough estimate to give a working value. When we make direct comparisons with the Newtonian models of LCCS in Section 3.4, we use their values $\rho_{\rm hm} = 7.24 \times 10^{14}\,{\rm g\,cm^{-3}}$ and $\rho_{\rm qm} = 25.2 \times 10^{14}\,{\rm g\,cm^{-3}}$, which slightly differ from our standard values.

We want to stress that this treatment of the EoS via Eqs. (3.5, 3.6) is extremely rough as a representation of matter in the mixed phase experiencing the phase transition, especially when one bears in mind the behaviour of fluid elements undergoing successive compression and decompression and changing the proportions of the phases. In particular, it neglects any possible effect from local heating and from the creation and subsequent emission of neutrinos during the collapse and the subsequent bounces. However, it does have the advantage of being simple and parametrisable. By changing the values of the free parameters (e.g. δ, $\rho_{\rm hm}$ or $\rho_{\rm qm}$) it allows us to modify easily the properties of the EoS.

3.3.3 Parameter space

The properties of our models for the phase-transition-induced collapse depend on a number of free parameters including the initial rotation period p, the total stellar rest mass M_0, the pressure contribution of the quark component in the mixed phase (controlled by δ), etc. In order to study how the collapse dynamics depends on these quantities, we performed simulations for various sequences of models where one parameter was held fixed. For instance, in order to investigate the impact of rotation we used the models A1 to A8 and B1 to B6 (see Table 3.1). The models of sequence A have a fixed central rest-mass density $\rho_{\rm c,i} = 11.25 \times 10^{15}\,{\rm g\,cm^{-3}}$ and a varying rotation period in the range from $p = 1.00$ to $6.18\,{\rm ms}$. The ones of sequence B have a fixed rest mass $M_0 = 1.75\,M_\odot$ and rotation periods from $p = 1.30$ to $2.89\,{\rm ms}$. The consequences of a variation in the rest mass of the initial NS are explored in the sequence of models C1 to C4, where the rotation period is held fixed at $p = 1.80\,{\rm ms}$ and the rest mass takes values from $M_0 = 1.65$ to $1.80\,M_\odot$.

These initial models were then evolved as sequences CA, CB, and CC with fixed EoS parameters, choosing $\delta = 2$ in each case. For the CD sequence, however, we used different values for δ (from 1 to 5) in order to assess how varying the quark contribution to the EoS in the mixed phase influences the dynamics. In this sequence, the models CD1 to CD5 use the initial model A2, while CD6 to CD9 are based on the initial model A5.

In addition, in order to validate our code and to discuss the results obtained by LCCS in more detail, we simulated some of their models with a Newtonian version of the `CoCoNuT` code. Our Newtonian models CN1, CN2 and CN3 (all based on the equilibrium model N) are identical to their models G1.95, R and G1.75, with the adiabatic index γ of the EoS being reduced everywhere as they had done. For these models we used exactly the same EoS as in LCCS, which differs from our regular EoS in various ways (see Section 3.3.2). The models labelled ${\rm CN_{nipr}}$ and ${\rm CN_{ipr}}$ are Newtonian test models whose properties are discussed in detail in Section 3.4.2.

In Table 3.2 we list important quantities obtained in the simulations of the collapse models which are discussed in the following sections. Note that the total evolution time for all models is $t_{\rm f} = 50\,{\rm ms}$. At that point we simply terminate the evolution, which however could be extended to much longer times given the long-term stability of our code.

Table 3.2: Summary of the set of collapse models: γ is the adiabatic index of the hadronic matter during the evolution, δ is the EoS parameter that specifies the contribution of the quark matter pressure in the mixed phase, $\rho_{\rm c,b}$ is the value of the central rest-mass density at bounce, $|h|_{\max}$ is the maximum value of the GW signal strain during the evolution, $E_{\rm gw}$ is the energy emitted in GWs (during a total emission time of $t_{\rm f} = 50$ ms), f_F and $f_{^2f}$ are the frequencies of the fundamental quasi-radial and quadrupolar modes, respectively, while τ_F and $\tau_{^2f}$ are the damping times of those modes in the GW signal. In addition, we give the phases ϕ_1 and ϕ_2 of the F-mode and the ^2f-mode and the relative amplitude A_1/A_2 as obtained from a fit to the GW signal according to Eq. (3.13). Note that the collapse models CA5, CB4 and CC3 are identical, as are models CB2 and CD2, and models CB5 and CD7. During the contraction, models CB6, CC4 and CD9 form an apparent horizon and become black holes. The phase-transition-induced collapse models CN1, CN2 and CN3, as well as the test collapse models $\mathrm{CN_{nipr}}$ and $\mathrm{CN_{ipr}}$ are computed with a Newtonian treatment. Where no values are given for the damping times, this signifies that the model either collapses to form a black hole or that no unambiguous damping could be diagnosed in the GW signal (mostly due to mode resonance; see Section 3.5.5).

Model	Initial model	γ	δ	$\rho_{\rm c,b}$ [10^{14} g cm^{-3}]	$\lvert h\rvert_{\max}$ $\left[\begin{smallmatrix}10^{-23}\\ \text{at 10 Mpc}\end{smallmatrix}\right]$	$E_{\rm gw}$ [$10^{-4} M_\odot c^2$]	f_F [kHz]	$f_{^2f}$ [kHz]	τ_F [ms]	$\tau_{^2f}$ [ms]	ϕ_1 [rad]	ϕ_2 [rad]	A_1/A_2
CA1	A1	2.00	2	15.81	1.45	0.04	0.87	2.01	40	12	0.06	−3.07	0.93
CA2	A2	2.00	2	16.04	1.33	0.29	0.99	2.08	49	130	−0.48	3.24	0.40
CA3	A3	2.00	2	15.81	1.90	0.59	1.05	2.08	—	18	−3.91	−6.44	0.15
CA4	A4	2.00	2	15.92	1.10	0.17	1.07	2.08	319	67	−0.15	0.30	0.64
CA5	A5	2.00	2	15.99	0.62	0.11	1.09	2.06	418	—	0.09	3.00	1.44
CA6	A6	2.00	2	16.02	0.52	0.11	1.12	2.04	270	51	−0.15	1.50	1.78
CA7	A7	2.00	2	16.10	0.25	0.05	1.16	2.02	711	—	−0.46	3.44	3.01
CA8	A8	2.00	2	16.07	0.09	0.01	1.19	2.00	—	—	5.98	6.35	1.69
CB1	B1	2.00	2	9.52	0.42	0.01	1.05	1.78	99	37	0.06	3.17	0.57
CB2	B2	2.00	2	11.70	0.69	0.05	1.06	1.90	133	44	0.04	3.06	0.71
CB3	B3	2.00	2	14.36	0.74	0.09	1.10	2.02	196	59	0.10	−3.11	0.87
CB4	B4	2.00	2	15.99	0.62	0.11	1.10	2.06	418	—	0.09	3.00	0.64
CB5	B5	2.00	2	17.92	2.41	1.16	1.08	2.10	687	76	6.16	6.02	0.06
CB6	B6	2.00	2	—	—	—	—	—	—	—	—	—	—
CC1	C1	2.00	2	10.31	0.36	0.01	1.14	1.76	143	53	0.13	3.21	0.77
CC2	C2	2.00	2	12.71	0.51	0.04	1.13	1.90	71	47	−0.03	3.27	0.86
CC3	C3	2.00	2	15.99	0.62	0.11	1.10	2.06	418	—	0.09	3.00	0.64
CC4	C4	2.00	2	—	—	—	—	—	—	—	—	—	—
CD1	B2	2.00	1	10.47	0.40	0.01	1.15	1.86	150	36	0.00	3.17	0.69
CD2	B2	2.00	2	11.70	0.69	0.05	1.07	1.90	133	44	0.04	3.06	0.71
CD3	B2	2.00	3	12.93	1.07	0.08	1.04	1.94	54	39	0.15	2.96	0.78
CD4	B2	2.00	4	14.16	1.47	0.14	1.10	1.96	19	48	0.35	−1.42	2.32
CD5	B2	2.00	5	15.35	1.84	0.15	1.14	1.97	8	44	0.04	3.17	0.80
CD6	B5	2.00	1	14.41	0.31	0.04	1.13	2.04	248	62	0.00	−3.18	1.04
CD7	B5	2.00	2	17.92	2.41	1.16	1.09	2.10	687	76	6.16	6.02	0.06
CD8	B5	2.00	3	24.80	1.14	0.24	1.02	2.15	—	34	−0.61	3.41	0.46
CD9	B5	2.00	4	—	—	—	—	—	—	—	—	—	—
CN1	N	1.95	1	10.37	4.41	0.88	2.68	1.98	73	80	3.17	0.00	1.12
CN2	N	1.85	1	12.31	15.38	4.10	2.88	2.14	9	20	2.95	−0.08	1.03
CN3	N	1.75	1	14.19	21.22	5.70	3.18	2.34	1	15	2.85	−0.38	0.98
$\mathrm{CN_{nipr}}$	N	1.90	—	12.32	10.11	4.96	2.67	2.04	71	67	3.32	0.06	1.10
$\mathrm{CN_{ipr}}$	N	2.00	—	11.82	7.63	2.86	2.83	2.04	86	67	2.97	−0.01	1.05

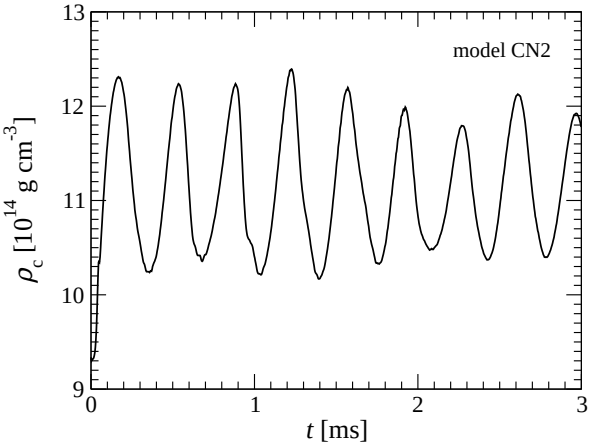

Figure 3.1: Time evolution of the central rest-mass density ρ_c for the Newtonian collapse model CN2 (which is identical to model R of LCCS).

3.4 Comparison with Newtonian models

Before discussing the results for our GR models, we present here our simulations of three of the Newtonian models also studied by LCCS. We begin, however, with a description of the qualitative features of phase-transition-induced collapse of a rotating NS to a HQS which is relevant also for the later GR models.

3.4.1 Collapse dynamics and gravitational radiation waveform

The EoS of the deconfined quark matter in the stellar core generally gives a smaller pressure contribution than that of the hadronic EoS[2] and so the phase transition in the NS core leads to an instability of the progenitor NS (which is in equilibrium before the transition) and the entire NS starts to contract. Depending on the parameters used and the phase transition timescale, the infall phase typically lasts between 0.3 and 0.5 ms. As the pressure in the core rises with increasing density, the infall decelerates and the contraction of the inner core is stopped, while the outer regions are still falling in. In the case of a rotating NS, the deceleration of the core can be augmented by the increase of centrifugal forces due to angular momentum conservation in the contraction phase.

Because of its inertia, the core overshoots its new equilibrium configuration, rebounds, expands again and then re-collapses. It typically experiences many such distinct sequences of infall, bounce, and re-expansion in the form of pronounced, mainly radial ring-down pulsations until it finally reaches a new equilibrium state. Fig. 3.1 shows the time evolution of the central rest-mass density ρ_c for the Newtonian model CN2, where this oscillatory behaviour can be clearly seen.

If the initial NS is non-rotating, then the newly-formed HQS pulsates only radially, and only $l = 0$ modes are present in the oscillation spectrum (unless significant convection develops). In this case, no GWs are emitted. However, if a rotating initial model undergoes a collapse and ring-down, then GWs of considerable amplitude can be emitted, as shown in the waveform plot in Fig. 3.2, again for model CN2.

Comparing a simple collapse model with a purely ideal-gas EoS to a regular collapse model with a quark contribution to the EoS, LCCS demonstrated that the phase-transition-induced collapse of a rotating NS to a HQS predominantly excites two quasi-normal pulsation modes: the fundamental $l = 0$ quasi-radial F-mode and the fundamental $l = 2$ quadrupolar ${}^2f$-mode. These stand out in the power spectrum of many fluid or

[2] In principle, the quark matter could give as large a pressure contribution as the hadronic matter (see, e.g. [11] for a recent discussion). However, in our study we do not consider those cases.

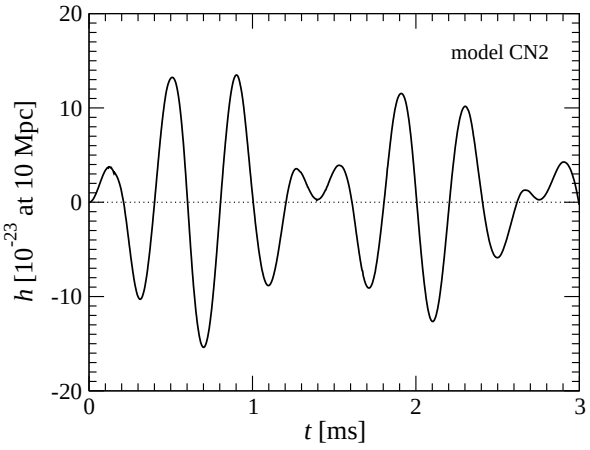

Figure 3.2: Time evolution of the GW strain h at a distance of $10\ \mathrm{Mpc}$ for the Newtonian collapse model CN2.

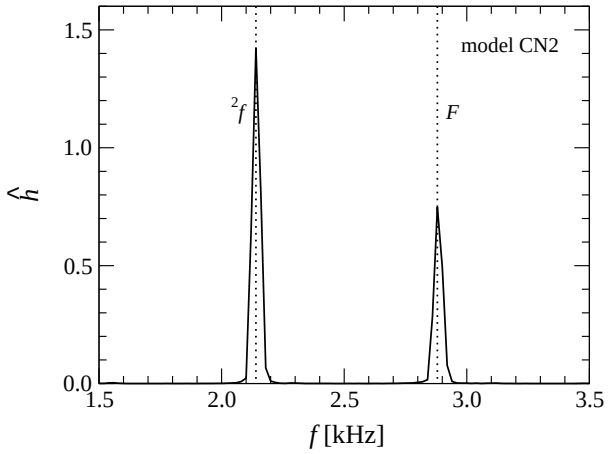

Figure 3.3: Power spectrum $\hat{h}$ (in arbitrary units) of the GW strain h for the Newtonian collapse model CN2. The narrow peaks of the F-mode and ${}^2f$-mode clearly dominate the spectrum.

Table 3.3: Comparison of various quantities as calculated in our simulations for the Newtonian collapse models CN1, CN2 and CN3 (top row for each model) with the results published by LCCS (bottom row). For each quantity we also give the relative difference between our results and theirs. Note that we multiply their values for $\langle \hat{h}^2 \rangle^{1/2}$ by $\sqrt{2}$ to undo the angular averaging and obtain $|h|_{\max}$. The values of $\rho_{\rm c,b}$ for models CN2 and CN3 are extracted from Figs. 6 and 10 in their article, respectively, while for model CN1 they present no data from which to read off the central rest-mass density at the bounce.

Model	$\rho_{\rm c,b}$ $[10^{14}\ {\rm g\ cm^{-3}}]$		$\lvert h\rvert_{\max}$ $[10^{-23}$ at 10 Mpc$]$		f_F [kHz]		f_{2f} [kHz]		τ_F [ms]		τ_{2f} [ms]	
CN1	10.37	—	4.41	4%	2.68	1%	1.98	1%	72.78	600%	80.23	670%
	—		4.24		2.66		2.00		10.39		10.42	
CN2	12.31	$< 1\%$	15.38	$< 1\%$	2.88	2%	2.14	3%	8.56	234%	20.10	325%
	12.30		15.41		2.82		2.08		2.56		4.73	
CN3	14.19	$< 1\%$	21.22	2%	3.18	2%	2.34	4%	1.45	245%	14.51	474%
	14.14		21.64		3.12		2.25		0.42		2.53	

metric quantities and, in particular, in that of the gravitational radiation waveform as presented in Fig. 3.3. All of our collapse models exhibit the predominance of these two modes as a generic feature[3]. For the more slowly rotating models, the contribution from higher order modes at higher frequencies can become comparable to that of the two fundamental $l = 0, 2$ modes, but these higher frequency modes have damping times that are significantly shorter than those of the fundamental modes and their impact on the waveform (and other quantities) dies out quickly.

Comparing our values of selected quantities describing the collapse dynamics with the corresponding ones in LCCS shows that our code is able to accurately reproduce the original results (see Table 3.3), despite being based on a different formulation of the hydrodynamic equations and utilising a different coordinate system. Furthermore, Figs. 3.1, 3.2 and 3.3, which correspond to the data plotted in Figs. 6, 7 (centre panel) and 12 (dashed line) of LCCS, also exemplify the excellent agreement both qualitatively and quantitatively. Making this comparison and demonstrating the good agreement obtained at a Newtonian level is important for removing possible doubts about the analysis which we present in the next subsection concerning the onset and development of convective instabilities.

3.4.2 The role of convection in generating differential rotation

A conspicuous difference from the results of LCCS that we observe in the simulations of Newtonian models performed with our code is the significantly *smaller* damping of the post-bounce oscillations. This is not only apparent from the much larger values that we find for the damping times τ_F and τ_{2f} (see Table 3.3) but can also be noticed by comparing our Figs. 3.1 and 3.2 to the corresponding Figs. 6 and 7 (centre panel) in LCCS. This has important consequences for the physical interpretation given in LCCS for the damping of the quasi-radial post-bounce pulsations: they suggested that the dominant damping mechanism is conversion of the kinetic energy of these pulsations into differential rotation. According to their discussion, another less significant part of that kinetic energy is lost when matter at the boundary of the HQS is ejected by shock waves, while yet another small amount of damping is due to numerical dissipation.

The 3D Newtonian code of LCCS used a coarser grid spacing than in our 2D GR calculations and this (together with some other possible numerical effects) would have led to a higher level of numerical dissipation. If the damping of post-bounce pulsations which they saw was indeed mostly caused by *physical*

[3]We perform the mode identification by perturbing equilibrium models that have similar structure to those of the collapse remnants using specific $l = 0$ and $l = 2$ trial eigenfunctions and analysing the response to these perturbations. This method is described in detail in LCCS.

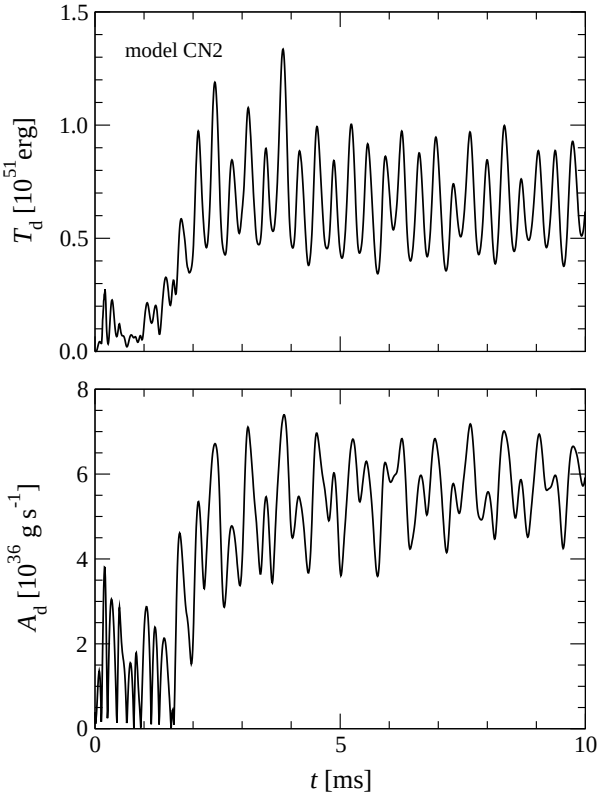

Figure 3.4: Time evolution of the differential rotation measures $T_{\rm d}$ (top panel) and $A_{\rm d}$ (bottom panel) for the Newtonian collapse model CN2.

processes such as the transformation of kinetic energy into differential rotation or mass shedding at the boundary, then we would not have seen much smaller damping in our simulations for the same models. We therefore conclude that numerical dissipation actually did play a major role for the damping seen in the simulations of LCCS (although physical processes certainly also played a role).

Furthermore, if the observed exponential damping, which removes energy from the pulsations at a constant relative rate, were directly feeding the generation of differential rotation, there should be a simple correlation between the evolution time t and the increase in the quantity used as a measure of differential rotation by LCCS,

$$T_{\rm d} = \frac{1}{2} \int \rho\, r^2 \sin^2\theta\, (\Omega - \bar{\Omega})^2\, dV, \tag{3.7}$$

where $\Omega = r^{-1} \sin^{-1}\theta\ v_\phi$ is the local angular velocity with v_ϕ being the rotation velocity of the fluid, and $\bar{\Omega}$ is the volume averaged angular velocity of the HQS[4]. Note that $T_{\rm d}$ does not follow the additive property for energies and so is not a fully satisfactory measure of the kinetic energy associated with differential rotation. We instead prefer to use as our measure of differential rotation, a quantity which is a volume-averaged and density-weighted measure of the relevant $r\phi$ component of the Newtonian shear tensor,

$$A_{\rm d} = \int \rho \left| \frac{dv_\phi}{dr} - \frac{v_\phi}{r} \right| dV. \tag{3.8}$$

[4]Note that in contrast to LCCS, we averaged $\bar{\Omega}$ at each time level and not only once at the time of bounce, because when we did the latter, we obtained a very oscillatory behaviour for $T_{\rm d}$; we are not clear why LCCS did not observe this.

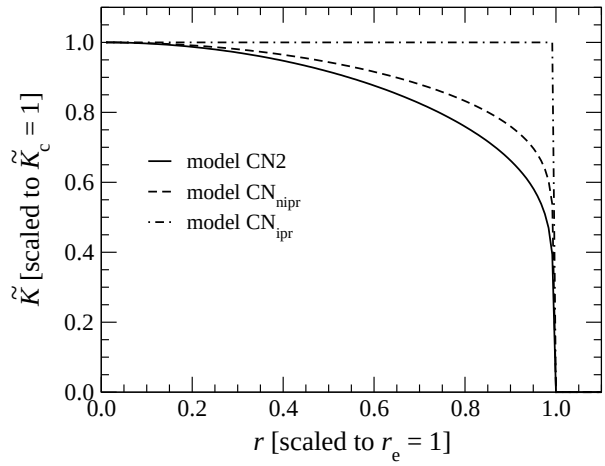

Figure 3.5: Radial profiles of the specific entropy measure $\tilde{K}$ (top panel) and of the r-component of its gradient (bottom panel), both calculated in the equatorial plane at the initial time for the Newtonian models CN2 (solid line), $\mathrm{CN_{nipr}}$ (dashed line) and $\mathrm{CN_{ipr}}$ (dash-dotted line). Both the entropy and the radius are scaled to give $\tilde{K}_{\mathrm{c}} = 1$ and $r_{\mathrm{e}} = 1$.

The two quantities (3.7) and (3.8) are related and they have similar time evolutions, as shown for model CN2 in Fig. 3.4 (and as found for all of the models considered), but we prefer to use A_{d} because of it having a clearer physical meaning.

Overall, the evolution of the two measures of differential rotation has the following general behaviour: after an initial peak associated with the initial collapse and the main bounce (with its height correlating with the intensity of the bounce), the average differential rotation stays roughly the same for around a millisecond (corresponding to several dynamical timescales during which a number of post-bounce oscillations occur) following which it grows considerably up to a maximum value, then decreases a little and finally oscillates around an almost constant state. This behaviour is not in accordance with having continuous conversion of pulsational kinetic energy into differential rotation as the main damping mechanism. Rather, it suggests that some other process is responsible for creating the observed differential rotation.

The initial peak of T_{d} and A_{d} can be readily explained by the fact that any initially uniform rotation profile will become non-uniform during the collapse as a result of the non-homology of the collapse. On the other hand, the intermittent behaviour after the initial peak and the saturation at a constant value can be interpreted straightforwardly in terms of differential rotation caused by large-scale convection developing in the HQS several dynamical timescales after the initial collapse when it is still pulsating but is already close to a new quasi-equilibrium state.

In rotating stellar models significant convection can occur if the Solberg–Høiland stability criteria are violated (see, e.g., [92] and references therein). For our simple EoS, these translate into the condition that convection can develop if there is a sufficiently strong negative radial gradient of specific entropy (depending on the rotation rate of the HQS). We find that the method of pressure reduction employed by LCCS, which involves uniformly lowering γ in the ideal-gas EoS (3.4) for the hadronic phase without adjusting the value for the internal specific energy ϵ at the initial time, indeed results in a very large negative specific-entropy gradient for their choices of γ. This is shown for model CN2 in Fig. 3.5 (solid line), where we plot the radial profile at $t = 0$ of the (density dependent) measure of specific entropy

$$\tilde{K} = \frac{\rho\epsilon(\gamma - 1)}{\rho^{\gamma}} \tag{3.9}$$

in the equatorial plane, assuming an ideal-gas EoS for the entire star with a γ that is reduced from its initial

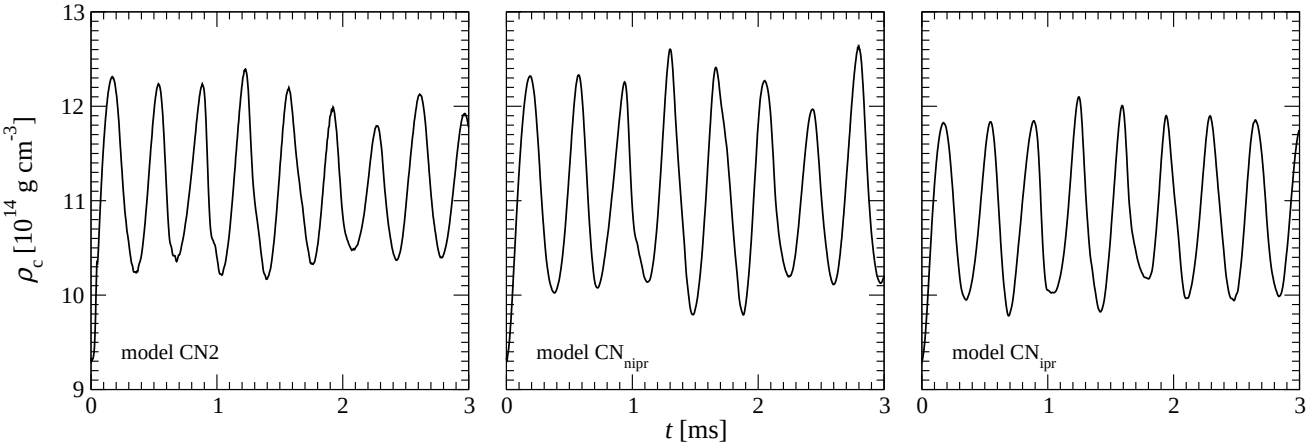

Figure 3.6: Time evolution of the central rest-mass density $\rho_{\rm c}$ for the Newtonian models CN2 (left panel), $\mathrm{CN_{nipr}}$ (centre panel) and $\mathrm{CN_{ipr}}$ (right panel).

value of 2 to 1.85. Note that for a polytrope $\tilde{K}$ is identical to the polytropic constant K.

In order to assess unambiguously the occurrence of artificially-produced convection and its impact on the development of differential rotation, we set up two simple Newtonian collapsing test models, which are both based on the initial model N and utilise a purely ideal-gas EoS (3.4), so as to simplify the discussion by removing the influence of quark matter on the results. In model $\mathrm{CN_{nipr}}$ (with non-isentropic pressure reduction) we reduce the pressure by lowering the adiabatic index γ from its initial value to 1.9 (without then adjusting ϵ); this creates a strong initial negative specific-entropy gradient that is comparable with the one in model CN2 (see Fig. 3.5). In model $\mathrm{CN_{ipr}}$ (for isentropic pressure reduction) γ remains at its pre-collapse value of 2 during the evolution, while the pressure reduction is now realized by a lowering the polytropic constant K by 10%, which keeps the specific entropy uniform throughout the entire NS.

Note that the parameters in the EoS for these two test models have been chosen in such a way that the collapse dynamics (represented by the maximum density reached at the first bounce and the amplitude of the post-bounce pulsations) is comparable with that of model CN2, as can be seen from Fig. 3.6. Consequently, the gravitational radiation waveforms of these models also have amplitudes and waveforms similar to those of model CN2.

However, because of the different behaviour regarding convective instability, the dynamics of the three models CN2, $\mathrm{CN_{nipr}}$ and $\mathrm{CN_{ipr}}$ fall into two very distinct classes, depending on whether the initial pressure reduction creates a strong negative specific-entropy profile or leaves the specific entropy constant. In all models, analysis of the meridional velocity fields shows no noticeable convection being present at early times (e.g. at the time of the main bounce, around $t = 0.2\,\mathrm{ms}$). In the isentropic collapse model $\mathrm{CN_{ipr}}$ convection continues to remain unimportant also at later times and, accordingly, both $T_{\rm d}$ and $A_{\rm d}$ remain very small at all times (see the right-hand panel of Fig. 3.7). In stark contrast, the non-isentropic models CN2 and $\mathrm{CN_{nipr}}$ develop several convection vortices in the bulk of the collapsed star at $t \sim 1\,\mathrm{ms}$ (corresponding to a few dynamical timescales), which is when the two differential rotation measures start to increase. This convection grows rapidly and reaches saturation almost instantaneously, with typical maximum convection velocities of $\sim 0.03\,c$. During the entire period when $T_{\rm d}$ and $A_{\rm d}$ are increasing, the convection remains practically constant and redistributes angular momentum and entropy locally within each vortex. By times $t \gtrsim 5\,\mathrm{ms}$ this has led to the specific entropy being almost constant within the spatial scale of each convection vortex. Convection then subsides again, and $T_{\rm d}$ and $A_{\rm d}$ remain approximately constant from then on. It is clear, therefore, that the distinct phases in the time evolution of the two quantities reflect very accurately the distinct phases of convection, which acts as the mechanism that redistributes angular momentum and thus

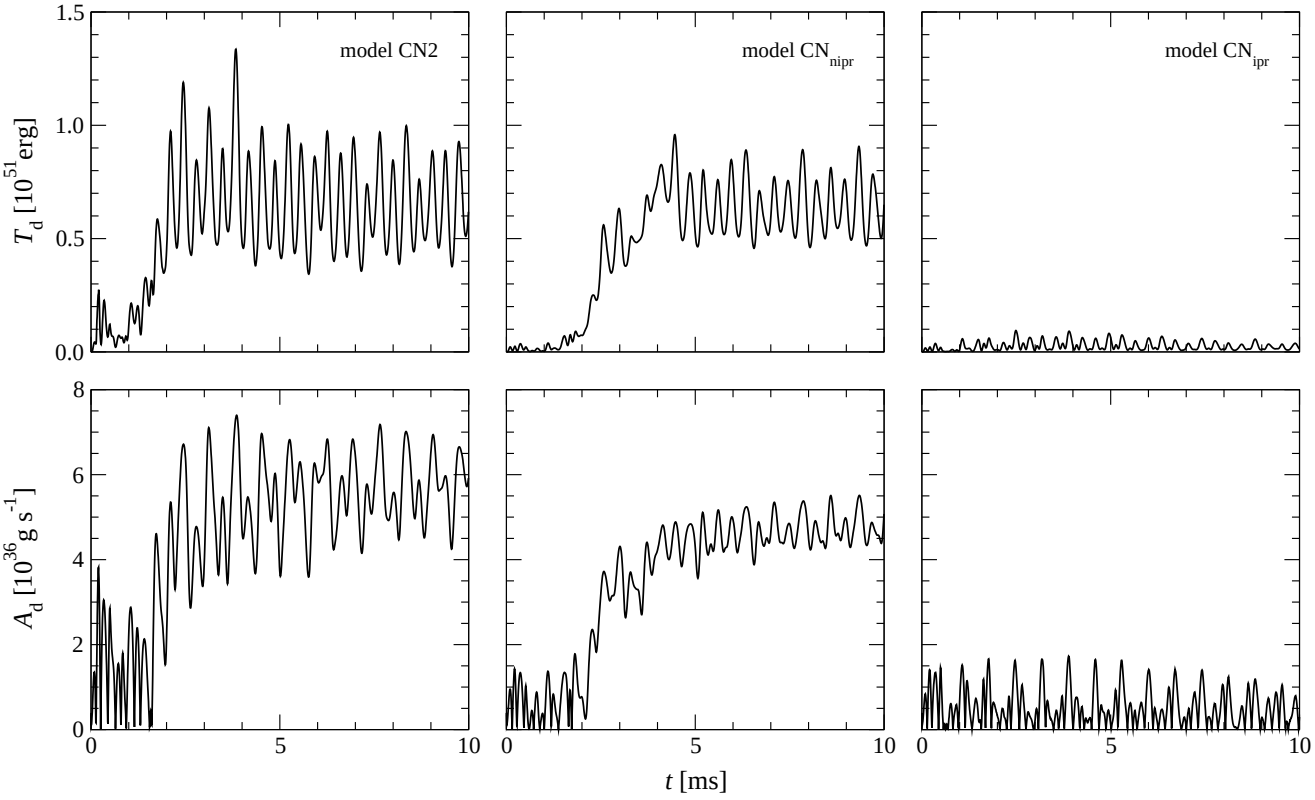

Figure 3.7: Time evolution of the differential rotation measures $T_{\rm d}$ (top row) and $A_{\rm d}$ (bottom row) for the Newtonian collapse models CN2 (left panels), $\mathrm{CN_{nipr}}$ (centre panels) and $\mathrm{CN_{ipr}}$ (right panels).

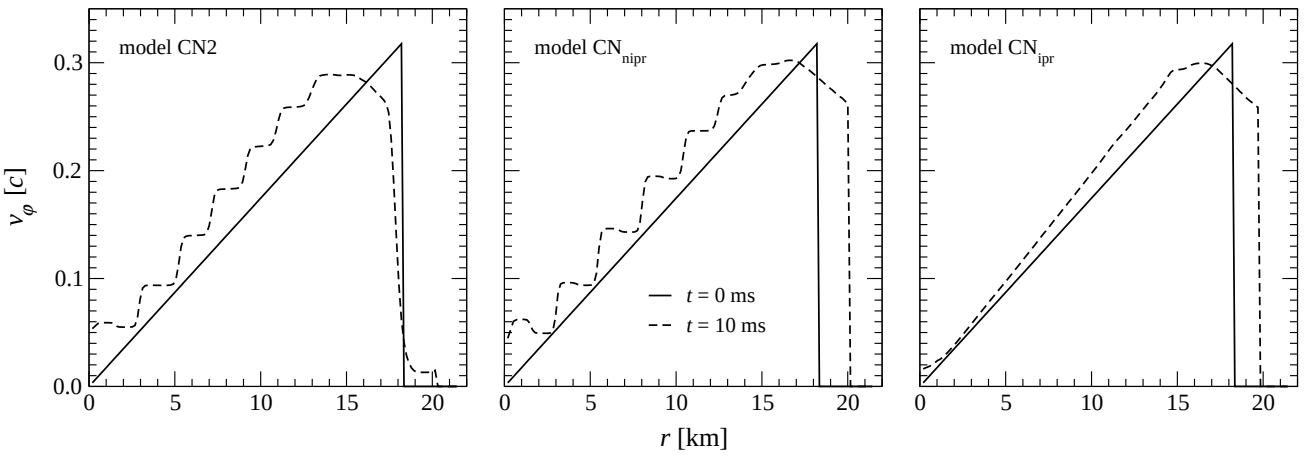

Figure 3.8: Radial profile of the rotation velocity v_ϕ in the equatorial plane for the the Newtonian collapse models CN2 (left panel), $\mathrm{CN_{nipr}}$ (centre panel) and $\mathrm{CN_{ipr}}$ (right panel) at the initial time (solid lines) and at $t = 10$ ms (dashed lines). For models that develop considerable convection, the initially uniform rotation profile is locally destroyed.

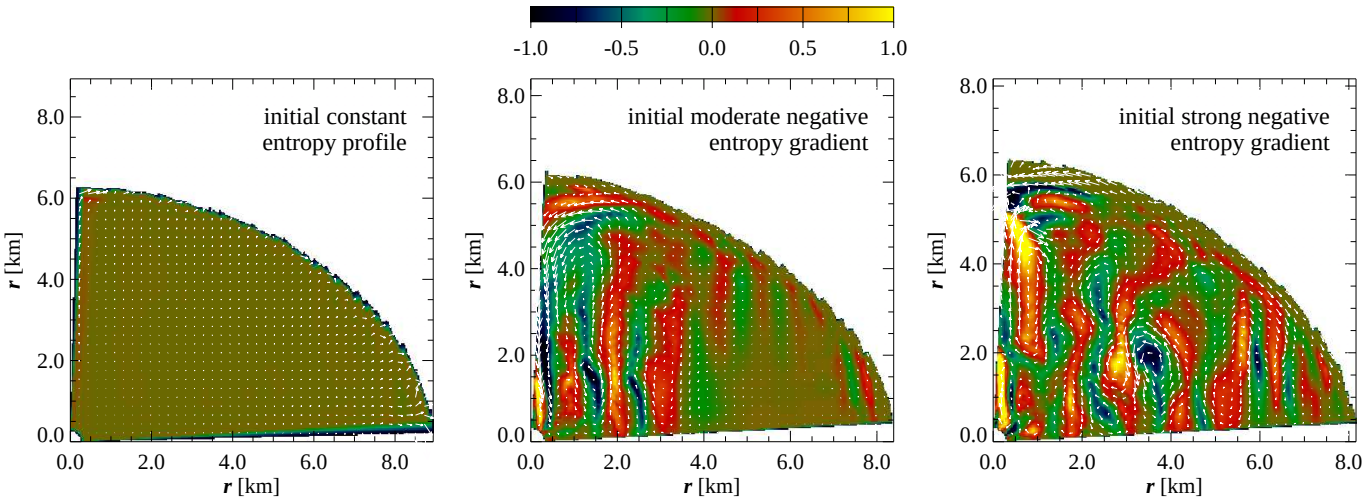

Figure 3.9: The velocity field $v_{r,\theta}$ in the meridional plane (with the rotation axis being in the vertical direction) and the colour-coded magnitude of the φ-component of the vorticity are shown for equilibrium models whose initial specific-entropy profile is, respectively, constant (left panel), comparable to model CN2 (right panel) and roughly halfway between those two cases (centre panel). The evolution time is at $t = 3.5$ ms when convection (if present) has saturated. The length-scale of the vectors is the same for all three models, with the maximum length corresponding to $\sim 0.03\,c$. The vorticity is measured in arbitrary units.

creates differential rotation.

The impact of angular momentum redistribution by convection on the initially uniform rotation profile can be seen from Fig. 3.8 which shows plots of the rotation velocity v_ϕ in the equatorial plane for the different models. For the strongly convective models CN2 (left panel) and $\mathrm{CN}_{\mathrm{nipr}}$ (centre panel), the v_ϕ curves are driven away from the initial uniform rotation (straight-line) profile to reach a step-like profile at late times, whereas the essentially non-convective model $\mathrm{CN}_{\mathrm{ipr}}$ (right panel) maintains an approximately uniform rotation profile[5].

It is worth stressing that the occurrence of convection here, and thus the creation of the differential rotation, is essentially independent of the presence and strength of post-bounce pulsations. Indeed, setting aside some small spurious convection close to the stellar boundary (caused by interaction of matter with the artificial low-density atmosphere), the strong *bulk* convection is caused by having a negative specific-entropy gradient and can be switched on and off at will, depending on whether the initial pressure reduction destroys isentropy or not.

In order to demonstrate this connection further, we constructed initial equilibrium models with a *local* polytropic EoS,

$$P = K(\rho)\,\rho^\gamma, \tag{3.10}$$

with $\gamma = 2$, where the polytropic "constant" $K(\rho)$ depends on the rest-mass density and thus varies inside the NS. By adjusting $K(\rho)$ we can thus create models with negative (as well as positive) specific-entropy gradients of arbitrary strengths. When these initial models are evolved with an ideal-gas EoS (3.4), they remain essentially in equilibrium, pulsating with only very small amplitudes. However, during the evolution they develop convection, and subsequently differential rotation, with a strength that directly corresponds to the strength of the negative specific-entropy gradient imposed initially. This is illustrated in Fig. 3.9 where we show plots of the meridional velocity field superimposed on the magnitude of the φ-component of the vorticity. For this figure we selected three such equilibrium models for which the initial specific-entropy

[5]This rather good preservation of uniform rotation is a consequence of the infall being nearly homologous here.

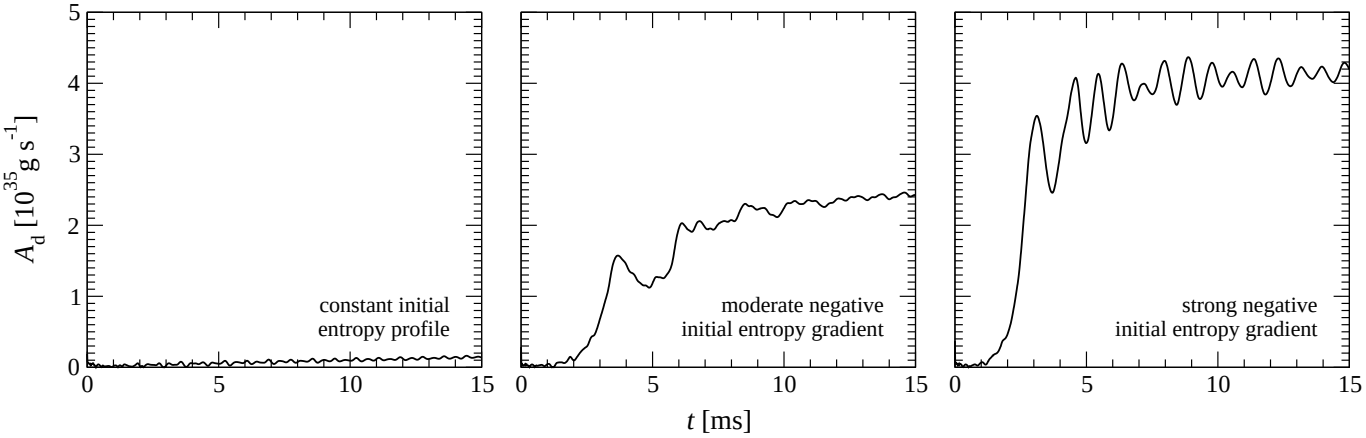

Figure 3.10: Time evolution of the differential rotation measure $A_{\rm d}$ for equilibrium models whose initial specific-entropy profile is, respectively, constant (left panel), comparable to model CN2 (right panel) and roughly halfway between these two cases (centre panel). For the isentropic model, $A_{\rm d}$ remains very close to zero at all times and is barely visible in the plot.

profile varies between constant specific entropy and a gradient that is comparable to model CN2[6]. Clearly, convection is practically nonexistent in the isentropic model (left panel), whereas the model with moderate initial non-isentropy (centre panel) develops considerable convection in those parts of the NS that are not too far from the rotation axis. Finally, for the model with the strong negative initial specific-entropy gradient (right panel), conspicuous convection vortices occur throughout the NS. Plots of the vorticity for collapsing models show similar patterns but there the meridional velocity field is also affected by the contribution from the large quasi-radial pulsations.

Also for these equilibrium models the time evolution of $A_{\rm d}$ exhibits the expected behaviour, as shown in Fig. 3.10 (we here no longer plot $T_{\rm d}$ which, however, exhibits a very similar time evolution to that of $A_{\rm d}$). Note that the quasi-periodic modulation of $A_{\rm d}$ is not caused by pulsations of the star, as their amplitudes are too small to be visible in $A_{\rm d}$ and they have higher frequencies. Instead, these oscillations (which can also be seen in a power spectrum of $A_{\rm d}$ for the collapse models CN2 and $\rm CN_{nipr}$) are due to temporal variations in the vortices, with their timescale being determined by the typical convection velocity and the average vortex size.

In summary, we find that the differential rotation reported by LCCS is almost exclusively caused by the transient convection that occurs if a negative specific-entropy gradient is generated by the initial pressure reduction. Therefore, we are convinced that the conclusion drawn by LCCS about the link between the damping of the large amplitude post-bounce pulsations and the creation of differential rotation, although seemingly plausible, is not correct. They observed that the kinetic energy stored in the pulsations is approximately equal to the maximum value of $A_{\rm d}$ for both model CN2 and model CN3 (their models R and G1.75; see their Fig. 8) but this is an unfortunate coincidence. Our models $\rm CN_{nipr}$ and $\rm CN_{ipr}$ demonstrate that convection and thus the maximum value of $A_{\rm d}$ can vary enormously for roughly constant pulsation amplitude.

[6]Note that these equilibrium models have central densities comparable with that of CN2 but they are more compact.

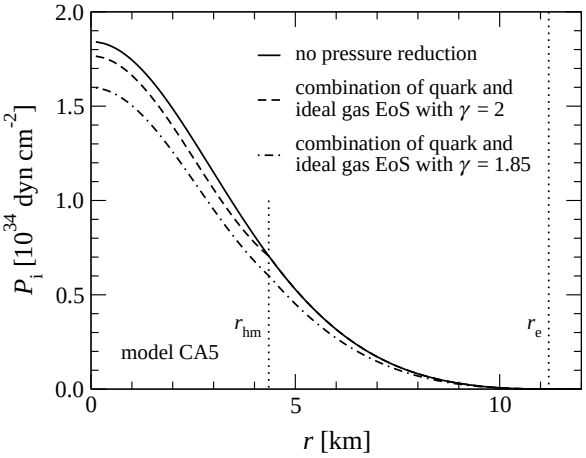

Figure 3.11: Radial profile of the initial pressure $P_{\rm i}$ in the equatorial plane for the GR collapse model CA5 without any pressure reduction (solid line), with the regular EoS treatment (combination of quark and ideal-gas EoS with $\gamma = 2$; dashed line) and with the EoS description used by LCCS (combination of quark and ideal-gas EoS with $\gamma = 1.85$; dash-dotted line). In the latter case P is reduced throughout the star and not just where $\rho > \rho_{\rm hm}$. The vertical dotted lines mark the radius $r_{\rm hm} = 4.35\,{\rm km}$ where $\rho = \rho_{\rm hm}$ and the equatorial radius $r_{\rm e} = 11.2\,{\rm km}$ of the initial NS.

3.5 General relativistic collapse models

3.5.1 Collapse dynamics and gravitational radiation waveform

We next present our results for the GR models, employing a quark contribution to the EoS that is slightly different from that used for the Newtonian models (see Section 3.3.2). Overall, we have performed simulations for 23 different models, and in Table 3.2 we summarize the most important quantities which characterize the dynamics of each model.

As discussed previously, our prescription for the triggering of the phase transition and of the subsequent collapse differs from the one proposed by LCCS in that we do not change the adiabatic index γ, leaving the EoS in the hadronic phase unchanged. Although still very idealized, we believe that this represents a more consistent description of the physics of the phase transition. As a consequence of this prescription, the phase transition and collapse in our GR models is solely caused by the lower pressure exerted by matter which is transformed to the quark phase. The difference between our approach and that of LCCS is exemplified in Fig. 3.11, where we show the different prescriptions for the initial pressure reduction when applied to the representative model CA5.

With our prescription, only a small (central) part of the NS loses pressure support, and thus the NS will not, in general, collapse to a black hole even if the initial model is close to the stability limit. Rather, it reaches a new stable equilibrium state in the form of an HQS. For instance, in model CA5 only $0.49\,M_\odot$ out of a total mass of $1.75\,M_\odot$ is subject to the pressure reduction. Nevertheless, the change of the central rest-mass density during the contraction from its initial value $\rho_{\rm c,i}$ to $\rho_{\rm c,b}$ at bounce reaches values of up to $\sim 50\%$ for some models (see Tables 3.1 and 3.2), which is comparable to what was obtained by LCCS in their Newtonian models with a larger overall pressure reduction. There are at least two different reasons behind this large and *local* increase of ρ: firstly, the stronger gravitational force that the NS experiences in a GR framework naturally amplifies the strength of the collapse. Secondly, our initial equilibrium models (in particular the ones with high $\rho_{\rm c,i}$) are already close to the limit beyond which the F-mode becomes unstable. For these models, therefore, even a moderate perturbation can lead to a strong local contraction and trigger

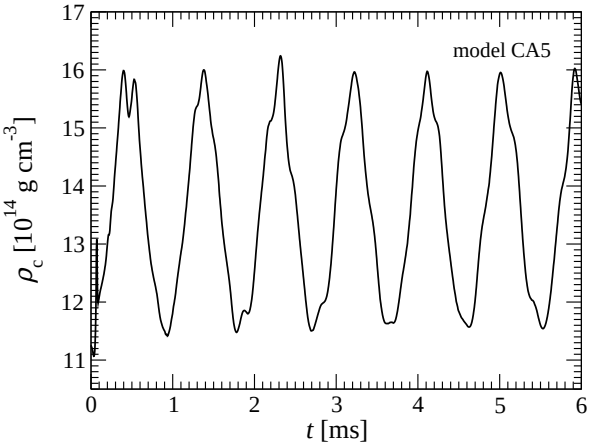

Figure 3.12: Time evolution of the central rest-mass density $\rho_{\rm c}$ for the GR collapse model CA5.

post-bounce oscillations of significant amplitude[7].

Despite this conceptually important difference in the way that the phase transition (and hence the resulting collapse) is triggered, no major *qualitative* differences appear when comparing results from the GR simulations with those from the Newtonian simulations of LCCS. This is shown for the representative model CA5 in Figs. 3.12 and 3.13, where we plot the time evolution of the central rest-mass density $\rho_{\rm c}$ and the GW strain h, respectively. We point out, however, that in our GR models of sequences CA, CB, CC, and CD we observe a small spike in the time evolution of the central rest mass density $\rho_{\rm c}$ at about 0.1 ms (see Fig. 3.12). This spike is caused by a density compression wave triggered by the non-uniform pressure reduction in those models, which at the start of the evolution leads to a noticeable gradient in the first radial derivative of the pressure at the interface between the mixed and pure hadronic matter phases.

As in the Newtonian case, the waveform is mainly composed of the fundamental $l = 0$ quasi-radial F-mode and of the fundamental $l = 2$ quadrupolar ${}^2f$-mode (see the Fourier spectrum of the GW signal in Fig. 3.14). However, in contrast to the Newtonian models, the F-mode is now at a lower frequency than the ${}^2f$-mode (with the F-mode now having frequencies between 0.87 and 1.19 kHz for our selection of models, and the ${}^2f$-mode having frequencies between 1.76 and 2.15 kHz). This difference is a consequence of the different density profile in the GR case and is in agreement with previous investigations of pulsating $\gamma = 2$ equilibrium polytropes (see [120] and references therein). The prominent peak next to that for the ${}^2f$-mode is a nonlinear self-coupling of the F-mode at twice the original frequency, which (like several other such nonlinear modes) is strongly excited due to the violent nature of the collapse. Using the fitting procedure described in Appendix B, we have extracted from the waveforms the damping times for these two modes, obtaining values between $\tau_F = 8$ and 687 ms, and $\tau_{2f} = 18$ and 130 ms, respectively. Because of the much smaller numerical dissipation of our code, the damping times computed for the GR models are considerably longer than those for the Newtonian models calculated by LCCS.

Another important quantitative difference with respect to the Newtonian models appears in the maximum GW strain $|h|_{\rm max}$ that is significantly smaller here for comparable overall rotation rates. The deeper gravitational potential well in GR gives a shorter contraction timescale and higher densities at bounce, which tend to amplify the GW signal, while this is counteracted by the more compact collapsed remnant in GR having a smaller quadrupole moment (for a detailed discussion of these two competing effects, see [118]). However, the main reason for $|h|_{\rm max}$ here being smaller than for the Newtonian models is that within our scenario for the destabilisation, a smaller proportion of the total matter content of the NS is directly involved

[7]For a non-rotating HQS with the EoS of Eq. (3.5) the unstable branch starts at $\rho_{\rm c} = 29.6 \times 10^{14}$ g cm^{-3}.

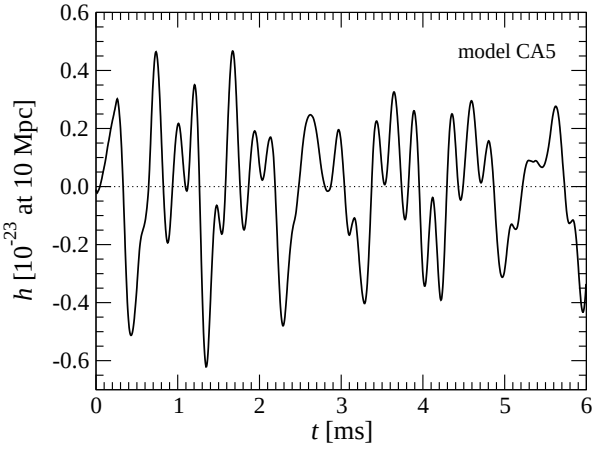

Figure 3.13: Time evolution of the GW strain h at a distance of $10\ \mathrm{Mpc}$ for the GR collapse model CA5.

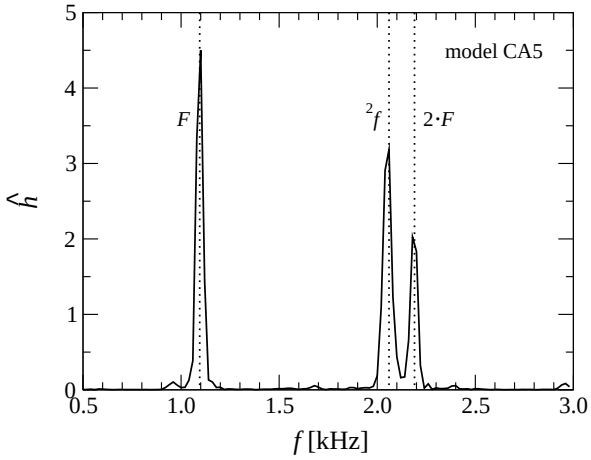

Figure 3.14: Power spectrum $\hat{h}$ (in arbitrary units) of the GW strain h for the GR collapse model CA5. The narrow peaks of the F- and ${}^2f$-modes (along with a prominent nonlinear self-coupling of the F-mode) clearly dominate the spectrum.

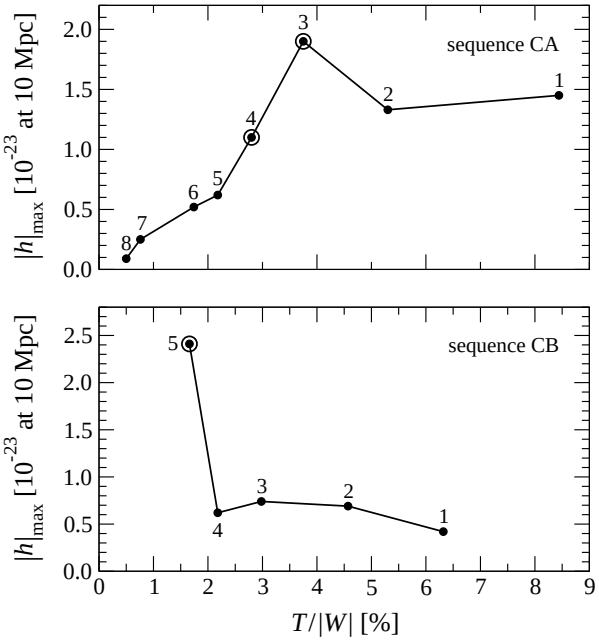

Figure 3.15: Dependence of $|h|_{\max}$ on the initial rotation strength $T/|W|$ for the collapse model sequences CA (top panel) and CB (bottom panel). Each model is denoted with a filled circle, and models with enhanced GW emission due to mode resonance (see Section 3.5.5) are shown with an additional large circle.

in the collapse and in undergoing large density variations. For a source at $10\,\mathrm{Mpc}$, $|h|_{\max}$ ranges between 0.08 and 1.72×10^{-23} for all of the models considered here, while the energy E_{gw} emitted in GWs during the first $50\,\mathrm{ms}$ of the evolution ranges between 10^{-6} and $10^{-4}\,M_{\odot}c^2$. A more detailed discussion about the detectability of these sources is presented in Section 3.5.6.

3.5.2 Influence of rotation, total rest mass and composition of the mixed phase

We next investigate the impact on the collapse dynamics of varying the values of the main model parameters: the initial rotation period p, the rest mass M_0, and the exponent δ used in the mixed phase.

Rotation. As in any gravitational collapse, the influence of rotation is twofold. On the one hand, the rotational flattening of the collapsing fluid produces an increase of the quadrupole moment, which could potentially lead to stronger GW emission. On the other hand, centrifugal forces also tend to slow down the collapse and, in cases where they are strong enough, they can considerably reduce the time variation of the quadrupole moment and hence the GW amplitude.

For the sequence CA, in which the initial central rest-mass density $\rho_{\mathrm{c,b}}$ is kept constant, the dependence of the maximum GW strain $|h|_{\max}$ on the rotation rate is rather straightforward to interpret (see the top panel of Fig. 3.15 and Table 3.2). Except for models CA3 and CA4, whose expected GW emission is altered by resonance effects (as discussed in detail in Section 3.5.5), $|h|_{\max}$ increases monotonically with increasing rotation (which we here measure in terms of the ratio $T/|W|$, as this quantity turns out to remain almost constant throughout the evolution). Since in this sequence the values of the central rest-mass density at bounce are all close to $16 \times 10^{14}\ \mathrm{g\ cm^{-3}}$, we conclude that centrifugal forces do not significantly retard the collapse for these models and so there is no significant associated weakening effect for the GW emission.

The effect of rotation is also investigated in the constant rest mass sequence CB, for which we observe a slight initial increase of $|h|_{\max}$ with increasing rotation (see the bottom panel of Fig. 3.15) that is then reversed for very rapid rotation (model CB5, whose GW emission is again enhanced by mode resonance,

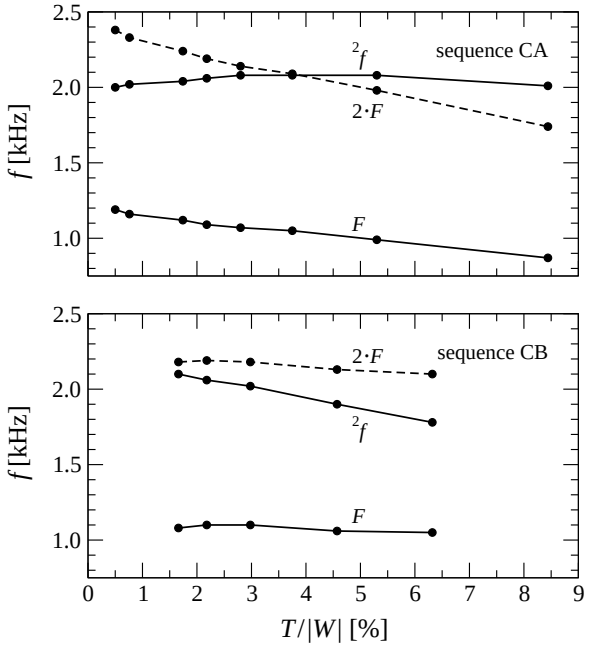

Figure 3.16: Dependence of the mode frequencies f_F, $f_{^2f}$ and $f_{2\cdot F}$ on the initial rotation strength $T/|W|$ for the collapse model sequences CA (top panel) and CB (bottom panel). Each model is marked by a filled circle.

is an exceptional case). We attribute this behaviour to the fact that in this sequence the central rest-mass density, both in the initial model and at bounce, drops significantly as rotation grows along the sequence, resulting in a much less violent collapse. This property can be seen in the central over-density at bounce, which amounts to $\rho_{\rm c,b}/\rho_{\rm c,i} - 1 = 39\%$ for model CB5, but reaches only 13% for model CB1. The interplay of growing rotation and decreasing collapse strength then explains the behaviour of the GW peak amplitude seen for sequence CB.

The influence of rotation on the frequencies of the F-mode and the ^2f-mode can be compared directly with the results of [120], who obtained relations between the frequencies of these two modes and the strength of rotation for pulsating equilibrium models of NSs with a $\gamma = 2$ polytropic EoS, both for sequences with constant central rest-mass density and with constant rest mass. In agreement with that work, for our dynamical collapse models, f_F decreases noticeably with more rapid rotation for sequence CA and CB, as shown in Fig. 3.16 (see also Table 3.2). Also, for $f_{^2f}$ our models reproduce the initial increase and subsequent decrease with growing rotation for the constant initial central rest-mass density sequence CA (sequence BU in [120]) as well as the monotonic decrease with increasing rotation for the constant rest mass sequence CB (their sequence AU). Our results therefore demonstrate that studies of linear pulsations of equilibrium models can be used also in the more general context of stellar gravitational collapse to predict the dependence of the fundamental mode frequencies on rotation. In our models, the creation of differential rotation by non-homologous contraction during the collapse phase is rather small. However, even if the deviation from uniform rotation were stronger, the study of [120] suggests that the influence on the mode frequencies would still be weak.

In Fig. 3.16 we also show the behaviour of the nonlinear self-coupling of the F-mode at twice the original frequency (the $2 \cdot F$-mode) which is strongly excited in all of our models (see also Fig. 3.14) including the Newtonian ones. Such nonlinear couplings of linear quasi-normal modes were also observed in the study of initially linearly perturbed equilibrium models by [120], although at much lower excitation levels. In contrast to the initial low-level perturbations used in their models, in our case the strong collapse

and rebound at bounce manages to channel a large amount of energy into this particular mode. A detailed discussion of the impact of exciting the $2 \cdot F$-mode for GW emission is presented in Section 3.5.5.

Rest mass. For their Newtonian models, LCCS reported that along a sequence with constant rotation period p, the maximum GW strain $|h|_{\max}$ first increases with M_0 and then decreases again. In contrast, we find that for our corresponding sequence CC, $|h|_{\max}$ increases monotonically with M_0 (see Table 3.2)[8]. This different behaviour is probably due to a fundamental difference between our GR models and their Newtonian counterparts. Besides the obvious differences in the structure of the HQS and hence in the mode frequencies, one should bear in mind that the rest mass of the GR models has an upper limit corresponding to the point of transition to the unstable branch of equilibrium solutions. This is particularly evident for sequence CC, where model CC4 does not reach a stable configuration after the collapse but instead produces a black hole as deduced from the appearance of an apparent horizon. As a result, the eventual decrease of $|h|_{\max}$ with increasing M_0 in the Newtonian case may not occur in GR simply because it might require rest masses above the upper limit.

Composition of the mixed phase. The impact on the collapse dynamics of varying the parameter δ (and hence varying the pressure reduction due to the presence of the quarks in the mixed phase) is quite obvious. Both for the collapse models CD1 to CD5, which are based on the initial model B2, and for the models CD6 to CD9, which use the initial model B5, the rest-mass density at bounce $\rho_{\rm c,b}$ and the amplitude of the post-bounce oscillations grow when the pressure reduction is enlarged by increasing the exponent δ (see Table 3.2). Since within each of the two subsequences the initial rotation rate is constant, the growth of $\rho_{\rm c,b}$, and hence of the compactness, with a greater pressure reduction is directly reflected in stronger GW emission and higher values for $|h|_{\max}$. Also in this case, an exception arises with model CD7 which is identical to the already mentioned model CB5. Interestingly, when $\delta = 4$, the pressure reduction in the mixed phase is so great that the corresponding model CD9 collapses directly to a black hole without experiencing a bounce.

Finally, we note that the F-mode frequencies in the sequence of models CD1 to CD5 first decrease with increasing δ and then increase again. This may be the result of a near cancellation of opposite effects: while a larger pressure reduction produces a higher overall density of the post-collapse HQS (potentially resulting in higher values of f_F), it also leads to more rapid rotation due the comparatively greater compactness (which should lower f_F). We also note that the large amplitude quasi-radial oscillations in the last model(s) of each subsequence of sequence CD are so strongly damped shortly after the collapse, that making a precise determination of the frequency f_F is difficult.

3.5.3 Damping of the stellar pulsations

Both from the values for the damping time τ_F of the fundamental quasi-radial F-mode in the GW signal given in Table 3.2 and from Fig. 3.17, where we plot the time evolution of $\rho_{\rm c}$ for the most and least rapidly rotating collapse models of sequence CA, it is evident that there can be significant damping of the post-bounce pulsations in the HQS, for some values of the model parameters. In Table 3.4 we also report the values for the damping time $\tau_{F,\rho_{\rm c}}$ extracted from the time evolution of the central rest-mass density $\rho_{\rm c}$: these values range from 8 to $200\,{\rm ms}$ for the models considered here. With the exception of those models for which the GW emission is dominated by mode resonance, the two estimated timescales τ_F and $\tau_{F,\rho_{\rm c}}$ are very similar.

In Section 3.4, we have argued that the kinetic energy stored in the quasi-radial post-bounce pulsations is not responsible for generating differential rotation, and therefore the observed damping cannot be attributed to this mechanism as previously suggested. Since, also, the numerical dissipation of our code is much too small to be the main cause for the strong damping observed in some models (and anyway affects all

[8] We have found the same qualitative behaviour also for another sequence with constant period $p = 1.4\,{\rm ms}$ and varying rest mass, for which we do not present the data here.

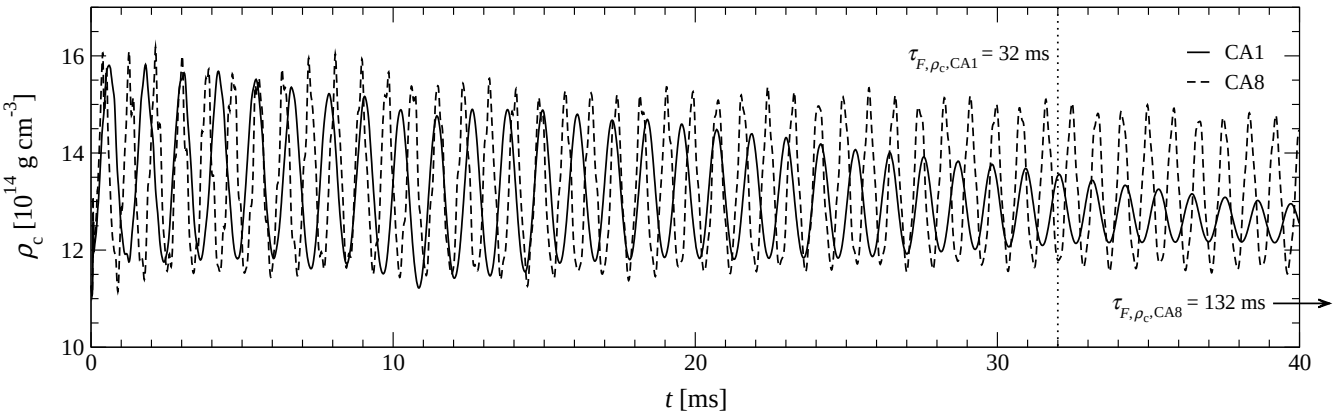

Figure 3.17: Time evolution of the central rest-mass density ρ_c for models CA1 and CA8, the most and the least rapidly rotating models of sequence CA. The dotted line marks the pulsation damping time τ_{F,ρ_c} for model CA1.

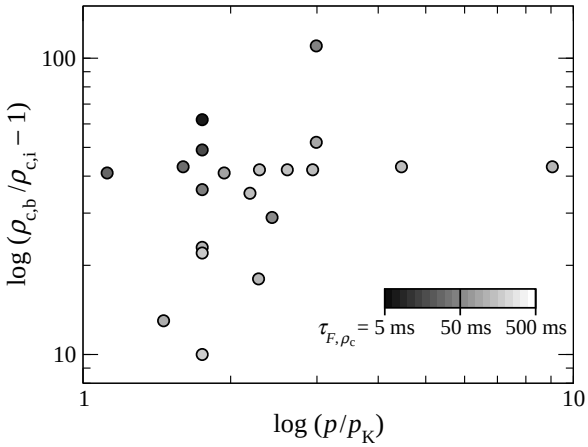

Figure 3.18: Location of all GR collapse models in the (p/p_{K})–$(\rho_{\mathrm{c,b}}/\rho_{\mathrm{c,i}} - 1)$ plane. The damping time τ_{F,ρ_c} of the F-mode, as calculated from the time evolution of the central rest-mass density, is encoded in the grey scale, with dark/light grey corresponding to strong/weak damping. Only models with very rapid rotation (close to the Kepler limit) *and* violent post-bounce oscillations due to a very dynamical collapse (upper left corner of the plot) have short damping times.

models in the same way) it is necessary to offer an alternative physical explanation for why the pulsations are strongly damped for some models, with τ_{F,ρ_c} being a few ms (and thus comparable with the dynamical timescale), while for other models the damping is much slower, with $\tau_{F,\rho_c} \sim 100\,\mathrm{ms}$ (and thus orders of magnitude longer than both the dynamical timescale and the pulsation period of the star; in this case, the damping seems to be limited essentially to that caused by numerical viscosity). Since the gravitational radiation back-reaction on the system is also negligible (and is not taken into account by our conformally flat approximation of the metric equations anyway), the strong damping seen can only be due to hydrodynamic effects.

A careful analysis of our model parameters reveals that damping is significant only for those models that both rotate very rapidly *and* experience strong pulsations. This can be seen in Fig. 3.18, where the value of τ_{F,ρ_c} for each model is given by the grey scale. Only models located in the upper left part of the plane spanned by the rotation period ratio p/p_{K} and the over-density at bounce $\rho_{\mathrm{c,b}}/\rho_{\mathrm{c,i}} - 1$, have the very short damping times.

Table 3.4: Relevant quantities for mass-shedding-induced damping: p is the rotation period of the NS, $p_{\rm K}$ is the rotation period of a free particle on a circular orbit at the equator (Kepler limit), $p/p_{\rm K}$ is the ratio of these two periods, $\rho_{\rm c,b}/\rho_{\rm c,i} - 1$ is the central over-density at bounce compared to the initial value, and $\tau_{F,\rho_{\rm c}}$ and τ_F are the F-mode damping times extracted from the time evolution of $\rho_{\rm c}$ and from the GW signal, respectively. Note that we omit here those models that collapse to a black hole. For completeness, we also include the Newtonian collapse models CN1, CN2 and CN3.

Model	p [ms]	$p_{\rm K}$ [ms]	$p/p_{\rm K}$	$\rho_{\rm c,b}/\rho_{\rm c,i} - 1$ [%]	$\tau_{F,\rho_{\rm c}}$ [ms]	τ_F [ms]
CA1	1.00	0.89	1.12	41	32	40
CA2	1.20	0.75	1.60	43	36	49
CA3	1.40	0.72	1.94	41	93	—
CA4	1.60	0.70	2.29	42	155	319
CA5	1.80	0.69	2.61	42	160	418
CA6	2.00	0.68	2.94	42	150	270
CA7	2.99	0.67	4.46	43	152	711
CA8	5.98	0.66	9.06	43	132	—
CB1	1.30	0.89	1.46	13	113	99
CB2	1.40	0.80	1.75	23	128	133
CB3	1.60	0.73	2.19	35	156	196
CB4	1.80	0.69	2.61	42	160	418
CB5	2.00	0.67	2.99	52	103	687
CC1	1.80	0.79	2.28	18	136	143
CC2	1.80	0.74	2.43	29	62	71
CC3	1.80	0.69	2.61	42	160	418
CD1	1.40	0.80	1.75	10	200	150
CD2	1.40	0.80	1.75	23	128	133
CD3	1.40	0.80	1.75	36	49	54
CD4	1.40	0.80	1.75	49	19	19
CD5	1.40	0.80	1.75	62	8	8
CD6	1.40	0.80	1.75	22	191	248
CD7	2.00	0.67	2.99	52	103	687
CD8	2.00	0.67	2.99	110	53	—
CN1	1.20	0.86	1.40	11	91	73
CN2	1.20	0.86	1.40	32	16	9
CN3	1.20	0.86	1.40	52	1	1

For models rotating close to the mass-shedding limit (the Kepler limit), the effective gravity near to the equator is significantly weakened, vanishing at the mass-shedding point. As one goes to models having larger amplitude quasi-radial post-bounce pulsations, an increasing amount of matter is ejected from low latitudes on the stellar surface during each oscillation. This matter goes into the initially artificial very-low-density atmosphere and creates an expanding envelope of weakly-bound (or even unbound) material around the HQS. This mass shedding causes strong damping of the pulsations, as pulsational kinetic energy is converted into gravitational potential energy of the ejected matter. Since polar perturbations (mainly radial ones) are coupled to axial perturbations in rotating stars, the damping rapidly affects all modes.

This mass-shedding-induced damping of oscillations in rapidly rotating NSs near to the Kepler limit was first observed and discussed by [392] for weakly pulsating equilibrium polytropic NS models in uniform rotation, treated within the Cowling approximation (neglecting the dynamics of the spacetime). In a subsequent study, [120] found that if the Cowling approximation is abandoned and the spacetime is dynamically evolved, the effect of mass-shedding is drastically reduced, giving a consequent decrease in the damping of the pulsations. However, both of these studies treated small-amplitude pulsations of equilibrium models (working within the linear regime), whereas in our collapse models the pulsations can have very large amplitudes.

Considering the example of model CD8: this has a large initial pulsation amplitude, with relative variations in $\rho_{\rm c}$ of around 55% (which is about half of the over-density at bounce) but it is rotating too slowly to be close to the Kepler limit (with $p/p_{\rm K} \simeq 3$) and does not show strong damping. The five models with the shortest damping timescales, however, ($\tau_{F,\rho_{\rm c}} < t_{\rm f} = 50\,{\rm ms}$) all have both quite large initial pulsation amplitudes $> 18\%$ and are also rapidly rotating, with rotation-period ratios $p/p_{\rm K} < 1.75$. This is consistent with equatorial mass-shedding being the predominant mechanism for the strong damping of the post-bounce pulsations seen for models that both rotate close to the Kepler limit *and* pulsate with large amplitude. For models that are not affected by equatorial mass shedding, other damping mechanisms predominate (such as the conversion of kinetic energy into internal energy by shocks, nonlinear coupling of modes, numerical or physical dissipation) but all of these operate on timescales much longer than the dynamical timescale[9].

3.5.4 The role of convection

As discussed above, the damping of post-bounce pulsations and the development of differential rotation seen by LCCS seems to have been mainly a manifestation of the convective motion artificially produced in their simulations by the way in which they induced the collapse. Real physical convection might well be induced by energy input coming from the phase transition but this has no connection with the artificially-induced convection. Calculating the real convection is beyond the scope of the present simplified treatments and remains a topic for future work. While we have eliminated from our calculations the main source of artificial convection present in the LCCS simulations, some artificially-induced convection still remains. There are at least two different origins for this which apply for two different classes of initial models.

The first origin is related to the CFC approximation itself: when the data from the initial-model solver are mapped to the evolution code and the initial-value problem is subsequently re-solved to satisfy the constraints (2.30)-(2.33), small errors due to the CFC approximation create spurious departures from constant entropy. This side effect of the CFC approximation is clearly larger for rapidly rotating and very compact models such as CA1, and becomes very small for slowly rotating models, vanishing in the non-rotating limit. Fig. 3.19 shows the initial radial profile of the specific-entropy measure $\tilde{K}$ [cf. Eq. (3.9)] for model CA1, together with those for the Newtonian models CN1 and CN3 discussed previously. It can be seen

[9] As far as viscosity is concerned, in the quark phase the shear viscous damping timescale is comparable to that of normal nuclear matter, which is of the order of 10^8 s for a typical NS, while the bulk viscous damping timescale is of the order of seconds, assuming a rotation period $p = 1$ ms and an s-quark mass $m_s = 100$ MeV [248].

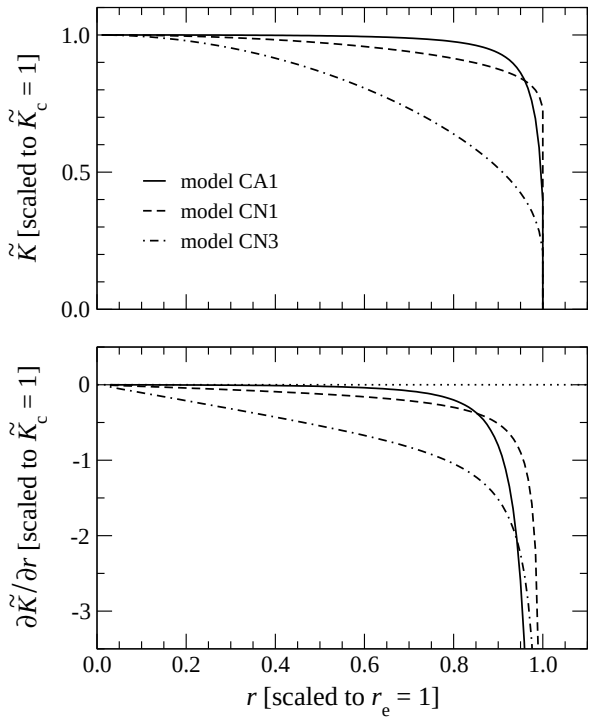

Figure 3.19: Radial profile of the specific-entropy measure $\tilde{K}$ (top panel) and its radial derivative (bottom panel) in the equatorial plane at the initial time for the GR model CA1 (solid line), and the corresponding profiles for the Newtonian models CN1 (dashed line) and CN3 (dash-dotted line). The specific-entropy measure and the radius are scaled to give $\tilde{K}_{\rm c} = 1$ and $r_{\rm e} = 1$.

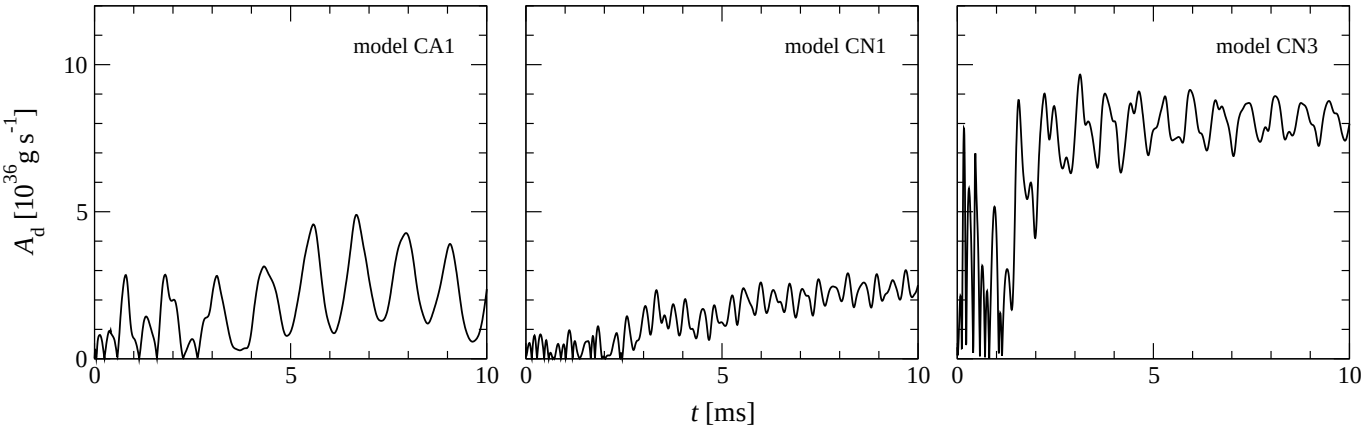

Figure 3.20: Time evolution of the differential rotation measure $A_{\rm d}$ for the GR collapse model CA1 (left panel) and the Newtonian collapse models CN1 (centre panel) and CN3 (right panel).

that the CFC approximation produces a negative specific-entropy gradient for model CA1 at the start of the evolution. While this gradient is very small in the bulk of the star (for $r/r_{\rm e} \lesssim 0.8$), near to the surface it becomes comparable to (or even greater than) that for model CN1, for which γ was initially decreased from 2 to 1.95. However, it is still much smaller than that occurring when reducing γ to 1.75 as in model CN3.

The CFC-induced violation of the Solberg–Høiland criteria drives this model (and other rapidly rotating ones) to develop significant convection, which we measure in terms of the general relativistic equivalent of the averaged shear [cf. Eq. (3.8)],

$$A_{\rm d} = \int \sqrt{\gamma}\, \rho h W^2 \left| \frac{dv_\phi}{dr} - \frac{v_\phi}{r} \right| dV, \tag{3.11}$$

where $v_\phi = \sqrt{v_3 v^3}$ is the rotation velocity of the fluid[10]. Fig. 3.20 shows the time evolution of $A_{\rm d}$ for model CA1 (whose convection is, in fact, among the strongest for the GR models; left-hand panel), as well as for the Newtonian models CN1 (centre panel) and CN3 (whose convection is among the strongest for the Newtonian models; right-hand panel). It can be seen that both the development of the convection with time for model CA1 and its maximum saturation level are comparable with those for the Newtonian model CN3, while the convection in model CN1 is stronger and occurs on a much shorter timescale, which is natural since the initial non-isentropy is larger in that case.

The second origin of spurious convection appears in slowly rotating models; this is not due to the CFC approximation since the errors coming from that are essentially negligible in these cases. Instead, convection is produced here by the small violation of isentropy caused by interaction of the matter just inside the surface of the HQS with the surrounding artificial atmosphere. This perturbation slowly propagates inwards and finally affects the entire star at late times. Since in uniformly rotating configurations, centrifugal forces tend to have a stabilising effect within the Solberg–Høiland criteria, it is easy to understand why this process occurs only for the slowly rotating models. An example of this mechanism in action is given by model CA8, which is the slowest rotator in our set of GR models: here $A_{\rm d}$ reaches a maximum that is close to the saturation level of models CA1 and CN1 but is still much smaller than the value for the strongly convective model CN3.

In models that are neither very rapidly nor very slowly rotating (e.g. model CC1), convection is almost absent and $A_{\rm d}$ remains at very low values, which can be explained as resulting from small deviations away from homology during the initial contraction and the subsequent post-bounce oscillations. We repeat, however, that consistent treatment of other possible real sources of convection remains a major topic for future work.

3.5.5 Enhanced emission of gravitational waves via mode resonance

In Section 3.5.2 we have discussed the influence of the initial rotation speed on the frequencies of the post-bounce oscillations and also commented that for models with the same rest mass, those with higher rotation generally have higher GW strain due to their increased quadrupole moments. This is indeed what is seen, for instance, in the sequence CB as reported in Table 3.2. This general behaviour, however, has a notable exception in the case of the comparatively slowly rotating model CB5, which has by far the largest GW strain for any of those in the sequence CB, with the energy emitted in GWs in the first $50\ {\rm ms}$ being at least an order of magnitude larger than for any of the other models in this sequence.

In the top panels of Fig. 3.21 we plot the time evolution of the central rest-mass density $\rho_{\rm c}$ for models CB3, CB4 and CB5. It can be seen that the collapse dynamics of model CB5 are not qualitatively different from those of the more rapidly rotating members of the same sequence. As rotation decreases from CB3 to

[10] As already noted for the Newtonian models, the Newtonian equivalent of $A_{\rm d}$ has a qualitatively very similar behaviour to that of $T_{\rm d}$ but only the first of these has a clearly-defined physical meaning.

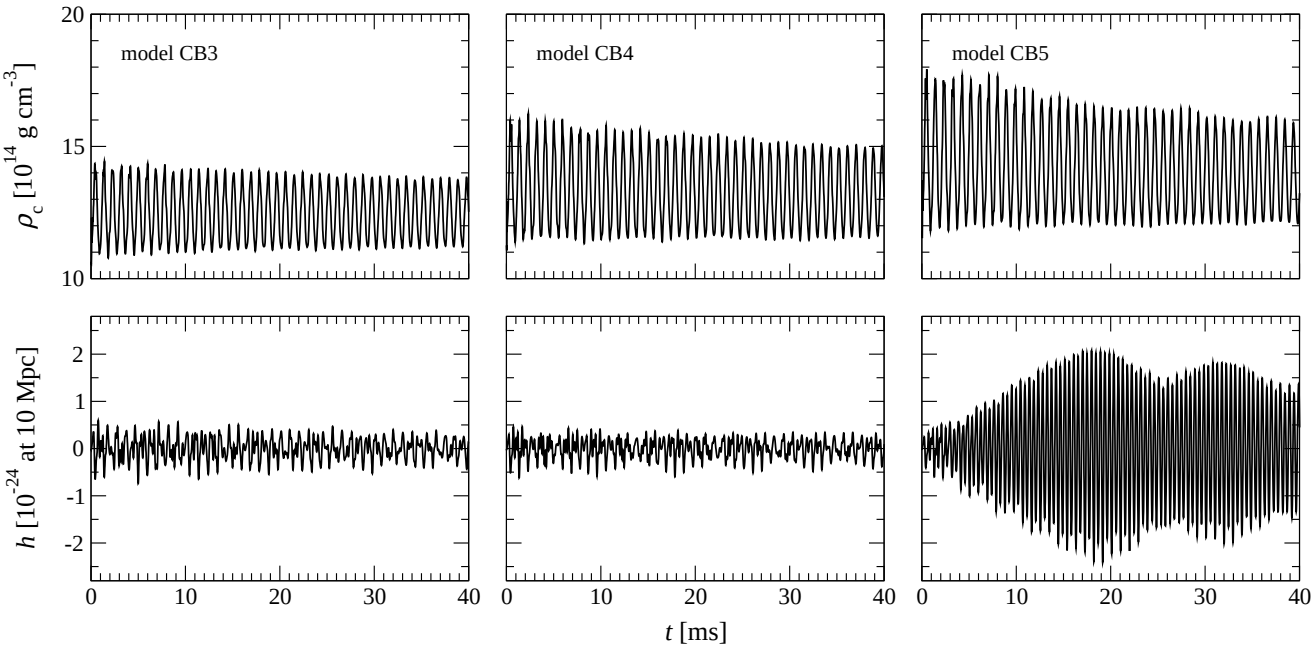

Figure 3.21: Time evolution of the central rest-mass density ρ_c (top panels) and the GW strain h at a distance of $10\,\mathrm{Mpc}$ (bottom panels) for the GR collapse models CB3 (left panels), CB4 (centre panels) and CB5 (right panels). The enhanced GW emission for model CN5 due to mode resonance is clearly visible.

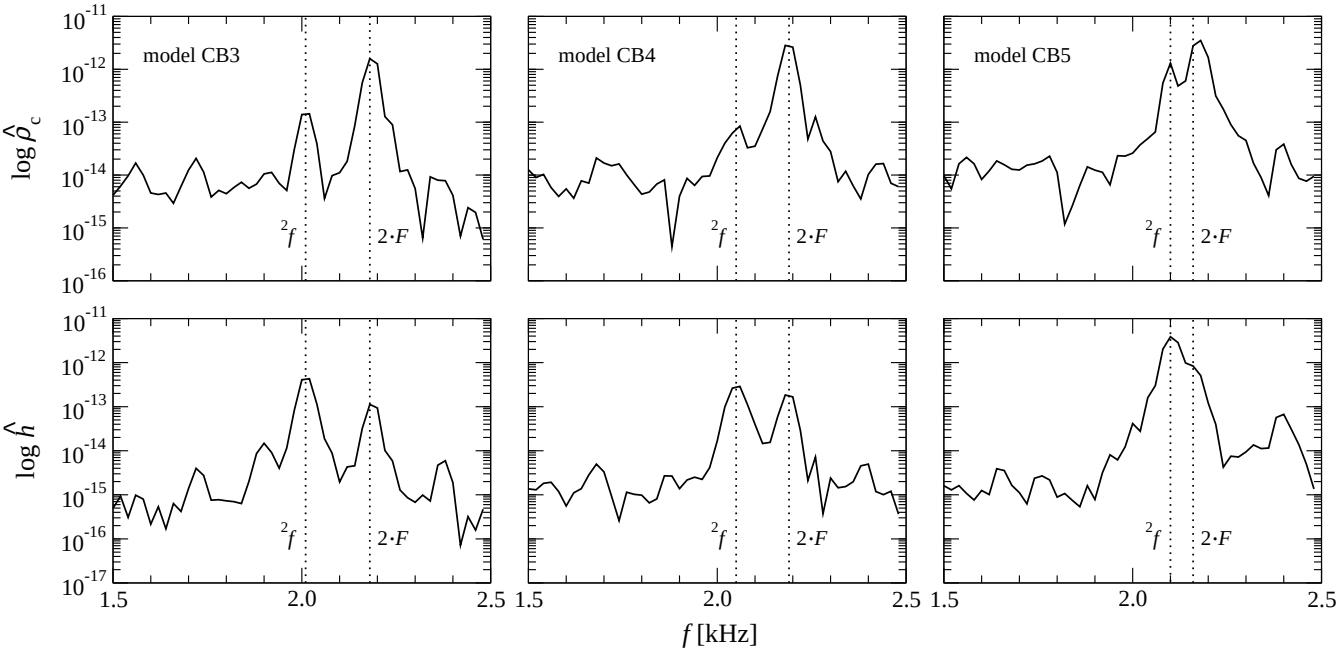

Figure 3.22: Logarithmic power spectrum (in arbitrary units) of the central rest-mass density ρ_c (top panels) and the GW strain h (bottom panels) for the same models as in Fig. 3.21. The resonance between the ^2f-mode and the $2 \cdot F$-mode sets in as their frequencies (marked by dotted lines) approach each other.

CB5, the strength of the contraction increases, leading to higher central over densities $\rho_{\rm c,b}$ at the bounce and stronger post-bounce oscillations. This, however, cannot account satisfactorily for the very large maximum GW strain amplitude $|h|_{\rm max}$ of model CB5, nor for the growth of h during the first $20\ {\rm ms}$ *after* the bounce in this case (see bottom panels of Fig. 3.21).

Rather, the time evolution of h in model CB5 (the delayed growth, the saturation and the subsequent decay) suggests the presence of a resonance effect among several modes, at least one of which should be an efficient emitter of GWs. One of the obstacles to having strong GW emission is that the modes which are most strongly excited during the bounce are (quasi-)radial modes which are not efficient GW emitters; indeed they would not emit at all if rotation were not present to introduce non-radial contributions. However, it was suggested many years ago (see, e.g., [132]) that the pulsational energy from a quasi-radial mode, which contains a significant amount of kinetic energy but radiates GWs only weakly, could be transferred to a much more strongly radiating quadrupolar mode by means of resonance effects and even parametric instabilities. Dimmelmeier et al. [120] and Passamonti et al. [322, 323] have discussed this possibility in the context of nonlinear coupling of quasi-normal modes for nearly-equilibrium models of NSs.

In order to investigate whether this mechanism might be responsible for the enhanced GW emission observed for model CB5, we performed a mode analysis for models CB3, CB4 and CB5. The power spectrum of the time evolution of the central rest-mass density $\rho_{\rm c}$, shown in the top panels of Fig. 3.22, indicates that there is a lot of energy in the $2\cdot F$-mode which has a peak about an order of magnitude higher than the corresponding one for the ${}^2f$-mode, located at slightly lower frequencies. As rotation decreases from model CB3 to model CB5, the frequencies of these two modes get closer until the two peaks almost merge for model CB5, with the relative difference between the two frequencies decreasing to about 4% (see the bottom panel of Fig. 3.16 and also Table 3.5)[11]. Under these conditions of resonance, the $2\cdot F$-mode is able to transfer a considerable amount of energy into the ${}^2f$-mode, as can be clearly seen in the power spectrum of the waveform amplitude shown in the lower panels of Fig. 3.22. If the spectra for model CB5 from Fig. 3.16 are produced for several time windows, this energy transfer between the two modes becomes visible. While the peaks of both $\rho_{\rm c}$ and h corresponding to the ${}^2f$-mode first gradually grow in the early phases of the evolution (showing the initial amplification at the expense of the $2\cdot F$-mode) and start decreasing only at later times, the peaks of the $2\cdot F$-mode always descrease.

The strong dependence of the maximum GW strain $|h|_{\rm max}$ on the rotation rate, as seen in Table 3.5 as well as in the bottom panel of Fig. 3.15, indicates that the resonant behaviour becomes important only when the frequencies of the ${}^2f$-mode and the $2\cdot F$-mode are very close to each other. This small difference between the two frequencies is also responsible for the clear beating pattern seen in the waveform for model CB5 (see the bottom right panel in Fig. 3.21). Fig. 3.15 also shows that while the pulsation energy contained in the F-mode (represented by the spectrum of $\rho_{\rm c}$ in the top panel) is always larger than the corresponding one in the $2\cdot F$-mode, when more resonance between the $2\cdot F$-mode and the ${}^2f$-mode is at work, the $2\cdot F$-mode becomes a very efficient emitter of GWs as well (see the spectrum of h in the lower panel), surpassing the F-mode here. This is most likely a consequence of the altering of the $2\cdot F$-mode's previously quasi-radial eigenfunction by the interaction with the quadrupolar ${}^2f$-mode (see, e.g., [120]).

Applying this analysis to the complete set of investigated models, we find that the same resonance between the ${}^2f$-mode and the $2\cdot F$-mode is also at work in models CA3 and CA4 (this is clearly visible in the top panel of Fig. 3.15) as well as in model CD8. Also in these cases, the waveforms show an initial growth in amplitude over several cycles and then a strong beating at later times. In the case of model CD8, the growth in h due to the mode resonance becomes prominent long after the bounce, at $t \gtrsim 20\ {\rm ms}$, not reaching its maximum $|h|_{\rm max}$ until $t \simeq 48\ {\rm ms}$, when the quasi-radial oscillations have already been damped to around 38% of their initial amplitude. In contrast, for models whose GW emission is not influenced by

[11] We have also performed simulations for models with other parameter values in the close vicinity of those for model CB5 and found that CB5 actually exhibits almost the maximum possible resonance between the $2\cdot F$-mode and the ${}^2f$-mode.

Table 3.5: The frequencies $f_{^2f}$ and $f_{2\cdot F}$ of the fundamental quadrupolar ^2f-mode and the self-coupling of the F-mode, for the collapse models of sequence CB. $\Delta f_{\rm rel} = f_{2\cdot F}/f_{^2f} - 1$ is the relative difference between the frequencies of these two modes.

Model	$f_{^2f}$ [kHz]	$f_{2\cdot F}$ [kHz]	$\Delta f_{\rm rel}$ [%]	$\left[\begin{array}{c}\lvert h\rvert_{\rm max} \\ 10^{-23} \\ \text{at } 10\ \text{Mpc}\end{array}\right]$	$E_{\rm gw}$ $[10^{-4} M_\odot c^2]$
CB1	1.78	2.10	18	0.38	0.01
CB2	1.90	2.13	12	0.57	0.05
CB3	2.02	2.18	8	0.10	0.09
CB4	2.06	2.19	6	0.10	0.11
CB5	2.10	2.18	4	1.72	1.16

this resonance, $|h|_{\rm max}$ is reached at the time of bounce or very close to it. In addition, here the spectral power of both the $2\cdot F$-mode and the ^2f-mode decreases at all times if successive spectra are obtained with the technique of shifted time windows.

3.5.6 Detectability prospects for the gravitational wave emission

Although the maximum GW strain $|h|_{\rm max}$ in the waveforms of our GR models is about an order of magnitude smaller than that computed by LCCS for Newtonian models, the long quasi-periodic GW emission that is possible for phase-transition-induced collapse may still make this scenario a plausible source for GW detectors. Assuming that the strong post-bounce oscillations are not damped by any other physical mechanisms apart from dissipation of kinetic energy by shocks, the damping times that we obtain suggest that the effective total emission time for GWs can be much longer than the time for which we have followed the evolution of our models ($t_{\rm f} = 50$ ms), extending to hundreds of oscillations.

The main GW emission modes are the F-mode and the ^2f-mode, which have comparable energies in the power spectra, except where the resonance between the ^2f-mode and the $2\cdot F$-mode is important, when the combined ^2f-mode/$2\cdot F$-mode dominates the GW spectrum. Model CA5, for which we show in Fig. 3.23 the power spectrum of the time evolution of $\rho_{\rm c}$ (top panel) and of the GW signal (bottom panel), is an example where the frequencies of ^2f-mode and $2\cdot F$-mode are already close and the two modes start to merge.

Exploiting the fact that, for most models, the waveform can be very well approximated as a combination of two essentially monochromatic damped sinusoids, it is straightforward to construct a phenomenological waveform expressed in terms of six parameters: the mode frequencies f_F and $f_{^2f}$, the damping times τ_F and $\tau_{^2f}$, and the initial phases and relative amplitude of the two modes (all of which can be found from Table 3.2). This can then be applied as a template in matched filtering data-analysis algorithms so as to search for the waveforms in the data stream more effectively.

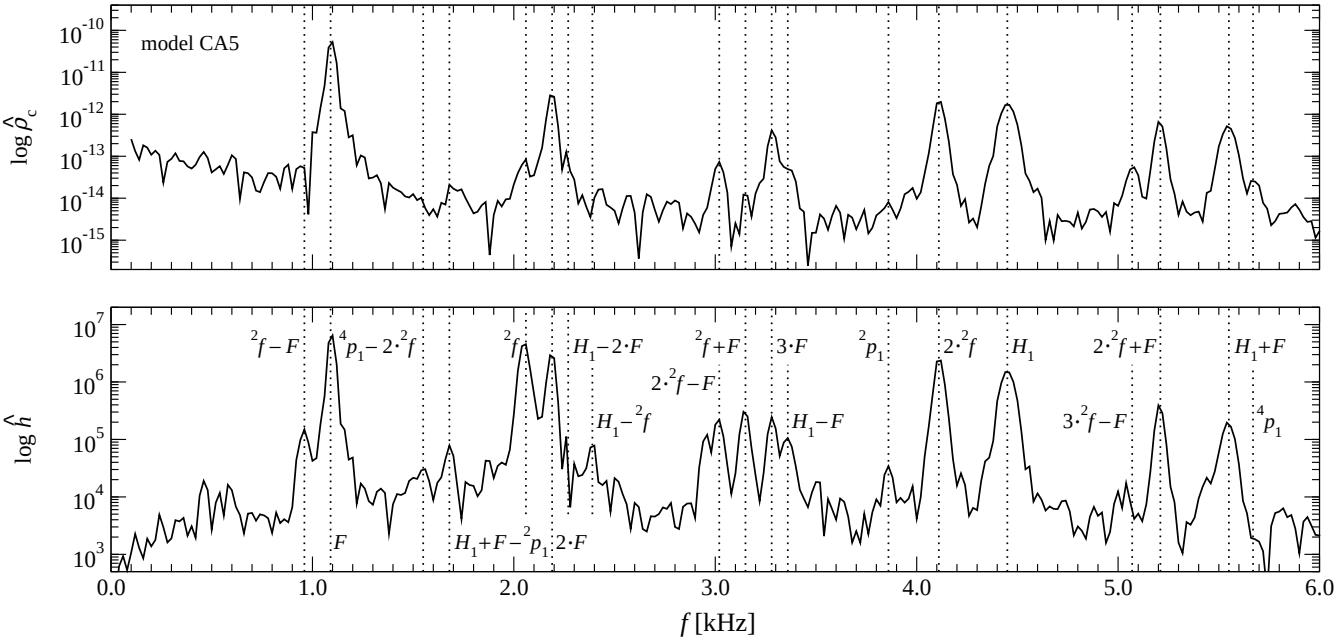

Figure 3.23: Logarithmic power spectrum (in arbitrary units) of the central rest-mass density ρ_c (top panel) and the GW strain h (bottom panel) for the GR collapse model CA5. The linear quasi-normal modes and the nonlinear (self-)couplings are marked with dotted lines and labelled. H_1 denotes the first overtone of the F-mode, while $^2p_1$ and $^4p_1$ are the first overtones of the fundamental $l = 2$ and $l = 4$ modes, respectively.

Table 3.6: Detection prospects for the GWs: $f_{\rm c}$ is the characteristic frequency, $h_{\rm c}$ is the integrated characteristic GW signal strain and SNR is the signal-to-noise ratio, each given for the current LIGO and VIRGO detectors, and for the future advanced LIGO detector. The values given for all of the quantities assume a total emission time of $t_{\rm f} = 50\ \mathrm{ms}$ and are dependent on the rms strain noise $h_{\rm rms}$ of the detector. Note that models CB6, CC4 and CD9 collapse to form a black hole as a result of the phase transition and so are omitted here.

Model	$f_{\rm c,LIGO}$ [kHz]	$f_{\rm c,VIRGO}$ [kHz]	$f_{\rm c,adv.\ LIGO}$ [kHz]	$h_{\rm c,LIGO}$ $\left[\begin{smallmatrix}10^{-20}\\ \text{at 10 kpc}\end{smallmatrix}\right]$	$h_{\rm c,VIRGO}$ $\left[\begin{smallmatrix}10^{-20}\\ \text{at 10 kpc}\end{smallmatrix}\right]$	$h_{\rm c,adv.\ LIGO}$ $\left[\begin{smallmatrix}10^{-20}\\ \text{at 10 kpc}\end{smallmatrix}\right]$	$\mathrm{SNR}_{\rm LIGO}$ [at 10 kpc]	$\mathrm{SNR}_{\rm VIRGO}$ [at 10 kpc]	$\mathrm{SNR}_{\rm adv.\ LIGO}$ [at 10 kpc]
CA1	0.954	0.978	1.029	2.55	2.59	2.68	7.5	12.0	179
CA2	1.755	1.798	1.864	5.65	5.75	5.92	6.8	11.8	201
CA3	1.845	1.876	1.923	8.52	8.63	8.80	9.4	16.6	287
CA4	1.619	1.660	1.735	3.56	3.62	3.75	4.8	8.3	139
CA5	1.349	1.382	1.450	1.78	1.81	1.87	3.1	5.3	86
CA6	1.415	1.452	1.527	1.55	1.58	1.63	2.5	4.4	71
CA7	1.449	1.485	1.572	0.72	0.73	0.76	1.1	2.0	32
CA8	1.609	1.672	1.788	0.29	0.30	0.31	0.4	0.7	11
CB1	1.349	1.374	1.417	1.31	1.33	1.36	2.3	4.0	64
CB2	1.304	1.335	1.388	2.12	2.16	2.22	3.9	6.7	108
CB3	1.322	1.353	1.411	2.09	2.12	2.18	3.8	6.4	104
CB4	1.349	1.382	1.450	1.78	1.81	1.87	3.1	5.3	86
CB5	2.073	2.078	2.086	13.18	13.27	13.24	12.3	21.9	389
CC1	1.370	1.394	1.435	1.06	1.08	1.10	1.8	3.1	51
CC2	1.370	1.394	1.442	1.48	1.50	1.54	2.6	4.4	71
CC3	1.349	1.382	1.450	1.78	1.81	1.87	3.1	5.3	86
CD1	1.346	1.370	1.407	1.23	1.25	1.27	2.2	3.7	61
CD2	1.304	1.335	1.388	2.12	2.16	2.22	3.9	6.7	108
CD3	1.313	1.345	1.406	2.79	2.84	2.93	5.1	8.7	140
CD4	1.555	1.585	1.636	4.54	4.60	4.71	6.5	11.2	188
CD5	1.661	1.682	1.718	5.09	5.14	5.23	6.6	11.6	197
CD6	1.350	1.383	1.449	0.82	8.36	0.86	1.5	2.5	40
CD7	2.073	2.078	2.086	13.18	13.21	13.24	12.3	22.0	389
CD8	1.722	1.780	1.862	3.88	3.99	4.13	4.8	8.3	141

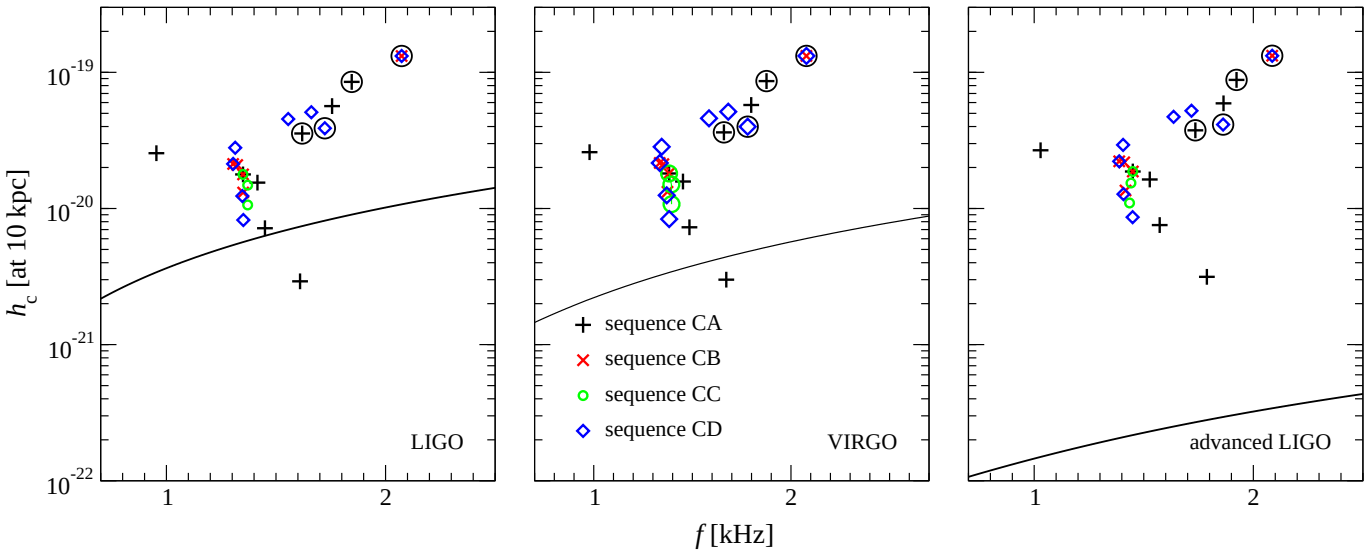

Figure 3.24: Location of the GW signals from all of our GR models in the h_c–f_c plane shown relative to the sensitivity curves (giving the rms strain noise $h_{\rm rms}$) for the current LIGO detector (left panel) and VIRGO detector (centre panel) and for the advanced LIGO detector (right panel). The sources are taken to be at a distance of $10\ {\rm kpc}$. Note that some of the models belong to more than one sequence. Models for which mode resonance boosts the GW emission are additionally marked with circles.

In Table 3.6 we summarize the values of f_c, h_c (given by equations 2.156 and 2.157, respectively) and the SNR for all of the models (except those which collapse to a black hole) for the currently operating LIGO and VIRGO detectors and for the future advanced LIGO detector. For all of the detectors we consider a source inside our own Galaxy at a reference distance of $10\ {\rm kpc}$. The proportion of NSs that undergo phase-transition-induced collapse at some stage in their lifetimes is not well-known. The phenomenon could occur at, or soon after, the formation stage (giving an event rate roughly proportional to that for core collapse supernovae) or it could come at a later stage when an old NS is spun up and has its mass increased by accretion from a binary partner in an LMXB (an interesting case but with an event rate which is thought to be very much lower, probably $\sim 10^{-5}\ {\rm yr}^{-1}$ for the Milky Way; see [328]). Another point is that a phase-transition-induced collapse occurring for a NS which is not rapidly rotating would not be so interesting for our purposes. Even under the most extremely optimistic assumption that the phase-transition-induced collapse rate equals that for core-collapse supernovae, that would only give a rate of up to 1 per $20\ {\rm yr}$ for our Galaxy, which is prohibitively low. On the other hand, if such an event did occur in our Galaxy, for current interferometric detectors of the LIGO class and assuming an emission time $t_{\rm f} = 50\ {\rm ms}$, all of our models except one have a SNR above 1. For the strongest emitting model CB5, where mode resonance significantly enhances the GW emission, the SNR even exceeds 10. With the advanced LIGO detector, the SNR lies comfortably above 10 for all models and reaches almost 400 in model CB5.

For substantially increasing the event rate, it would be necessary for the detector to be sensitive to signals coming from distances out to the Virgo cluster, at $\sim 20\ {\rm Mpc}$, (for which the supernova rate would rise to more than 1 per year). However, at this distance the SNR for our models drops to well below 1 even for advanced LIGO. Therefore, as for GW signals from supernova core collapse (see the discussion in [122]), the second generation detectors will improve the SNR of a local event, but will not increase the event rate much on account of the inhomogeneous galaxy distribution in the local region of the Universe. Only third generation detectors will have the required sensitivity in the kHz range to achieve a robust SNR at the distance of the Virgo cluster.

Note that for most of the models the *integrated* characteristic frequency $f_{\rm c}$ given in Table 3.6 is not very close to either of the two main GW emission frequencies f_F and $f_{^2f}$. This is because $f_{\rm c}$ reflects the frequency dependence of the sensitivity of the detector, because nonlinear mode couplings and higher order linear modes also contribute to the GW signal (although with lower relative amplitudes; see Fig. 3.23) and, most importantly, because for many models the GW power spectrum of the signal exhibits nearly equally strong peaks in the F-mode and the ^2f-mode.

The detector dependence of $f_{\rm c}$ and $h_{\rm c}$ is also illustrated in Fig. 3.24, where the locations of the GW signals for all of the models are plotted relative to the rms strain noise $h_{\rm rms}$ of the current LIGO and VIRGO detectors (left and centre panels, respectively) and the future advanced LIGO detector (right panel), all for a distance to the source of $10\,{\rm kpc}$. As a general feature, we note that the upper parts of these sensitivity diagrams are occupied by those models whose GW signal strength is enhanced by mode resonance. When mode resonance is not important, the largest characteristic amplitudes occur for those models which are most rapidly rotating, unless strong post-bounce damping is in action as in model CA1.

Both in Table 3.6 and in Fig. 3.24 the GW characteristics have been evaluated for a total emission time of $t_{\rm f} = 50\,{\rm ms}$. In Appendix B we describe how to obtain the characteristic GW strain $h_{\rm c}$ for an *arbitrary* emission time using simple scaling laws.

3.6 Conclusion

In this work, we have described numerical simulations of the phase-transition-induced collapse of rotating neutron stars to become hybrid quark stars. The simulations were made using a code which solves the general relativistic hydrodynamic equations in axisymmetry and within the conformally flat approximation. The initial stellar models were taken as being rapidly rotating $\gamma = 2$ polytropes, while during the evolution we used an equation of state composed of three parts, depending on density: a normal hadronic-matter phase, a mixed phase of normal matter together with deconfined quark matter, and a pure quark-matter phase. The hadronic component of the equation of state was described with an ideal-gas type of equation of state, while for the deconfined quark matter phase we used the MIT bag model.

To validate our code, we first repeated several of the Newtonian simulations performed previously by [233]. We found that the differential rotation which develops in these models during the post-bounce phase is almost entirely due to strong transient convection which arises because the way in which they treated the onset of the phase transition leads to an artificial negative specific-entropy gradient. We argue that their conclusion about there being a causal link between the large amplitude post-bounce pulsations and the creation of differential rotation was a misinterpretation of the results. We also suggest that a significant part of the damping of the pulsations which they observed was a consequence of the numerical dissipation present in their calculations, rather than being related to differential rotation, although a part of this damping was related to the other physical processes which we have discussed here and which were present in both calculations.

Having clarified the dynamics of the collapse in the Newtonian framework, we then investigated the corresponding situation within general relativity, using a modified prescription for triggering the phase transition and initiating the collapse. Here we change the equation of state only in the regions where the phase transition has taken place and leave it unchanged elsewhere. We recognize that our procedure for describing the phase transition remains extremely idealized but we believe that it represents a step forward.

Despite this difference in the way in which the phase transition is triggered, we have not found any major qualitative differences in the waveforms produced when comparing the relativistic simulations with the earlier Newtonian ones. Also in the general relativistic simulations, the waveforms produced are mainly composed of the fundamental $l = 0$ quasi-radial F-mode and the fundamental $l = 2$ quadrupolar ^2f-mode. However, in contrast to the Newtonian models, the F-mode is at a lower frequency than the ^2f-mode as a

consequence of the different density profiles. In addition to these modes, a nonlinear self-coupling of the F-mode at twice the original frequency, the $2 \cdot F$-mode, is strongly excited due to the violent nature of the collapse. Although qualitatively similar to their Newtonian counterparts, the relativistic models exhibit quantitative differences in their dynamics. In order to investigate these, we have considered a set of 23 different models organized in several sequences. In each of these sequences, only one of the characteristic parameters of the models was allowed to vary.

The main trends observed were as follows. For the sequence with constant initial central rest-mass density, the maximum gravitational wave strain $|h|_{\max}$ increases monotonically with the rotation rate (except for some models where the waveform is strongly altered by mode resonances). For the constant rest mass sequence, on the other hand, we observe first an increase of $|h|_{\max}$ with the rotation rate and then a decrease for very rapid rotation. For the sequence with constant rotation period but varying rest mass, we see $|h|_{\max}$ increasing monotonically with the rest mass, which is a different behaviour from that seen for the Newtonian models, where $|h|_{\max}$ first increases and then decreases again as the rest mass is increased. The reason for this difference may simply be that having a decreasing part of the curve would require progenitor neutron stars with rest masses beyond the upper limit for general-relativistic models. Finally, changing the equation of state in the mixed phase has straightforward consequences: the central rest-mass density at bounce, the amplitude of the post-bounce oscillations, and the maximum gravitational wave strain all increase as the overall pressure in the mixed phase is reduced.

Other points to arise include the following. Firstly, the influence of rotation on the frequencies of the F and ${}^2f$-modes agrees well with what was found by [120] for pulsations of equilibrium neutron stars, suggesting that studies of linear pulsations of equilibrium models can (at least in some cases) correctly predict the properties of the eigenfrequencies also when the pulsations are excited in a dynamical situation. Secondly, in some models the emission of gravitational radiation is considerably enhanced by the nonlinear resonance between the $2{\cdot}F$-mode and the ${}^2f$-mode. When the frequencies of these two modes are sufficiently close, the weakly radiating quasi-radial $2 \cdot F$-mode transfers some of its kinetic energy to the strongly radiating quadrupolar ${}^2f$-mode, leading to a considerable increase in $|h|_{\max}$. Thirdly, we have proposed a simple explanation for the strong damping of the post-bounce pulsations seen for a sub-set of our models. Our analysis reveals that that these models are all both rotating close to the Kepler limit and also undergoing large-amplitude post-bounce pulsations, resulting in significant mass shedding from the stellar surface close to the equator. As already discussed by [392], this ejection of loosely bound matter is very efficient in the damping quasi-radial pulsations.

In order to assess the prospects for the detection of phase-transition-induced collapse events by gravitational wave interferometers, special attention has been paid to making an accurate calculation of the gravitational wave emission resulting from this scenario. We find that the dimensionless gravitational wave strain h from a source at a distance of $10\ \mathrm{Mpc}$ ranges between 0.1 to 2.4×10^{-23} for all of the models considered and that the total energy emitted in gravitational waves during first $50\ \mathrm{ms}$ of evolution is between 10^{-6} and $10^{-4} M_\odot c^2$, corresponding to 2×10^{48} and $2 \times 10^{50}\ \mathrm{erg}$, respectively. These numbers are considerably smaller than those presented by [233] for their Newtonian calculations and so are disappointing for the prospects of detecting these sources. The damping times for the post-bounce oscillations, as computed from the gravitational radiation waveform, range from 8 to $687\ \mathrm{ms}$ for the F-mode, and from 18 to $130\ \mathrm{ms}$ for the ${}^2f$-mode. For all of the models considered, we have also calculated the characteristic frequency f_{c}, the characteristic strain h_{c}, and the signal-to-noise ratio for current and future detectors. For current detectors such as LIGO or VIRGO, all of the models (except one) have a signal-to-noise ratio above 1 for a source at $10\ \mathrm{kpc}$. For the advanced LIGO detector, the signal-to-noise ratio rises to well above 10 for a source at $10\ \mathrm{kpc}$ for all of the models and reaches almost 400 when mode resonance is active. However, for detecting sources within the Virgo cluster at a distance of $20\ \mathrm{Mpc}$, which is probably necessary in order to reach a realistic event rate, third generation detectors would be needed.

In conclusion, we note that while our study represents an improvement over previous ones, it still lacks a number of very important aspects which would be necessary for a properly realistic modelling of these objects. Firstly, there is the treatment of the phase transformation itself which remains extremely crude, containing no detailed picture of the transformation of the material, the local heat input or the emission of neutrinos or photons. A consistent treatment of radiative transfer is likely to be essential for following the cooling phase of the newly formed hybrid quark star and could highlight that the radiative losses would produce differences in the specific-entropy stratification and hence trigger real convection. Also, in our discussion, we have been considering the phase transition as occurring by means of a detonation; the conclusions would be drastically altered if it takes place instead via a slow deflagration. A second aspect concerns the treatment of the standard neutron-star matter: while using a gamma-law equation of state to model this can be reasonable for some simplified calculations, it gives an extremely poor approximation to the complex physics actually occurring in real neutron stars. Thirdly, we have not been considering the influence of magnetic fields, which would probably not significantly affect the dynamics, but could lead to a dramatic modification of the phase transition process itself [243]. It is clear that future studies will need to take these aspects into account.

3.7 Appendix A: Finite time for the initial phase-transformation

In the study by LCCS, it was assumed that the timescale of the phase transition is much smaller than the hydrodynamic timescale for a NS, which is roughly $0.1\ \mathrm{ms}$. They then ignored the finite velocity of the conversion process and instead induced the phase transition by instantaneously replacing the initial polytropic EoS by one including the quark matter, which gives a lower pressure.

However, since the timescale for the phase transition even to two-flavour quark matter can be as long as $0.05\ \mathrm{ms}$ within our picture (which is comparable to the hydrodynamic timescale), it is far from clear that treating it as instantaneous will not significantly affect the subsequent dynamics of the forming HQS. To check on this, we performed simulations for a set of representative collapse models in which we take the initial phase transformation to occur gradually over a finite timescale with the values of ρ_{nm} and ρ_{qm} in Eqs. (3.5, 3.6) depending on the time t according to

$$\begin{aligned}
\rho_{\mathrm{hm}}(t) &= \begin{cases} \rho_{\mathrm{c}} - \dfrac{t}{\tau_{\mathrm{conv}}}(\rho_{\mathrm{c}} - \rho_{\mathrm{hm}}) & \text{for } t < \tau_{\mathrm{conv}}, \\ \rho_{\mathrm{hm}} & \text{for } t \geq \tau_{\mathrm{conv}}, \end{cases} \\
\rho_{\mathrm{qm}}(t) &= \begin{cases} \rho_{\mathrm{qm}} + \rho_{\mathrm{c}} - \rho_{\mathrm{hm}} & \text{for } t < \tau_{\mathrm{conv}}, \\ \qquad - \dfrac{t}{\tau_{\mathrm{conv}}}(\rho_{\mathrm{c}} - \rho_{\mathrm{hm}}) & \\ \rho_{\mathrm{qm}} & \text{for } t \geq \tau_{\mathrm{conv}}, \end{cases}
\end{aligned} \tag{3.12}$$

where τ_{conv} is the timescale of the initial phase transformation and ρ_{c} is the central rest-mass density. This means that $\rho_{\mathrm{hm}}(t)$ starts initially at ρ_{c} and then evolves linearly with time to reach its final value ρ_{hm} at $t = \tau_{\mathrm{conv}}$, while $\rho_{\mathrm{qm}}(t)$ has a similar behaviour shifted by $\rho_{\mathrm{qm}} - \rho_{\mathrm{hm}}$. For this test we set the timescale equal to the approximate upper limit for a detonation type phase transition, $\tau_{\mathrm{conv}} = 0.05\ \mathrm{ms}$, and compared the results obtained with those for the regular models (corresponding to $\tau_{\mathrm{conv}} = 0\ \mathrm{ms}$).

We expected that having the initial phase transformation occuring gradually in this way would produce a time lag of the same order as τ_{conv} in the initial contraction and give a less violent bounce occuring at a lower density with post-bounce pulsations of smaller amplitude than before. All of this was indeed the case for the models which we investigated, as can be seen in Fig. 3.25, where we show the time evolution of the central rest-mass density ρ_{c} for the representative model CA5 with $\tau_{\mathrm{conv}} = 0$ and $0.05\ \mathrm{ms}$. The

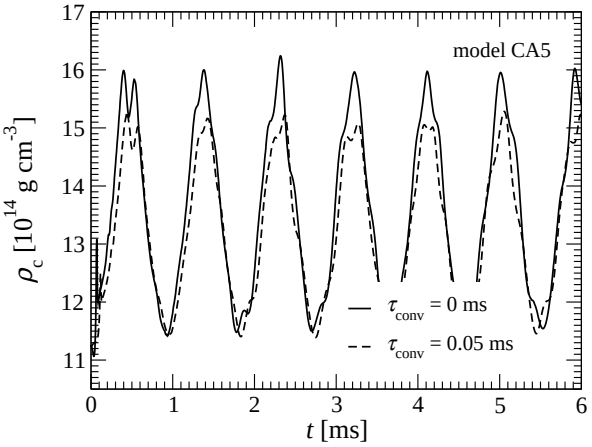

Figure 3.25: Time evolution of the central rest-mass density $\rho_{\rm c}$ for the GR collapse model CA5 with $\tau_{\rm conv} = 0\,{\rm ms}$ (solid line) and $\tau_{\rm conv} = 0.05\,{\rm ms}$ (dashed line).

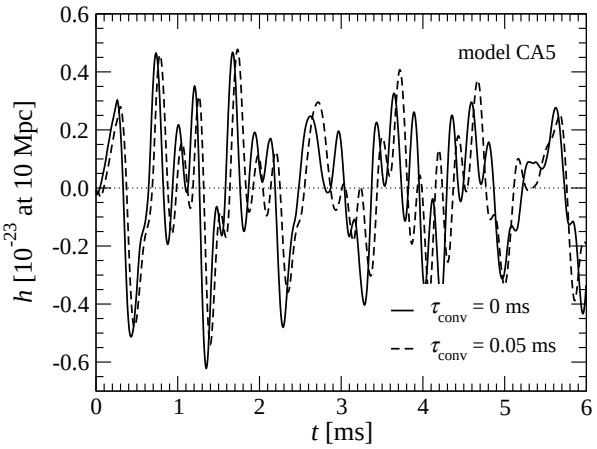

Figure 3.26: Time evolution of the GW strain h at a distance of $10\,{\rm Mpc}$ for the GR collapse model CA5 with $\tau_{\rm conv} = 0\,{\rm ms}$ (solid line) and $\tau_{\rm conv} = 0.05\,{\rm ms}$ (dashed line).

waveform of the emitted GWs remains essentially unaltered except for a small reduction in the first large amplitude peaks and the expected phase shift (see Fig. 3.26). As the final HQS is less compact in the case of a noninstantaneous phase transition due to the less dynamic initial contraction, the frequencies of the predominantly excited quasi-normal modes, the F- and ${}^2f$-mode, are modified only slightly, changing from 1.09 to $1.12\,{\rm kHz}$ and from 2.04 to $2.06\,{\rm kHz}$, giving relative changes of 3% and 1%, respectively.

The result that the differences seen when the finite $\tau_{\rm conv}$ is introduced are so small is a direct consequence of $\tau_{\rm conv} = 0.05\,{\rm ms}$ still being about an order of magnitude smaller than the collapse timescale in the case of an instantaneous initial phase transformation (although it is of the same order as the *dynamical* timescale). The collapse timescale can be approximated by the time of bounce, which is $0.40\,{\rm ms}$ for model CA5 and takes similar values for all of the other models. Since the choice $\tau_{\rm conv} = 0.05\,{\rm ms}$ is an upper limit within our picture, we conclude that the taking $\tau_{\rm conv} = 0\,{\rm ms}$ for our regular collapse models was reasonable, giving values for quantities such as $\rho_{\rm c,b}$, $|h|_{\rm max}$, f_F and $f_{^2f}$ that are upper, but close, limits for a detonation type phase-transition-induced collapse of a NS to a HQS.

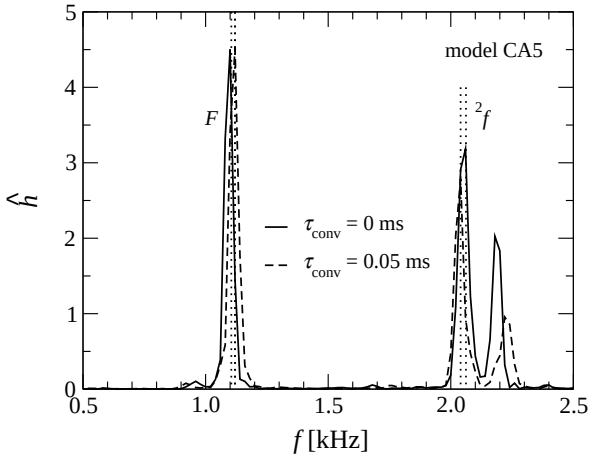

Figure 3.27: Power spectrum $\hat{h}$ (in arbitrary units) of the GW strain h for the GR collapse model CA5 with $\tau_{\rm conv} = 0\,{\rm ms}$ (solid line) and $\tau_{\rm conv} = 0.05\,{\rm ms}$ (dashed line).

3.8 Appendix B: Calculation of the damping times of the waveforms

In order to determine the damping times for the GW emission we apply a curve fitting method to the numerically-obtained waveform: the waveform is fitted by a series of damped sinusoids,

$$A_{20}^{\rm E2} = \sum_{i=0}^{n} A_i\, e^{-t/\tau_i}\, \cos(2\pi f_i t + \phi_i). \tag{3.13}$$

The parameters of this series (the damping times τ_i, the amplitudes A_i and the phases ϕ_i) are fixed by finding the best fitting curve. Depending on the model, we use $n = 4-5$ terms for the fitting procedure.

Note that this method of determining the damping times is more general than that presented in LCCS, where the series consisted of only two terms, so that only the fundamental $l = 0$ and $l = 2$ modes are taken into account, which leads to some inaccuracies at early post-bounce times when higher frequency modes in the GW signal are present. Also, they take $A_1 = A_2$ and $\phi_i = 0$, which may not be the case in general. With our approach we are able fit the original waveform with the correlation coefficient between the numerical data and Eq. (3.13) exceeding 0.99 for all models, whereas the method used by LCCS gives a correlation coefficient of less than 0.9 for some models.

Assuming that the GW signal is essentially a linear combination of the F-mode and the ${}^2f$-mode, approximating each of them as a damped sinusoid and using knowledge of the mode frequencies f_F and f_{2f}, the amplitudes A_1 and A_2, and the phases ϕ_1 and ϕ_2, one can obtain the value of the characteristic GW strain $h_{\rm c}$ for an *arbitrary* emission time using simple scaling laws. For a single damped sinusoid,

$$h = h_0\, e^{-t/\tau} \sin\left(2\pi f t - \phi\right) \tag{3.14}$$

where h_0 is the amplitude, τ is the damping timescale, f is the frequency and ϕ is the phase. If $h_{\rm c}$ is known for some emission time $t_{\rm f}$, then its value for a multiple n of the original emission time can be calculated as

$$h_{\rm c}(n\, t_{\rm f}) = h_{\rm c}(t_{\rm f}) \sqrt{\frac{1 - e^{-2nt_{\rm f}/\tau}}{1 - e^{-2t_{\rm f}/\tau}}}, \tag{3.15}$$

provided that $f^{-1} \ll \tau$ (which is fulfilled for most of our models) and the power spectral density S_h of the detector is reasonably constant in the vicinity of f. For an undamped sinusoid with $\tau = \infty$, Eq. (3.15) gives

$h_{\rm c}(n\,t_{\rm f}) = \sqrt{n}\,h_{\rm c}$ as expected; in other words, $h_{\rm c}$ scales like the square root of the number of cycles in the GW signal. In the limit of infinite emission time, but with finite τ, the exponential damping of the signal results in a finite value for the total characteristic GW strain,

$$h_{\rm c}(t=\infty) = h_{\rm c}(t_{\rm f})\,\frac{1}{\sqrt{1-e^{-2t_{\rm f}/\tau}}}, \tag{3.16}$$

For many of our models, we have F-mode damping times τ_F which are much longer than $t_{\rm f}$. On these timescales, other damping mechanisms such as physical viscosity or GW back-reaction (which are not taken into account in our study) could become important. We therefore do not give values of the total characteristic GW strain $h_{\rm c}(t=\infty)$ for our models.

Chapter 4

Accretion-induced collapse of white dwarfs

4.1 Introduction

Single stars with main-sequence masses $M \lesssim 100\,M_\odot$ end their nuclear-burning lives as electron-degenerate objects or with central electron-degenerate cores. More specifically, the end state is a carbon-oxygen or oxygen-neon white dwarf (WD) in the case of low-mass stars (i.e., with $M \lesssim 6 - 8\,M_\odot$), or a degenerate oxygen-neon or iron core embedded in an extended non-degenerate stellar envelope in the case of more massive stars (i.e., $6 - 8\,M_\odot \lesssim M \lesssim 100\,M_\odot$) (see, e.g., [187, 448, 334] and references therein). Electron-degenerate spherically-symmetric objects become unstable to radial contraction once their mass exceeds the Chandrasekhar mass which, assuming zero temperature and no rotation, is given by $M_{\rm Ch} = 1.4575\,(Y_e/0.5)^2\,M_\odot$, where Y_e is the number of electrons per baryon, or "electron fraction" [95, 370]. The *effective* Chandrasekhar mass $M_{\rm Ch,eff}$ of a WD or a stellar core increases somewhat with WD/core entropy (e.g., [448]) and can grow considerably by rotation, in which case it is limited only by the onset of nonaxisymmetric instability (e.g., [305, 456, 370]).

The iron core of a massive star is pushed over its Chandrasekhar limit by the ashes of silicon shell burning and undergoes collapse to a protoneutron star (PNS), accelerated by photodisintegration of heavy nuclei and electron capture [48]. In a high-density sub-$M_{\rm ch}$ oxygen-neon core of a less massive star, electron capture may decrease $M_{\rm Ch,eff}$, also leading to collapse [294, 179]. In both cases, if an explosion results, the observational display is associated with a Type II/Ibc supernova (SN).

On the other hand, a carbon-oxygen WD can be pushed over its stability limit through merger with or accretion from another WD (double-degenerate scenario) or by accretion from a non-degenerate companion star (single-degenerate scenario). Here, the WD generally experiences carbon ignition and thermonuclear runaway, leading to a Type Ia SN and leaving no compact remnant [238]. However, at least theoretically, it is possible that massive oxygen-neon WDs[1] formed by accretion or merger, and, depending on initial mass, temperature, and accretion rate, also carbon-oxygen WDs, may grow to reach their $M_{\rm Ch,eff}$ or reach central densities sufficiently high ($\gtrsim 10^{9.7} - 10^{10}\,{\rm g\,cm^{-3}}$) for rapid electron capture to take place, triggering collapse to a PNS rather than thermonuclear explosion [83, 359, 295, 273, 297, 360, 425, 361, 456, 455, 454, 204, 179]. This may result in a peculiar, in most cases probably sub-energetic, low-nickel-yield and short-lived transient [295, 445, 157, 111, 113, 265]. This alternative to the Type Ia SN scenario is called *"accretion-induced collapse"* (AIC) and will be the focus of this chapter.

The details of the progenitor WD structure and formation and the fraction of all WDs that evolve to AICs are presently uncertain. Binary population synthesis models [459, 39, 204] and constraints on r-

[1] Previously, such WDs were expected to have a significant central $^{24}{\rm Mg}$ mass fraction, hence were referred to as oxygen-neon-magnesium WDs. Recent work based on up-do-date input physics and modern stellar evolution codes suggests that the mass fraction of $^{24}{\rm Mg}$ is much smaller than previously thought (e.g., [380, 195, 347]).

process nucleosynthetic yields from previous AIC simulations [157, 336] predict AIC to occur in the Milky Way at a frequency of $\sim 10^{-5}$ to $\sim 10^{-8}\,\mathrm{yr}^{-1}$ which is $\sim 20-50$ times less frequent than the expected rate of standard Type Ia SNe (e.g., [427, 247, 365, 251]). In part as a consequence of their rarity, but probably also due to their short duration and potentially weak electromagnetic display, AIC events have not been directly observed (but see [325], who discovered a peculiar type-Ib SN in NGC 1032 that can be interpreted as resulting from an AIC).

The chances of seeing a rare galactic AIC are dramatically boosted by the possibility of guiding electromagnetic observations by the detection of neutrinos and gravitational waves (GWs) emitted during the AIC process and a subsequent SN explosion. GWs, similar to neutrinos, are extremely difficult to observe, but can carry "live" dynamical information from deep inside electromagnetically-opaque regions. The inherent multi-D nature of GWs (they are lowest-order quadrupole waves) makes them ideal messengers for probing multi-D dynamics such as rotation, turbulence, or NS pulsations [414, 14, 316]. The detection prospects for a GW burst from an AIC are significantly enhanced if theoretical knowledge of the expected GW signature of such an event is provided by computational modelling. In reverse, once a detection is made, detailed model predictions will make it possible to extract physical information on the AIC dynamics and the properties of the progenitor WD and, hence, will allow "parameter-estimation" of the source.

Early spherically-symmetric (1D) simulations of AIC [260, 30, 445] and more recent axisymmetric (2D) ones [157, 111, 113] have demonstrated that the dynamics of AIC is quite similar to standard massive star core collapse: During collapse, the WD separates into a subsonically and homologously collapsing ($v \propto r$) inner core and a supersonically collapsing outer core. Collapse is halted by the stiffening of the equation of state (EOS) at densities near nuclear matter density and the inner core rebounds into the still infalling outer core. An unshocked low-entropy PNS of inner-core material is formed. At its edge, a bounce shock is launched and initially propagates rapidly outward in mass and radius, but loses energy to the dissociation of heavy nuclei as well as to neutrinos that stream out from the optically thin postshock region. The shock stalls and, in the AIC case (but also in the case of the oxygen-neon core collapse in super-AGB stars [207, 80]), is successfully revived by the deposition of energy by neutrinos in the postshock region (i.e., the "delayed-neutrino mechanism" [47, 48]) or by a combination of neutrino energy deposition and magnetorotational effects in very rapidly rotating WDs [113]. But even without shock revival, explosion would occur when the WD surface layer is eventually accreted through the shock. Following the onset of explosion, a strong long-lasting neutrino-driven wind blows off the PNS surface, adding to the total explosion energy and establishing favorable conditions for r-process nucleosynthesis [445, 157, 111, 113, 15]. If the progenitor WD was rotating rapidly (and had a rotationally-enhanced $M_{\mathrm{Ch,eff}}$), a quasi-Keplerian accretion disk of outer-core material may be left after the explosion [111]. Metzger et al. [264, 265] recently proposed that this may lead to nickel-rich outflows that could significantly enhance the AIC observational display.

Rotating iron core collapse and bounce is the most extensively studied and best understood GW emission process in the massive star collapse context (see, e.g., [123] and the historical overview in [316]). However, most massive stars (perhaps up to $\sim 99\%$ in the local universe) are likely to be rather slow rotators that develop little asphericity during collapse and in the early postbounce phase [185, 450, 309] and produce PNSs that cool and contract to neutron stars with periods above $\sim 10\,\mathrm{ms}$ and parameter $\beta = E_{\mathrm{rot}}/|W| \lesssim 0.1\%$ [309], where E_{rot} is the rotational kinetic energy and $|W|$ is the gravitational binding energy. This does not only reduce the overall relevance of this emission process, but also diminishes the chances for postbounce gravito-rotational nonaxisymmetric deformation of the PNS which could boost the overall GW emission [316]. Axisymmetric rapidly rotating stars become unstable to nonaxisymmetric deformations if a nonaxisymmetric configuration with a lower total energy exists at a given β (see [391] for a review). The classical high-β instability develops in Newtonian stars on a dynamical timescale at $\beta \gtrsim \beta_{\mathrm{dyn}} \simeq 27\%$ (the general-relativistic value is $\beta \gtrsim 25\%$ [22, 250]). A "secular" instability, driven by fluid viscosity or GW backreaction, can develop already at $\beta \gtrsim \beta_{\mathrm{sec}} \simeq 14\%$ [391]. Slower, but strongly differentially rotating stars

may also be subject to a nonaxisymmetric dynamical instability at β as small as $\sim 1\%$. This instability at low β was observed in a number of recent 3D simulations (e.g., [90, 377, 307, 318, 310, 93, 311, 312, 367]), and may be related to corotation instabilities in disks, but its nature and the precise conditions for its onset are presently not understood [435, 357].

Stellar evolution theory and pulsar birth spin estimates suggest that most massive stars are rotating rather slowly (e.g., [185, 309], but also [84, 450] for exceptions). Hence, rotating collapse and bounce and nonaxisymmetric rotational instabilities are unlikely to be the dominant GW emission mechanisms in most massive star collapse events [316]. The situation may be radically different in AIC: Independent of the details of their formation scenario, AIC progenitors are expected to accrete significant amounts of mass and angular momentum in their pre-AIC evolutions [456, 361, 455, 425, 330]. They may reach values of β of up to $\sim 10\%$ *prior* to collapse, according to the recent work of Yoon & Langer [456, 455], who studied the precollapse stellar structure and rotational configuration of WDs with sequences of 2D rotational equilibria. Depending on the distribution of angular momentum in the WD, rotational effects may significantly affect the collapse and bounce dynamics and lead to a large time-varying quadrupole moment of the inner core, resulting in a strong burst of GWs emitted at core bounce. In addition, the postbounce PNS may be subject to the high-β rotational instability (see [236, 237] for an investigation via equilibrium sequences of PNSs formed in AIC) or to the recently discovered low-β instability.

Most previous (radiation-)hydrodynamic studies of AIC have either been limited to 1D [260, 30, 445] or were 2D, but did not use consistent 2D progenitor models in rotational equilibrium [157]. Fryer, Hughes and Holz [160] presented the first estimates for the GW signal emitted by AIC based on one model of [157]. Drawing from the Yoon & Langer AIC progenitors [456, 455], Dessart et al. [111, 113] have recently performed 2D Newtonian AIC simulations with the multi-group flux-limited diffusion (MGFLD) neutrino radiation-(M)HD code VULCAN/2D [239, 241, 81]. They chose two representative WD configurations for slow and rapid rotation with central densities of $5 \times 10^{10}\ \mathrm{g\,cm^{-3}}$ and total masses of $1.46 M_\odot$ and $1.92 M_\odot$. Both models were set up with the differential rotation law of [456, 455]. The $1.46 M_\odot$ model had zero rotation in the inner core and rapid outer core rotation while the $1.92 M_\odot$ was rapidly rotating throughout (ratio $\Omega_{\mathrm{max,initial}}/\Omega_{\mathrm{center,initial}} \sim 1.5$). Dessart et al. [111, 113] found that rapid electron capture in the central regions of both models led to collapse to a PNS within only a few tens of milliseconds and reported successful neutrino-driven [111] and magnetorotational explosions [113] with final values of β (i.e., a few hundred milliseconds after core bounce) of $\sim 6\%$ and $\sim 26\%$, for the $1.46 M_\odot$ and $1.92 M_\odot$ models, respectively[2]. The analysis in [111, 310, 316] of the GW signal of the Dessart et al. models showed that the morphology of the AIC rotating collapse and bounce gravitational waveform is reminiscent of the so-called Type III signal first discussed by Zwerger & Müller [466] and associated with small inner core masses and a large pressure reduction at the onset of collapse in the latter's polytropic models.

In this work, we follow a different approach than Dessart et al. [111, 113]. We omit their detailed and computationally-expensive treatment of neutrino radiation transport in favor of a simple, yet effective deleptonization scheme for the collapse phase [229]. This simplification, while limiting the accuracy of our models at postbounce times $\gtrsim 5 - 10\,\mathrm{ms}$, (i) enables us to study a very large set of precollapse WD configurations and their resulting AIC dynamics and GW signals and, importantly, (ii) allows us to perform these AIC simulations in *general relativity*, which is a crucial ingredient for the accurate modeling of dynamics in regions of strong gravity inside and near the PNS. Furthermore, as demonstrated by [118, 122, 123], general relativity is required for qualitatively and quantitatively correct predictions of the GW signal of rotating core collapse.

We focus on the collapse and immediate postbounce phase of AIC and perform an extensive set of 114 2D general-relativistic hydrodynamics simulations. We analyze systematically the AIC dynamics and the

[2]These numbers are for the non-MHD simulations of [111]. In the MHD models of [113], an Ω-dynamo builds up toroidal magnetic field, reducing the overall rotational energy and β.

properties of the resulting GW signal. We explore the dependence of nonrotating and rotating AIC on the precollapse WD rotational setup, central density, core temperature, and core deleptonization, and study the resulting PNS's susceptibility to rotational nonaxisymmetric deformation. Furthermore, motivated by the recent work of Metzger et al. [264, 265], who discussed the possible enhancement of the AIC observational signature by outflows from PNS accretion disks, we study the dependence of disk mass and morphology on WD progenitor characteristics and rotational setup.

We employ the general-relativistic hydrodynamics code CoCoNuT [118, 119] and neglect MHD effects since they were shown to be small in the considered phases unless the precollapse magnetic field strength is extremely large ($B \gtrsim 10^{12}\,\mathrm{G}$, e.g., [302, 113, 79]). We employ a finite-temperature microphysical nuclear EOS in combination with the aforementioned deleptonization treatment of [229]. The precollapse 2D rotational-equilibrium WDs are generated according to the prescription of Yoon & Langer [456, 455].

The plan of the rest of this chapter is as follows. In Sec. 4.2, we introduce the numerical methods employed and discuss the generation of our 2D rotational-equilibrium precollapse WD models as well as the parameter space of WD structure and rotational configuration investigated. In Sec. 4.3, we discuss the overall AIC dynamics and the properties of the quasi-Keplerian accretion disks seen in many models. Sec. 4.4 is devoted to a detailed analysis of the GW signal from rotating AIC. There, we also assess the detectability by current and future GW observatories and carry out a comparison of the GW signals of AIC and massive star iron core collapse. In Sec. 4.5, we study the postbounce rotational configurations of the PNSs in our models and assess the possibility for nonaxisymmetric rotational instabilities. In Sec. 4.6, we present a summary of our results.

4.2 Methods and initial models

4.2.1 The general-relativistic hydrodynamics Code

We perform our simulations in $2+1$ dimensions using the CoCoNuT code [117, 119] which adopts the conformally-flat approximation of general relativity [196]. This has been shown to be a very good approximation in the context of stellar collapse to PNSs [311, 312, 91]. For the computational grid, we choose 250 logarithmically-spaced, centrally-condensed radial zones with a central resolution of 250 m and 45 equidistant angular zones covering 90°. We have performed test calculations with different grid resolutions to ascertain that the grid setup specified above is appropriate for our simulations. The space between the surface of the star and outer boundary of the finite difference grid is filled with an artificial atmosphere. We assume a constant density and stationary atmosphere in all zones where density drops below a prescribed threshold of $7 \times 10^5\,\mathrm{g\,cm^{-3}}$, a value marginally larger than the lowest density value in the EOS table employed in our calculations (cf. Sec. 4.2.1). For further details of the formulations of the hydrodynamics and metric equations as well as their numerical implementation in CoCoNuT, the reader is referred Section 2.3 and to papers by [123, 119, 107].

The version of CoCoNuT employed in this study does not include a nuclear reaction network. Hence, we, like Dessart et al. [111, 113], ignore nuclear burning which may be relevant in the outer core of AIC progenitors where material is not in nuclear statistical equilibrium (NSE), but still sufficiently hot for oxygen/neon/magnesium burning to occur. This approximation is justified by results from previous work of [445, 207] who included nuclear burning and did not observe a strong dynamical effect.

Equation of state

We make use of the finite-temperature nuclear EOS of Shen et al. ("Shen-et-al EOS" in the following, [372, 373]) which is based on a relativistic mean-field model and is extended with the Thomas-Fermi

approximation to describe the homogeneous phase of matter as well as the inhomogeneous matter composition. The parameter for the incompressibility of nuclear matter is 281 MeV and the symmetry energy has a value of 36.9 MeV. The Shen-et-al EOS is used in tabulated fashion and in our version (equivalent to that used in [252, 123]) includes contributions from baryons, electrons, positrons and photons.

The Shen-et-al EOS table used in our simulation has 180, 120, and 50 equidistant points in $\log_{10}\rho$, $\log_{10}T$, and Y_e, respectively. The table ranges are $6.4\times10^5\,\mathrm{g\,cm^{-3}} \leq \rho \leq 1.1\times10^{15}\,\mathrm{g\,cm^{-3}}$, $0.1\,\mathrm{MeV} \leq T \leq 100.0\,\mathrm{MeV}$, and $0.015 \leq Y_e \leq 0.56$. Our variant of the Shen-et-al EOS assumes that NSE holds throughout the entire $\{\rho, T, Y_e\}$ domain. In reality, NSE generally holds only at $T \gtrsim 0.5$ MeV. At lower temperatures, a nuclear reaction network and, the advection of multiple chemical species and accounting for their individual ideal-gas contributions to the EOS is necessary for a correct thermodynamic description of the baryonic component of the fluid. However, since the electron component of the EOS is vastly dominant in the central regions of AIC progenitors (and also in the central regions of iron cores), the incorrect assumption of NSE at low temperatures can lead to only a small error in the overall (thermo)dynamics of the collapse and early postbounce phase.

Deleptonization during collapse and neutrino pressure

To account for the dynamically highly important change of the electron fraction Y_e by electron capture during collapse, we employ the approximate prescription proposed by Liebendörfer [229]. Liebendörfer's scheme is based on the observation that the local Y_e of each fluid element during the contraction phase can be rather accurately parametrized from full radiation-hydrodynamics simulations as a function of density alone. Liebendörfer demonstrated the effectiveness of this parametrization in the case of spherical symmetry, but also argued that it should still be reliable to employ a parametrization $\overline{Y_e}(\rho)$ obtained from a 1D radiation-hydrodynamics calculation in a 2D or 3D simulation, since electron capture depends more on local matter properties and less on the global dynamics of the collapsing core. On the basis of this argument, a $\overline{Y_e}(\rho)$ parametrization was applied in the rotating iron core collapse calculations of [311, 312, 122, 123, 367]. Here, we use the same implementation as discussed in [123] and track the changes in Y_e up to the point of core bounce. After bounce, we simply advect Y_e. Furthermore, as in [123], we approximate the pressure contribution due to neutrinos in the optically-thick regime ($\rho \gtrsim 2\times10^{12}\,\mathrm{g\,cm^{-3}}$) by an ideal Fermi gas, following the prescription of [229]. This pressure contribution and the energy of the trapped neutrino radiation field are included in the matter stress-energy tensor and coupled with the hydrodynamics equations via the energy and momentum source terms specified in [312].

The deleptonization scheme described here is applicable only until core bounce and can neither track the postbounce neutrino burst (see, e.g., [410]) nor neutrino cooling/heating and the postbounce deleptonization of the PNS. The dynamics in the very early postbounce evolution (up to $\sim 10\,\mathrm{ms}$) are unlikely to be dramatically affected by this limitation, but it should be kept in mind when interpreting results from later postbounce times.

For our AIC simulations we obtain $\overline{Y_e}(\rho)$ data from the 2D Newtonian radiation-hydrodynamics simulations carried out by Dessart et al. [111] with the VULCAN/2D code [79, 239, 241] in its MGFLD variant. We use these data because of their ready availability, but point out that the microphysics [77] used in VULCAN/2D does not yet include the updated electron capture rates of [219]. Moreover, VULCAN/2D presently does not treat velocity-dependent terms in the transport equation and neglects neutrino–electron scattering, both of which my have some impact on the evolution of Y_e in the collapse phase [410, 71]. In Fig. 4.1 we plot representative $\overline{Y_e}(\rho)$ trajectories obtained from VULCAN/2D AIC simulations. At nuclear density, these data predict $Y_e \sim 0.18$ which is low compared to $Y_e \gtrsim 0.22 - 0.26$ seen in simulations of iron core collapse [71, 410, 229, 123] and oxygen-neon core collapse [207]. This difference is not fully understood, but (*i*) could be physical and due to the WD initial data used here and in [111] or (*ii*) may be related to

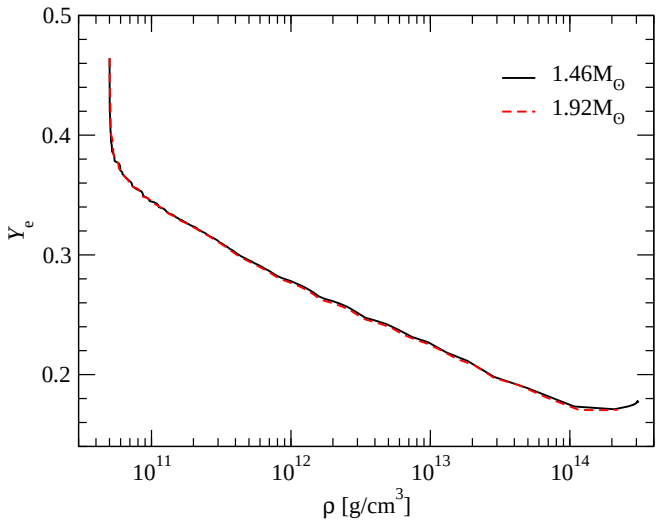

Figure 4.1: Average electron fraction Y_e in the innermost 2 km in the collapsing WD as a function of density obtained from 2D MGFLD simulations with the VULCAN/2D code for models $1.46 M_\odot$ and $1.92 M_\odot$ of Dessart et al. [111]. Both models were set up with the same initial dependence of temperature on density and a temperature $T_0 = 1.0 \times 10^{10}$ K (see Sec. 4.2.2 for details).

the radiation transport approximations and microphysics treatment in VULCAN/2D. To measure the importance of these uncertainties in $\overline{Y_e}(\rho)$, we perform calculations with systematic variations of $\overline{Y_e}(\rho)$ due either to changes in the precollapse WD temperature or to an ad-hoc scaling (see Sec. 4.2.3).

Since AIC progenitors may be extremely rapidly rotating, it is not clear that the $\overline{Y_e}(\rho)$ parametrization is indeed independent of the specific model and rotational setup. The $\overline{Y_e}(\rho)$ trajectories shown in Fig. 4.1 result from the collapse simulations of the slowly rotating $1.46\,M_\odot$ model and of the rapidly rotating $1.92\,M_\odot$ model of Dessart et al. The very close agreement of the two curves suggests that rotational effects have only a small influence on the prebounce deleptonization and confirm the supposition of [229] at the level of the MGFLD and microphysics treatment in VULCAN/2D. All $\overline{Y_e}(\rho)$ data used in this study are available from [387].

4.2.2 Precollapse white dwarf models

For constructing 2D WD models in rotational equilibrium with a given rotation law, we follow [455] and employ the self-consistent field (SCF) method [304, 305, 180, 209] in Newtonian gravity. For the purpose of the SFC method, we assume that the WD is cold and has a constant Y_e of 0.5. After finding the 2D equilibrium configuration, we impose a temperature and Y_e distribution motivated by previous work [111, 445]. Ideally, the WD initial model should be evolved in a multi-dimensional stellar evolution code with a finite-temperature EoS and accounting for weak processes such as neutrino cooling and electron capture. Due to the unavailability of such self-consistent AIC progenitors, we resort to the treatment that we discuss in detail in the remainder of this section.

Implementation of the self-consistent field Method

Our implementation of the Newtonian SFC method has been tested by reproducing the WD models presented in [180, 455], and finding excellent agreement. The compactness parameter GM/Rc^2 of the highest-density WD models considered here reaches $\sim 5 \times 10^{-3}$, hence general-relativistic effects at the precollapse stage

are small and the error introduced by Newtonian WD models is therefore negligible. Hereafter we will assume that the *Newtonian mass* of the equilibrium model represents the *baryon mass* accounted for when solving the general-relativistic equations.

The equation governing the stellar equilibrium is given by

$$\int \rho^{-1}\, dP + \Phi - \int \Omega^2\, \varpi\, d\varpi = C\,, \tag{4.1}$$

where Φ is the gravitational potential, Ω is the angular velocity, ϖ is the radial cylindrical coordinate and C is a constant that will be determined from boundary conditions using the SCF iterations as discussed below.

White dwarfs are stabilized against gravity by electron degeneracy pressure. For constructing precollapse WDs, we assume complete degeneracy for which the WD EOS (e.g., [305]) is given by

$$P = A[x(2x^2-3)(x^2+1)^{1/2} + 3\sinh^{-1} x]\,;\;\; x = (\rho/B)^{1/3}\,, \tag{4.2}$$

where $A = 6.01 \times 10^{22}$ dyn cm^{-2} and $B = 9.82 \times 10^5\, Y_e^{-1}$ g cm^{-3}. We set $Y_e = 0.5$, assuming at this stage that no electron capture has taken place. The integral $\int \rho^{-1} dP$ in Eq. (4.1) is the enthalpy H which, given our choice of WD EOS, can be expressed analytically as

$$H = \frac{8A}{B}\left[1 + \left(\frac{\rho}{B}\right)^{2/3}\right]\,. \tag{4.3}$$

With this, Eq. (4.1) trivially becomes

$$H = C - \Phi + \int \Omega^2\, \varpi\, d\varpi\,. \tag{4.4}$$

Following the SCF method, we proceed to first produce a trial density distribution $\rho(r,\theta)$ and impose a rotation law (discussed in the following Sec. 4.2.2).

We then calculate C by using the value for the maximum density and the angular velocity at the center of the star $\Omega(\varpi = 0) = \Omega_{\rm c,i}$. Based on the trial density distribution, we calculate H via Eq. (4.4) and then update the density distribution based on H using the analytic expression (4.3). This updated density distribution in turn results in a new value for H. We iterate this procedure until all the maximum absolute values of three relative differences of H, Ω and ρ become less than 10^{-3}.

Progenitor rotational configuration

Our axisymmetric progenitor WD models are assumed to be either in *uniform* rotation or to follow the *differential* rotation law proposed by Yoon & Langer [455]. The latter argued that the rotation law of a WD that accretes matter at high rates ($> 10^{-7}\, M_\odot\, {\rm yr}^{-1}$) is strongly affected by angular momentum transport via the dynamical shear instability (DSI) in the inner region, and due to the secular shear instability (as well as Eddington-Sweet circulations [409]) in the outer layers. According to their results, the shear rate in the core remains near the threshold value for the onset of the DSI. This results in a characteristic rotation law which has an absolute maximum in the angular velocity just above the shear-unstable core. We define $\varpi_{\rm p}$ as the position of this maximum. This position is linked to layers with a density as low as several percent of the WD central density so that

$$\rho_{\rm i}(\varpi = \varpi_{\rm p},\; z = 0) = f_{\rm p}\rho_{\rm c,i}, \tag{4.5}$$

and where, following [111, 455], we choose $f_{\rm p} = \{0.05,\; 0.1\}$ in our models. (Note that the differential rotation law adopted for the models of [111] had $f_{\rm p} = 0.05$). In the inner regions with $\varpi < \varpi_{\rm p}$, we have

$$\Omega(\varpi) = \Omega_{\rm c,i} + \int_0^{\varpi} \frac{f_{\rm sh}\sigma_{\rm DSI,crit}}{\varpi'} d\varpi', \tag{4.6}$$

where $\Omega_{\rm c,i}$ is the angular velocity at the center and $\sigma_{\rm DSI,crit}$ is the threshold value of the shear rate in the inner core for the onset of the DSI. $f_{\rm sh}$ is a dimensionless parameter (≤ 1.0) describing the deviation of the shear rate from $\sigma_{\rm DSI,crit}$. We compute $\sigma_{\rm DSI,crit}$ assuming homogeneous chemical composition and constant temperature, in which case $\sigma_{\rm DSI,crit}$ can be estimated as (cf. Eq.(7) of [456]):

$$\begin{aligned} \sigma^2_{\rm DSI,crit} &\simeq 0.2 \left(\frac{g}{10^9 \text{ cm s}^{-2}}\right) \\ &\times \left(\frac{\delta}{0.01}\right) \left(\frac{H_{\rm p}}{8\times 10^7 \text{ cm}}\right)^{-1} \left(\frac{\nabla_{\rm ad}}{0.4}\right) , \end{aligned} \tag{4.7}$$

where g is the free-fall acceleration, $H_{\rm p}$ is the pressure scale height ($= -dr/d\ln P$), $\nabla_{\rm ad}$ is the adiabatic temperature gradient ($= -(\partial \ln T/\partial \ln P)_s$ where s is the specific entropy) and $\delta = (\partial \ln \rho/\partial \ln T)_P$. The quantities δ, $H_{\rm p}$ and $\nabla_{\rm ad}$ are computed using the routines of Blinnikov et al. [54].

At the equatorial surface, the WD is assumed to rotate at a certain fraction $f_{\rm K}$ of the local Keplerian angular velocity $\Omega_{\rm K}$:

$$\Omega(R_{\rm e}) = f_{\rm K}\Omega_{\rm K}(R_{\rm e}), \tag{4.8}$$

where $R_{\rm e}$ is the equatorial radius of the WD and where we have set $f_{\rm K} = 0.95$. In the region between $\varpi_{\rm p}$ and $R_{\rm e}$, we again follow [455] and adopt the following rotation law:

$$\Omega(\varpi)/\Omega_{\rm K} = \Omega(\varpi_{\rm p})/\Omega_{\rm K}(\varpi_{\rm p}) + \mathcal{C}(\varpi - \varpi_{\rm p})^a , \tag{4.9}$$

where the constant $\mathcal{C}$ is determined for a given value of a as

$$\mathcal{C} = \frac{f_{\rm K} - \Omega(\varpi_{\rm p})/\Omega_{\rm K}(\varpi_{\rm p})}{(R_{\rm e} - \varpi_{\rm p})^a} . \tag{4.10}$$

The choice of the exponent a does not have a strong impact on the WD structure because of the constraints imposed by $\Omega(\varpi_{\rm p})$ and $\Omega(R_{\rm e})$ at each boundary. In our study, we adopt $a = 1.2$. For further details, we refer the reader to Sec. 2.2 of [455].

Saio & Nomoto [361] argued that turbulent viscosity resulting from a combination of a baroclinic instability (see, e.g., [324]; neglected by Yoon & Langer [456, 455]) and the DSI is so efficient in transporting angular momentum that the angular velocity becomes nearly uniform in the WD interior, while only surface layers with mass $\lesssim 0.01 M_\odot$ rotate differentially [361]. Piro [332], who also considered angular momentum transport by magnetic stresses, confirmed these results. Hence, in order to study the suggested case of uniform precollapse WD rotation, we complement our differentially rotating WD models with a set of uniformly rotating AIC progenitors.

Initial temperature profile

Because our initial models are constructed by imposing hydrostatic equilibrium (Eq. (4.1)) with a barotropic EOS (Eq. (4.2)), the WD structure is independent of temperature. However, the latter is needed as input for the finite-temperature nuclear EOS used in our AIC simulations. We follow Dessart et al. [111] and impose a scaling of the temperature with density according to

$$T(\varpi, z) = T_0 \left[\rho_{\rm c,i}/\rho(\varpi, z)\right]^{0.35} , \tag{4.11}$$

where (ϖ, z) are cylindrical coordinates and ρ_0 is the density at which the stellar temperature equals T_0.

Initial electron fraction profile

For the purpose of constructing AIC progenitor WDs in rotational equilibrium we assume that no electron capture has yet taken place and set $Y_e = 0.5$. A real AIC progenitor, however, will have seen some electron captures on Ne/Mg/Na nuclei (e.g., [179]) before the onset of dynamical collapse. In addition, electrons will be captured easily by free protons that are abundant at the temperatures of the WD models considered here. Hence, a Y_e of 0.5 is rather inconsistent with real WD evolution. Dessart et al. [111], who started their simulations with $Y_e = 0.5$ models, observed an early burst of electron capture. This led to a significant initial drop of Y_e that leveled off after $5 - 10$ ms beyond which the Y_e profile evolved in qualitatively similar fashion to what is known from iron core collapse (see Fig. 4.1 which depicts this drop of Y_e at low densities). To account for this, we adopt as initial $\overline{Y}_e(\rho)$ a parametrization obtained from the equatorial plane of the models of Dessart et al. [111] at $\sim$ 7 ms into their evolution when the initial electron capture burst has subsided. We use these $\overline{Y}_e(\rho)$ data for the Y_e evolution of the low-density ($\rho < \rho_{\rm c,i}$) part of the WD during collapse.

4.2.3 Parameter space

The structure and thermodynamics of the AIC progenitor and the resulting dynamics of the collapse depend on a variety of parameters that are constrained only weakly by theory and observation (e.g., [297, 456, 455]). Here, we study the dependence on the central density, rotational configuration and the core temperature. In the following we lay out our parameter choices and discuss the nomenclature of our initial models whose key properties we summarize in Table 4.1.

Progenitor white dwarf central density

In order to investigate the impact of the precollapse central WD density $\rho_{\rm c,i}$ on the collapse dynamics, we consider sequences of WD models with central densities in the range from $4\times10^9\,{\rm g\,cm^{-3}}$ to $5\times10^{10}\,{\rm g\,cm^{-3}}$. This range of densities is motivated by previous studies arguing that WDs in this range of $\rho_{\rm c,i}$ may experience AIC [297, 456, 111].

We therefore choose a set of four central densities, i.e., $4\times10^9,\ 1\times10^{10},\ 2\times10^{10},\ 5\times10^{10}\ {\rm g\,cm^{-3}}$, and correspondingly begin our model names with letters A, B, C, D. We perform AIC simulations of nonrotating (spherically-symmetric) WDs with central density choices A-D and restrict the rotating models to the limiting central density choices A and D.

In Fig. 4.2 we plot radial density profiles of our nonrotating WD models to show the strong dependence of the WD compactness on the choice of central density. This aspect will prove important for the understanding of the collapse dynamics of rapidly rotating models.

Progenitor white dwarf rotational configuration

Since the rotational configuration of AIC progenitor WDs is constrained only poorly, we consider uniformly rotating ($\Omega_{\rm i} = \Omega_{\rm c,i}$ everywhere) as well as a variety of differentially rotating WD configurations. To denote the general rotation type, we use the letter U (D) for uniform (differential) rotation as the second letter in each model name.

The low-density uniformly rotating model sequence AU{1-5} is set up with initial angular velocities $\Omega_{\rm c,i}$ from 1 to $3.5\,{\rm rad\,s^{-1}}$, where the latter value corresponds to rotation very close to the mass-shedding limit. The more compact uniformly-rotating sequence DU{1-7} is set up with precollapse $\Omega_{\rm c,i}$ from 2 to $9.5\,{\rm rad\,s^{-1}}$, where, again, the latter value corresponds to near-mass-shedding rotation.

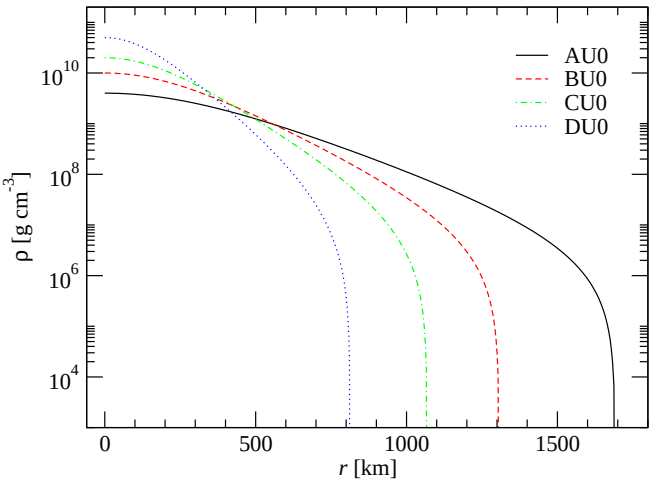

Figure 4.2: The radial profile of the rest-mass density for nonrotating white dwarf models AU0, BU0, CU0 and DU0.

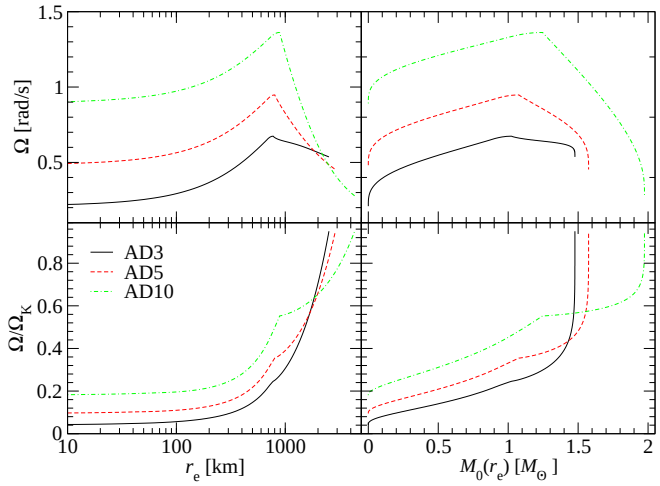

Figure 4.3: Upper panels: angular velocity as a function of equatorial radius (left panel) and enclosed mass coordinate (right panel) for three representative precollapse WD models AD3, AD5 and AD10. Lower panels: Angular velocity normalized to the local Keplerian value as a function of equatorial radius and enclosed mass for the same models.

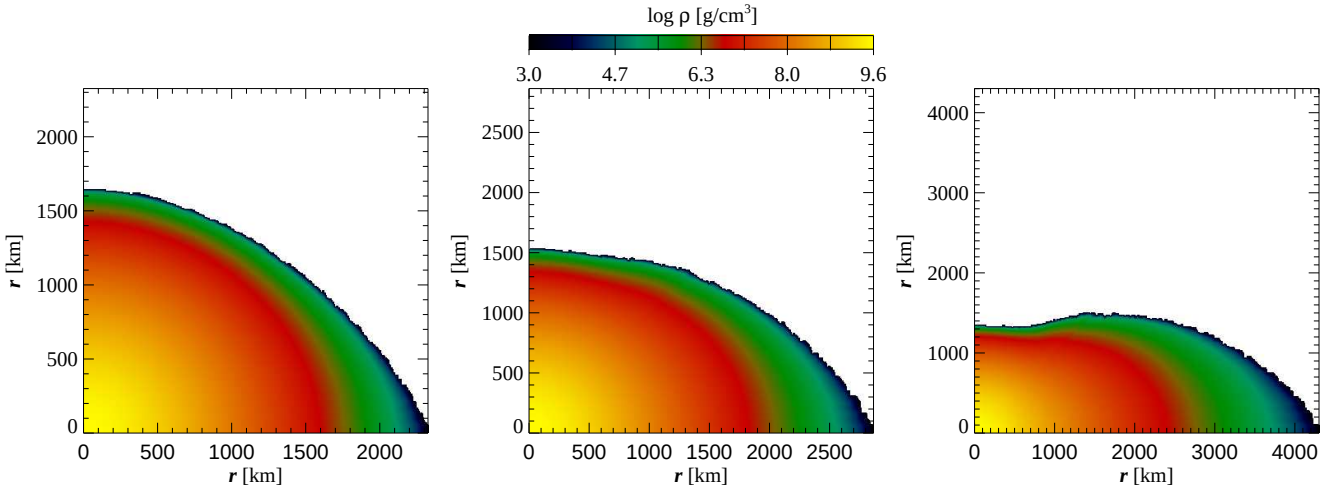

Figure 4.4: Colormap of the rest mass density for the precollapse white dwarf models AD1 (right panel) AD5 (center panel), and AD10 (right panel). The apparent ruggedness of the WD surface layers is a results of the finite resolution of our computational grid and the mapping procedure in the visualization tool. The ruggedness has no influence on the collapse and postbounce dynamics of the inner core.

Model sequences AD{1-10}, DD{1-7} are differentially rotating according to the rotation law discussed in Sec. 4.2.2 and specified by Eqs. (4.6) and (4.9), with the parameter choice $f_{\rm sh} = 1$ and $f_{\rm p} = 0.1$ for the AD sequence and $f_{\rm sh} = 1$ and $f_{\rm p} = 0.05$ for the DD sequence. We recall that $f_{\rm p}$ is the fraction of the central density where the angular velocity has a global maximum. While $f_{\rm p} = 0.1$ is the standard choice of [455], we adopt $f_{\rm p} = 0.05$ for the high-density sequence DD to be in line with the parameter choices made for the models of Dessart et al. [111]. Test calculations with AD models show that the variation of $f_{\rm p}$ between 0.05 and 0.10 affects the rotational configuration of the outer WD layers only and does not have any appreciable effect on the AIC dynamics. For the AD{1-10} sequence, we chose $\Omega_{\rm c,i}$ in the range from 0 to $5.6\,{\rm rad\,s^{-1}}$, resulting in maximum angular velocities $\Omega_{\rm max,i}$ in the range of 2.88 to $8.49\,{\rm rad\,s^{-1}}$. The higher-density DD{1-7} sequence rotates with $\Omega_{\rm c,i}$ in the range from 0 to $18\,{\rm rad\,s^{-1}}$, corresponding to maximum Ω in the range of 7.69 to $25.84\,{\rm rad\,s^{-1}}$. The values of $\Omega_{\rm c,i}$ and $\Omega_{\rm max,i}$ for the individual AD and DD models are given in Table 4.1. As representative examples resulting from our assumed rotation law, we plot in Fig. 4.3 for models AD3, AD5, and AD10 the angular velocity and the ratio of the angular velocity to the local Keplerian value as a function of cylindrical radius and of the enclosed rest mass. In Fig. 4.4, we plot the colormaps of the rest mass density on the $r-\theta$ plane for the representative precollapse WD models AD1, AD5 and AD10.

In order to study the effect of variations in the degree of differential rotation, we vary the dimensionless shear parameter $f_{\rm sh}$ for a subsequence of AD models and append suffices $f\{1-4\}$ to their names corresponding to $f_{\rm sh} = \{0.8, 0.6, 0.4, 0.2\}$, respectively. Figure 4.5 shows the behavior of the initial angular velocity distribution with decreasing $f_{\rm sh}$ in the rapidly differentially rotating model AD10.

An important point to mention is the large range of precollapse WD masses covered by our models. Depending on the initial central density and the rotational setup, our WDs masses range from a sub-$M_{\rm Ch}$ value of $1.39\,M_\odot$ in the nonrotating low-$\rho_{\rm c,i}$ model AU0 to a rotationally-supported super-$M_{\rm Ch}$ mass of $2.05\,M_\odot$ in the rapidly differentially rotating model AD13f4. The maximum mass in our sequence of uniformly rotating WDs is $1.462\,M_\odot$ and is obtained in model DU7.

To conclude the discussion of our initial rotational configurations, we present in Fig. 4.6 for all models the initial values ($\beta_{\rm i}$) of the parameter β as a function of their precollapse central angular velocity $\Omega_{\rm c,i}$.

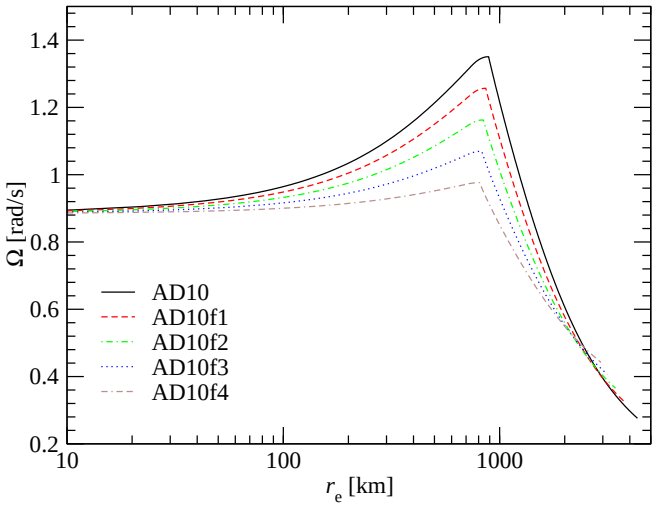

Figure 4.5: Angular velocity as a function of equatorial radius for model AD10 and varying values of the dimensionless shear parameter $f_{\rm sh}$ that controls the rate at which the angular velocity increases with ϖ in the region $\varpi < \varpi_{\rm p}$.

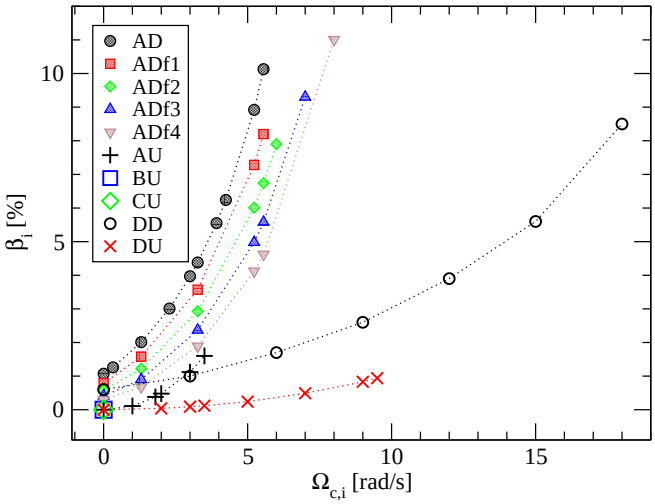

Figure 4.6: Parameter $\beta_{\rm i}$ versus central angular velocity $\Omega_{\rm c,i}$ for our AIC progenitor WD model set.

Differentially rotating WD models can reach $\beta_{\rm i}$ of up to $\sim 10\%$ while staying below the mass-shedding limit. This number is more than a factor of 2 larger than what seems possible in massive star iron core collapse (see, e.g., [123]), making these rapidly rotating AIC progenitor models potential candidates for a dynamical nonaxisymmetric rotational instability during their postbounce AIC evolution (see Sec. 4.5).

Progenitor white dwarf core temperature and $\overline{Y_e}(\rho)$ parametrization

We use Eq. (4.11) to set up the initial temperature distribution as a function of density. Dessart et al. chose $\rho_0 = \rho_{\rm c,i}$ ($= 5\times10^{10}\,{\rm g\,cm^{-3}}$ in their models) and $T_0 = 10^{10}$ K for their $1.46 M_\odot$ model, and $T_0 = 1.3\times10^{10}$ K for their $1.92 M_\odot$ model. These values (i) are similar to what was used in the earlier work of Woosley & Baron [445] and (ii) work well with the tabulated EOS employed and the assumption of NSE, but may be higher than the temperatures prevailing in accreting precollapse WDs in nature (see, e.g., [179, 361, 456]).

While the fluid pressure is affected very little by different temperature distributions, this is not the case for the free proton fraction which increases strongly with T in the range from 10^9 to 10^{10} K and at precollapse core densities. This increase of the proton fraction can lead to enhanced electron capture during AIC and in this way may have a significant influence on the AIC dynamics. In order to test the sensitivity of our AIC simulations on the assumed T_0, we not only study models with $T_0 = 10^{10}$ K (at $\rho_0 = 5\times10^{10}\,{\rm g\,cm^{-3}}$, herafter the *"high-$T$" models*), but perform also simulations for models set up with $T_0 = 5\times10^9$ K (at $\rho_0 = 5\times10^{10}\,{\rm g\,cm^{-3}}$, hereafter the *"low-$T$" models*). To obtain the $\overline{Y_e}(\rho)$ parametrization (see Sec. 4.2.1) for the latter temperature, we re-ran with VULCAN/2D the $1.46 M_\odot$ AIC model of Dessart et al. up to core bounce with the same setup as discussed in [111], but using the lower value of T_0. We do not indicate the two different initial temperatures in the model names, but list the results obtained in the two cases side-by-side in Table 4.2.

In addition to variations in deleptonization due to differences in the precollapse WD thermodynamics, we must also consider the possibility of unknown systematic biases that lead to small values of Y_e in the inner core at bounce (see Sec. 4.2.1). In order to study the effect that larger values of Y_e in the inner core have on the AIC dynamics, we perform a set of test calculations with scaled $\overline{Y_e}(\rho)$ trajectories. We implement this by making use of the fact that $Y_e(\rho)$ is to good approximation a linear function of $\log(\rho)$ (see Fig. 4.1). We change the slope of this function between $\rho = 5\times10^{10}\,{\rm g\,cm^{-3}}$ and $\rho = 2.5\times10^{14}\,{\rm g\,cm^{-3}}$ by increasing $Y_e(\rho = 2.5\times10^{14}\,{\rm g\,cm^{-3}})$ by 10% and 20%. We pick these particular scalings, since the 20% increase yields inner-core values of Y_e at bounce that are very close to those obtained in 1D Boltzmann neutrino transport simulations of oxygen-neon core collapse [207, 284]. The 10% scaling yields values in between those of [111] and [207, 284] and, hence, allows us to study trends in AIC dynamics with variations in deleptonization in between constraints provided by simulations. We will not list the results of these tests in our summary tables, but discuss them wherever the context requires their consideration (i.e., Sect. 4.3.1, 4.3.2, 4.4, 4.4.1).

4.3 Collapse dynamics

The AIC starts when the progenitor WD reaches its effective Chandrasekhar mass and pressure support is reduced due to electron capture in the core. Similar to the case of massive star iron core collapse (e.g., [306, 275, 117, 466] and references therein), the collapse evolution can be divided into three phases:

Infall: This is the longest phase of collapse and, depending on model parameters, lasts between ~ 25 ms and ~ 300 ms. The inner part of the WD core (the "inner core"), which is in sonic contact, contracts homologously ($v_r \propto r$), while the "outer core" collapses supersonically. Fig. 4.7 shows the time evolution of the central density for the nonrotating high-T AIC models. In the infall phase, the core contracts slowly, which is reflected in the slow increase of $\rho_{\rm c}$.

Table 4.1: Summary of the initial WD models: $\Omega_{\rm c,i}$ is the central angular velocity and $\Omega_{\rm max,i} = \Omega(\varpi_{\rm p})$, M_0 is the total rest-mass and J is the total angular momentum. $|W_{\rm i}|$ and $E_{\rm rot,i}$ are the gravitational energy and rotational kinetic energy of the WD, respectively. $R_{\rm e}$ and $R_{\rm p}$ are the equatorial and polar radii.

Initial model	$\Omega_{\rm c,i}$ [rad/s]	$\Omega_{\rm max,i}$ [rad/s]	$\rho_{\rm c,i}$ [10^{10} g cm^{-3}]	M_0 [$M_\odot$]	J [10^{50} ergs]	$\lvert W_{\rm i}\rvert$ [10^{50} ergs]	$E_{\rm rot,i}$ [10^{50} ergs]	$\beta_{\rm i}$ [%]	$R_{\rm e}$ [km]	$R_{\rm e}/R_{\rm p}$
AU0	0.000	0.000	0.4	1.390	0.00	37.32	0.00	0.00	1692	1.000
AU1	1.000	1.000	0.4	1.394	0.09	37.50	0.04	0.11	1710	0.988
AU2	1.800	1.800	0.4	1.405	0.16	37.90	0.15	0.38	1757	0.953
AU3	2.000	2.000	0.4	1.409	0.18	38.04	0.18	0.48	1775	0.943
AU4	3.000	3.000	0.4	1.437	0.29	39.04	0.44	1.12	1938	0.848
AU5	3.500	3.500	0.4	1.458	0.36	39.78	0.64	1.60	2172	0.748
BU0	0.000	0.000	1.0	1.407	0.00	51.44	0.00	0.00	1307	1.000
CU0	0.000	0.000	2.0	1.415	0.00	65.28	0.00	0.00	1069	1.000
DU0	0.000	0.000	5.0	1.421	0.00	89.11	0.00	0.00	813	1.000
DU1	2.000	2.000	5.0	1.423	0.03	89.25	0.03	0.04	817	0.995
DU2	3.000	3.000	5.0	1.425	0.05	89.42	0.08	0.09	822	0.988
DU3	3.500	3.500	5.0	1.426	0.06	89.53	0.11	0.12	825	0.983
DU4	5.000	5.000	5.0	1.432	0.09	90.00	0.22	0.24	840	0.963
DU5	7.000	7.000	5.0	1.442	0.13	90.87	0.44	0.49	871	0.920
DU6	9.000	9.000	5.0	1.458	0.17	92.12	0.77	0.83	931	0.853
DU7	9.500	9.500	5.0	1.462	0.18	92.50	0.86	0.94	956	0.828
AD1	0.000	2.881	0.4	1.434	0.28	38.74	0.41	1.07	2344	0.71
AD2	0.327	3.204	0.4	1.443	0.31	39.04	0.49	1.26	2382	0.69
AD3	1.307	4.198	0.4	1.477	0.42	40.25	0.81	2.01	2521	0.64
AD4	2.287	5.174	0.4	1.526	0.56	42.01	1.27	3.01	2707	0.58
AD5	3.000	5.903	0.4	1.575	0.69	43.77	1.74	3.97	2888	0.54
AD6	3.267	6.173	0.4	1.595	0.75	44.47	1.95	4.38	2964	0.53
AD7	3.920	6.833	0.4	1.659	0.93	46.77	2.59	5.55	3200	0.47
AD8	4.247	7,161	0.4	1.706	1.05	48.45	3.02	6.24	3366	0.44
AD9	5.227	8.155	0.4	1.884	1.58	54.69	4.88	8.92	4008	0.35
AD10	5.554	8.485	0.4	1.974	1.87	57.80	5.85	10.13	4338	0.313
DD1	0.000	7.688	5.0	1.446	0.13	90.85	0.51	0.60	1097	0.73
DD2	3.000	10.70	5.0	1.467	0.19	92.52	0.95	1.00	1156	0.69
DD3	6.000	13.73	5.0	1.498	0.26	95.05	1.61	1.70	1238	0.63
DD4	9.000	16.74	5.0	1.544	0.35	98.70	2.57	2.60	1353	0.56
DD5	12.00	19.77	5.0	1.612	0.48	104.08	4.01	3.90	1528	0.48
DD6	15.00	22.81	5.0	1.716	0.68	111.95	6.31	5.60	1819	0.39
DD7	18.00	25.84	5.0	1.922	1.10	126.69	10.77	8.50	2430	0.28
AD1f1	0.000	2.305	0.4	1.422	0.23	38.33	0.30	0.79	2283	0.730
AD1f2	0.000	1.723	0.4	1.413	0.19	38.03	0.22	0.58	2233	0.753
AD1f3	0.000	1.152	0.4	1.406	0.15	37.79	0.16	0.41	2188	0.770
AD1f4	0.000	0.576	0.4	1.401	0.11	37.64	0.11	0.29	2151	0.785
AD3f1	1.307	3.610	0.4	1.457	0.36	39.56	0.62	1.58	2434	0.673
AD3f2	1.307	3.032	0.4	1.441	0.31	39.01	0.47	1.22	2361	0.700
AD3f3	1.307	2.457	0.4	1.428	0.26	38.56	0.36	0.90	2298	0.723
AD3f4	1.307	1.883	0.4	1.417	0.21	38.20	0.26	0.70	2243	0.745
AD6f1	3.267	5.574	0.4	1.555	0.64	43.13	1.54	3.57	2798	0.555
AD6f2	3.267	5.003	0.4	1.522	0.55	41.96	1.23	2.93	2666	0.590
AD6f3	3.267	4.423	0.4	1.494	0.47	41.00	0.97	2.37	2554	0.625
AD6f4	3.267	3.842	0.4	1.472	0.41	40.20	0.76	1.89	2462	0.655
AD9f1	5.227	7.564	0.4	1.772	1.23	50.92	3.71	7.28	3574	0.400
AD9f2	5.227	6.978	0.4	1.691	1.00	48.13	2.89	6.01	3264	0.448
AD9f3	5.227	6.392	0.4	1.630	0.84	46.00	2.29	4.98	3029	0.493
AD9f4	5.227	5.808	0.4	1.584	0.71	44.38	1.83	4.12	2851	0.533
AD10f1	5.554	7.896	0.4	1.833	1.41	53.06	4.35	8.20	3793	0.370
AD10f2	5.554	7.305	0.4	1.741	1.13	49.93	3.37	6.74	3434	0.420
AD10f3	5.554	7.721	0.4	1.665	0.93	47.28	2.64	5.58	3149	0.468
AD10f4	5.554	6.134	0.4	1.611	0.78	44.40	2.10	4.62	2942	0.510
AD11f2	6.000	7.756	0.4	1.815	1.35	52.60	4.16	7.90	3696	0.380
AD12f3	7.000	8.175	0.4	1.914	1.65	56.27	4.23	9.30	4010	0.340
AD12f4	7.000	7.586	0.4	1.798	1.29	52.29	3.99	7.64	3574	0.393
AD13f4	8.000	8.585	0.4	2.049	2.09	61.30	6.75	11.01	4436	0.295

Table 4.2: Summary of key quantitative results from our AIC simulations. $\rho_{\max,\mathrm{b}}$ is the maximum density in the core at the time of bounce t_b, $|h|_{\max}$ is the peak value of the GW signal amplitude, while $\beta_{\mathrm{ic,b}}$ is the inner core parameter β at bounce. Models marked by unfilled/filled circles (●/○) undergo a pressure-dominated bounce with/without significant early postbounce convection. Models marked with the cross sign (×) undergo centrifugal bounce at subnuclear densities. The values left/right of the vertical separator (|) are for the models with low/high temperature profiles.

Collapse model		$\rho_{\max,\mathrm{b}}$ [10^{14} g cm^{-3}]	t_b [ms]	$\left[\begin{smallmatrix}\lvert h\rvert_{\max}\\ 10^{-21}\\ \text{at 10 kpc}\end{smallmatrix}\right]$	$\beta_{\mathrm{ic,b}}$ [%]
AU0	○|○	2.782|2.807	214.1|204.9	0.27|0.20	0.00|0.00
AU1	●|●	2.697|2.719	214.9|205.5	0.78|0.62	1.27|1.20
AU2	●|●	2.628|2.629	216.7|206.9	2.33|1.90	3.75|3.56
AU3	●|●	2.610|2.613	217.3|207.4	2.79|2.29	4.49|4.28
AU4	●|●	2.525|2.508	221.4|210.8	5.01|4.23	8.48|8.19
AU5	●|●	2.461|2.444	224.2|212.9	5.90|5.05	10.46|10.17
BU0	○|○	2.805|2.800	100.9|95.3	0.19|0.16	0.00|0.00
CU0	○|○	2.782|2.788	56.3|51.4	0.20|0.24	0.00|0.00
DU0	○|○	2.797|2.781	27.5|25.2	0.34|0.42	0.00|0.00
DU1	○|○	2.786|2.777	27.6|25.2	0.23|0.27	0.18|0.17
DU2	○|○	2.774|2.763	27.6|25.2	0.24|0.31	0.39|0.38
DU3	○|○	2.756|2.758	27.6|25.2	0.31|0.27	0.53|0.51
DU4	●|●	2.728|2.719	27.6|25.3	0.64|0.55	1.07|1.03
DU5	●|●	2.669|2.658	27.7|25.3	1.21|1.07	2.04|1.97
DU6	●|●	2.642|2.640	27.8|25.4	1.97|1.73	3.27|3.17
DU7	●|●	2.627|2.619	27.9|25.5	2.17|1.92	3.61|3.50
AD1	●|●	2.661|2.679	218.7|208.5	2.24|1.75	2.96|2.62
AD2	●|●	2.620|2.616	220.1|209.5	2.85|2.30	3.93|3.55
AD3	●|●	2.547|2.547	225.5|213.7	4.62|3.93	7.20|6.71
AD4	●|●	2.447|2.442	232.9|219.4	5.89|5.19	10.58|10.01
AD5	●|●	2.361|2.389	241.1|225.5	6.37|5.68	13.09|12.33
AD6	●|●	2.324|2.355	246.7|229.7	6.39|5.78	14.03|13.18
AD7	●|●	2.226|2.228	260.0|238.8	6.00|5.73	16.34|15.23
AD8	●|●	2.145|2.167	264.3|240.9	6.01|5.70	17.48|16.30
AD9	×|×	1.817|1.911	319.7|267.3	3.40|4.00	23.38|20.69
AD10	×|×	1.629|1.790	393.6|284.5	2.36|3.54	24.41|21.25
DD1	○|○	2.779|2.772	27.5|25.2	0.46|0.37	0.70|0.58
DD2	●|●	2.684|2.686	27.7|25.3	1.24|1.06	1.95|1.81
DD3	●|●	2.642|2.638	27.8|25.5	2.41|2.08	3.76|3.56
DD4	●|●	2.586|2.571	28.1|25.7	3.78|3.29	5.93|5.71
DD5	●|●	2.526|2.498	28.4|25.9	5.22|4.61	8.27|8.09
DD6	●|●	2.457|2.425	28.8|26.3	6.52|5.82	10.57|10.51
DD7	●|●	2.389|2.352	29.2|26.5	7.58|6.81	12.75|12.79

Collapse model		$\rho_{\max,\mathrm{b}}$ [10^{14} g cm^{-3}]	t_b [ms]	$\left[\begin{smallmatrix}\lvert h\rvert_{\max}\\ 10^{-21}\\ \text{at 10 kpc}\end{smallmatrix}\right]$	$\beta_{\mathrm{ic,b}}$ [%]
AD1f1	●|●	2.718|2.733	217.1|207.2	1.57|1.24	2.06|1.80
AD1f2	●|●	2.759|2.767	215.8|206.2	0.96|0.75	1.26|1.10
AD1f3	○|○	2.787|2.795	214.9|205.5	0.47|0.36	0.59|0.49
AD1f4	○|○	2.803|2.803	214.4|205.0	0.26|0.18	0.14|0.12
AD3f1	●|●	2.560|2.564	222.5|211.5	4.09|3.41	6.26|5.81
AD3f2	●|●	2.583|2.597	220.1|209.6	3.46|2.85	5.23|4.85
AD3f3	●|●	2.622|2.631	218.2|208.1	2.76|2.25	4.17|3.87
AD3f4	●|●	2.656|2.662	216.7|207.0	2.03|1.63	3.10|2.90
AD6f1	●|●	2.356|2.377	237.6|222.9	6.47|5.77	13.20|12.52
AD6f2	●|●	2.395|2.399	233.1|219.7	6.41|5.63	12.31|11.79
AD6f3	●|●	2.421|2.424	229.1|216.7	6.28|5.43	11.47|11.06
AD6f4	●|●	2.463|2.444	225.7|214.1	5.95|5.12	10.56|10.20
AD9f1	×|×	1.913|1.994	282.0|250.9	3.88|5.77	20.80|18.84
AD9f2	●|●	2.000|2.073	265.1|241.7	5.25|6.17	20.10|18.09
AD9f3	●|●	2.092|2.115	253.9|234.6	6.96|6.41	18.44|17.45
AD9f4	●|●	2.159|2.166	244.7|228.3	7.30|6.74	17.67|16.74
AD10f1	×|×	1.797|1.899	303.4|261.3	3.99|4.14	23.71|21.04
AD10f2	×|×	1.901|1.980	272.4|245.2	4.15|5.91	21.07|19.30
AD10f3	×|●	1.984|2.042	261.2|239.3	5.52|6.39	20.40|18.53
AD10f4	●|●	2.096|2.098	249.8|231.7	7.32|6.67	18.70|17.83
AD11f2	×|×	1.734|1.845	296.9|257.6	3.78|4.13	24.23|21.65
AD12f3	×|×	0.319|1.555	372.3|249.4	1.61|4.08	22.88|23.08
AD12f4	×|×	1.432|1.677	298.1|257.9	3.14|4.44	24.58|22.97
AD13f4	×|×	7×10^{-4}|0.312	331.8|322.9	0.40|2.01	15.39|24.02

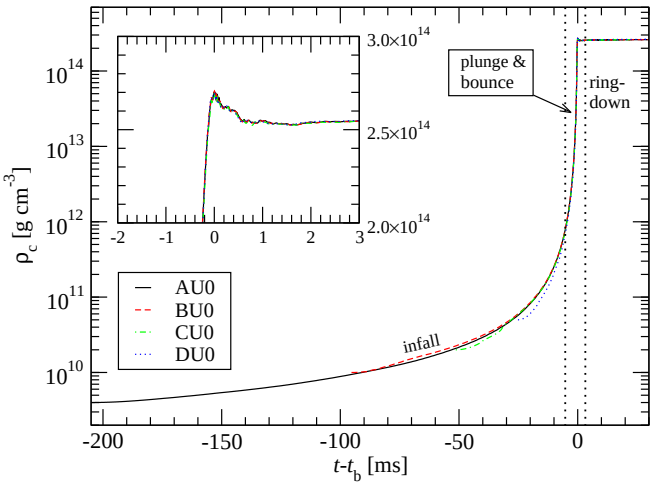

Figure 4.7: Evolution of the maximum (central) density for the nonrotating low-T models AU0, BU0, CU0 and DU0. The inset plot displays a zoomed-in view of the maximum density around the time of core bounce on a linear scale. As clearly discernible from this figure, the collapse dynamics in the plunge and bounce phase are essentially independent of the initial WD central density. Time is normalized to the time of bounce $t_{\rm b}$.

Plunge and bounce: The short dynamical "plunge" phase sets in when $\rho_{\rm c}$ reaches $\sim 10^{12}\,{\rm g\,cm^{-3}}$, and the peak radial infall velocity is $\sim 0.1c$. At this point, neutrinos begin to be trapped in the inner core. The latter rapidly contracts to reach nuclear densities ($\rho_{\rm nuc} \simeq 2.7 \times 10^{14}$ g cm^{-3}) at which the nuclear EOS stiffens, decelerating and eventually reversing the infall of the inner core on a millisecond timescale. Because of its large inertia and kinetic energy, the inner core does not come to rest immediately. It overshoots its equilibrium configuration, then bounces back, launching a shock wave at its outer edge into the still infalling outer core. The bounce and the re-expansion of the inner core is also evident in the time evolution of $\rho_{\rm c}$ shown in Fig. 4.7 which, at core bounce, reaches a value of $\sim 2.8 \times 10^{14}\,{\rm g\,cm^{-3}}$ in the nonrotating AIC models, after which the core slightly re-expands and settles down at $\sim 2.5 \times 10^{14}\,{\rm g\,cm^{-3}}$. As pointed out by extensive previous work (see, e.g., [48, 174, 452, 431, 123] and references therein), the extent of the inner core at bounce determines the initial kinetic energy imparted to the bounce shock, the mass cut for the material that remains to be dissociated, and the amount of angular momentum that may become dynamically relevant at bounce.

Ringdown: Following bounce, the inner core oscillates with a superposition of various damped oscillation modes with frequencies in the range of $500 - 800\,{\rm Hz}$, exhibiting weak low-amplitude variations in $\rho_{\rm c}$ (Fig. 4.7). These oscillations experience rapid damping on a timescale of $10\,{\rm ms}$ due to the emission of strong sound waves into the postshock region which steepen into shocks. The newly born PNS thus *rings* down to its new equilibrium state.

The ringdown phase is coincident with the burst of neutrinos that is emitted when the bounce shock breaks out of the energy-dependent neutrinospheres (see, e.g., [410, 111]). The neutrino burst removes energy from the postshock regions and enhances the damping of the PNS ringdown oscillations (e.g., [309]), but, due to the limitations of our present scheme (see Sec. 4.2.1), is not accounted for in our models.

4.3.1 Nonrotating AIC

The set of nonrotating AIC models that we consider here consists of models AU0, BU0, CU0, DU0. As noted in Section 4.2.3, these models have different central densities with values in the range from 4×10^9 to 5×10^{10} g cm^{-3} which, because of the strong dependence of the WD compactness on the central

density, corresponds to a range of WD radii from 1692 to 813 km (see Fig. 4.2). Once mapped onto our computational grid and after the initial $\overline{Y}_e(\rho)$ parametrization is applied (see Sec. 4.2.2), all WD models start to collapse by themselves and no additional artificial pressure reduction is necessary. This is in contrast to previous work that employed a simple analytic EOS and required an explicit and global change of the adiabatic exponent to initiate collapse (e.g., [466, 118]).

The free-fall collapse time $\tau_{\rm ff}$ of a Newtonian self-gravitating object of mean density $\rho_{\rm mean}$ is proportional to $\rho_{\rm mean}^{-1/2}$. For our set of spherically-symmetric AIC models we find a scaling $\tau_{\rm ff} \propto \rho_{\rm c}^{-0.87}$, where $\rho_{\rm c}$ is the precollapse central density of the WD. This stronger scaling is due to the fact that WD cores are not constant density objects and that the collapse is not pressureless. Furthermore, the pressure reduction initiating and accelerating collapse is due primarily to electron capture which scales roughly with $\rho^{5/3}$ (e.g., [48]). Hence, lower-density WDs collapse only slowly, spending much of their collapse time near their initial equilibrium states.

In Fig. 4.7, we plot the evolution of the central densities of the nonrotating high-T models. Despite the strong dependence of the collapse times on the initial central densities, the evolution of $\rho_{\rm c}$ around bounce does not exhibit a dependence on the initial central density. Moreover, the mass and the size of the inner core is rather insensitive to the initial value of $\rho_{\rm c}$.

These features, somewhat surprising in the light of the strong dependence of the collapse times on the initial value of $\rho_{\rm c}$, are a consequence of the fact that the inner core mass is determined primarily not by hydrodynamics, but by the thermodynamic and compositional structure of the inner core set by nuclear and neutrino physics [48]. However, an important role is played also by the fact that an increase (decrease) of the central density of an equilibrium WD leads to a practically exact homologous[3] contraction (expansion) of the WD structure in the inner regions ($m(\varpi) \lesssim 1\,M_\odot$) in the nonrotating case (this can be seen in Fig. 4.11), at least in the range of central densities considered in this work (as we shall see in Section 4.3.2, this feature also holds to good accuracy in the case of rotating WDs). These aspects, in combination with the homologous nature of WD inner-core collapse, make the size and dynamics of the inner core in the bounce phase practically independent of the central density of the initial equilibrium WDs. Early analytical work [174, 452, 48] demonstrated (neglecting thermal corrections [74] and rotation) that the mass $M_{\rm ic}$ of the inner core is proportional to Y_e^2 in the infall phase during which the fluid pressure is dominated by the contribution of degenerate electrons. Around bounce, at densities near nuclear matter density, the nuclear component dominates and the simple Y_e^2 dependence does not hold exactly any longer. As discussed in Sec. 4.2.2, we adopt the parametrization $\overline{Y_e}(\rho)$ as extracted from the simulations of Dessart et al. [111] which predict very efficient electron capture, resulting in an average inner-core Y_e at bounce of ~ 0.18 in the high-T models. This is significantly lower than in standard iron core collapse where the inner-core Y_e at bounce is expected to be around $\sim 0.25 - 0.30$ [410, 230, 71]. In our nonrotating AIC models, we find inner core masses at bounce $M_{\rm ic,b} \sim 0.27 M_\odot$ [4] (see Fig. 4.13) which are, as expected, significantly smaller than in iron core collapse (where $M_{\rm ic,b} \sim 0.5 M_\odot$ [71, 72, 230]). Due to their small mass, our AIC inner cores have less kinetic energy at bounce and reach lower densities than their iron core counterparts. For example, the nonrotating AIC models exhibit central densities at bounce of $\sim 2.8 \times 10^{14}$ g cm^{-3}, while in nonrotating iron core collapse, maximum densities of $\gtrsim 3 \times 10^{14}$ g cm^{-3} are generally reached at bounce

[3] For a discussion of homology in the stellar structure context, see [206].

[4] We define the inner core as the region which is in sonic contact at the time of bounce, i.e.,

$$M_{\rm ic,b} \equiv \int_{|v_r|<c_{\rm s}} \rho W dV \,, \tag{4.12}$$

where W is the Lorentz factor and dV is the invariant 3-volume element. The bounce time is defined as the time when the radial velocity of the outer edge of the inner core becomes positive. Note that such a measure of the inner core is strictly valid only at the time of bounce.

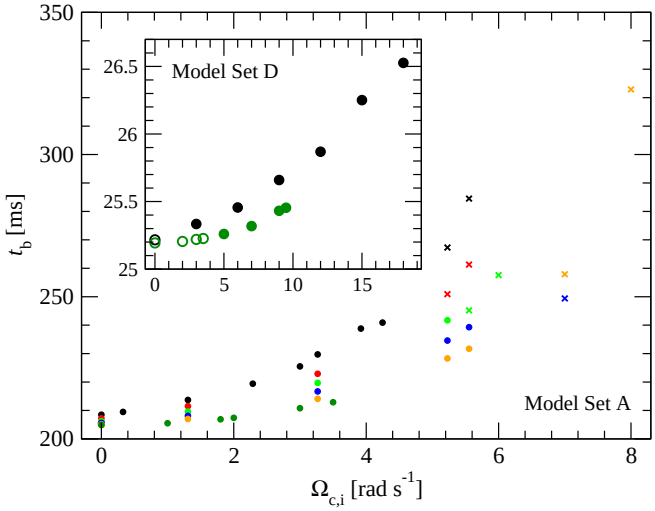

Figure 4.8: Times to core bounce from the onset of collapse as a function of initial central angular velocity $\Omega_{\rm c,i}$. Shown are the results of the high-T model sequence (the low-T models exhibit identical systematics). Models denoted by an unfilled (filled) circle undergo a pressure-dominated bounce with (without) significant prompt postbounce convection. Models marked by a cross undergo centrifugal bounce at subnuclear densities and models marked with a small (large) symbol are of set A (D). The colors correspond to various precollapse rotational configurations (see the legend in Fig. 4.9). Note that due to their much higher initial compactness, the high-density D models (shown in the inset plot) have much shorter collapse times than their lower-density A counterparts.

in simulations (e.g., [123]). In addition to $M_{\rm ic,b}$, the bounce density depends also on the stiffness of the nuclear EOS whose variation we do not explore here (see, e.g., [123, 402]).

Since the free proton fraction at precollapse and early collapse densities grows rather rapidly with temperature in the range from $\sim 10^9$ to $\sim 10^{10}$ K (e.g., [69]), the efficiency of electron capture is sensitive to the temperature of WD matter. For example, in the low-T models, the value of Y_e drops to $\simeq 0.32$ when the density reaches $10^{12}\,{\rm g\,cm^{-3}}$, while in the high-$T$ models, we obtain $Y_e \simeq 0.3$ at that time. Due to this dependence of Y_e on T, the inner core masses of low-T models are larger by $\sim 10\%$ compared to those of high-T models. Moreover, since the electron degeneracy pressure is proportional to $(Y_e\rho)^{4/3}$ [48], the collapse times of the low-T models are longer by $\sim 5\%$. We find similar systematics in test calculations in which we modify the $\overline{Y_e}(\rho)$ trajectories of low-T models to yield larger Y_e at bounce (see Sec. 4.2.3). An increase of the inner-core Y_e by 10% (20%) leads to an increase of $M_{\rm ic,b}$ by $\sim 11\%$ ($\sim 25\%$).

It is important to note that the nonrotating AIC models discussed above as well as all of the other models considered in this study, experience prompt hydrodynamic explosions. The bounce shock, once formed, does slow down, but never stalls and steadily propagates outwards. While the shock propagation is insensitive to the initial WD temperature profile, it shows significant dependence on the initial WD central density: Owing to the greater initial compactness and the steeper density gradient of the higher-density models, the shock propagation in those models is faster and the shock remains stronger when it reaches the WD surface. For example, in the lowest-density progenitor model AU0, the shock reaches the surface within ~ 120 ms after its formation, while in the highest density model DU0, it needs only ~ 80 ms. We point out that Dessart et al. [111, 113] and previous AIC studies [445, 157] reported significant shock stagnation in the postbounce phase of AIC due to the dissociation of infalling material and neutrino losses from the postshock region. Our present computational approach includes dissociation (through the EOS, see Sec. 4.2.1), but does not account for neutrino losses in the postbounce phase. Hence, the "prompt" explosions in our models are most likely an artifact of our incomplete treatment of the postbounce physics.

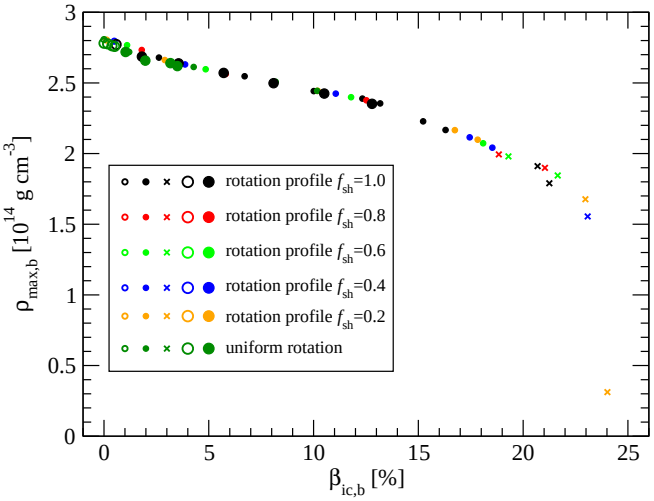

Figure 4.9: The maximum density $\rho_{\rm max,b}$ at bounce as a function of the inner core parameter $\beta_{\rm ic,b}$ at bounce for the entire set of high-T AIC models. Due to the increasing role of centrifugal support, $\rho_{\rm max,b}$ decreases monotonically with increasing rotation (see the main text for details). The symbol convention for the various sets is explained in the caption of Fig. 4.8.

4.3.2 Rotating AIC

The AIC of rotating models proceeds through the same stages as AIC without rotation and exhibits similar general features, including the well defined split of the WD into an inner core that is in sonic contact and collapses quasi-homologously[5], and a supersonically infalling outer core. Conservation of angular momentum leads to an increase of the angular velocity $\Omega \propto \varpi^{-2}$ and of the centrifugal acceleration $a_{\rm cent} = \Omega^2\varpi \propto \varpi^{-3}$. The latter has opposite sign to gravitational acceleration, hence provides increasing *centrifugal support* during collapse, slowing down the contraction and, if sufficiently strong, leading to centrifugally-induced core bounce only slightly above nuclear density or even at subnuclear density [422, 275].

Just as in the case of nonrotating AIC, models of set A collapse more slowly than D models because of the dependence of the collapse times on the initial central densities. However, due to centrifugal support, the collapse times grow with increasing precollapse rotation. This is visualized in Fig. 4.8 in which we plot the time to core bounce as a function of the initial central angular velocity $\Omega_{\rm c,i}$. The maximum angular velocity of uniformly rotating models is limited by the WD surface mass-shedding limit and is $\sim 3.5\,{\rm rad\,s^{-1}}$ ($\sim 9.5\,{\rm rad\,s^{-1}}$) in model AU5 (DU7). The effect of rotation on the collapse time of uniformly rotating models (dark-green symbols in Fig. 4.8) is small and the time to core bounce increases by $\sim 5\%$ from zero to maximum precollapse rotation in model set A. The more compact D models collapse much faster than their lower initial density A counterparts and, in addition, experience a smaller spin-up of their more compact inner cores. Hence, uniformly rotating D models are less affected by rotation and their collapse times vary by only $\sim 0.8\%$ from zero to maximum rotation.

As mentioned in Sec. 4.2.2, WD models that rotate differentially according to the rotation law of Yoon & Langer [455, 456] have an angular velocity that increases from its central value $\Omega_{\rm c,i}$ with ϖ up to a maximum $\Omega_{\rm max,i}$ at the cylindrical radius $\varpi_{\rm p}$, beyond which Ω decreases to sub-Keplerian values at the surface (see Fig. 4.3). The rate at which Ω increases in the WD core is controlled by the shear parameter $f_{\rm sh}$, which we choose in the range from 0.2 to 1. The case $f_{\rm sh} = 0.2$ corresponds to a *nearly uniformly*

[5]The collapse is *quasi*-homologous because in this case the relation between the infall velocity v_r depends on both the radial coordinate and on the polar coordinate [466].

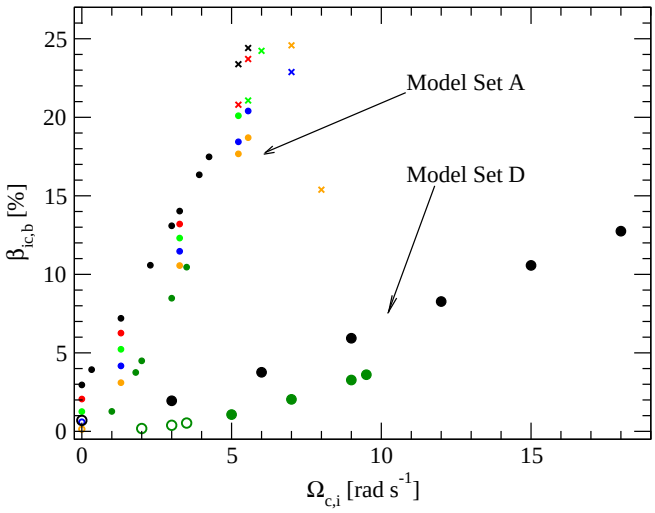

Figure 4.10: The inner core parameter $\beta_{\rm ic,b}$ at the time of bounce for all low-T AIC models plotted as a function of the precollapse central angular velocity $\Omega_{\rm c,i}$. For models with slow to moderately-rapid rotation, $\beta_{\rm ic,b}$ increases roughly linearly with $\Omega_{\rm c,i}$ (at fixed $\rho_{\rm c,i}$ and rotation law). In more rapidly rotating models, the growth of $\beta_{\rm ic,b}$ saturates at $\sim 24.5\,\%$, and further increase of the progenitor rotation results in a decrease of $\beta_{\rm ic,b}$. Since D models experience less spin-up during collapse than A models, an increase of $\rho_{\rm c,i}$ at fixed $\Omega_{\rm c,i}$ and rotation law results in a decrease of $\beta_{\rm ic,b}$. A uniformly rotating model with a given $\Omega_{\rm c,i}$ and $\rho_{\rm c,i}$ reaches smaller $\beta_{\rm ic,b}$ than the differentially rotating model with the same $\Omega_{\rm c,i}$ and $\rho_{\rm c,i}$. The symbol convention for the various sets is explained in the caption of Fig. 4.8.

rotating inner region, while $f_{\rm sh} = 1$ corresponds to strong differential rotation with $\Omega(\varpi_{\rm p})/\Omega_{\rm c,i} \sim 2-3$. In mass coordinate, this corresponds to a ratio $\Omega(M_{\rm ic,b})/\Omega_{\rm c,i}$ of $\sim 1.4-2.4$, where $M_{\rm ic,b} \simeq 0.3\,M_\odot$ is the approximate mass that constitutes the inner core at bounce in a nonrotating WD model.

In contrast to uniformly rotating models, differentially rotating WDs are *not limited* by the mass shedding limit at the surface. As a result, $\Omega_{\rm c,i}$ can in principle be increased up to the point beyond which the precollapse WD inner core becomes fully centrifugally supported and does not collapse at all. For model set AD, this maximum of $\Omega_{\rm c,i}$ is $\sim 8\,{\rm rad\,s^{-1}}$ (the low-T model AD13f4, which becomes centrifugally supported already at a central density of $\sim 7\times10^{10}\,{\rm g\,cm^{-3}}$) while the more compact DD models still collapse rapidly at $\Omega_{\rm c,i} \sim 18\,{\rm rad\,s^{-1}}$ (model DD7). As shown in Fig. 4.8, the most rapidly rotating AD model (AD13f4) reaches core bounce after a time which is $\sim 55\%$ larger than a nonrotating A model. For the most rapidly rotating DD model this difference is only $\sim 5\%$.

In Fig. 4.9 we plot the maximum density $\rho_{\rm max,b}$ at bounce as a function of the inner core parameter $\beta_{\rm ic,b}$ at bounce. Slowly to moderately-rapidly rotating WDs that reach $\beta_{\rm ic,b} \lesssim 15\%$ are only mildly affected by rotation and their $\rho_{\rm max,b}$ decrease roughly linearly with increasing $\beta_{\rm ic,b}$, but stay close to $\rho_{\rm nuc}$. The effect of rotation becomes nonlinear in more rapidly rotating WDs. Models of our set that reach $\beta_{\rm ic,b} \gtrsim 18\%$ (i.e., AD models with $\Omega_{\rm c,i} \gtrsim 5\,{\rm rad\,s^{-1}}$) undergo core bounce induced partly or completely centrifugally at subnuclear densities.

As shown in Fig. 4.10, $\beta_{\rm ic,b}$ is a monotonic function of $\Omega_{\rm c,i}$, but is very sensitive to both the rotation law and the initial WD compactness. Our most rapidly uniformly rotating models AU5 and DU7 (both near the mass-shedding limit) reach $\beta_{\rm ic,b}$ of $\sim 10.5\%$ and $\sim 3.6\%$, respectively. Hence, uniformly rotating WDs always undergo core bounce due to the stiffening of the nuclear EOS and with little influence of rotation on the dynamics.

In models where centrifugal effects remain subdominant during collapse, $\beta_{\rm ic,b}$ grows practically linearly with $\Omega_{\rm c,i}$. This relationship flattens off for models that become partially or completely centrifugally sup-

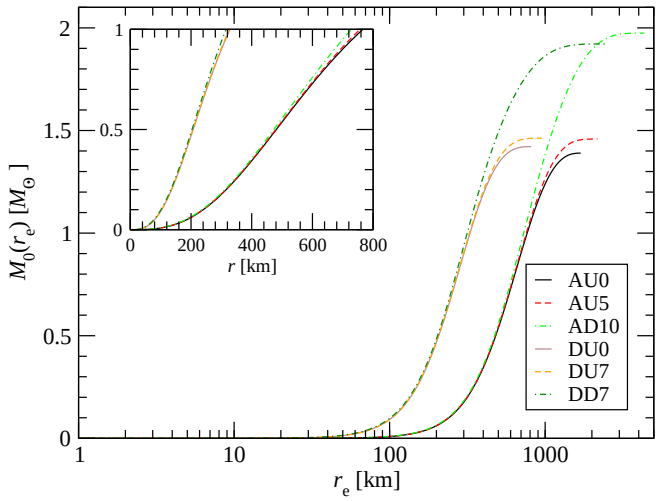

Figure 4.11: Mass $M_0(r_e)$ in units of solar masses of the WD inner region plotted as a function of the equatorial radial coordinate r_e for a number of AIC models with slow and rapid rotation as well as high and small central densities. The inset plot shows the same on a linear radial scale. The mass distribution of the inner $M_0(r_e) \lesssim 0.5 M_\odot$ region is largely independent of the rotational configuration, while an increase (decrease) of the central density leads to homologous contraction (expansion) of the inner regions. See Sec. 4.2.3 for details of the model setups.

ported near bounce. $\beta_{\rm ic,b}$ grows with increasing rotation up to $\sim 24.5\%$ (model AD13f4), beyond which any further increase in precollapse rotation leads to a *decrease* of $\beta_{\rm ic,b}$, since the inner core becomes fully centrifugally supported before reaching high compactness and spin-up. In other words, there exists a *"centrifugal limit"* beyond which centrifugal forces dominate and, as a result, increasing precollapse rotation leads to a decreasing $\beta_{\rm ic,b}$ at core bounce. This result is analogous to what previous studies [123, 306] found in the rotating core collapse of massive stars and has consequences for the appearance of nonaxisymmetric rotational instabilities in PNSs. This will be discussed in more detail in Sec. 4.5.

The influence of the precollapse compactness on the dynamics of rotating AIC can also easily be appreciated from Fig. 4.10. The higher-density, more-compact WDs of set D spin up much less than their A counterparts since their inner cores are already very compact at the onset of collapse. Hence, a higher-density WD that reaches a given value of $\beta_{\rm ic,b}$ must have started out with a larger $\Omega_{\rm c,i}$ than a lower-density WD reaching the same $\beta_{\rm ic,b}$. For the particular choice of initial central densities represented by D and A models and in the case of uniform or near-uniform rotation, the ratio between the $\Omega_{\rm c,i}$ of a D and A model required to reach the same $\beta_{\rm ic,b}$ is ~ 5.3. This factor can be understood by considering Fig. 4.11 in which we plot the enclosed mass as a function of equatorial radial coordinate r_e of selected A and D initial WD configurations with slow and rapid rotation. The important thing to notice is that the WD core structure ($M \lesssim 0.5 M_\odot$) is insensitive to the rotational configuration and obeys a homology relation. Stated differently, for a model of set D, a homologous expansion in the radial direction by a factor of ~ 2.3 yields an object whose inner part is very similar to a lower-density A model. In turn, the collapse of A models corresponds to a ~ 2.3 times greater contraction of the WD core compared to their D model counterparts and a spin up that is greater by a factor of $\sim (2.3)^2 \simeq 5.3$. This explains the strong dependence of the inner-core angular velocity and $\beta_{\rm ic,b}$ on the initial central density observed in Fig. 4.10. Furthermore, it suggests that one can find A$-$D model pairs that differ greatly in their precollapse angular velocities, but yield the same rotational configuration at bounce. An example for this is shown in Fig. 4.12 in which we plot for the uniformly rotating model pair AU2-DU7 the equatorial angular velocity profile at the time of bounce as well as the evolution of the central density around the time of bounce. AU2 and DU7 have practically identical angular velocity profiles and their core structure, core mass and $\beta_{\rm ic,b}$ agree very closely. As can be seen in

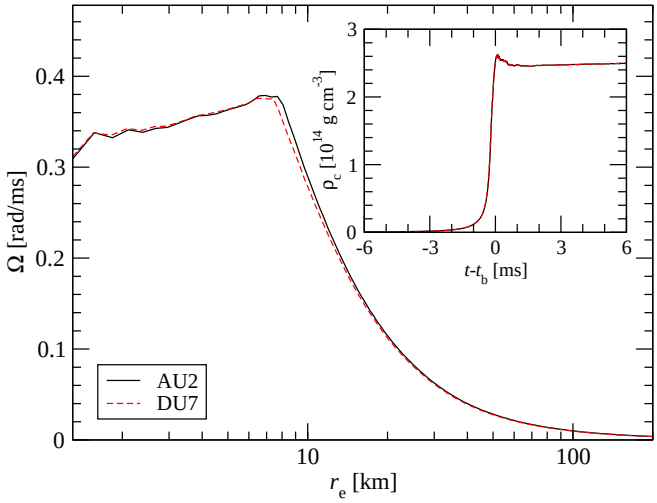

Figure 4.12: Angular velocity profiles in the equatorial plane at the time of core bounce and time-evolution of the central density ρ_c (in the inset) for models AU2 and DU7. The initial angular velocity of model DU7 is larger by a factor of ~ 5.3 than that of model AU2, but the latter experiences a ~ 5.3 greater spin-up during collapse. As a result, these models produce inner cores with almost identical rotational configurations and similar masses in the bounce phase. This is reflected in an identical evolution of the central densities at bounce.

the inset plot of Fig. 4.12, this results in nearly identical ρ_c time evolutions around bounce and demonstrates that WDs with quite different precollapse structure and rotational setup can produce identical bounce and postbounce dynamics. This can also occur for pairs of differentially rotating models and is an important aspect to keep in mind when interpreting the GW signal from AIC discussed in Sec. 4.4.

Figure 4.13 shows the mapping between $\beta_{\rm ic,b}$ and the inner core mass $M_{\rm ic,b}$ at bounce for all high-T models. Rapid (differential) rotation not only increases the equilibrium mass of WDs (see Table 4.1), but rotational support also increases the extent of the region in sonic contact during collapse. Hence, it may be expected that $M_{\rm ic,b}$ grows with increasing rotation. However, for WDs below $\beta_{\rm ic,b} \lesssim 13\%$, $M_{\rm ic,b}$ is essentially unaffected by rotation and stays within $0.02\,M_\odot$ of the nonrotating value of $0.28\,M_\odot$. Only when the effects of rotation become strong at $\beta_{\rm ic,b} \gtrsim 13-18\%$ does $M_{\rm ic,b}$ increase roughly linearly with $\beta_{\rm ic,b}$. WDs that undergo centrifugal bounce have $\beta_{\rm ic,b} \gtrsim 18\%$ and correspondingly large inner cores that are more massive than $\sim 0.5\,M_\odot$. Such values of $M_{\rm ic,b}$ are accessible only to differentially rotating WDs.

Also for rotating models, the dependence of the AIC dynamics on the initial temperature of AIC progenitor WDs is simple and straightforwardly understood from the nonrotating results discussed in Sec. 4.3.1. These show that the low-T models yield inner cores that are $\sim 10\%$ larger in mass than in their twice-as-hot high-T counterparts. Due to their larger mass, the inner cores of collapsing low-T AIC progenitors also contain a larger amount of angular momentum. At fixed rotation law and $\Omega_{\rm c,i}$, they reach values of $\beta_{\rm ic,b}$ that are larger by up to $\sim 5\%$ (in absolute value!). Hence, lower-T WDs become affected by centrifugal support, bounce centrifugally, and reach the centrifugal limit at lower $\Omega_{\rm c,i}$ than their higher-T counterparts. Along the same lines behave test calculations in which we impose increased inner-core values of Y_e (see Secs. 4.2.1 and 4.2.3). The increased Y_e leads to more massive and more extend inner cores which, in turn, are more likely to experience a centrifugal support.

To conclude our discussion of rotating AIC, we summarize for the reader that the PNSs born from the set of differentially (uniformly) rotating AIC models considered here have average angular velocities[6] in

[6]The average angular velocity $\bar{\Omega}$ of the differentially rotating models considered here is computed using the approximation $\bar{\Omega} = J_{\rm ic}/I_{\rm ic}$, where $J_{\rm ic}$ is the inner core angular momentum and $I_{\rm ic}$ is the (Newtonian) inner core moment of inertia.

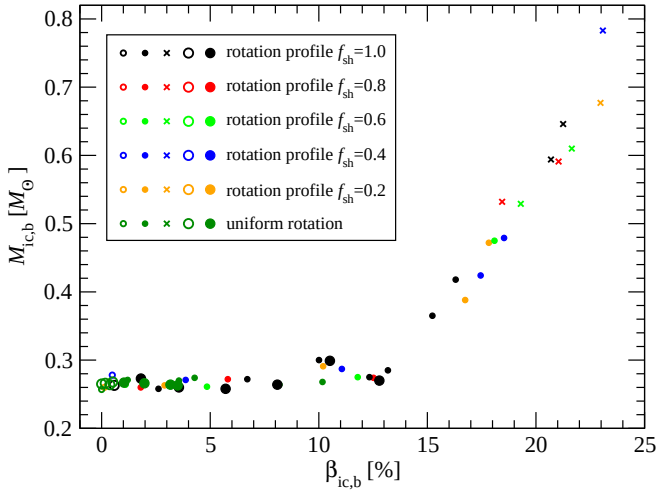

Figure 4.13: Mass $M_{\rm ic,b}$ of the inner core at bounce for all high-T models versus the parameter $\beta_{\rm ic,b}$ of the inner core at bounce. The systematics of $M_{\rm ic,b}$ with $\beta_{\rm ic,b}$ are identical for the set of low-T models, but their $M_{\rm ic,b}$ are generally $\sim 10\%$ larger. The symbol convention for the various sets is explained in the caption of Fig. 4.8.

the range from 0 to $\sim 5\,{\rm rad\,ms^{-1}}$ ($\sim 3.3\,{\rm rad\,ms^{-1}}$), while their pole to equator axis ratios vary from 1 to ~ 0.4 (~ 0.6)[7]. Some of the rapidly rotating WDs produce PNSs with a slightly off-center maximum in density, though the density distribution of the inner regions does not exhibit a pronounced toroidal geometry. The clearest deviation from a centrally-peaked density distribution is produced in the case of model AD10, which reaches $\beta_{\rm ic,b} \simeq 21.3\,\%$ ($\beta_{\rm ic,b} \simeq 24.4\,\%$) in its high-$T$ (low-T) variant. In this model, the point of highest density after bounce is located at $r \simeq 0.94$ km, but the maximum value is larger than the central density value by only $\sim 0.3\,\%$. For models with less rapid rotation, the off-center maximum is much less pronounced, and completely disappears for $\beta_{\rm ic,b}$ below $\sim 20\,\%$.

4.3.3 Shock propagation and the formation of quasi-keplerian disks

As pointed out earlier (see Sec. 4.3.1), all AIC models considered in this study undergo weak hydrodynamic explosions. This is an artifact of our approach that neglects postbounce neutrino emission, but is unlikely to strongly affect the results presented in this section, since in the MGFLD simulations of [111], the shock stalls only for a very short period and a weak explosion is quickly initiated by neutrino heating.

In moderately-rapidly and rapidly rotating AIC (with $\beta_{\rm ic,b} \gtrsim 5\,\%$), the shock propagation is significantly affected by centrifugal effects. The material near the equatorial plane of rotating WDs experiences considerable centrifugal support, and its collapse dynamics is slowed down. As a consequence, the bounce is less violent and the bounce shock starts out weaker near the equatorial plane than along the poles. Centrifugal support of low-latitude material also leads to reduced postbounce mass accretion rates near the equatorial plane, facilitating steady propagation of the shock at low latitudes. In the polar direction, where centrifugal support is absent, the shock propagates even faster due to the steeper density gradient and smaller polar radius of the WD. This quickly leads to a prolate deformation of the shock front in all rotating models and the shock hits the polar WD surface much before it breaks out of the equatorial envelope. This is shown in Fig. 4.14, where we plot the equatorial and polar profiles of the radial velocity and specific entropy per baryon for model DD7 at various postbounce times. Due to the prolateness of the shock front, it breaks out

[7]The PNS formed in the AIC of WDs is surrounded by hot low density material in the early postbounce phase, making it hard to define the boundary of the PNS unambiguously. For the present rough estimate of the axis ratio, we assume a density threshold of $10^{12}\,{\rm g\,cm^{-3}}$ to mark the boundary of the PNS.

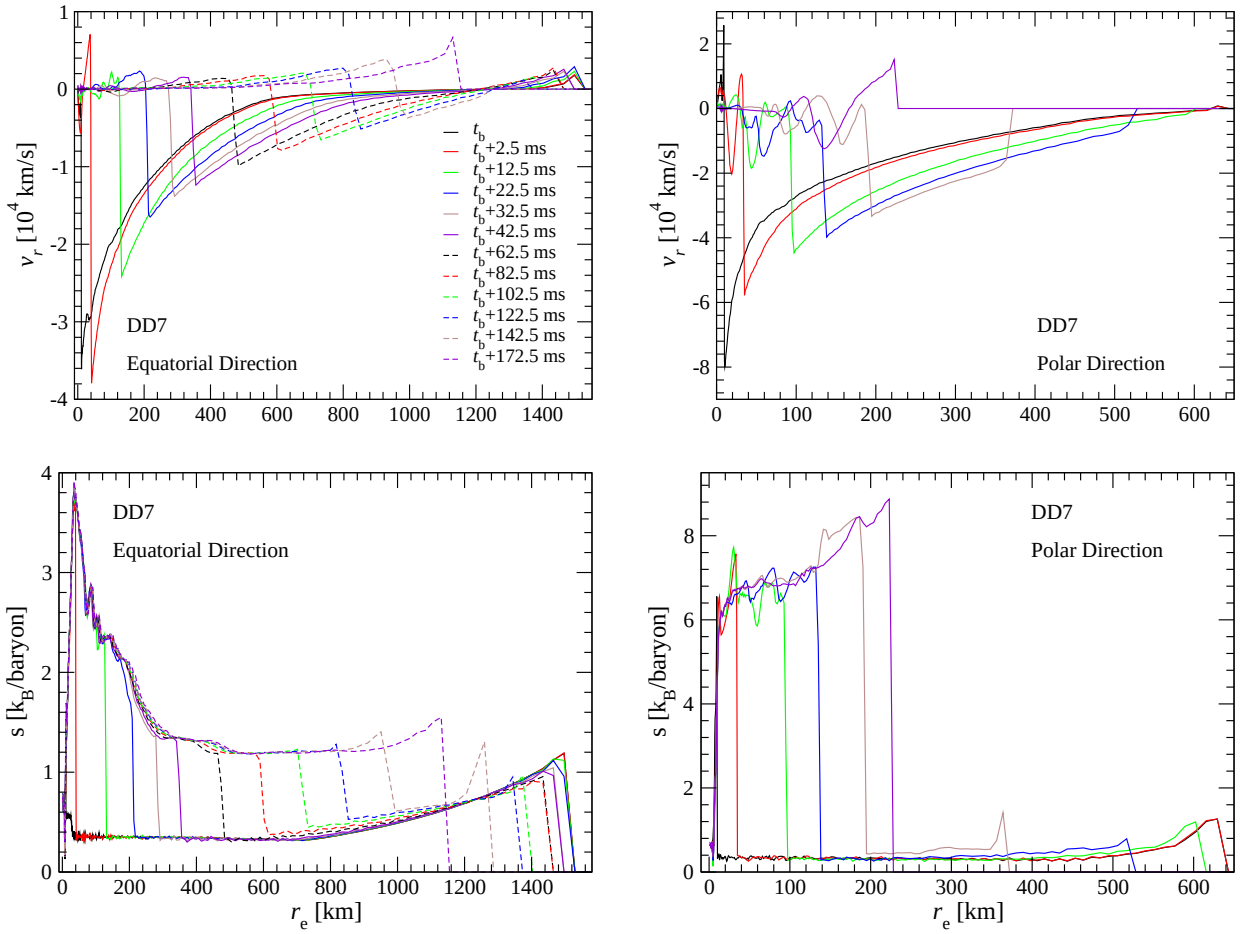

Figure 4.14: Profiles of radial velocity (top panels) and specific entropy per baryon (bottom panels) at different postbounce times for AIC model DD7.

of the polar surface ~ 130 ms before reaching the WD's equatorial surface. Moreover, due to the anisotropy of the density gradient and the initial shock strength, the specific entropy of the shock-heated material is larger by a factor of $\sim 2-3$ along the polar direction.

The asphericity of the shock front and the anisotropy of the shock strength become more pronounced in AIC with increasing rotation [118, 309]. As pointed out in Section 4.3.1, due to the their greater initial compactness and thus steeper density gradients, the shock propagates faster in D models: In model DD1, for example, the shock reaches the surface in the equatorial plane within ~ 88 ms, while for model AD1, the corresponding time is ~ 143 ms.

Rapid rotation and, in particular, rapid differential rotation, increases the maximum allowable WD mass. The most rapidly uniformly rotating WDs in our model set (i.e., models DU7 and AU5) have an equilibrium mass of $\sim 1.46 M_\odot$, which is only slightly above $M_{\rm Ch}$ in the nonrotating limit. Our most rapidly differentially rotating WDs (models AD13f2 and DD7), on the other hand, reach equilibrium masses of up to $\sim 2\,M_\odot$. Much of the rotationally supported material is situated at low latitudes in the outer WD core, falls in only slightly during collapse, and forms a quasi-Keplerian disk-like structure. The equatorial bounce shock is not sufficiently strong to eject much of the disk material and "wraps" around the disk structure, producing only a small outflow of outer disk material at $v_r \lesssim 0.025c$. This is in agreement with Dessart et al. [111], who first pointed out that rapidly rotating AIC produces PNSs surrounded by massive quasi-

Table 4.3: Summary of properties of the quasi-Keplerian disks formed in the set of AIC models AD, AU, DD and DU. $H_{\rm disk}$ is the thickness and $R_{\rm e}$ is the equatorial radius of the disk, while $M_{\rm disk}$ is its mass. These quantities are computed at the time when the shock reaches the WD surface in the equatorial plane. The disk parameters do not vary significantly between the two choices of WD temperature considered in this study.

Collapse model	$R_{\rm e}$ [km]	$H_{\rm disk}/R_{\rm e}$	$M_{\rm disk}$ [$M_\odot$]
AU1	347	0.928	$\lesssim 10^{-3}$
AU2	401	0.903	$\lesssim 10^{-3}$
AU3	447	0.848	$\lesssim 10^{-3}$
AU4	732	0.577	0.002
AU5	907	0.484	0.030
DU1	248	0.980	$\lesssim 10^{-3}$
DU2	249	0.971	$\lesssim 10^{-3}$
DU3	249	0.952	$\lesssim 10^{-3}$
DU4	261	0.916	$\lesssim 10^{-3}$
DU5	291	0.801	$\lesssim 10^{-3}$
DU6	332	0.701	$\lesssim 10^{-3}$
DU7	350	0.671	0.007
AD1	866	0.479	0.030
AD2	935	0.452	0.038
AD3	1118	0.437	0.093
AD4	1321	0.410	0.222
AD5	1558	0.374	0.323
AD6	1638	0.370	0.356
AD7	1784	0.377	0.470
AD8	1912	0.382	0.507
AD9	2278	0.342	0.607
AD10	2700	0.296	0.805
DD1	360	0.669	0.005
DD2	402	0.597	0.008
DD3	461	0.525	0.019
DD4	554	0.466	0.054
DD5	670	0.436	0.161
DD6	853	0.374	0.279
DD7	1313	0.255	0.507

Keplerian disk-like structures in the early postbounce phase. As recently investigated by Metzger et al. [264] (but not simulated here), the hot disk will experience neutrino-cooling on a timescale of ~ 0.1 s, driving the disk composition neutron-rich to reach $Y_e \sim 0.1$ [264, 111], depleting the pressure support and leading to limited contraction of the inner parts of the disk. The outer and higher-latitude regions expand with a neutrino-driven wind [111]. As discussed by [264], subsequent irradiation of the disk by neutrinos from the PNS increases its proton-to-neutron ratio, and Y_e may reach values as high as ~ 0.5 by the time the weak interactions in the disk freeze out. The disk becomes radiatively inefficient, α-particles begin to recombine and a powerful disk wind develops, blowing off most of the disk's remaining material. Metzger et al. [264] argue that, depending on disk mass, the outflows synthesize of the order of $10^{-3} - 10^{-2}\,M_\odot$ of ^{56}Ni, but very small amounts of intermediate-mass isotopes, making such AIC explosions spectroscopically distinct from ^{56}Ni outflows in standard core-collapse and thermonuclear SNe.

Our results, summarized in Tab. 4.3, show that the masses and the geometry of the disks produced in AIC are sensitive to the angular momentum distribution in the precollapse WDs. In models with uniform rotation below the mass-shedding limit, only a very small amount of low-latitude material rotates at near-Keplerian angular velocities. Therefore, most of the outer core material of such models undergoes significant infall, so that uniformly rotating WDs will generally produce small disks. The largest disk mass for uniform rotation is $M_{\rm disk} \sim 0.03 M_\odot$[8] and is produced in model AU5 which rotates near the mass-shedding limit. Since

[8]We point out that because the disks do not settle down to exact equilibrium right after bounce or not even after shock passage,

the angular velocity of the outer ($\varpi > \varpi_{\rm p}$) core of differentially rotating models is set to reach nearly-Keplerian values (cf. Eq. (4.9)), most of the outer WD envelope has substantial centrifugal support and thus the differentially rotating models yield significantly larger $M_{\rm disk}$. For example, model AD4 which has $\beta_{\rm ic,b}$ and total angular momentum comparable to model AU5 yields a disk mass of $\sim 0.2 M_\odot$.

The total mass of the disk and its equatorial radius (the disk thickness $H_{\rm disk}$) grow with increasing rotation (see Tab. 4.3). Slowly rotating models such as AD1 have little centrifugally supported material and acquire spheroidal shape soon after bounce, resulting in a disk mass as small as $\sim 0.03 M_\odot$. More rapidly rotating models such as AD10 produce significantly more strongly flattened disks, with $R_{\rm e} \sim 2700$ km, $H_{\rm disk} \sim 800$ km and a disk mass $M_{\rm disk}$ of $\sim 0.8 M_\odot$. Due to the greater initial compactness of the higher-density D models, their disks are less massive and have smaller equatorial radii when compared to A models. Hence, when considering two WDs of set A and D with the same total angular momentum, the mass and equatorial extent of the disk in the D model will be smaller by a factor of $\sim 1.5 - 2$.

These results indicate that massive disks of $M_{\rm disk} \gtrsim 0.1 M_\odot$ are unlikely to be compatible with the assumption of uniformly rotating accreting WDs argued for by [361, 332]. In order to produce disks of appreciable mass and significant ^{56}Ni-outflows in AIC, the progenitor must either be an accreting WD obeying a differential rotation law similar to that proposed by [456, 455], or may be the remnant of a binary-WD merger event. However, for the latter, the differential rotation law is unknown and may be very different from what we consider here (for a discussion of binary-WD merger simulations, see, e.g., [353] and references therein).

4.4 Gravitational wave emission

In Fig. 4.15, we present the time evolution of the GW strain h at an assumed source distance of $10\,{\rm kpc}$ for a representative set of AIC models evolved with the $\overline{Y_e}(\rho)$ parametrization obtained from [111]. The GW signals of all models have the same overall morphology. This general AIC GW signal shape bears strong resemblance to GW signals that have been classified as "type III" in the past [466, 118, 316], but also has features in common with the GW signals predicted for rotating iron core collapse ("type I", [123]).

The GW strain h in our AIC models is positive in the infall phase and increases monotonically with time, reaching its peak value in the plunge phase, just $\sim 0.1\,{\rm ms}$ before bounce. Then, h rapidly decreases, reaching a negative peak value within $\sim 1-2\,{\rm ms}$. While the first positive peak is produced by rapid infall of the inner core, the first negative peak is caused by the reversal of the infall velocities at bounce. Following the large negative peak, h oscillates with smaller amplitude with a damping time of ~ 10 ms, reflecting the hydrodynamical ringdown oscillations of the PNS. Although all AIC models of our baseline set produce Type III signals, we can introduce three subtypes whose individual occurrence depends on the parameter $\beta_{\rm ic,b}$ of the inner core at bounce:

Type IIIa. In slowly rotating WDs (that reach $\beta_{\rm ic,b} \lesssim 0.7\,\%$), strong prompt convective overturn develops in the early postbounce phase, adding a lower-frequency contribution to the regular ringdown signal (e.g., models AD1f4, DU3). The largest-amplitude part of this GW signal type comes from the prompt convection. Nevertheless, the GW signal produced by the bouncing centrifugally-deformed inner core is still discernible, with the first positive peak being generally larger by a factor of ~ 2 than the first negative peak. Subsequent ringdown peaks are smaller by a factor of $\gtrsim 3$. We point out that the observed prompt postbounce convection is most likely overestimated in our approach, since we do not take into account neutrino losses and energy deposition by neutrinos in the immediate postshock region, whose effect will quickly smooth out the negative entropy gradient left behind by the shock and thus significantly damp

it is hard to introduce an unambiguous definition of the disk mass. In the present study, we define the disk as the structure that surrounds the PNS at $\varpi > 20$ km with densities below $10^{11}\ {\rm g\,cm^{-3}}$ and angular velocity $\Omega > 0.58\,\Omega_{\rm K}$. The latter condition ensures that the disk cannot contract by more than a factor of ~ 3 as a result of cooling.

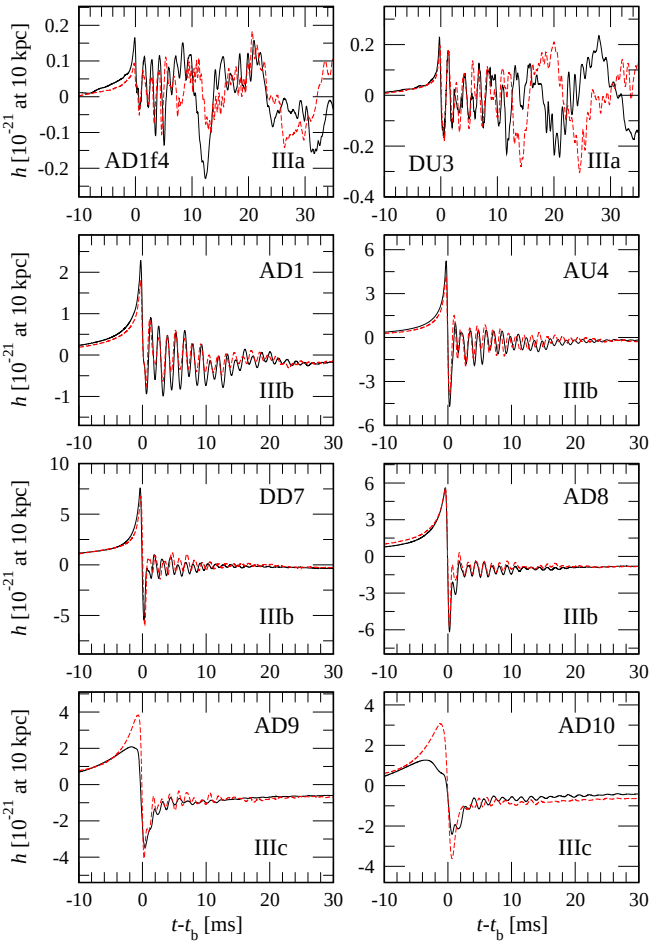

Figure 4.15: Evolution of the dimensionless GW strain h (in units of 10^{-21} at a source distance of 10 kpc) as a function of postbounce time for representative models with different precollapse rotation profiles, central densities and temperatures (low-T models with solid black lines and high-T with dashed red lines). Models with slow and (almost) uniform precollapse rotation (e.g., AD1f4 or DU3) develop considerable prompt postbounce convection visible as a dominating lower-frequency contribution in the waveform. Centrifugal effects damp this prompt convection and the waveforms of models with moderately-rapid rotation (e.g., AD1, AU4, DD7 and AD8) and of rapidly rotating models (e.g., AD9 or AD10) exhibit no such contribution to the signal.

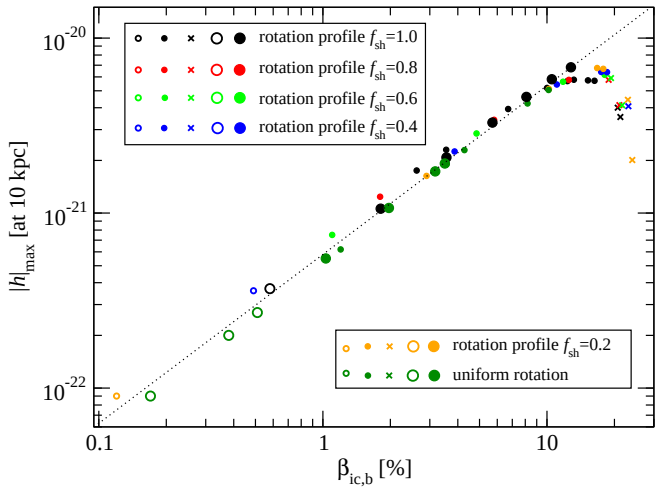

Figure 4.16: Peak value $|h|_{\rm max}$ of the GW amplitude at a source distance of 10 kpc distance for the *burst* signal of all models versus the parameter $\beta_{\rm ic,b}$ of the inner core at the time of bounce. At slow to moderately rapid rotation, $|h|_{\rm max}$ scales almost linearly with $\beta_{\rm ic,b}$ (marked by the dotted straight line), while for $\beta_{\rm b} \gtrsim 16\%$ centrifugal effects reduce $|h|_{\rm max}$. The symbol convention for the various sets is explained in the caption of Fig. 4.8.

this early convective instability in full postbounce radiation-hydrodynamics calculations (see, e.g., [283, 71, 316]).

Type IIIb. In moderately rapidly rotating WDs that reach $0.7 \lesssim \beta_{\rm ic,b} \lesssim 18\,\%$ and still experience a pressure-dominated bounce, convection is effectively suppressed due to a sufficiently large positive specific angular momentum gradient (e.g., [314]). Hence, there is no noticeable convective contribution to the postbounce GW signal (see, e.g., models AD1, AU4, DD7, AD8). For this signal subtype, the peak GW strain $|h|_{\rm max}$ is associated with the first positive peak while relative values of the amplitudes of the first several peaks are similar to type IIIa.

Type IIIc. If rotation is sufficiently rapid and leading to $\beta_{\rm ic,b} \gtrsim 18\,\%$, the core bounces at subnuclear densities due to strong centrifugal support. This is reflected in the GW signal by an overall lower-frequency emission and a significant widening of the bounce peak of the waveform (see, e.g., models AD9, AD10). In some models of this subtype, the negative peak can be comparable to or slightly exceed that of the first positive peak in the waveform. This reflects the fact that the plunge acceleration is apparently reduced more significantly by rotation than is the re-expansion acceleration at core bounce. The postbounce ringdown peaks in all type IIIc models are smaller by a factor of $\gtrsim 2$ compared to the bounce signal. As pointed out in Sec. 4.3.2, uniformly rotating models do not rotate sufficiently rapidly to experience centrifugal bounce. Hence, they do not produce a type IIIc signal.

The AIC GW signal morphology is affected only slightly by variations in WD temperature and their resulting changes in the inner core Y_e that are on the few-percent level for the range of precollapse temperatures considered here. In test calculations with more substantially increased inner-core values of Y_e (see Secs. 4.2.1 and 4.2.3) and, in turn, significantly larger values of $M_{\rm ic,b}$, we find signals that are intermediate between type III and type I.

Key quantitative results from our model simulations are summarized in Tables. 4.2 and 4.4. The waveform data for all models are available for download from [388].

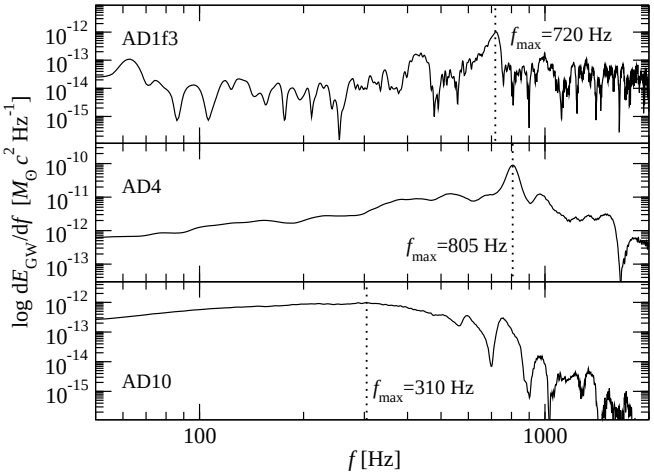

Figure 4.17: Spectral energy density of the GW signal for representative AIC models AD0f3 (top panel), AD4 (center panel), and AD10 (bottom panel). $f_{\rm max}$ is the peak frequency of the GWs emitted at core bounce.

4.4.1 Peak gravitational wave amplitude

Across our entire model set, the peak GW amplitude $|h|_{\rm max}$ covers a range of almost two orders of magnitude, from $\sim 10^{-22}$ to $\sim 10^{-20}$ (at distance to the source of $10\,{\rm kpc}$; see Tab. 4.2). $|h|_{\rm max}$ depends on various parameters and it is difficult to provide a simple description of its systematics that encompasses all cases. In order to gain insight into how $|h|_{\rm max}$ depends on $\Omega_{\rm c,i}$, on differential rotation, on the initial $\rho_{\rm c}$, on the precollapse WD temperature, and on the degree of deleptonization in collapse, we describe below the effects of variations in one of these parameters while holding all others fixed.

(i) In a sequence of precollapse WDs with fixed differential rotation, $\rho_{\rm c}$, and T_0, the peak GW amplitude $|h|_{\rm max}$ increases steeply with $\Omega_{\rm c,i}$ in slowly rotating models that do not come close to being centrifugally supported. When centrifugal effects become dynamically important, $|h|_{\rm max}$ saturates at $\sim 7\times10^{-21}$ (at $10\,{\rm kpc}$) and then decreases with increasing $\Omega_{\rm c,i}$. This reflects the fact that such rapidly spinning inner cores produced by AIC cannot reach high densities and high compactness and that the slowed-down collapse decreases the deceleration at bounce, thus reducing $|h|_{\rm max}$ and pushing the GW emission to lower frequencies.

(ii) In a sequence of precollapse WDs with fixed $\Omega_{\rm c,i}$, T_0, and $\rho_{\rm c}$, an increase in the degree of WD differential rotation leads to an increase in the amount of angular momentum present in the WD inner core at bounce. This translates into an increase of $|h|_{\rm max}$ in models that do not become centrifugally supported and experience a pressure-dominated bounce. The transition to centrifugal bounce is now reached at lower values of $\Omega_{\rm c,i}$ (see Sec. 4.3.2), so that the centrifugal saturation of $|h|_{\rm max}$ described above in *(i)* is reached at much smaller values of $\Omega_{\rm c,i}$.

(iii) In a sequence of precollapse WDs with fixed $\Omega_{\rm c,i}$, T_0, and differential rotation and varying $\rho_{\rm c}$, models with lower (higher) $\rho_{\rm c}$ yield larger (smaller) values of $|h|_{\rm max}$. This is because models that are initially less compact spin up more during collapse (cf. the discussion in Sec. 4.3.2). However, this systematics holds only as long as the model does not become centrifugally supported, which happens for lower (higher) ρ_c WDs at smaller (greater) $\Omega_{\rm c,i}$.

(iv) When only the WD temperature is varied, we find that for slowly to moderately-rapidly rotating WDs, high-T models generally reach smaller $|h|_{\rm max}$ than their low-T counterparts. This is because high-T WDs yield smaller inner cores at bounce, which hold less angular momentum and, as a consequence, are less centrifugally deformed (see Tab. 4.2 and in Fig. 4.15). However, this behavior reverses in rapidly rotating WDs for which low-T models are more centrifugally affected and, hence, yield a smaller $|h|_{\rm max}$ than their

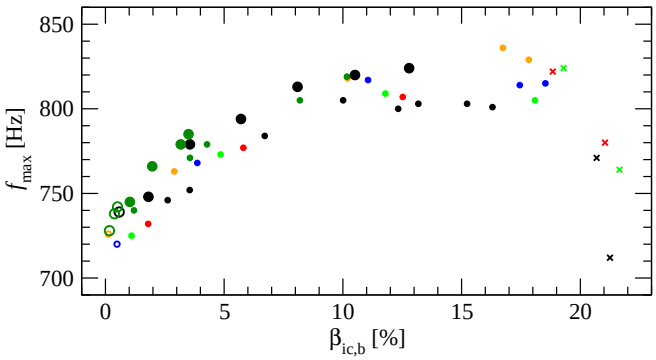

Figure 4.18: Frequency $f_{\rm max}$ at the maximum of the GW spectral energy density in pressure-dominated bounce and a subset of centrifugal bounce models versus the parameter $\beta_{\rm ic,b}$ of the inner core at bounce. The symbol convention for the various sets is explained in the caption of Fig. 4.8.

high-T counterparts.

(v) If the degree of deleptonization is decreased by an ad-hoc increase of inner-core Y_e (see Secs. 4.2.1 and 4.2.3) and all else is kept fixed, $M_{\rm ic,b}$ increases and for slowly to moderately rapidly rotating WDs, $|h|_{\rm max}$ increases. As for the low-T case discussed in the above, this behavior reverses in rapidly rotating WDs for which high-Y_e models are more centrifugally affected and yield smaller $|h|_{\rm max}$ than their lower-Y_e counterparts.

To demonstrate the dependence of $|h|_{\rm max}$ on the overall rotation of the inner core at bounce, we plot in Fig. 4.16 $|h|_{\rm max}$ as a function of the inner core parameter $\beta_{\rm ic,b}$ at bounce for our high-T models. $|h|_{\rm max}$ depends primarily on $\beta_{\rm ic,b}$ and is rather independent of the particular precollapse configuration that leads to a given $\beta_{\rm ic,b}$. For small $\beta_{\rm ic,b}$ far away from the centrifugal limit, we find $|h|_{\rm max} \propto \beta_{\rm ic,b}^{0.74}$, where we have obtained the exponent by a power-law fit of high-T models with $1\% \lesssim \beta_{\rm ic,b} \lesssim 13\%$. This finding is in qualitative agreement with what [123] saw for iron core collapse. The overall maximum of $|h|_{\rm max}$ is reached in WDs that yield $\beta_{\rm ic,b} \sim 16\%$, beyond which $|h|_{\rm max}$ decreases with increasing $\beta_{\rm ic,b}$.

4.4.2 Gravitational-wave energy spectrum

The total energy emitted in GWs is in the range of $\sim 10^{-10} M_\odot c^2 \lesssim E_{\rm GW} \lesssim 2 \times 10^{-8} M_\odot c^2$ in the entire set of models considered in this article. In Fig. 4.17, we plot the GW spectral energy density $dE_{\rm GW}/df$ of the three models AD1f3, AD4 and AD10 as representative examples of the three signal subtypes IIIa - IIIc. The top panel shows model AD1f3 as a representative pressure-dominated bounce model with prompt convection. In such models, there is a strong structured, but broad contribution to the spectrum at low frequencies. The integral of such a contribution (which is present in all models with slow rotation) can exceed that from core bounce in these models. This is not the case in model AD1f3, whose GW burst from bounce is the one leading to the peak at $f_{\rm max} = 720\,{\rm Hz}$.

The central panel of Fig. 4.17 depicts $dE_{\rm GW}/df$ of model AD4 as a representative pressure-dominated bounce model in which no significant postbounce convection occurs. The spectrum of this model exhibits a distinct and narrow high-frequency peak at $f_{\rm max} \sim 805$ Hz. Finally, the bottom panel of Fig. 4.17 refers to model A10 that experiences centrifugal bounce. In this model, the dynamics is dominated by centrifugal effects, leading to low frequency emission and $f_{\rm max} = 310\,{\rm Hz}$, but higher-frequency components are still discernible and are most likely related to prolonged higher-frequency GW emission from the PNS ringdown.

In Fig. 4.18, we plot the peak frequencies $f_{\rm max}$ of the GW energy spectrum as a function of the inner core parameter $\beta_{\rm ic,b}$ for high-T AIC models (the low-T and higher-Y_e models show the same overall systematics). In models that undergo pressure-dominated bounce, $f_{\rm max}$ increases nearly linearly with $\beta_{\rm ic,b}$ in the region

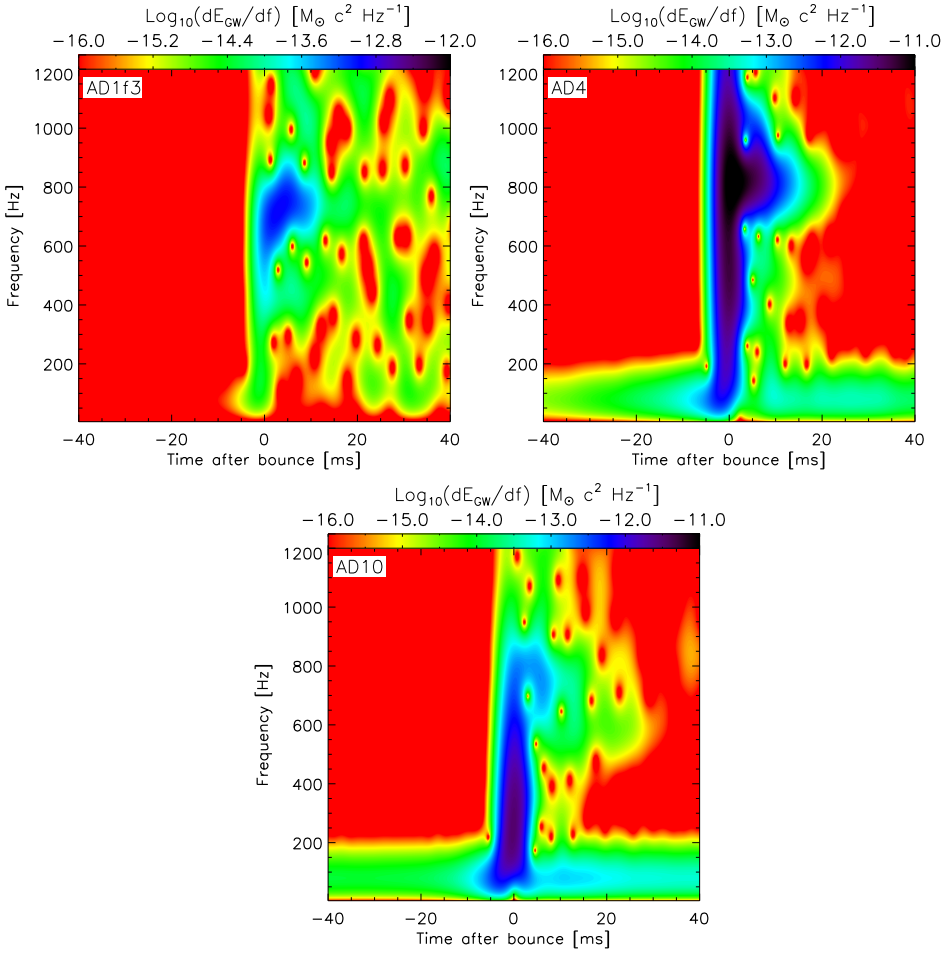

Figure 4.19: Time-frequency colormaps of the GW signals of models AD1f3 (type IIIa), AD4 (type IIIb), and AD10 (type IIIc, see also Fig. 4.17). Plotted is the "instantaneous" spectral GW energy density $dE_{\rm GW}/df$ in a 2-ms Gaussian window as a function of postbounce time. Note the prebounce low-frequency contribution in the moderately-rapidly rotating models (model AD4, center panel) and rapidly rotating models (model AD10, right panel). The range of the colormap of the left panel (model AD1f3) is smaller by one dex than those of the other panels.

$\beta_{\rm ic,b} \lesssim 10\ \%$, while at $\beta_{\rm ic,b}$ in the range of $10\ \% \lesssim \beta_{\rm ic,b} \lesssim 20\ \%$, the growth of $f_{\rm max}$ saturates at ~ 800 Hz and $f_{\rm max}$ does not change significantly with further increase of rotation. For very rapid rotation ($\beta_{\rm ic,b} \gtrsim 20\ \%$), $f_{\rm max}$ decreases steeply with $\beta_{\rm ic,b}$, reaching a value of ~ 400 Hz at $\beta_{\rm ic,b} \simeq 23\,\%$ (not shown in the figure, see Table 4.4).

While it is straightforward to understand the systematics of $f_{\rm max}$ at high $\beta_{\rm ic,b}$ where centrifugal effects slow down collapse and thus naturally push the GW emission to low frequencies, the increase of $f_{\rm max}$ with rotation at low to intermediate $\beta_{\rm ic,b}$ is less intuitive. If one assumes that the dominant GW emission at core bounce in all models is due to the quadrupole component of the fundamental quasi-radial mode of the inner core, one would expect a monotonic decrease of $f_{\rm max}$ with increasing rotation and, hence, decreasing mean core density (see, e.g., [14]). A possible explanation for the increase of $f_{\rm max}$ at slow to moderately-rapid rotation is that the primary GW emission in these models is due to the fundamental quadrupole ${}^2f$-mode, whose frequency may increase with rotation. This has been demonstrated by Dimmelmeier et al. [120] who studied oscillation modes of sequences of $\gamma = 2$ polytropes. To confirm this interpretation, and following

the technique of mode-recycling outlined in [120], we perturb a subset of our postbounce cores with the eigenfunction of the ${}^2f$-mode of a Newtonian nonrotating neutron star. As expected, we find that the resulting dynamics of the postbounce core is dominated by a single oscillation mode with a frequency that matches within $\lesssim 10\%$ the peak frequency $f_{\max}$ of $dE_{\rm GW}/df$ of the corresponding slowly or moderately rapidly rotating AIC model. The interesting details of the mode structure of the inner cores of AIC and iron core collapse will receive further scrutiny in a subsequent publication.

Finally, in Fig. 4.19, we provide time-frequency analyses of the GW signals of the same representative models shown in Fig. 4.17. The analysis is carried out with a short-time Fourier transform employing a Gaussian window with a width of $2\,{\rm ms}$ and a sampling interval of $0.2\,{\rm ms}$. In all three cases, the core bounce is clearly visible and marked by a broadband increase of the emitted energy. The slowly-rotating model AD1f3 emits its strongest burst at $600 - 800\,{\rm Hz}$ ($f_{\max} = 720\,{\rm Hz}$) and subsequently exhibits broadband emission with significant power at lower frequencies due to prompt convection. Model AD4 is more rapidly rotating and shows significant pre-bounce low-frequency emission due to its increased rotational deformation. At bounce, a strong burst, again with power at all frequencies, but primarily at frequencies about its $f_{\max} = 805\,{\rm Hz}$, is emitted. Much of the postbounce $E_{\rm GW}$ is emitted through ringdown oscillations at $f_{\max}$ that may be related to the ${}^2f$ mode of this model's PNS. Finally, in the rapidly rotating and centrifugally bouncing model AD10, we observe again low-frequency emission before bounce, but only a small increase of the primary emission band at bounce to $\sim 200 - 400\,{\rm Hz}$. Nevertheless, there is still an appreciable energy emitted from higher-frequency components of the dynamics at bounce and postbounce times.

4.4.3 Comparing GW signals from AIC and iron core collapse

Recent studies [122, 311, 312, 123] have shown that the collapse of rotating iron cores (ICC) produces GW signals of uniform morphology (so-called "type I" signals, see, e.g., [466]) that generically show one pronounced spike associated with core bounce with a subsequent ringdown and are similar to the type III signals found here for AIC. As in the AIC case, the GW signal of ICC has subtypes for slow, moderately rapid, and very rapid rotation. For comparing AIC and ICC GW signals, we chose three representative AIC models and then pick three ICC models with similar $\beta_{\rm ic,b}$ from the study of Dimmelmeier et al. [123] whose waveforms are freely available from [438]. This should ensure that we compare collapse models that are similarly affected by centrifugal effects for a one-to-one comparison. However, one should keep in mind that the inner core masses $M_{\rm ic,b}$ at bounce of ICC models are generally larger by $\sim 0.2 - 0.3\,M_\odot$ than in our AIC models (see Sec. 4.3.1).

In Fig. 4.20 we present this comparison and plot the GW signals of the high-T AIC models DU2 (slow rotation, type IIIa), AU5 (moderately-rapid rotation, type IIIb), and AD10 (very rapid rotation, type IIIc). In the same order, we superpose the GW signals of the Dimmelmeier et al. [123] models s20A1O05, s20A3O07 and s20A3O15. These models started with the precollapse iron core of a $20\,M_\odot$ star and were run with the same code, EOS, and deleptonization algorithm as our AIC models, though with different, ICC specific $Y_e(\rho)$ trajectories.

The left panel of Fig. 4.20 compares the slowly rotating models DU2 and s20A1O05 that undergo pressure dominated bounce and exhibit strong postbounce convection. As pointed out before, the latter is most likely overestimated in our current approach as well as in Dimmelmeier et al.'s. Note that the width of the waveform peaks associated with core bounce is very similar, indicating very similar emission frequencies. Model s20A1O05 exhibits a significantly larger signal amplitude at bounce. This is due to s20A1O05's larger $M_{\rm ic,b}$ but also to the fact that its $\beta_{\rm ic,b}$ is $\sim 0.7\%$ compared to the $\sim 0.4\%$ of DU2 (a closer match was not available from [438]). The prompt convection in model s20A1O05 is more vigorous and generates a larger-amplitude GW signal than in model DU2. This is due to the much steeper density gradient in the WD core that allows the AIC shock to remain stronger out to larger radii. Hence, it leaves

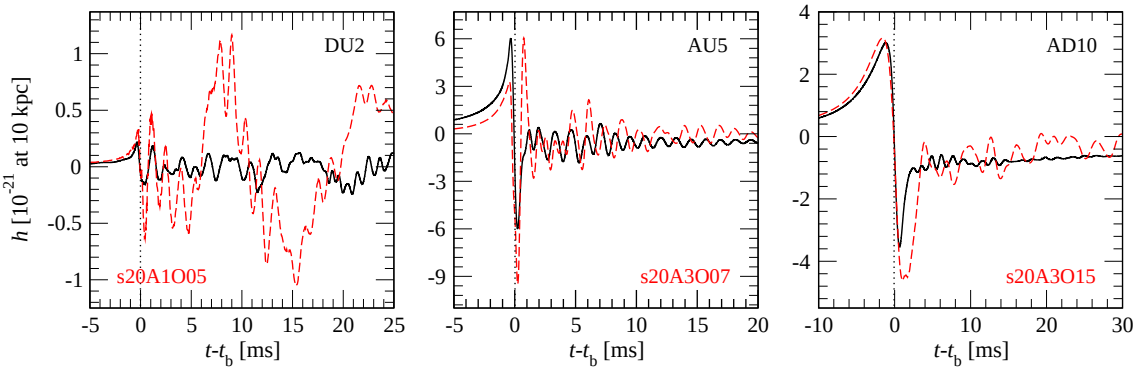

Figure 4.20: Evolution of GW signals in the high-T AIC models DU2, AU5, AD10 (black solid lines) and three massive star iron core-collapse models s20A1O05, s20A3O07 and s20A3O15 (red dashed lines) from the model set of Dimmelmeier et al. [123]. The AIC model DU2 and the iron core collapse model s20A1O05 undergo pressure-dominated bounce with significant prompt convection. Models AU5 and s20A3O7 experience pressure-dominated bounce without significant convection, and models AD10 and s20A3O15 undergo centrifugal bounce. The inner cores of models DU2, AU5 and AD10 (s20A1O05, s20A3O07 and s20A3O15) reach values of $\beta_{\rm ic,b}$ of about 0.4%, 10.2% and 21.3% (0.7%, 10.1%, and 21.6%). Times are given relative to the time of core bounce which we mark with a vertical line.

behind a shallower negative entropy gradient, leading to weaker convection and postbounce GW emission.

In the central panel of Fig. 4.20 we compare two moderately-rapidly rotating models with nearly identical $\beta_{\rm ic}$ of $\sim 10\%$. Both models show a pre-bounce rise due to the inner core's accelerated collapse in the plunge phase. The AIC inner core, owing to its lower Y_e and weaker pressure support, experiences greater acceleration and emits a higher-amplitude signal than its ICC counterpart in this phase. At bounce, the stiff nuclear EOS decelerates the inner core, leading to the large negative peak in the GW signal. Because of the more massive inner core in ICC and since the EOS governing the dynamics is identical in both models, the magnitude of this peak is greater in the ICC model. Following bounce, the ICC model's GW signal exhibits a large positive peak of comparable or larger amplitude than the pre-bounce maximum. This peak is due to the re-contraction of the ICC inner core after the first strong expansion after bounce. With increasing rotation, this re-contraction and the associated feature in the waveform become less pronounced. On the other hand, due to its smaller inertia, the AIC inner core does not significantly overshoot its new postbounce equilibrium during the postbounce expansion. Hence, there is no appreciable postbounce re-contraction and no such large positive postbounce peak in the waveform.

Example waveforms of AIC and ICC models experiencing core bounce governed by centrifugal forces are shown in the right panel of Fig. 4.20. In this case, the pre-bounce plunge dynamics are significantly slowed down by centrifugal effects and the GW signal evolution is nearly identical in AIC and ICC. At bounce, the more massive inner core of the ICC model leads to a larger and broader negative peak in the waveform and its ringdown signal exhibits larger amplitudes than in its AIC counterpart.

Finally, we consider AIC models with variations in the inner-core Y_e due either to different precollapse WD temperatures or ad-hoc changes of the $\overline{Y_e}(\rho)$ parametrization (see Secs. 4.2.1 and 4.2.3). Lower-T WDs yield larger inner-core values of Y_e and, in turn, larger $M_{\rm ic,b}$ and GW signals that are closer to their iron-core counterparts. The same is true for models in which we impose an increased inner-core Y_e: AIC models with inner-core Y_e 10% larger than predicted by [111] still show clear type III signal morphology while models with 20% larger Y_e fall in between type III and type I.

To summarize this comparison: rotating AIC and rotating ICC lead to qualitatively and quantitatively fairly similar GW signals that most likely could not be distinguished by only considering general signal characteristics, such as maximum amplitudes, characteristic frequencies and durations. A detailed knowl-

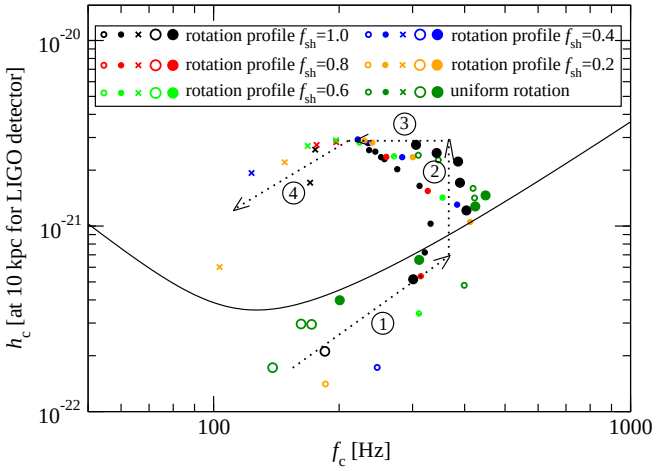

Figure 4.21: Detector-dependent characteristic amplitudes of the GW signals of all models at an assumed distance of 10 kpc. The symbol convention for the various sets is described in the caption of Fig. 4.8. See the text for a discussion of the numbers and arrows.

edge of the actual waveform would be necessary, but even in this case, a distinction between AIC and ICC on the basis of the comparison presented here would be difficult. It could only be made for moderately-rapidly spinning cores based on the presence (ICC, type Ib) or absence (AIC, type IIIb) of a first large positive peak in the waveform, but, again, *only* if AIC inner cores indeed have significantly smaller Y_e than their iron-core counterparts. ICC and AIC waveforms of types Ia/IIIa and Ic/IIIc are very similar. Additional astrophysical information concerning the distance to the source and its orientation as well as knowledge of the neutrino and electromagnetic signatures will most likely be necessary to distinguish between AIC and ICC.

4.4.4 Detection prospects for the gravitational wave signal from AIC

In order to assess the detection prospects for the GW signal from AIC, we evaluate the characteristic signal frequency f_c and the dimensionless characteristic GW amplitude h_c. Both quantities are detector-dependent and are computed using Eq. (2.156) and (2.157), respectively.

In Fig. 4.21, we show h_c for all models as a function of f_c for an initial 4-km LIGO detector, assuming a source distance of 10 kpc. For comparison with detector sensitivity, we include initial LIGO's design $h_{\rm rms}$ curve [232]. The distribution of our set of models in this figure obeys simple systematics. A number of very slowly rotating models that undergo pressure-dominated bounce with prompt convection (type IIIa) form a cluster in frequency in one region (near arrow 1). These models have the overall lowest values of h_c and exhibit low values of f_c in the range of $130 - 350$ Hz. Both f_c and h_c grow with increasing rotation (along arrow 1). For the pressure-dominated bounce models without significant prompt convection (type IIIb), h_c grows with increasing rotation (along arrow 2), now at practically constant f_c of ~ 350 Hz. Even for these models, f_c is always lower than the typical peak frequency $f_{\rm max} \sim 700 - 800$ Hz of their spectral GW energy densities. This is due to the specific characteristics of the LIGO detector, whose highest sensitivity is around 100 Hz, thus leading to a systematic decrease of f_c with respect to $f_{\rm max}$.

In more rapidly rotating models, centrifugal effects become more important, leading to greater rotational deformation of the inner core, but also slowing down the dynamics around core bounce, ultimately limiting h_c and reducing f_c (along arrow 3). Models that rotate so rapidly that they undergo centrifugal bounce (type IIIc) cluster in a separate region in the $h_c - f_c$ plane (along arrow 4), somewhat below the maximum value of h_c and at considerably lower f_c. The systematics for the lower-T models and for other detectors is very similar. Not surprisingly, given the analogies in the two signals, a similar behavior of h_c and f_c was

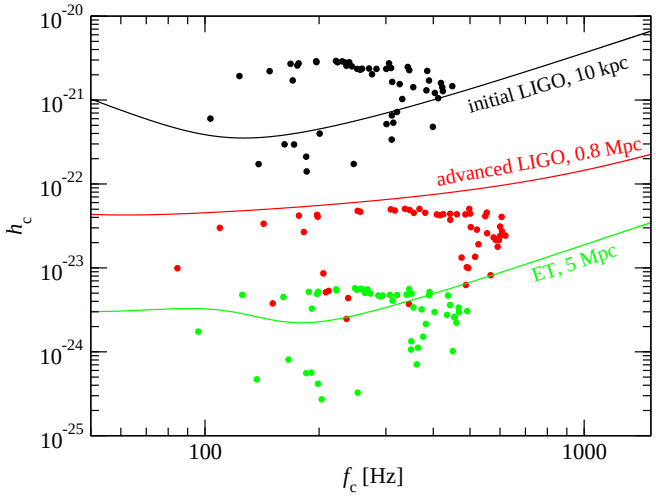

Figure 4.22: Location of the GW signals from core bounce in the h_c–f_c plane relative to the sensitivity curves of various interferometer detectors (as color-coded) for an extended set of models AD. The sources are at a distance of 10 kpc for LIGO, 0.8 Mpc for Advanced LIGO, and 5 Mpc for the Einstein Telescope.

observed in the context of rotating iron core collapse [123].

Figure 4.22 provides the same type of information shown in Fig. 4.21 but also for the advanced LIGO detector when the source is at 0.8 kpc (e.g., within the Andromeda galaxy), or for the proposed Einstein Telescope (ET) [138] and a source distance of 5 Mpc. Initial LIGO is sensitive only to GWs coming from a moderately-rapidly or rapidly rotating AIC event in the Milky Way, but its advanced version will probably be able to reveal sources also outside the Galaxy, although only within the local group. Finally, third-generation detectors such as ET, may be sensitive enough to detect some AIC events out to ~ 5 Mpc.

As pointed out in Secs. 4.4.1 and 4.4.2, the GW signal amplitudes and the spectral GW energy distribution is determined primarily by $\beta_{\rm ic,b}$. Hence, given the systematics shown in Fig. 4.21, one may be optimistic about being able to infer $\beta_{\rm ic,b}$ to good precision from the observation of GWs from a rotating AIC event. For example, as demonstrated in Fig. 4.18, even the knowledge of only $f_{\rm max}$ can put some constraints on $\beta_{\rm ic,b}$. However, inferring accurately the properties of the progenitor WD using exclusively information provided by GWs may be extremely difficult given the highly degenerate dependence of $\beta_{\rm ic,b}$ on the various precollapse WD model parameters discussed in Sec. 4.3.2. To elaborate on this point, we show in Fig. 4.23 the relation between $\beta_{\rm ic,b}$ and the precollapse WD parameter $\beta_{\rm i}$. Even if GWs can provide good constraints on $\beta_{\rm ic,b}$, a rather large variety of models with different initial rotational properties would be able to lead to that same $\beta_{\rm ic,b}$ and additional astrophysical information on the progenitor will be needed to determine the precollapse rotational configuration. The only exception to this is the possibility of ruling out uniform WD progenitor rotation if $\beta_{\rm ic,b} \gtrsim 18\%$ (cf. Sec. 4.3.2).

4.5 Prospects for nonaxisymmetric rotational instabilities

Nonaxisymmetric rotational instabilities in PNSs formed in AIC or iron core collapse have long been proposed as strong and possibly long-lasting sources of GWs (see, e.g., [316] for a recent review). The post-bounce GW emission by nonaxisymmetric deformations of rapidly rotating PNSs could be of similar amplitude as the signal from core bounce and, due to its potentially much longer duration, could exceed it in emitted energy (e.g., [312, 311, 367]). Moreover, since the characteristic GW amplitude $h_{\rm c}$ scales with the square root of the number of cycles, the persistence of the nonaxisymmetric dynamics for many rotation

Table 4.4: GW signal characteristics for the high-T AIC models: $E_{\rm GW}$ is the total GW energy, $f_{\rm max}$ is the peak frequency of the GW energy spectrum, Δf_{50} is the frequency interval around $f_{\rm max}$ that emits $50\ \%$ of $E_{\rm GW}$. The nonrotating models are omitted here.

AIC model	$E_{\rm GW}$ $[10^{-9} M_\odot c^2]$	$f_{\rm max}$ [Hz]	Δf_{50} [Hz]
AU1	1.1	742.7	31
AU2	5.7	782.7	28
AU3	7.8	786.7	27
AU4	15.7	816.0	49
AU5	17.0	831.9	120
DU1	0.1	768.0	343
DU2	0.3	770.0	556
DU3	0.4	747.0	473
DU4	0.9	745.0	304
DU5	2.0	765.7	26
DU6	4.6	778.3	21
DU7	5.8	788.3	20
AD1	2.2	752.6	33
AD2	3.7	765.4	30
AD3	8.7	790.5	37
AD4	11.8	812.5	115
AD5	14.2	813.6	173
AD6	15.0	815.0	201
AD7	15.5	815.1	220
AD8	13.8	811.0	245
AD9	1.8	806.0	413
AD10	1.0	304.0	126
DD1	0.3	740.0	324
DD2	1.4	746.7	62
DD3	4.6	780.1	21
DD4	9.3	793.6	22
DD5	15.2	813.7	21
DD6	18.5	820.2	48
DD7	22.3	826.9	152
AD1f1	1.3	745.7	54
AD1f2	0.6	731.4	69
AD1f3	0.2	726.5	315
AD1f4	0.1	737.0	476
AD3f1	7.7	787.0	36
AD3f2	7.0	781.2	31
AD3f3	5.5	777.2	27
AD3f4	3.7	769.8	27
AD6f1	15.7	818.0	175
AD6f2	16.0	819.5	165
AD6f3	16.0	822.6	145
AD6f4	15.8	827.6	123
AD9f1	5.4	805.5	323
AD9f2	11.8	813.0	273
AD9f3	15.9	833.0	263
AD9f4	19.5	844.0	254
AD10f1	1.9	808.0	137
AD10f2	5.8	809.0	333
AD10f3	12.1	826.6	269
AD10f4	16.5	840.0	263
AD11f2	3.4	794.0	105
AD12f3	0.8	165.5	44
AD12f4	1.4	231.0	73
AD13f4	0.07	62.5	60

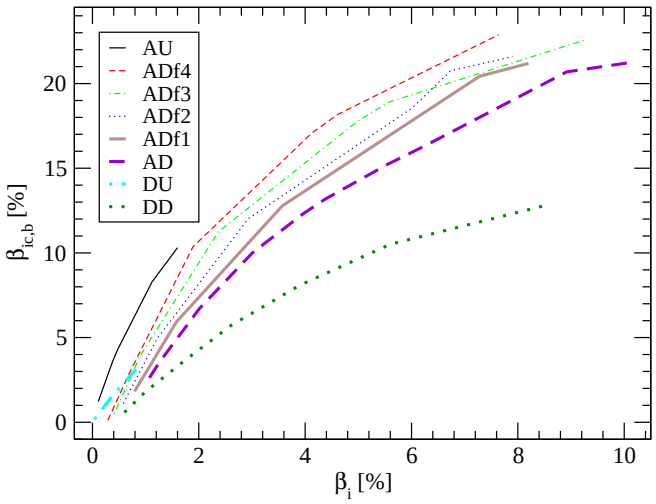

Figure 4.23: The inner core parameter $\beta_{\rm ic,b}$ at bounce is plotted as a function of the precollapse parameter $\beta_{\rm i}$ for high-T models. Due to different central densities and rotation profiles of the precollapse WD models, there is no one-to-one correspondence between $\beta_{\rm ic,b}$ and $\beta_{\rm i}$. Hence, although one can extract $\beta_{\rm ic,b}$ accurately from the bounce AIC GW signal, it is impossible to put strong constraints on $\beta_{\rm i}$ using the GW signal.

periods can drastically increase the chances for detection.

The simulations presented in this work impose axisymmetry, hence we are unable to track the formation and evolution of rotationally induced nonaxisymmetric structures. Nonetheless, since the dynamical high-β instability can develop only at β above $\beta_{\rm dyn} \simeq 0.25$ [22, 250], we can still assess the prospects for such instabilities by studying the values of β reached by our AIC models. Moreover, as we shall see below, the analysis of the rotational configuration of the newly formed PNS can give a rough idea about the outlook also for low-β instabilities.

As shown in Sec. 4.3.2, for not very rapidly rotating models, the parameter $\beta_{\rm ic,b}$ of the inner core at bounce increases with the progenitor rotation and saturates at $\sim 24.5\,\%$ (see Fig. 4.10). Immediately after bounce, the inner core re-expands and, after undergoing several damped oscillations, settles into a new quasi-equilibrium state with a $\beta_{\rm ic,pb}$ typically smaller by $\sim 3\,\%$ (in relative value) than that at bounce. The highest value of $\beta_{\rm ic,pb}$ of our entire model set is $\sim 24\,\%$ (observed in model AD12f4) and most other rapidly rotating models reach values of $\beta_{\rm ic,pb}$ that are well below this value (cf. Tab. 4.2). Hence, we do not expect the high-β instability to occur immediately after bounce in most AIC events.

On the other hand, the matter around the PNS experiences rapid neutrino-cooling (not modeled by our approach) and the PNS contracts significantly already in the early postbounce phase. This results in spin-up and in a substantial increase of $\beta_{\rm ic,pb}$. Using the VULCAN/2D code, Ott [310] studied the postbounce evolution of the PNS rotation of the Dessart et al. AIC models [111]. He found that, in the case of the rapidly rotating $1.92 M_\odot$ model, the postbounce contraction leads to a growth of $\beta_{\rm ic,pb}$ by $\sim 50\,\%$ from $\sim 14\,\%$ to $\sim 22\,\%$ in the initial ~ 50 ms after bounce. We expect that a similar increase of the parameter $\beta_{\rm ic,pb}$ should take place also for the rapidly rotating AIC models considered here. More specifically, if we assume that β increases by $\sim 50\,\%$ within ~ 50 ms after bounce, we surmise that AIC models with $\beta_{\rm ic,b} \gtrsim 17\,\%$ at bounce should reach $\beta_{\rm ic,pb} \gtrsim \beta_{\rm dyn}$ within this postbounce interval and thus become subject to the high-β dynamical instability.

As mentioned in Sec. 4.3.2, uniformly rotating WDs cannot reach $\beta_{\rm ic,pb}$ in excess of $\sim 10.5\,\%$. Hence, they are unlikely to become subject to the high-β dynamical nonaxisymmetric instability, but may contract and spin up to $\beta \geq \beta_{\rm sec} \simeq 14\,\%$ at which they, in principle, could experience a secular nonaxisymmetric

instability in the late postbounce phase. However, other processes, e.g., MHD dynamos and instabilities (see, e.g., [25, 92]) may limit and/or decrease the PNS spin on the long timescale needed by a secular instability to grow.

In addition to the prospects for the high-β instability, the situation appears favorable for the low-β instability as well. The latter can occur at much lower values of β as long as the PNS has significant *differential* rotation (see, e.g., [377, 435, 357, 93, 307, 367, 312] and references therein). While this instability's true nature is not yet understood, a necessary condition for its development seems to be the existence of a corotation point inside the star, i.e., a point where the mode pattern speed coincides with the local angular velocity [435, 357]. Bearing in mind that the lowest order unstable modes have pattern speeds of the order of the characteristic Keplerian angular velocity $\mathcal{O}(\Omega_{\rm char})$ [90], we can easily verify whether such a criterion is ever satisfied in our models. Assuming a characteristic mass of the early postbounce PNS of $\sim 0.8 M_\odot$ and a radius of $\sim$ 20 km, we obtain a characteristic Keplerian angular velocity of $\Omega_{\rm char} \sim 4\ {\rm rad\,ms^{-1}}$. Because most AIC models that reach $\beta_{\rm ic,pb} \gtrsim 15\,\%$ have a peak value of $\Omega \gtrsim 5\ {\rm rad\ ms^{-1}}$, it is straightforward to conclude that these models will have a corotation point and, hence, that the low-β instability may be a generic feature of rapidly rotating AIC. We note that even uniformly rotating precollapse models have strong differential rotation in the postshock region outside the inner core. However, further investigation is needed to infer whether such models may be also be subject to low-β dynamical instability.

As a concluding remark we stress that the above discussion is based on simple order-of-magnitude estimates and is therefore rather inaccurate. Reliable estimates can be made only by performing numerical simulations in 3D that adequately treat the postbounce deleptonization and contraction of the PNS and that investigate the dependence of the instability on $\beta_{\rm ic,pb}$, on the degree of differential rotation, and on the thermodynamic and MHD properties of the PNS. Finally, these calculations will also establish what is the effective long-term dynamics of the bar-mode deformation. In simulations of isolated polytropes [22, 250] and from perturbative calculations [358], it was found that coupling among different modes tends to counteract the bar-mode instability on a dynamical timescale after its development. It is yet unclear whether this behavior will be preserved also in the AIC scenario, where infalling material with high specific angular momentum may lead to significant changes. This will be the subject of future investigations.

4.6 Summary and conclusions

In this work we have presented the first general-relativistic simulations of the axisymmetric AIC of massive white dwarfs to protoneutron stars. Using the general-relativistic hydrodynamics code CoCoNuT, we performed 114 baseline model calculations, each starting from a 2D equilibrium configuration, using a finite-temperature microphysical EOS, and a simple, yet effective parametrization scheme of the electron fraction Y_e that provides an approximate description of deleptonization valid in the collapse, bounce, and very early postbounce phases. The precollapse structure and rotational configuration of WDs that experience AIC is essentially unconstrained. This prompted us to carry out this work. With our large set of model calculations, we have investigated the effects on the AIC evolution of variations in precollapse central density, temperature, central angular velocity, differential rotation, and deleptonization in collapse. The inclusion of general relativity enabled us to correctly describe the AIC dynamics and our extended model set allowed us for the first time to study systematically GW emission in the AIC context.

We find that the overall dynamics in the collapse phase of AIC events is similar to what has long been established for rotating iron core collapse. A universal division in homologously collapsing inner core and supersonically infalling outer core obtains and the self-similarity of the collapse nearly completely washes out any precollapse differences in stellar structure in the limit of slow rotation. Due to the high degeneracy of the electrons in the cores of AIC progenitor WDs, electron capture is predicted to be strong already in early phases of collapse [111], leading to a low trapped lepton fraction and consequently small inner

core masses $M_{\rm ic,b}$ at bounce of around $0.3\,M_\odot$ which decrease somewhat with increasing precollapse WD temperature due to the temperature dependent abundance of free protons. Test calculations motivated by potential systematic biases of the AIC $\overline{Y_e}(\rho)$ trajectories obtained from [111] (see Secs. 4.2.1 and 4.2.3) with inner-core values of Y_e increased by $\sim 10\%$ and $\sim 20\%$ yielded values $M_{\rm ic,b}$ larger by $\sim 11\%$ and $\sim 25\%$.

Our simulations show that rotation can have a profound influence on the AIC dynamics, but will *always* stay subdominant in the collapse of uniformly rotating WDs whose initial angular velocity is constrained by the Keplerian limit of surface rotation. In rapidly differentially rotating WDs, on the other hand, centrifugal support can dominated the plunge phase of AIC and lead to core bounce at subnuclear densities. We find that the parameter $\beta_{\rm ic,b} = (E_{\rm rot}/|W|)_{\rm ic,b}$ of the inner core at bounce provides a unique mapping between inner core rotation and late-time collapse and bounce dynamics, but the mapping between precollapse configurations and $\beta_{\rm ic,b}$ is highly degenerate, i.e., multiple, in many cases very different precollapse configurations of varying initial compactness and total angular momentum, can yield practically identical $\beta_{\rm ic,b}$ and corresponding collapse/bounce dynamics.

Recent phenomenological work presented in [264, 265] on the potential EM display of an AIC event has argued for both uniform WD rotation [264, 332] and massive quasi-Keplerian accretion disks left behind at low latitudes after AIC shock passage. The analysis of our extensive model set, on the other hand, shows that uniformly rotating WDs produce no disks at all or, in extreme cases that are near mass shedding at the precollapse stage, only very small disks ($M_{\rm disk} \lesssim 0.03 M_\odot$). Only rapidly differentially rotating WDs yield the large disk masses needed to produce the enhanced EM signature proposed in [264, 265].

An important focus of this work has been on the GW signature of AIC. GWs, due to their inherently multi-D nature, are ideal messengers for the rotational dynamics of AIC. We find that all AIC models following our standard $\overline{Y_e}(\rho)$ parametrizations yield GW signals of a generic morphology which has been classified previously as *type III* [466, 118, 310]. This signal type is due primarily to the small inner core masses at bounce obtained in these models. We distinguish between three subtypes of AIC GW signals. Type IIIa occurs for $\beta_{\rm ic,b} \lesssim 0.7\%$ (slow rotation), is due in part to early postbounce prompt convection and results in peak GW amplitudes $|h_{\rm max}| \lesssim 5\times10^{-22}$ (at 10 kpc) and emitted energies $E_{\rm GW} \lesssim$ few $\times$ $10^{-9}\,M_\odot\,c^2$. Most of our AIC models produce type IIIb GW signals that occur for $0.7 \lesssim \beta_{\rm ic,b} \lesssim 18\%$ (moderate/moderately rapid rotation) and yield $6\times10^{-22} \lesssim |h_{\rm max}|\,({\rm at\,10\,kpc}) \lesssim 8\times10^{-21}$ and emitted energies of $9\times10^{-10} M_\odot\,c^2 \lesssim E_{\rm GW} \lesssim 2\times10^{-8}\,M_\odot\,c^2$. Rotation remains subdominant in type IIIa and type IIIb models and we find that there is a monotonic and near-linear relationship between maximum GW amplitude and the rotation of the inner core which is best described by the power law $|h_{\rm max}| \propto 10^{-21}\beta_{\rm ic,b}^{0.74}$. Furthermore, we find that the frequencies $f_{\rm max}$ at which the GW spectral energy densities of type IIIa and IIIb models peak are in a rather narrow range from ~ 720 Hz to ~ 840 Hz and exhibit a monotonic growth from the lower to the upper end of this range with increasing rotation. This finding suggests that the GW emission in these models is driven by the fundamental quadrupole (^2f) mode of the inner core.

In the dynamics of AIC models that reach $\beta_{\rm ic,b} \gtrsim 18\%$, centrifugal effects become dominant and lead to core bounce at subnuclear densities. Such models must be differentially rotating at the onset of collapse and produce type IIIc GW signals with maximum amplitudes of $4.0\times10^{-22} \lesssim |h_{\rm max}|\,({\rm at\,10\,kpc}) \lesssim 5.5\times10^{-21}$, emitted energies of $10^{-10} M_\odot\,c^2 \lesssim E_{\rm GW} \lesssim 10^{-8} M_\odot\,c^2$, and peak frequencies of $62\,{\rm Hz} \lesssim f_{\rm max} \lesssim 800\,{\rm Hz}$. In contrast too type IIIa and IIIb models, in type IIIc models, $|h_{\rm max}|$, $E_{\rm GW}$, and $f_{\rm max}$ decrease monotonically with increasing $\beta_{\rm ic,b}$.

Combining the information from signal morphology, $|h_{\rm max}|$, $E_{\rm GW}$ and $f_{\rm max}$, we conclude that already first-generation interferometer GW detectors should be able to infer the rotation of the inner core at bounce (as measured by $\beta_{\rm ic,b}$) from a Galactic AIC event. Due to the degenerate dependence of $\beta_{\rm ic,b}$ on initial model parameters, this can put only loose constraints on the structure and rotational configuration of the progenitor WD. However, the observation of an AIC with $\beta_{\rm ic,b} \gtrsim 18\%$ would rule out uniform progenitor

rotation.

Studying the configurations of the protoneutron stars formed in our AIC models, we find that none of them are likely to experience the high-β nonaxisymmetric bar-mode instability at very early postbounce times. We estimate, however, that all models that reach $\beta_{\rm ic,b} \gtrsim 17\%$ will contract and reach the instability threshold within $\sim 50\,{\rm ms}$ after bounce. Less rapidly spinning models will require more time or will go unstable to the low-β instability. The latter requires strong differential rotation which is ubiquitous in the outer PNS and in the postshock region of our AIC models. AIC progenitors, due to their evolution through accretion or formation through merger, are predestined to be rapidly rotating and form PNSs that are likely to become subject to nonaxisymmetric instabilities. This is in contrast to the precollapse iron cores of ordinary massive stars that are expected to be mostly slowly-spinning objects [185, 309]. We conclude that the appearance of nonaxisymmetric dynamics driven by either the low-β or high-β instability and the resulting great enhancement of the GW signature may be a generic aspect of AIC and must be investigated in 3D models.

The comparison of the GW signals of our axisymmetric AIC models with the gravitational waveforms of the iron core collapse models of Dimmelmeier et al. [123] reveals that the overall characteristics of the signals are rather similar. It appears unlikely that AIC and iron core collapse could be distinguished on the basis of the axisymmetric parts of their GW signals alone, unless detailed knowledge of the signal time series as well as of source orientation and distance is available to break observational degeneracies.

The results of our AIC simulations presented in this work and the conclusions that we have drawn on their basis demonstrate the complex and in many cases degenerate dependence of AIC outcomes and observational signatures on initial conditions. The observation of GWs from an AIC event can provide important information on the rotational dynamics of AIC. However, to lift degeneracies in model parameters and gain full insight, GW observations must be complemented by observations of neutrinos and electromagnetic waves. These multi-messenger observations require underpinning by comprehensive and robust computational models that have no symmetry constraints and include all the necessary physics to predict neutrino, electromagnetic, and GW signatures.

As a point of caution, we note that the generic type III GW signal morphology observed in our AIC models is due to the small inner-core values of Y_e and consequently small inner core masses predicted by the $\overline{Y_e}(\rho)$ parametrization obtained from the approximate Newtonian radiation-hydrodynamic simulations of [111]. Tests with artificially reduced deleptonization show that the signal shape becomes a mixture of type III found in our study and type I observed in rotating iron core collapse [123] if the Y_e in the inner core is larger by $\sim 20\%$. In a follow-up study, we will employ $\overline{Y_e}(\rho)$ data from improved general-relativistic radiation-hydrodynamics simulations [284] to better constrain the present uncertainties of the AIC inner-core electron fraction.

Although performed using general-relativistic hydrodynamics, the calculations discussed here are limited to conformally-flat spacetimes and axisymmetry. We ignored postbounce deleptonization, neutrino cooling, and neutrino heating. We also neglected nuclear burning, employed only a single finite-temperature nuclear EOS, and were forced to impose ad-hoc initial temperature and electron fraction distributions onto our precollapse WD models in rotational equilibrium. Future studies must overcome the remaining limitations to build accurate models of AIC. Importantly, extensive future 3D radiation-hydrodynamic simulations are needed to address the range of possible, in many cases probably nonaxisymmetric, postbounce evolutions of AIC and to make detailed predictions of their signatures in GWs, neutrinos, and in the electromagnetic spectrum.

Chapter 5

The Magnetosphere of Oscillating Neutron Stars in General Relativity

5.1 Introduction

Study of the internal structure of neutron stars (NSs) is of fundamental importance for subatomic physics since these objects provide a laboratory for studying the properties of high-density matter under very extreme conditions. In particular, there is the intriguing possibility of using NS oscillation modes as a probe for constraining models of the equation of state of matter at supranuclear densities. It was suggested long ago that if a NS is oscillating, then traces of this might be revealed in the radiation which it emits [320, 424, 66, 51, 125, 131]. Recently, a lot of interest has been focussed on oscillations of magnetized NSs because of the discovery of gamma-ray flare activity in Soft Gamma-Ray Repeaters (SGRs) which are thought to be the very highly magnetised NSs known as magnetars (for recent review on the SGRs see [444, 437]). The giant flares in these objects are thought to be powered by global reconfigurations of the magnetic field and it has been suggested that the giant flares might trigger starquakes and excite global seismic pulsations of the magnetar crust [411, 412, 369, 131]. Indeed, analyses of the observations of giant flares have revealed that the decaying part of the spectrum exhibits a number of quasi-periodic oscillations (QPOs) with frequencies in the range from a few tens of Hz up to a few hundred Hz [197, 394, 436] and there has been a considerable amount of theoretical effort attempting to identify these with crustal oscillation modes [167, 362, 226, 383, 384]. While there is substantial evidence that the observed SGR QPOs are caused by neutron star pulsations, there is a great deal of uncertainty about how stellar surface motion gets translated into the observed features of the X-ray radiation [393, 394, 421]. To make progress with this, it is necessary to develop a better understanding of the processes occurring in the magnetospheres of oscillating neutron stars.

Standard pulsars typically have magnetic fields of around 10^{12} G while magnetars may have fields of up to $10^{14} - 10^{15}$ G near to the surface. Rotation of a magnetized star generates an electric field:

$$E^{\rm rot} \sim \frac{\Omega R}{c} B \,, \tag{5.1}$$

where B is the magnetic field strength, c is the speed of light and Ω is the angular velocity of the star with radius R. Depending on the rotation velocity and the magnetic field strength, the electric field may be as strong as 10^{10} V cm^{-1} and it has a longitudinal component (parallel to B) which can be able to pull charged particles away from the stellar surface, if the work function is sufficiently small, and accelerate them up

to ultra-relativistic velocities. This result led Goldreich & Julian [173] to suggest that a rotating NS with a sufficiently strong magnetic field should be surrounded by a magnetosphere filled with charge-separated plasma which screens the accelerating electric field and thus hinders further outflow of charged particles from the stellar surface. Even if the binding energy of the charged particles is sufficiently high to prevent them being pulled out by the electric field, the NS should nevertheless be surrounded by charged particles produced by plasma generation processes [395, 354], which again screen the longitudinal component of the electric field. These considerations led to the development of a model for pulsar magnetospheres which is frequently called the "standard model" (an in depth discussion and review of this can be found in, e.g., [267, 44, 45]).

Timokhin, Bisnovatyi-Kogan & Spruit (2000) [418] (referred to as TBS from here on) showed that an oscillating magnetized NS should also have a magnetosphere filled with charge-separated plasma, even if it is not rotating, since the vacuum electric field induced by the oscillations would have a large radial component which can be of the same order as rotationally-induced electric fields. One can show this quantitatively by means of the following simple arguments. To order of magnitude, the radial component of the vacuum electric field generated by the stellar oscillations is given by

$$E^{\rm osc} \sim \frac{\omega\xi}{c} B \,, \tag{5.2}$$

where ω is the oscillation frequency and ξ is the displacement amplitude. Using this together with Eq.(5.1), it follows immediately that the electric field produced by oscillations will be stronger than the rotationally induced one for sufficiently slowly-rotating neutron stars, having

$$\Omega \lesssim \frac{\omega\xi}{R} \,. \tag{5.3}$$

For stellar oscillations with $\xi/R \sim 0.001$ and $\omega \sim 1$ kHz, the threshold is $\Omega \sim 1$ Hz. Within this context, TBS developed a formalism extending the basic aspects of the standard pulsar model to the situation for a non-rotating magnetized NS undergoing arbitrary oscillations. This formalism was based on the assumption of low current densities in the magnetosphere, signifying that the influence of currents outside the NS on electromagnetic processes occurring in the magnetosphere is negligibly small compared to that of currents in the stellar interior. This assumption leads to a great simplification of the Maxwell equations, which then can be solved analytically. As an application of the formalism, TBS considered toroidal oscillations of a NS with a dipole magnetic field, and obtained analytic expressions for the electromagnetic field and charge density in the magnetosphere. (Toroidal oscillations are thought to be particularly relevant for magnetar QPO phenomena.) They found that the low current density approximation (LCDA) is valid for at least half of all toroidal oscillation modes and analyzed the energy losses due to plasma outflow caused by these modes for cases where the size of the polar cap (the region on the stellar surface that is crossed by open magnetic field lines) is small, finding that the energy losses are strongly affected by the magnetospheric plasma. For oscillation amplitudes larger than a certain critical value, they found that energy losses due to plasma outflow were larger than those due to the emission of the electromagnetic waves (assuming in that case that the star was surrounded by vacuum). Recently, [420] considered spheroidal oscillations of a NS with a dipole magnetic field, using the TBS formalism, and found that the LCDA again holds for at least half of these modes. Discussion in [420] also provided some useful insights into the role of rotation for the magnetospheric structure of oscillating NSs.

The TBS model was a very important contribution and, to the best of our knowledge, remains the only model for the magnetosphere of oscillating NSs available in the literature. However, it should be pointed out that it does not include several ingredients that a fully consistent and realistic model ought to include. Most importantly, it does not treat the magnetospheric currents in a fully consistent way: although

it gives a consistent solution for around half of the oscillation modes, the remaining solutions turn out to be unphysical and, as TBS pointed out, this is a symptom of the LCDA failing there. Also, rotation and the effects of general relativity can be very relevant; in particular, several authors have stressed that using a Newtonian approach may not give very good results for the structure of NS magnetospheres (see, e.g., [43, 287, 276, 279]). However, a more realistic model would naturally be more complicated than the TBS one whose relative simplicity can be seen as a positive advantage when using it as the basis for further applications.

The aim of the present work is to give a general relativistic reworking of the TBS model so as to investigate the effects of the changes with respect to the Newtonian treatment. We derive the general relativistic Maxwell equations for arbitrary small-amplitude oscillations of a non-rotating spherical NS with a generic magnetic field configuration and show that they can be solved analytically within the LCDA as in Newtonian theory. We then apply this solution to the case of toroidal oscillations of a NS with a dipole magnetic field and find that the LCDA is again valid for at least half of all toroidal oscillation modes, as in Newtonian theory. Using an improved formula for the determination of the last closed field line, we calculate the energy losses resulting from these oscillations for *all* of the modes for which the size of the polar cap is small and discuss the influence of GR effects on the energy losses.

The rest of this chapter is organized as follows. In Sec. 5.2 we introduce some definitions and derive the quasi-stationary Maxwell equations in Schwarzschild spacetime as well as the boundary conditions for the electromagnetic fields at the stellar surface. In Sec. 5.3 we sketch our method for analytically solving the Maxwell equations for arbitrary NS oscillations with a generic magnetic field configuration. In Sec. 5.4 we apply our formalism to the case of purely toroidal oscillations of a NS with a dipole magnetic field and also discuss the validity of the LCDA and the role of GR effects. In Sec. 5.5 we calculate the energy losses due to plasma outflow caused by the toroidal oscillations. Some detailed technical calculations related to the discussion in the main part of this work are presented in Appendices A-C.

5.2 General formalism

5.2.1 Quasi-stationary Maxwell equations in Schwarzschild spacetime

The study of electromagnetic processes related to stellar oscillations in the vicinity of NSs should, in principle, use the coupled system of Einstein-Maxwell equations. However, such an approach would be overly complicated for our study here, as it is for many other astrophysical problems. Here we simplify the problem by neglecting the contributions of the electromagnetic fields, the NS rotation and the NS oscillations to the spacetime metric and the structure of the NS[1], noting that this is expected to be a good approximation for small-amplitude oscillations. Indeed, for a star with average mass-energy density $\bar{\rho}$, mass M and radius R, the maximum fractional change in the spacetime metric produced by the magnetic field is typically of the same order as the ratio between the energy density in the surface magnetic field and average mass-energy density of the NS, i.e.,

$$\frac{B^2}{8\pi\bar{\rho}c^2} \simeq 10^{-7}\left(\frac{B}{10^{15}\,\mathrm{G}}\right)^2\left(\frac{1.4\,M_\odot}{M}\right)\left(\frac{R}{10\,\mathrm{km}}\right)^3 . \tag{5.4}$$

The corresponding fractional change in the metric due to rotation is of order

$$0.1\left(\frac{\Omega}{\Omega_\mathrm{K}}\right)^2 = 10^{-7}\left(\frac{\Omega}{1\,\mathrm{Hz}}\right)^2\left(\frac{1\,\mathrm{kHz}}{\Omega_\mathrm{K}}\right)^2 \tag{5.5}$$

[1]Several authors have, in fact, studied the equilibrium configurations of magnetars by solving the Einstein-Maxwell equations in full general relativity [58, 60, 87] or by using perturbative techniques [101, 183].

where $\Omega_{\rm K}$ is the Keplerian angular velocity at the surface of the NS. Moreover, in the case of magnetars, which we consider in our study, the oscillations are thought to be triggered by the global reconfiguration of the magnetic field. Due to this reason, the corrections due to the oscillations should not exceed the contribution due to the magnetic field itself given by estimate (5.4). Therefore, we can safely work in the background spacetime of a static spherical star, whose line element in a spherical coordinate system (t, r, θ, ϕ) is given by

$$ds^2 = g_{00}(r)dt^2 + g_{11}(r)dr^2 + r^2 d\theta^2 + r^2 \sin^2\theta d\phi^2 \,, \tag{5.6}$$

while the geometry of the spacetime external to the star (i.e. for $r \geq R$) is given by the Schwarzschild solution:

$$ds^2 = -N^2 dt^2 + N^{-2}dr^2 + r^2 d\theta^2 + r^2 \sin^2\theta d\phi^2 \,, \tag{5.7}$$

where $N \equiv (1 - 2M/r)^{1/2}$ and M is the total mass of the star. For the part of the spacetime inside the star, we represent the metric in terms of functions Λ and Φ as

$$g_{00} = -e^{2\Phi(r)} \,, \quad g_{11} = e^{2\Lambda(r)} = \left(1 - \frac{2m(r)}{r}\right)^{-1} \,, \tag{5.8}$$

where $m(r) = 4\pi \int_0^r r'^2 \rho(r') dr'$ is the volume integral of the total energy density $\rho(r)$ over the spatial coordinates. The form of these functions is given by solution of the standard TOV equations for spherical relativistic stars (see, e.g., [370] and they are matched continuously to the external Schwarzschild spacetime through the relations

$$g_{00}(r = R) = N_{_R}^2 \,, \quad g_{11}(r = R) = N_{_R}^{-2} \,, \tag{5.9}$$

where $N_{\rm R} \equiv (1-2M/R)^{1/2}$. Within the external part of the spacetime, we select a family of static observers with four-velocity components given by

$$(u^\alpha)_{_{\rm obs}} \equiv N^{-1}\Big(1, 0, 0, 0\Big) \,. \tag{5.10}$$

and associated orthonormal frames having tetrad four vectors $\{\mathbf{e}_{\hat{\mu}}\} = (\boldsymbol{e}_{\hat{0}}, \boldsymbol{e}_{\hat{r}}, \boldsymbol{e}_{\hat{\theta}}, \boldsymbol{e}_{\hat{\phi}})$ and 1-forms $\{\boldsymbol{\omega}^{\hat{\mu}}\} = (\boldsymbol{\omega}^{\hat{0}}, \boldsymbol{\omega}^{\hat{r}}, \boldsymbol{\omega}^{\hat{\theta}}, \boldsymbol{\omega}^{\hat{\phi}})$, which will become useful when determining the "physical" components of the electromagnetic fields. The components of the vectors are given by equations (6)-(9) of [344].

The general relativistic Maxwell equations have the following form [217]

$$3F_{[\alpha\beta,\gamma]} = F_{\alpha\beta,\gamma} + F_{\gamma\alpha,\beta} + F_{\beta\gamma,\alpha} = 0 \,, \tag{5.11}$$

$$F^{\alpha\beta}{}_{;\beta} = 4\pi J^\alpha \,, \tag{5.12}$$

where $F^{\alpha\beta}$ is the electromagnetic field tensor and $\boldsymbol{J}$ is the electric-charge 4-current. We consider the region close to the star (the near zone), at distances from the NS much smaller than the wavelength $\lambda = 2\pi c/\omega$. In the near zone the electromagnetic fields are quasi-stationary, therefore we neglect the displacement current term in the Maxwell equations. Once expressed in terms of the physical components of the electric and magnetic fields, equations (5.11) and (5.12) become (see Section 2 of [344] for details of the derivation)

$$\sin\theta \partial_r \left(r^2 B^{\hat{r}}\right) + N^{-1} r \partial_\theta \left(\sin\theta B^{\hat{\theta}}\right) + N^{-1} r \partial_\phi B^{\hat{\phi}} = 0 \,, \tag{5.13}$$

$$(r\sin\theta)\frac{\partial B^{\hat{r}}}{\partial t} = N\left[\partial_\phi E^{\hat{\theta}} - \partial_\theta\left(\sin\theta E^{\hat{\phi}}\right)\right] , \tag{5.14}$$

$$\left(N^{-1}r\sin\theta\right)\frac{\partial B^{\hat{\theta}}}{\partial t} = -\partial_\phi E^{\hat{r}} + \sin\theta\partial_r\left(rNE^{\hat{\phi}}\right) , \tag{5.15}$$

$$\left(N^{-1}r\right)\frac{\partial B^{\hat{\phi}}}{\partial t} = -\partial_r\left(rNE^{\hat{\theta}}\right) + \partial_\theta E^{\hat{r}} , \tag{5.16}$$

$$N\sin\theta\partial_r\left(r^2E^{\hat{r}}\right) + r\partial_\theta\left(\sin\theta E^{\hat{\theta}}\right) + r\partial_\phi E^{\hat{\phi}} = 4\pi\rho_e r^2\sin\theta , \tag{5.17}$$

$$\left[\partial_\theta\left(\sin\theta B^{\hat{\phi}}\right) - \partial_\phi B^{\hat{\theta}}\right] = 4\pi r\sin\theta J^{\hat{r}} , \tag{5.18}$$

$$\partial_\phi B^{\hat{r}} - \sin\theta\partial_r\left(rNB^{\hat{\phi}}\right) = 4\pi r\sin\theta J^{\hat{\theta}} , \tag{5.19}$$

$$\partial_r\left(NrB^{\hat{\theta}}\right) - \partial_\theta B^{\hat{r}} = 4\pi r J^{\hat{\phi}} , \tag{5.20}$$

where ρ_e is the proper charge density. We further assume that the force-free condition,

$$\vec{E}_{\rm SC}\cdot\vec{B} = 0 , \tag{5.21}$$

is fulfilled everywhere in the magnetosphere, implying that the magnetosphere of the NS is populated with charged particles that cancel the longitudinal component of the electric field. The charge density $\rho_{\rm SC}$ responsible for the electric field $\vec{E}_{\rm SC}$ (cf. equation 5.17) is the characteristic charge density of the force-free magnetosphere; this is appropriate for describing the charge density in the inner parts of the NS magnetosphere. We will refer to $\vec{E}_{\rm SC}$ as the space-charge (SC) electric field, and to $\rho_{\rm SC}$ as the SC charge density.

Finally, we introduce the perturbation of the NS crust in terms of its four-velocity, with the components being given by

$$w^\alpha \equiv e^{-\Phi}\left(1, \frac{dx^i}{dt}\right) = e^{-\Phi}\left(1, e^{-\Lambda}\delta v^{\hat{r}}, \frac{\delta v^{\hat{\theta}}}{r}, \frac{\delta v^{\hat{\phi}}}{r\sin\theta}\right) , \tag{5.22}$$

where $\delta v^i = dx^i/dt$ is the relative oscillation three-velocity of the conducting stellar surface with respect to the unperturbed state of the star.

5.2.2 Boundary conditions at the surface of star

We now begin our study of the internal electromagnetic field induced by the stellar oscillations. We assume here that the material in the crust can be treated as a perfect conductor and the induced electric field then depends on the magnetic field and the pulsational velocity field according to the following relations (see [344] for details of the derivation):

$$E^{\hat{r}}_{in} = -e^{-\Phi}\left[\delta v^{\hat{\theta}}B^{\hat{\phi}} - \delta v^{\hat{\phi}}B^{\hat{\theta}}\right] , \tag{5.23}$$

$$E^{\hat{\theta}}_{in} = -e^{-\Phi}\left[\delta v^{\hat{\phi}}B^{\hat{r}} - \delta v^{\hat{r}}B^{\hat{\phi}}\right] , \tag{5.24}$$

$$E^{\hat{\phi}}_{in} = -e^{-\Phi}\left[\delta v^{\hat{r}}B^{\hat{\theta}} - \delta v^{\hat{\theta}}B^{\hat{r}}\right] . \tag{5.25}$$

Boundary conditions for the magnetic field at the stellar surface ($r = R$) can be obtained from the requirement of continuity for the radial component, while leaving the tangential components free to be discontinuous because of surface currents:

$$B^{\hat{r}}_{ex}|_{r=R} = B^{\hat{r}}_{in}|_{r=R} \,, \tag{5.26}$$

$$B^{\hat{\theta}}_{ex}|_{r=R} = B^{\hat{\theta}}_{in}|_{r=R} + 4\pi i^{\hat{\phi}} \,, \tag{5.27}$$

$$B^{\hat{\phi}}_{ex}|_{r=R} = B^{\hat{\phi}}_{in}|_{r=R} - 4\pi i^{\hat{\theta}} \,, \tag{5.28}$$

where $i^{\hat{i}}$ is the surface current density. Boundary conditions for the electric field at the stellar surface are obtained from requirement of continuity of the tangential components, leaving $E^{\hat{r}}$ to have a discontinuity proportional to the surface charge density Σ_s:

$$E^{\hat{r}}_{ex}|_{r=R} = E^{\hat{r}}_{in}|_{r=R} + 4\pi\Sigma_s = -N_R^{-1}\left[\delta v^{\hat{\theta}} B^{\hat{\phi}} - \delta v^{\hat{\phi}} B^{\hat{\theta}}\right]|_{r=R} + 4\pi\Sigma_s \,, \tag{5.29}$$

$$E^{\hat{\theta}}_{ex}|_{r=R} = E^{\hat{\theta}}_{in}|_{r=R} = -N_R^{-1}\left[\delta v^{\hat{\phi}} B^{\hat{r}} - \delta v^{\hat{r}} B^{\hat{\phi}}\right]|_{r=R} \,, \tag{5.30}$$

$$E^{\hat{\phi}}_{ex}|_{r=R} = E^{\hat{\phi}}_{in}|_{r=R} = -N_R^{-1}\left[\delta v^{\hat{r}} B^{\hat{\theta}} - \delta v^{\hat{\theta}} B^{\hat{r}}\right]|_{r=R} \,, \tag{5.31}$$

where Σ_s is the surface charge density.

5.2.3 The low current density approximation

The low current density approximation was introduced by TBS, and in the present section we present a brief introduction to it for completeness. Close to the NS surface, the current flows along the magnetic field lines, and so in the inner parts of the magnetosphere, it can be expressed as

$$\vec{J} = \alpha(r,\theta,\phi)\cdot\vec{B} \,, \tag{5.32}$$

where α is a scalar function. The system of equations (5.13)–(5.20), (5.21) and (5.32) forms a complete set but is overly complicated for solving in the general case. However, within the LCDA these equations can, as we show below, be solved analytically for arbitrary oscillations of a NS with a generic magnetic field configuration.

The LCDA scheme is based on the assumption that the perturbation of the magnetic field induced by currents flowing in the NS interior is much larger than that due to currents in the magnetosphere, which are neglected to first order in the oscillation parameter $\bar{\xi} \equiv \xi/R$:

$$\frac{4\pi}{c}\vec{J} \ll \nabla\times\vec{B} \,, \tag{5.33}$$

and

$$\nabla\times\vec{B}^{(1)} = 0 \,, \tag{5.34}$$

where $\vec{B}^{(1)}$ is the first order term of the expansion in $\bar{\xi}$. This also implies that the current density satisfies the condition

$$J \ll \frac{1}{r}\left(B_{(0)}\,\frac{\xi}{R}\right) c \approx \rho_{\rm GJ}(R)\, c\left(\frac{c}{\omega r}\right) \,, \tag{5.35}$$

where $\rho_{\rm SC}(R)$ is the SC density near to the surface of the star. Here we have used the relation $\rho_{\rm SC}(R) \simeq B^{(0)}\eta/cR$, where η is the velocity amplitude of the oscillation and ω is its frequency.

In regions of complete charge separation, the maximum current density is given by $\rho_{\rm SC}c$. Since the absolute value of $\rho_{\rm SC}$ decreases with increasing r and because $r \ll c/w$ in the near zone, condition (5.35) is satisfied in the magnetosphere if there is complete charge separation there. Since the current in the magnetosphere flows along magnetic field lines, its magnitude does not change and so condition (5.35) is also satisfied along magnetic field lines in non-charge-separated regions as long as they have crossed regions with complete charge separation.

In the following, we solve the Maxwell equations assuming that condition (5.35) is satisfied throughout the whole near zone. As discussed above, a regular solution of the system of equations (5.13)-(5.20), (5.21) and (5.32) should exist for arbitrary oscillations and arbitrary configurations of the NS magnetic field and so, as shown by TBS, if a solution has an unphysical behaviour, this would imply that the LCDA fails for this oscillation and that the accelerating electric field cannot be screened only by a stationary configuration of the charged-separated plasma. In some regions of the magnetosphere, the current density could be as high as

$$J \simeq \rho_{\rm SC} c \left(\frac{c}{\omega r}\right) \ . \tag{5.36}$$

For a more detailed discussion of the LCDA and its validity, we refer the reader to Sections 2.3 and 3.2.1 of TBS.

5.3 The LCDA solution

5.3.1 The electromagnetic field in the magnetosphere

We now begin our solution of the Maxwell equations, assuming that the LCDA condition (5.35) is satisfied everywhere in the magnetosphere. Within the LCDA, equations (5.18)-(5.20) for the magnetic field in the magnetosphere take the form

$$\partial_\theta \left(\sin\theta B^{\hat{\phi}}\right) - \partial_\phi B^{\hat{\theta}} = 0 \ , \tag{5.37}$$

$$\partial_\phi B^{\hat{r}} - \sin\theta \partial_r \left(rNB^{\hat{\phi}}\right) = 0 \ , \tag{5.38}$$

$$\partial_r \left(NrB^{\hat{\theta}}\right) - \partial_\theta B^{\hat{r}} = 0 \ . \tag{5.39}$$

As demonstrated in [344], the components of the magnetic field $B^{\hat{r}}, B^{\hat{\theta}}$ and $B^{\hat{\phi}}$ can be expressed in terms of a scalar function S in the following way:

$$B^{\hat{r}} = -\frac{1}{r^2\sin^2\theta}\left[\sin\theta\partial_\theta\left(\sin\theta\partial_\theta S\right) + \partial_\phi\partial_\phi S\right] \ , \tag{5.40}$$

$$B^{\hat{\theta}} = \frac{N}{r}\partial_\theta\partial_r S \ , \tag{5.41}$$

$$B^{\hat{\phi}} = \frac{N}{r\sin\theta}\partial_\phi\partial_r S \ . \tag{5.42}$$

Substituting these expressions into the Maxwell equations (5.14)–(5.16), we obtain a system of equations for the electric field components which has the following general solution

$$E^{\hat{r}}_{\rm SC} = -\partial_r(\Psi_{\rm SC}) \,, \tag{5.43}$$

$$E^{\hat{\theta}}_{\rm SC} = -\frac{1}{Nr\sin\theta}\partial_t\partial_\phi S - \frac{1}{Nr}\partial_\theta(\Psi_{\rm SC}) \,, \tag{5.44}$$

$$E^{\hat{\phi}}_{\rm SC} = \frac{1}{Nr}\partial_t\partial_\theta S - \frac{1}{Nr\sin\theta}\partial_\phi\left(\Psi_{\rm SC}\right) \,, \tag{5.45}$$

where $\Psi_{\rm SC}$ is an arbitrary scalar function. The terms proportional to the gradient of $\Psi_{\rm SC}$ are responsible for the contribution of the charged particles in the magnetosphere. The vacuum part of the electric field is given by the derivatives of the scalar function S. Substituting (5.43)-(5.45) into equation (5.17), we get an expression for the SC charge density in terms of $\Psi_{\rm SC}$:

$$\rho_{\rm SC} = -\frac{1}{4\pi r^2}\left[N\partial_r\left(r^2\partial_r\Psi_{SC}\right) + \frac{1}{N}\triangle_\Omega\Psi_{SC}\right] \,, \tag{5.46}$$

where $\triangle_\Omega$ is the angular part of the Laplacian:

$$\triangle_\Omega = \frac{1}{\sin\theta}\partial_\theta\left(\sin\theta\partial_\theta\right) + \frac{1}{\sin^2\theta}\partial_{\phi\phi}. \tag{5.47}$$

5.3.2 The equation for $\Psi_{\rm SC}$

Substituting expressions (5.40)–(5.42) and (5.43)–(5.45) for the components of the electric and magnetic fields into the force-free condition (5.21), we get the following equation for $\Psi_{\rm SC}$

$$\frac{1}{\sin^2\theta}\left[\sin\theta\partial_\theta\left(\sin\theta\partial_\theta S\right) + \partial_\phi\partial_\phi S\right]\partial_r(\Psi_{\rm SC}) - \frac{1}{\sin\theta}\left[\partial_\phi\partial_t S\partial_\theta\partial_r S - \partial_\theta\partial_t S\partial_\phi\partial_r S\right]$$
$$-\partial_\theta\partial_r S\partial_\theta(\Psi_{\rm SC}) - \frac{1}{\sin^2\theta}\partial_\phi\partial_r S\partial_\phi\left(\Psi_{\rm SC}\right) = 0 \,. \tag{5.48}$$

If the amplitude of the NS oscillations is suitably small ($\bar{\xi} \ll 1$), the function S can be series expanded in terms of the dimensionless perturbation parameter $\bar{\xi}$ and can be approximated by the sum of the two lowest order terms

$$S(t,r,\theta,\phi) = S_0(r,\theta,\phi) + \delta S(t,r,\theta,\phi) \,. \tag{5.49}$$

Here the first term S_0 corresponds to the unperturbed static magnetic field of the NS, while δS is the first order correction to it. At this level of approximation, equation (5.48) for $\Psi_{\rm SC}$ takes the form

$$\frac{1}{\sin^2\theta}\left[\sin\theta\partial_\theta\left(\sin\theta\partial_\theta S_0\right) + \partial_\phi\partial_\phi S_0\right]\partial_r(\Psi_{\rm SC}) - \frac{1}{\sin\theta}\left[\partial_\phi\partial_t(\delta S)\partial_\theta\partial_r S_0 - \partial_\theta\partial_t(\delta S)\partial_\phi\partial_r S_0\right]$$
$$-\partial_\theta\partial_r S_0\partial_\theta(\Psi_{\rm SC}) - \frac{1}{\sin^2\theta}\partial_\phi\partial_r S_0\partial_\phi\left(\Psi_{\rm SC}\right) = 0 \,. \tag{5.50}$$

Next we expand S in terms of the spherical harmonics:

$$S = \sum_{\ell=0}^{\infty}\sum_{m=-\ell}^{\ell} S_{\ell m}(t,r)Y_{\ell m}(\theta,\phi) \,. \tag{5.51}$$

where the functions $S_{\ell m}$ are given in terms of Legendre functions of the second kind Q_ℓ by [342]

$$S_{\ell m}(t,r) = -\frac{r^2}{M^2}\frac{d}{dr}\left[r\left(1-\frac{2M}{r}\right)\frac{d}{dr}Q_\ell\left(1-\frac{r}{M}\right)\right]s_{\ell m}(t)\ . \tag{5.52}$$

Note that all of the time dependence in (5.52) is contained in the integration constants $s_{\ell m}(t)$ which, as we will see later, are determined by the boundary conditions at the surface of the star. We now series expand the coefficients $S_{\ell m}(t,r)$ and $s_{\ell m}(t)$ in terms of $\bar{\xi}$

$$S_{\ell m}(t,r) = S_{0\ell m}(r) + \delta S_{\ell m}(t,r), \qquad s_{\ell m}(t) = s_{0\ell m} + \delta s_{\ell m}(t)\ , \tag{5.53}$$

where all of the time dependence is now confined within the coefficients $\delta S_{\ell m}(r,t)$ and $\delta s_{\ell m}(t)$, while the coefficients $S_{0\ell m}$ and $s_{0\ell m}$ are responsible for the unperturbed static magnetic field of the star. Using these results, we can also express S and δS in terms of a series in $Y_{\ell m}(\theta,\phi)$ in the following way

$$S_0 = \sum_{\ell=0}^{\infty}\sum_{m=-\ell}^{\ell} S_{0\,\ell m}(r)Y_{\ell m}(\theta,\phi), \tag{5.54}$$

$$\delta S = \sum_{\ell=0}^{\infty}\sum_{m=-\ell}^{\ell} \delta S_{\ell m}(t,r)Y_{\ell m}(\theta,\phi)\ . \tag{5.55}$$

The variables r and t in the functions $S_{\ell m}(t,r)$ and $S_{\ell m}(t,r)$ can be separated using relation (5.52):

$$S_{0\ell m}(r) = -\frac{r^2}{M^2}\frac{d}{dr}\left[r\left(1-\frac{2M}{r}\right)\frac{d}{dr}Q_\ell\left(1-\frac{r}{M}\right)\right]s_{0\ell m}\ , \tag{5.56}$$

$$S_{\ell m}(t,r) = -\frac{r^2}{M^2}\frac{d}{dr}\left[r\left(1-\frac{2M}{r}\right)\frac{d}{dr}Q_\ell\left(1-\frac{r}{M}\right)\right]\delta s_{\ell m}(t)\ . \tag{5.57}$$

5.3.3 The boundary condition for $\Psi_{\rm SC}$

We now derive a boundary condition for $\Psi_{\rm SC}$ at the stellar surface using the behaviour of the electric and magnetic fields in that region. Following TBS, we assume that near to the stellar surface the interior magnetic field has the same behaviour as the exterior one:

$$B^{\hat{r}} = -\frac{C_1}{r^2\sin^2\theta}\left[\sin\theta\partial_\theta\left(\sin\theta\partial_\theta S\right) + \partial_{\phi\phi}S\right]\ , \tag{5.58}$$

$$B^{\hat{\theta}} = C_1\frac{e^{-\Lambda}}{r}\partial_\theta\partial_r S\ , \tag{5.59}$$

$$B^{\hat{\phi}} = C_1\frac{e^{-\Lambda}}{r\sin\theta}\partial_\phi\partial_r S\ . \tag{5.60}$$

Using the continuity condition for the normal component of the magnetic field $\left[B^{\hat{r}}\right] = 0$ at the stellar surface [335] together with the condition $e^{-\Lambda}|_{r=R} \equiv N_R$, one finds that the integration constant C_1 is equal to one. The interior electric field components can then be obtained by substituting (5.58) – (5.60) (with

$C_1 = 1$) into (5.23) – (5.25):

$$E^{\hat{r}}_{in} = -\frac{e^{-(\Phi+\Lambda)}}{r\sin\theta}\left\{\delta v^{\hat{\theta}}\partial_\phi\partial_r S - \sin\theta\delta v^{\hat{\phi}}\partial_\theta\partial_r S\right\}\ , \tag{5.61}$$

$$E^{\hat{\theta}}_{in} = \frac{e^{-(\Phi+\Lambda)}}{r\sin\theta}\left\{\delta v^{\hat{r}}\partial_\phi\partial_r S + \frac{\delta v^{\hat{\phi}}e^{\Lambda}}{r\sin\theta}\left[\sin\theta\partial_\theta\left(\sin\theta\partial_\theta S\right) + \partial_\phi\partial_\phi S\right]\right\}\ , \tag{5.62}$$

$$E^{\hat{\phi}}_{in} = -\frac{e^{-(\Phi+\Lambda)}}{r}\left\{\delta v^{\hat{r}}\partial_\theta\partial_r S + \frac{\delta v^{\hat{\theta}}e^{\Lambda}}{r\sin^2\theta}\left[\sin\theta\partial_\theta\left(\sin\theta\partial_\theta S\right) + \partial_\phi\partial_\phi S\right]\right\}\ . \tag{5.63}$$

The continuity condition for the θ component of the electric field across the stellar surface (5.30) gives a boundary condition for $\partial_\theta\Psi_{\rm SC}|_{r=R}$:

$$\Psi_{{\rm SC},\theta}|_{r=R} = -\left\{\frac{\delta v^{\hat{\phi}}}{R\sin^2\theta}\left[\sin\theta\partial_\theta\left(\sin\theta\partial_\theta S\right) + \partial_\phi\partial_\phi S\right] + \frac{N\delta v^{\hat{r}}}{\sin\theta}\partial_\phi\partial_r S + \frac{1}{\sin\theta}\partial_t\partial_\phi S\right\}|_{r=R}\ , \tag{5.64}$$

while the continuity condition for $E^{\hat{\phi}}$ (5.31) gives a boundary condition for $\partial_\phi\Psi_{\rm SC}|_{r=R}$:

$$\Psi_{{\rm SC},\phi}|_{r=R} = \left\{\frac{\delta v^{\hat{\theta}}}{R\sin\theta}\left[\sin\theta\partial_\theta\left(\sin\theta\partial_\theta S\right) + \partial_\phi\partial_\phi S\right] + N\delta v^{\hat{r}}\sin\theta\partial_\theta\partial_r S + \sin\theta\partial_t\partial_\theta S\right\}|_{r=R}\ . \tag{5.65}$$

Integration of equation (5.64) or equation (5.65) over θ or ϕ respectively, gives a boundary condition for $\Psi_{\rm SC}$. We will use the result of integrating equation (5.64) over θ. Assuming that the perturbation depends on time t as $e^{-i\omega t}$, we obtain the following condition, correct to first order in $\bar{\xi}$,

$$\Psi_{\rm SC}|_{r=R} = -\int\left\{\frac{\delta v^{\hat{\phi}}}{R\sin^2\theta}\left[\sin\theta\partial_\theta\left(\sin\theta\partial_\theta S_0\right) + \partial_\phi\partial_\phi S_0\right] + \frac{N\delta v^{\hat{r}}}{\sin\theta}\partial_\phi\partial_r S_0 + \frac{1}{\sin\theta}\partial_t\partial_\phi(\delta S)\right\}d\theta|_{r=R} + e^{i\omega t}F(\phi)\ , \tag{5.66}$$

where $F(\phi)$ is a function only of ϕ which we will determine below.

The components of the stellar-oscillation velocity field are continuously differentiable functions of r, θ and ϕ. The boundary conditions for the electric field (5.30)-(5.31) imply that the tangential components of the electric field $\vec{E}_{\rm SC}$ must be finite. The vacuum terms on the right-hand side of (5.44)-(5.45) and the terms on both sides of equation (5.45) are also finite. Consequently, the term

$$-\frac{\partial_\phi(\Psi_{\rm SC})}{\sin\theta}|_{r=R} \tag{5.67}$$

should also be finite. Hence we obtain that $\partial_\phi(\Psi_{\rm SC})|_{\theta=0,\pi;r=R} = 0$ and so the function $F(\phi)$ in the expression for boundary condition (5.66) must satisfy the condition $(\Psi_{\rm SC})|_{\theta=0,\pi;r=R} = C\,e^{-i\omega\,t}$, where C is a constant. Using gauge invariance, we choose

$$\Psi_{\rm SC}|_{\theta=0;r=R} = 0, \tag{5.68}$$

and from this and equation (5.66), we obtain our expression for the boundary condition for $\Psi_{\rm SC}$ at the stellar surface:

$$\Psi_{\rm SC}|_{r=R} = -\int_0^\theta\left\{\frac{\delta v^{\hat{\phi}}}{R\sin^2\theta}\left[\sin\theta\partial_\theta\left(\sin\theta\partial_\theta S_0\right) + \partial_\phi\partial_\phi S_0\right] + \frac{N\delta v^{\hat{r}}}{\sin\theta}\partial_\phi\partial_r S_0 + \frac{1}{\sin\theta}\partial_t\partial_\phi(\delta S)\right\}d\theta|_{r=R}\ . \tag{5.69}$$

5.4 Toroidal oscillations of a NS with a dipole magnetic field

As an important application of this formalism, we now consider small-amplitude toroidal oscillations of a NS with a dipole magnetic field. For toroidal oscillations in the (ℓ', m') mode, a generic conducting fluid element is displaced from its initial location (r, θ, ϕ) to a perturbed location $(r, \theta + \xi^\theta, \phi + \xi^\phi)$ with the velocity field [426],

$$\delta v^{\hat{r}} = 0 \,, \quad \delta v^{\hat{\theta}} = \frac{d\xi^\theta}{dt} = \frac{e^{-i\omega t}\eta(r)}{\sin\theta}\partial_\phi Y_{\ell' m'}(\theta,\phi) \,, \quad \delta v^{\hat{\phi}} = \frac{d\xi^\phi}{dt} = -e^{-i\omega t}\eta(r)\partial_\theta Y_{\ell' m'}(\theta,\phi) \,, \tag{5.70}$$

where ω is the oscillation frequency and $\eta(r)$ is the transverse velocity amplitude. Note that in the above expressions (5.70), the oscillation mode axis is directed along the z-axis. We use a prime to denote the spherical harmonic indices in the case of the oscillation modes.

5.4.1 The unperturbed exterior dipole magnetic field

If the static unperturbed magnetic field of the NS is of a dipole type, then the coefficients $s_{0\ell m}$ involved in specifying it have the following form (see eq. 117 of [344])

$$s_{0\,10} = -\frac{\sqrt{3\pi}}{2}\mu\cos\chi \,, \qquad\qquad s_{0\,11} = \sqrt{\frac{3\pi}{2}}\mu\sin\chi \,, \tag{5.71}$$

where μ is the magnetic dipole moment of the star, as measured by a distant observer, and χ is the inclination angle between the dipole moment and z-axis. Substituting expressions (5.71) into (5.56) and then the latter into (5.54), we get

$$S_0 = -\frac{3\mu r^2}{8M^3}\left[\ln N^2 + \frac{2M}{r}\left(1+\frac{M}{r}\right)\right](\cos\theta\cos\chi + e^{i\phi}\sin\theta\sin\chi) \tag{5.72}$$

The corresponding magnetic field components have the form

$$B_0^{\hat{r}} = -\frac{3\mu}{4M^3}\left[\ln N^2 + \frac{2M}{r}\left(1+\frac{M}{r}\right)\right](\cos\chi\cos\theta + \sin\chi\sin\theta e^{\mathrm{i}\phi}) \,, \tag{5.73}$$

$$B_0^{\hat{\theta}} = \frac{3\mu N}{4M^2 r}\left[\frac{r}{M}\ln N^2 + \frac{1}{N^2} + 1\right](\cos\chi\sin\theta - \sin\chi\cos\theta e^{\mathrm{i}\phi}) \,, \tag{5.74}$$

$$B_0^{\hat{\phi}} = \frac{3\mu N}{4M^2 r}\left[\frac{r}{M}\ln N^2 + \frac{1}{N^2} + 1\right](-\mathrm{i}\sin\chi \mathrm{e}^{\mathrm{i}\phi}) \,. \tag{5.75}$$

At the stellar surface, these expressions for the unperturbed magnetic field components become

$$B_{R}^{\hat{r}} = f_{R} B_0(\cos\chi\cos\theta + \sin\chi\sin\theta e^{\mathrm{i}\phi}) \,, \tag{5.76}$$

$$B_{R}^{\hat{\theta}} = h_{R} B_0(\cos\chi\sin\theta - \sin\chi\cos\theta e^{\mathrm{i}\phi}) \,, \tag{5.77}$$

$$B_{R}^{\hat{\phi}} = -i h_{R} B_0(\sin\chi e^{\mathrm{i}\phi}) \,, \tag{5.78}$$

where B_0 is defined as $B_0 = 2\mu/R^3$. In Newtonian theory B_0 would be the value of the magnetic strength at the magnetic pole but this becomes modified in GR. The GR modifications are contained within the parameters

$$h_{R} = \frac{3R^2 N_{R}}{8M^2}\left[\frac{R}{M}\ln N_{R}^2 + \frac{1}{N_{R}^2} + 1\right] \,, \qquad f_{R} = -\frac{3R^3}{8M^3}\left[\ln N_{R}^2 + \frac{2M}{R}\left(1+\frac{M}{R}\right)\right] \,. \tag{5.79}$$

For a given μ, the magnetic field near to the surface of the NS is stronger in GR than in Newtonian theory, as already noted by [166].

5.4.2 The equation for $\Psi_{\rm SC}$

Substituting S_0 from (5.72) into equation (5.50), we obtain a partial differential equation containing two unknown functions $\Psi_{\rm SC}$ and δS for arbitrary oscillations of a NS with a dipole magnetic field

$$
\begin{aligned}
&-2r^2 q_1(r)\left(\cos\theta\cos\chi + e^{i\phi}\sin\theta\sin\chi\right)\,\partial_r(\Psi_{\rm SC}) \qquad (5.80)\\
&+\partial_r\left[r^2 q_1(r)\right]\left(\sin\theta\cos\chi - e^{i\phi}\cos\theta\sin\chi\right)\partial_\theta(\Psi_{\rm SC}) - \partial_r\left[r^2 q_1(r)\right]\frac{e^{i\phi}\sin\chi}{\sin\theta}\partial_\phi(\Psi_{\rm SC})\\
&+\frac{\partial_r\left[r^2 q_1(r)\right]}{\sin\theta}\left[\left(\sin\theta\cos\chi - e^{i\phi}\cos\theta\sin\chi\right)\partial_\phi\partial_t(\delta S) + ie^{i\phi}\sin\chi\sin\theta\partial_\theta\partial_t(\delta S)\right] = 0\,,
\end{aligned}
$$

where we have introduced a new function $q_1(r)$ for simplicity of notation [see Eq. (5.121) for the definition of $q_1(r)$].

From (5.69), the boundary condition for $\Psi_{\rm SC}$ at the stellar surface is

$$
\Psi_{\rm SC}|_{r=R} = \int_0^\theta \left\{ B_0 R f_{_R} \delta v^{\hat\phi}\partial_\theta\left(\cos\theta\cos\chi + e^{i\phi}\sin\theta\sin\chi\right) - \frac{1}{\sin\theta}\partial_t\partial_\phi(\delta S)\right\} d\theta|_{r=R}\,. \qquad (5.81)
$$

Using the expressions for the velocity field of the toroidal oscillations (5.70) and for the boundary conditions for the partial derivatives of the SC potential (5.64)-(5.65), we find that $\partial_t\delta S$ is given by (see Appendix A for details of the derivation)

$$
\begin{aligned}
\partial_t\delta S(r,t) &= \sum_{\ell=0}^{\infty}\sum_{m=-\ell}^{\ell}\frac{B_0 R f_{_R}\tilde\eta_{\rm R}}{\ell\,(\ell+1)}\frac{r^2\,q_\ell\,(r)}{R^2\,q_\ell\,(R)} \qquad (5.82)\\
&\times \int_{4\pi}\left[\partial_\theta Y_{\ell m}\left(\sin\theta\cos\chi - e^{i\phi}\cos\theta\sin\chi\right) + ie^{i\phi}\partial_\phi Y_{\ell m}\sin\theta\sin\chi\right]\frac{Y^*_{\ell' m'}(\theta,\phi)}{\sin\theta}d\Omega\,.
\end{aligned}
$$

From here on, for simplicity, we will consider only the case with $\chi = 0$. Although our solution depends on the angle between the magnetic field axis and the oscillation mode axis, focusing on the case $\chi = 0$ does not actually imply a loss of generality because any mode with its axis not aligned with a given direction can be represented as a sum of modes with axes along this direction. We have developed a MATHEMATICA code for analytically solving equation (5.50) and hence obtaining analytic expressions for the electric and magnetic fields and for the SC density.

The solution of equation (5.80) for the case $\chi = 0$ is given in Appendix B, where we show that the general solution has the following form

$$
\begin{aligned}
\Psi_{\rm SC} = -\frac{1}{2}\frac{m'^2}{\ell'(\ell'+1)}B_0 R f_{_R}\tilde\eta_R\int_R^r \frac{\partial_{r'}[r'^2 q_1(r')]}{q_1(r')}\frac{q_{\ell'}(r')}{R^2 q_{\ell'}(R)}\frac{Y_{\ell' m'}(\theta(r'),\phi)}{\cos\theta(r')}\,dr' \qquad (5.83)\\
+\Phi_2\left[\sqrt{-r^2 q_1(r)}\,\sin\theta,\phi,t\right]\,,
\end{aligned}
$$

where r' is the integration variable. In order to solve this integral, the function $\theta(r')$ is expressed in terms r' and a constant φ_2 through the characteristic equation (5.135) and, after performing the integration, φ_2

is removed again using (5.135). The unknown function Φ_2 is determined using the boundary condition for $\Phi_2|_{r=R}$ given by (5.142). Once the integral on the right-hand side of (5.142) has been evaluated, we then express all of the trigonometric functions resulting from the integral, in terms of $\sin\theta$. This θ is the value at $r = R$. To obtain an expression for the value of Φ_2 at a general radius, we write this θ (at $r = R$) in terms of the value of θ at a general point (with $r > R$) using the characteristic relation (5.135), i.e.,

$$\sin\theta \to \sqrt{[r^2 q_1(r)]/[R^2 q_1(R)]} \times \sin\theta \,, \tag{5.84}$$

so that

$$\cos\theta \to \left[1 - \frac{r^2 q_1(r)}{R^2 q_1(R)} \sin^2\theta\right]^{1/2} \mathrm{sign}(\cos\theta) \,, \tag{5.85}$$

where $\mathrm{sign}(x)$ is defined such that $\mathrm{sign}(x) = +1$ if $x > 0$, and $\mathrm{sign}(x) = -1$ if $x < 0$. There are then different expressions for $\Psi_{\rm SC}$ in the two regions $\theta \in [0,\, \pi/2]$ and $\theta \in [\pi/2,\, \pi]$. If these two expressions do not coincide at the equatorial plane for $r > R$, then there will be a discontinuity in $\Psi_{\rm SC}$ at $\theta = \pi/2$, and quantities that depend on $\partial_\theta \Psi_{\rm SC}$ will become singular there. As shown by TBS, the function $\Psi_{\rm SC}$ is indeed discontinuous at $\theta = \pi/2$ for some oscillation modes and, as we discussed in Section 5.2.3 above, this unphysical behaviour indicates that the LCDA ceases to be valid for those modes. In these cases, the accelerating electric field cannot be canceled without presence of strong currents which may become as large as (5.36) in some regions of the magnetosphere. The occurrence of such singularities was explained by TBS and the reader is referred to Section 3.2 of their paper for a detailed discussion.

Next we discuss how GR effects contribute to our solution. As discussed above, for a given magnetic moment μ (as measured by a distant observer) the strength of the unperturbed magnetic field near to the surface of the NS is larger in GR than in Newtonian theory. Due to the linearity of the Maxwell equations, a perturbation of a stronger magnetic field should produce a larger electric field for the same oscillation parameters. This in turn should lead to a larger absolute value of the SC density in GR, since the SC density takes the value necessary to cancel the electric field. In the next Section, we will give a more quantitative analysis of the GR contribution in our solution.

We point out that the function $\Psi_{\rm SC}$ does not depend on $\ell > 1$ perturbations to the stellar magnetic field in the case of axisymmetric ($m' = 0$) toroidal modes. This can be seen from the fact that these perturbations are confined within the δS terms which enter equation (5.80) for the function $\Psi_{\rm SC}$ only through a derivative with respect to ϕ; hence vanish for the axisymmetric modes. Therefore, the only perturbation to the magnetic field is due to the $\ell = 1$ term, and the solution for these modes is much simpler than that for non-axisymmetric ($m' \neq 0$) modes. It is then convenient to discuss separately the axisymmetric and non-axisymmetric cases.

The solution (5.83) for the $m' = 0$ modes at $r = R$ has the following form

$$\Psi_{\rm SC}\,(r,\theta,\phi,t)\,|_{r=R} = -B_0 R f_{_R} \tilde{\eta}_R \int_0^\theta \cos\vartheta\, \partial_\vartheta Y_{\ell' 0}(\vartheta,\phi)\, d\vartheta \,. \tag{5.86}$$

Using the properties of the spherical harmonics, we can express $\Psi_{\rm SC}\,(r,\theta,\phi,t)\,|_{r=R}$ for odd ℓ' modes in the general form

$$\Psi_{\rm SC}\,(r,\theta,\phi,t)\,|_{r=R} \sim \sum_{n=1}^{\mathcal{N}} A_{2n} \sin^{2n}\theta \,, \tag{5.87}$$

while for even ℓ' modes, the general form of $\Psi_{\rm SC}$ is

$$\Psi_{\rm SC}\,(r,\theta,\phi,t)\,|_{r=R} \sim (A + B\cos\theta) \sum_{n=1}^{\mathcal{N}} A_{2n} \sin^{2n}\theta \,, \tag{5.88}$$

where the coefficients A, B and A_{2n} do not depend on r and θ. The value of $\mathcal{N}$ equals $\ell'/2+1$ for even ℓ' and $(\ell'+1)/2$ for odd ℓ'. As we discussed above, in order to obtain the solution for $\Psi_{\rm SC}$ for $r > R$, one has use $\sin\theta \to \sqrt{r^2 q_1(r)/R^2 q_1(R)}\,\sin\theta$ on the right-hand sides of (5.87) and (5.88). Thus the GR effects contribute to the solution for $m' = 0$ modes only through terms $f_{_R}\left[r^2 q_1(r)/R^2 q_1(R)\right]^n$, where $n \geq 1$. Note that the factor $f_{_R}$ in this term appears due to the boundary condition at the surface of the star, namely from the continuity of the tangential components of the electric field, while the factor $\left[r^2 q_1(r)/R^2 q_1(R)\right]^n$ appears due to the presence of charged particles in the magnetosphere. The second factor is equal to 1 at the stellar surface and approaches its Newtonian value $(R/r)^n$ at large r and small M/R. Since $f_{_R} > 1$, the absolute value of $\Psi_{\rm SC}$ should be greater in GR than in Newtonian theory. For example, in the case of small θ, the only term which is important is that with $n = 1$ and hence we get $(\Psi_{\rm SC})_{\rm GR}/(\Psi_{\rm SC})_{\rm Newt} = f_{_R} r^3 q_1(r)/R^3 q_1(R)$. This quantity is shown in Figure 5.1 (left panel), where we can see that, near to the stellar surface, the function $\Psi_{\rm SC}$ is larger in GR than in Newtonian theory, while at larger r it asymptotically approaches its Newtonian value.

Analysis of the GR contribution to the solution in the case of non-axisymmetric modes is more complicated because in this case the solution depends not only on $\ell = 1$ perturbations to the magnetic field but also on $\ell > 1$ perturbations, which are contained in the term $\partial_t\partial_\phi\delta S$ of equation (5.80), and contribute to the solution due to the integral in (5.83). Nevertheless, some rough estimates of the GR effects can be made in the following way. Near to the stellar surface the integral in (5.83) can be approximated as

$$f_{_R}\int_R^r \frac{\partial_z[z^2 q_1(z)]}{q_1(z)}\,\frac{q_\ell(z)}{R^2 q_\ell(R)}\,\frac{Y_{\ell m}(\theta(z),\phi)}{\cos\theta(z)}\,dz \simeq f_{_R}\,\frac{r^2 q_\ell(r)}{R^2 q_\ell(R)}\,\frac{Y_{\ell m}(\theta(r),\phi)}{\cos\theta(r)}\,. \tag{5.89}$$

Close to the star, $(r^2 q_\ell(r))/(R^2 q_\ell(R)) \simeq 1$ and so the leading GR contribution comes from the factor $f_{_R}$ which increases the absolute value of $\Psi_{\rm SC}$ with respect to the Newtonian case. Further away from the star, $r^2 q_\ell$ is approximately proportional to $r^{-\ell}$ and so the integral in (5.89) can be approximated as $\sim f_{_R}(R/r)^{\ell'+1+m'/2}$ to leading order in R/r. Therefore, while this integral makes an important contribution to $\Psi_{\rm SC}$ near to the star, it becomes negligibly small for $\ell > 1$ at $r > R$ as compared with Φ_2. The GR effects contribute to Φ_2 through the terms $f_{_R}\left[r^2 q_1(r)/R^2 q_1(R)\right]^n$ in a similar way to their contribution to $\Psi_{\rm SC}$ for the axisymmetric modes discussed above. This increase of the function $\Psi_{\rm SC}$ due to the GR effects also leads to an increase in the absolute values of the SC density $\rho_{\rm SC}$ near to the star, as shown in Figures 5.1 (right panel) and 5.2 for some toroidal oscillation modes.

5.5 Energy losses

It was shown by TBS that the kinetic energy of the stellar oscillations should be lost through being passed to plasma near to the stellar surface which then flows out along the open magnetic field lines. Note that within the framework of the TBS model, electromagnetic fields are considered only in the near zone and so the existence of the plasma outflow cannot be shown explicitly; however, qualitatively, the mechanism for the plasma outflow should be the following. The charged particles that were accelerated to high energies by the longitudinal electric field move along the magnetic field lines in the near zone. If the kinetic energy density of the plasma at the equator becomes comparable to the energy density of the magnetic field at some point, then the field line which crosses the equator at that point becomes open. Plasma flowing along open field lines forms an electromagnetically driven wind which closes at infinity. There is then an electric current flowing along the stellar surface between positive and negative emission regions. Because this current must cross the magnetic field lines at the stellar surface, it exerts a braking torque on the NS oscillations and thus reduces their kinetic energy (see Section 3.2.2 of TBS for more details).

In the following, we carry out a GR calculation of the energy lost by toroidal stellar oscillations due to plasma outflow. First we calculate the energy losses due to the outflow of a particle along an open field line

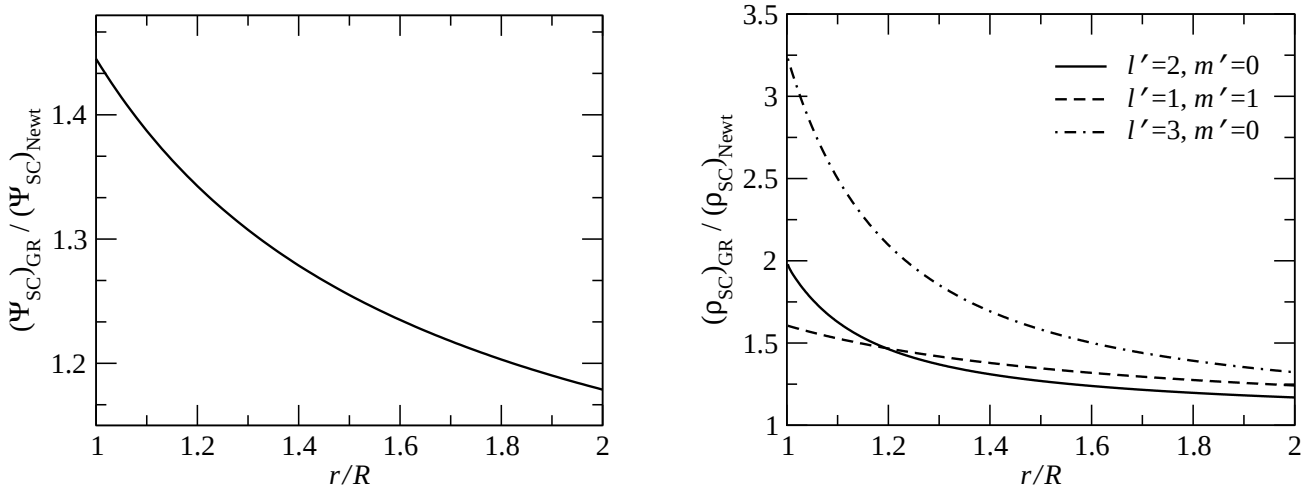

Figure 5.1: *Left panel:* The ratio $(\Psi_{\rm SC})_{\rm GR}/(\Psi_{\rm SC})_{\rm Newt}$ along the polar axis plotted as a function of the distance from the star, for axisymmetric toroidal modes of a NS with compactness $M/R = 0.2$. *Right panel:* The ratio $(\rho_{\rm SC})_{\rm GR}/(\rho_{\rm SC})_{\rm Newt}$ in the equatorial plane plotted as a function of r, for a star with $M/R = 0.2$, for toroidal oscillation modes $(2, 0)$, $(1, 1)$ and $(3, 0)$.

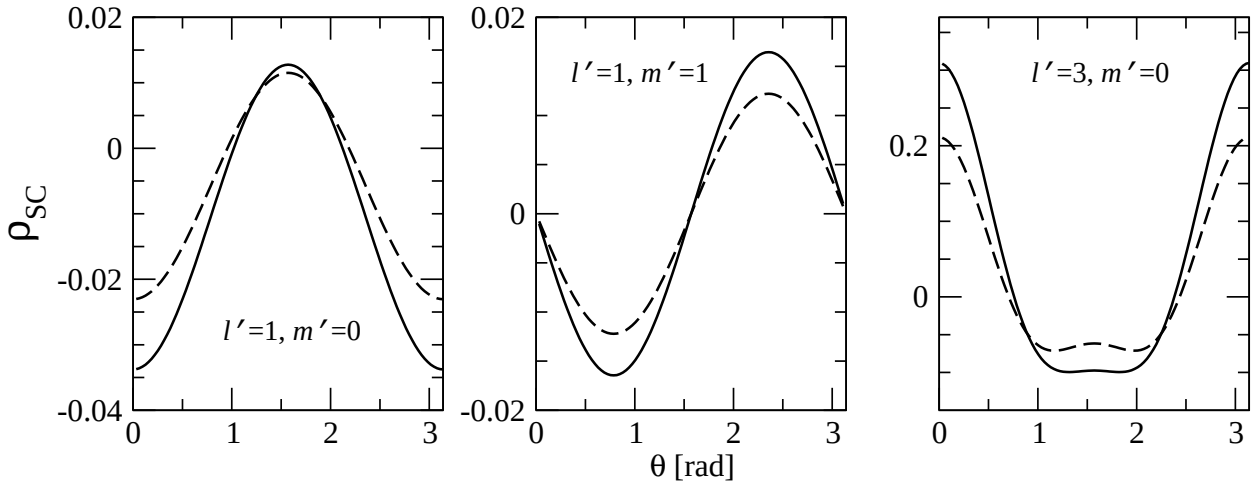

Figure 5.2: The space-charge density $\rho_{\rm SC}$ at $r = 1.5R$ (in units with $B_0 = \eta = 1$) plotted as a function of θ for the toroidal oscillation modes $(1, 0)$, $(1, 1)$ and $(3, 0)$. The solid lines refer to the SC density $\rho_{\rm SC}$ in the relativistic theory, while its Newtonian value is shown by the dashed lines.

from a given point on the stellar surface. For this purpose, we start by considering the motion of the charged particle along the θ-direction on the stellar surface (where it crosses the magnetic field lines, hence exerts a braking torque on the stellar oscillations). The equation of motion for a test particle of mass m in a generic electromagnetic field has the general form [217]

$$m\frac{Dw^\alpha}{d\tau} = eF^{\alpha\beta}w_\beta \,, \tag{5.90}$$

where $D/d\tau$ is a comoving derivative, w^α is the four-velocity of the particle given by

$$w_\alpha = \frac{u_\alpha + v_\alpha}{\sqrt{1-v^2}} \,, \tag{5.91}$$

u^α is the 4-velocity of the static observer (5.10), and v^α is the velocity of the particle relative to the static observer.

Because of time-invariance, there exists a timelike Killing vector ξ^α such that $\xi^\alpha\xi_\alpha = -N^2$. The four-velocity of the static observer can be expressed in terms of ξ^α as $u^\alpha = N^{-1}\xi^\alpha$, and therefore the energy of the particle is given by

$$\mathcal{E} = -p_\alpha\xi^\alpha = -mw_\alpha\xi^\alpha \,. \tag{5.92}$$

Contracting the equation of motion (5.90) with the Killing vector ξ_α gives

$$\xi_\alpha m w^\alpha_{;\beta}w^\beta = -eF^{\alpha\beta}\frac{u_\alpha + v_\alpha}{\sqrt{1-v^2}}\xi_\beta \,, \tag{5.93}$$

The right-hand side of this can be rewritten as

$$-eF^{\alpha\beta}\frac{u_\alpha + v_\alpha}{\sqrt{1-v^2}}\xi_\beta = eF^{\alpha\beta}\frac{v_\beta\xi_\alpha}{\sqrt{1-v^2}} = eF^{\alpha\beta}N\frac{u_\beta v_\alpha}{\sqrt{1-v^2}} = e\frac{E^{\hat\alpha}v_{\hat\alpha}N}{\sqrt{1-v^2}} \,, \tag{5.94}$$

while the left-hand side can be transformed as

$$\xi_\alpha m w^\alpha_{;\beta}w^\beta = m(w_\alpha\xi^\alpha)_{;\beta}w^\beta - m\xi_{\alpha;\beta}w^\alpha w^\beta \,, \tag{5.95}$$

The second term on the right-hand of this equation vanishes due to antisymmetry of the tensor $\xi_{\alpha;\beta}$. Therefore, the projection of the equation of motion onto the Killing vector can be written as

$$\frac{d\mathcal{E}}{d\tau} = eN\frac{E^{\hat\alpha}v_{\hat\alpha}}{\sqrt{1-v^2}} \,. \tag{5.96}$$

For particles moving along the θ-direction, this equation takes the form

$$d\mathcal{E} = e\frac{E^{\hat\alpha}RN_R^2}{\sqrt{1-v^2}}d\theta \,. \tag{5.97}$$

Integrating this over the interval $(0,\theta)$, we get

$$\Delta\mathcal{E} = eRN_R^2\int_0^\theta E^{\hat\alpha}d\theta. \tag{5.98}$$

Note that in deriving this last equation, we have used the fact that $v \ll 1$. The quantity $\Delta\mathcal{E}$ measures the energy that would be carried away by a particle that leaves the surface of the star from a point with coordinates (R,θ,ϕ). In order to calculate the energy loss per unit time through a given surface element

dS, $\Delta\mathcal{E}$ needs to be multiplied by the the current density, j^α and integrated over the surface element $n_\alpha dS$, where n_α is the unit spacelike vector orthogonal to the surface $r = R$. The energy loss per unit time due to plasma emission through the surface element dS is then given by

$$dL = \Delta\mathcal{E}(\theta,\phi) j^{\hat{\alpha}}(R,\theta,\phi) n_{\hat{\alpha}}\, R^2 \sin\theta d\theta d\phi \,, \tag{5.99}$$

while the total energy loss L from the NS is obtained by integrating dL over the entire open field line region on the stellar surface.

Now we determine the angle θ_0 at which the last closed magnetic field line intersects the stellar surface. Following TBS, we define the last closed line as being that for which the kinetic energy density of the outflowing plasma at the equator becomes equal to the corresponding energy density of the NS magnetic field. We now derive a mathematical condition for this. The energy-momentum tensor of the electromagnetic field is [217]

$$T^{\alpha\beta}_{em} = \frac{1}{4\pi}\left(F^{\alpha\sigma}F^{\beta}_{\sigma} - \frac{1}{4}g^{\alpha\beta}F^{\mu\nu}F_{\mu\nu}\right) \,. \tag{5.100}$$

Using this expression, one can obtain an expression for the energy density of the electromagnetic field

$$\mathcal{E}_{em} = NT^{\alpha\beta}u_\alpha u_\beta = N\frac{B^2+E^2}{8\pi} \,. \tag{5.101}$$

The method for the calculation of the last closed field line proposed by TBS [equation (65) of TBS] is based on an implicit assumption that the plasma flows out from the star isotropically and its kinetic energy is distributed uniformly over the surface of a sphere with radius $r = R_a$, where R_a is the radial coordinate of the point where the last closed field line crosses the equatorial plane. However, according to the definition of the last closed field line, the outflowing plasma should move along the field lines throughout the region $r < R_a$ and so its energy cannot be distributed uniformly over the sphere $r = R_a$. In the following, we derive an alternative formula for the calculation of θ_0 that takes into account the correction due to the anisotropic plasma outflow along the magnetic field lines.

If the stellar magnetic field is dipolar, then the density of the field lines decreases with distance from the centre of the star. Since the charged particles move along the field lines, this implies that the kinetic energy density of a comoving element of plasma should decrease monotonically with r as the field lines separate (we are assuming here that the plasma speed along the field lines is roughly constant). Since for dipole magnetic field lines $f_r \sin^2\theta/r = \mathrm{const}$, it is easy to show the energy density of the plasma when it reaches the equatorial plane is smaller by a factor of $0.5R^3/(R_a^3 f_{_R})$ compared to its value at the stellar surface (assuming that the angle θ is small). Therefore, the kinetic energy density of the outflowing plasma at the point $(R_a, 0, \phi)$ is given by

$$\epsilon_{pl}(R_a,0,\phi) = \frac{1}{2f_{_R}}\frac{N_R}{N_{R_a}}\frac{R^3}{R_a^3}\Delta\mathcal{E} j^{\hat{\alpha}} n_{\hat{\alpha}} \,, \tag{5.102}$$

where $N_{R_a} = \sqrt{1-2M/R_a}$ and the factor N_R/N_{R_a} accounts for the gravitational redshift of the energy of the plasma. The energy density of the magnetic field lines at the same point is determined from (5.101) and has the following form

$$\epsilon_{em}(R_a,0,\phi) = \frac{N_{R_a}}{32\pi}\frac{R^6}{R_a^6}B_0^2 \,, \tag{5.103}$$

Note that $R_a \gg R$ for small θ_0, and so in this case $N_{\mathrm{R_a}} \approx 1$ to good accuracy; from here on we will consider only the case of small θ_0 and take $N_{\mathrm{R_a}} = 1$. Also $j^{\hat{r}} \gg j^{\hat{\theta}}$ for small θ, and so in the following we

will neglect the θ component of the current above the polar cap. The last closed field line is determined by the conditions

$$\epsilon_{pl}(R_a, 0, \phi) = \epsilon_{em}(R_a, 0, \phi) \ . \tag{5.104}$$

Substituting (5.103) and (5.102) into (5.104), one can obtain an algebraic equation

$$16\pi N_R \Delta\mathcal{E}\rho_{\rm SC} = f_R^4 B_0^2 \theta_0^6 \tag{5.105}$$

for determining θ_0 after expressing $\Delta\mathcal{E}$ in terms of θ_0. Once we know θ_0, we can calculate the total energy of the outflowing plasma by integrating (5.99) over the entire open field line region of the stellar surface:

$$L = \int_0^{2\pi} d\phi \int_0^{\theta_0} d\theta \ |j^{\hat{r}}(R, \theta, \phi) \ \Delta\mathcal{E}(\theta, \phi)| R^2 \sin\theta \ . \tag{5.106}$$

The motion of charged particles in strong magnetic fields can be approximated as a relativistic motion along the field lines. This is a reasonable approximation because the electrons are estimated to become relativistic at a height of a few centimeters above the stellar surface. Therefore in the frame of the static observer we take [287]

$$j^{\hat{r}} = \rho c \frac{B^{\hat{r}}}{B} \tag{5.107}$$

where $\rho(R, \theta, \phi)$ is the SC density.

TBS solved the Newtonian version of (5.105)[2] and calculated L for three modes: (1,1), (2,0) and (3,0). They also estimated the order of magnitude of the energy loss L and the angle θ_0 for all of the oscillation modes for which θ_0 is small. They found that θ_0 is small for modes with $m' < 3$ and, as we will see later, this result also holds in GR. We will next solve the relativistic equation (5.105) and calculate θ_0 and L for *all* of the modes (ℓ', m') for which the angle θ_0 is small. We will present elsewhere a study of the case for large θ_0.

In order to solve equation (5.105) and calculate L in the case of small θ_0, we use the following procedure. First, we approximate equation (5.131) and the boundary condition (5.130) for small θ by expanding all of the functional dependence on θ in a Taylor series, taking into account only terms of the two lowest orders in θ. Secondly, we solve this equation and calculate $\rho_{\rm SC}$ and $\Delta\mathcal{E}$ using the approximate solution for $\Psi_{\rm SC}$. Then, we calculate the angle θ_0 by substituting $\rho_{\rm SC}$ and $\Delta\mathcal{E}$ into (5.105). Finally, substituting the expressions for θ_0, $\rho_{\rm SC}$ and $\Delta\mathcal{E}$ into (5.106), gives us the expression for L. Since the methods for solving equation (5.131) for $m' = 0$ and $m' \neq 0$ exploit a similar technique, we present just the solution for $m' = 0$ below, in this Section, while the solution for non-axisymmetric modes is presented in Appendix C.

For small angles θ, the spherical harmonic $Y_{\ell m}(\theta, \phi)$ can be approximated by the sum of the first two lowest order terms in the expansion in terms of θ

$$Y_{\ell m}(\theta, \phi) \approx A^{(1)}_{\ell m}(\phi) \, \theta^m + A^{(2)}_{\ell m}(\phi) \, \theta^{m+2} \ . \tag{5.108}$$

In this case, the characteristics (5.135) take the form

$$\varphi = \sqrt{-r^2 q_1(r)} \, \theta \ . \tag{5.109}$$

Specialising to small θ in the boundary condition (5.130) for $\Psi_{\rm SC}$, gives the following expression:

$$\Psi_{\rm SC}|_{r=R} = -B_0 R f_R \tilde{\eta}_R A^{(2)}_{\ell' 0} \, \theta^2 \ . \tag{5.110}$$

[2]It should be noted here that, as we mentioned above, TBS uses a slightly different formula for the determination of θ_0 which does not take into account the anisotropy of the plasma outflow.

In order to calculate $\Psi_{\rm SC}$ for arbitrary r, one has to replace θ in this equation by $\sqrt{[r^2 q_1(r)]/[R^2 q_1(R)]}\,\theta$, following the argument given earlier for $\sin\theta$, and this then gives the solution:

$$\Psi_{\rm SC} = -B_0 R f_{_R} \tilde{\eta}_{_R} \frac{r^2 q_1(r)}{R^2 q_1(R)} A^{(2)}_{\ell' 0}\, \theta^2 \,. \tag{5.111}$$

Substituting this into formula (5.46), we obtain the expression for the SC density:

$$\rho_{\rm SC} = \frac{B_0 f_{_R} \tilde{\eta}_{_R}}{\pi\, N_{\rm R} R} \frac{r^2 q_1(r)}{R^2 q_1(R)} A^{(2)}_{\ell' 0} \,. \tag{5.112}$$

Substituting $\Psi_{\rm SC}$ as given by (5.111) into (5.44), we obtain the expression for electric field $E^{\hat{\theta}}_{\rm SC}$. Substituting this into (5.98) gives $\Delta\mathcal{E}$:

$$\Delta\mathcal{E}(\theta,\phi) = B_0 R f_{_R} \tilde{\eta}_{_R} N_{\rm R} A^{(2)}_{\ell' 0}\, \theta^2 \,. \tag{5.113}$$

Using this expression for $\Delta\mathcal{E}$ in equation (5.105), we obtain an algebraic equation for θ_0, which has the following solution:

$$\theta_0 = 2 N_R^{1/4} \left[\frac{\tilde{\eta}_{_R} A^{(2)}_{\ell' 0}}{f_{_R}} \right]^{1/2} \,. \tag{5.114}$$

Substituting (5.113) and (5.107) into (5.106), gives us the following expression for the total energy loss:

$$L_{\ell' 0} = \frac{1}{2} \left[B_0 R f_{_R} \tilde{\eta}_{_R} A^{(2)}_{\ell' 0} \right]^2 \theta_0^4 \,, \tag{5.115}$$

and then using (5.114) in equation (5.115), gives

$$L_{\ell' 0} = 8 N_R \left[B_0 R\, \tilde{\eta}_R^2 (A^{(2)}_{\ell' 0})^2 \right]^2 \,. \tag{5.116}$$

The energy losses for non-axisymmetric modes are calculated in Appendix C. The angle θ_0 and the energy loss L are given by expressions (5.149) and (5.151) in that case. Note that determining θ_0 using the direct relativistic extension of the TBS method would give a value that is smaller than (5.114) by a constant factor of $2^{0.5}$, causing L to be smaller by a factor of 4. For the $m' = 1$ modes, these correction factors are $(2\pi)^{0.25}$ and 2π respectively, while for the $m' = 2$ modes they are $(3\pi)^{0.5}$ and $(3\pi)^3$.

We now continue our discussion with analysis of the contribution of the effects of GR to the quantities θ_0 and $L_{\ell' 0}$. The ratio of θ_0 in GR to its Newtonian counterpart for a given oscillation amplitude [i.e., for $(\tilde{\eta}_{_R})_{\rm GR} = (\tilde{\eta}_{_R})_{\rm Newt}$] can be obtained using equation (5.114):

$$\frac{(\theta_0)_{_{\rm GR}}}{(\theta_0)_{_{\rm Newt}}} = \frac{N_R^{1/4}}{f_R^{1/2}} \,. \tag{5.117}$$

This ratio is shown in Figure 5.3 (left panel) plotted as a function of the stellar compactness parameter M/R. It can be seen that in GR, the angle θ_0 is smaller than in Newtonian theory (it approaches its Newtonian value as $M/R \to 0$), meaning that GR effects lead to the polar cap being smaller. The reason for this can be understood in the following way. The angle θ_0 is determined from equation (5.105) and it is convenient to analyze the relativistic effects by looking at this equation. The contribution from the curvature is contained here in three terms: i) the factor f_R^4 on the right-hand side, ii) the factor N_R on the left-hand side and iii) a factor f_R^2 on the left-hand side that is contained implicitly within the term $\Delta\mathcal{E}\rho_{\rm SC}$. The first of these three terms accounts for the modification of the geometry of the background dipole magnetic field lines due to the curvature. As we discussed above, the magnetic field lines obey the relation $f_r \sin\theta/r^2 = {\rm const}$,

with $f_r = 1$ in the Newtonian case but $f_r > 1$ in GR. This means that a magnetic field line with a given energy density at $r = R_a$ on the equatorial plane, crosses the stellar surface closer to the pole in GR than in Newtonian theory. The second relativistic factor accounts for the redshift of the kinetic energy of the plasma due to the displacement from $r = R$ to $r = R_a$. Finally, the third factor is responsible for the amplification of the energy density of the outflowing plasma caused by the increase of the magnetic field strength (for a given magnetic moment) due to GR effects. The last of these would obviously lead to an increase of θ_0 in GR if it were acting alone. However, this effect is counteracted by the change of the geometry of the magnetic field lines and the gravitational redshift and those two effects are substantially stronger, giving the result that the angle θ_0 is smaller in GR than in Newtonian theory. Note that, as expected, the ratio $(\theta_0)_{\rm GR} / (\theta_0)_{\rm Newt}$ for the axisymmetric toroidal modes does not depend on ℓ', while for the general $m' \neq 0$ modes, there *is* dependence on ℓ'. This is because, as discussed above, the function $\Psi_{\rm SC}$ for $m' = 0$ depends only on the lowest $\ell = 1$ perturbation to the magnetic field since the higher ℓ perturbations are contained in the term $\partial_\phi \partial_t \delta S$ which disappears in axisymmetry.

The ratio of the angle θ_0 in GR to its Newtonian counterpart, for $m' \neq 0$ modes, can be obtained using equation (5.149) (see Appendix C for details of the derivation):

$$\frac{(\theta_0)_{\rm GR}}{(\theta_0)_{\rm Newt}} = \left(\frac{N_R}{f_R^2} \frac{|D_{\ell' m'}|_{\rm GR}}{|D_{\ell' m'}|_{\rm Newt}} \right)^{\frac{1}{6-2m'}} . \tag{5.118}$$

Figure 5.3 (central and right panels) shows the ratio of angle θ_0 in GR to its Newtonian equivalent for the modes $m' = 1, 2$ for several values of ℓ'. As can be seen in these plots, θ_0 is smaller in GR than in Newtonian theory also for the $m' = 1$ and $m' = 2$ modes. The reason for this is similar to that for the $m' = 0$ modes which we discussed above. We have made the analysis for values of ℓ' up to $\ell' = 10$ and the ratio $(\theta_0)_{\rm GR} / (\theta_0)_{\rm Newt}$ was found to be rather insensitive to the values of ℓ'. (The dependence on ℓ' is due to the fact that $(\rho_{\rm SC})_{\rm GR} / (\rho_{\rm SC})_{\rm Newt}$ is generally larger for higher ℓ' at small θ_0.)

The ratio of the energy losses for the $m' = 0$ modes in GR and in Newtonian theory is equal to N_R, as one can obtain using equation (5.116), and this is plotted in the left panel of Figure 5.4. The GR modification is caused by the gravitational redshift of the plasma energy; the other "magnetic" GR effects do not influence this, because the shrinking of the polar cap and the increase in the plasma energy density exactly compensate each other.

The ratio of the energy losses for the $m' \neq 0$ modes in GR and in Newtonian theory can be straightforwardly obtained using equation (5.151):

$$\frac{(L_{\ell' m'})_{\rm GR}}{(L_{\ell' m'})_{\rm Newt}} = f_R^4 N_R^{\frac{1+m'}{3-m'}} \left(f_R^{-2} \frac{|D_{\ell' m'}|_{\rm GR}}{|D_{\ell' m'}|_{\rm Newt}} \right)^{\frac{4}{3-m'}} . \tag{5.119}$$

This is also shown in Figure 5.4 where one can see that the energy loss of the $m' \neq 0$ modes is smaller in GR than in Newtonian theory. The reason for this is the same as for the $m' = 0$ modes discussed above, i.e., the increase in the energy density of the outflowing plasma cannot compensate the shrinking of the polar cap. Moreover, for the $m' = 2$ modes, the energy density of the outflowing plasma is proportional to $\theta^{2m'}$ (see eqs. (5.98) and (5.147)) and so the total energy losses are very sensitive to the size of the polar cap. Because of this, the ratios of the total energy losses for the $m' = 2$ modes in GR and in Newtonian theory are much smaller than those for the $m' = 0$ and $m' = 1$ modes.

5.6 Summary

In this work, we have described our general relativistic model for the force-free magnetosphere of an oscillating, non-rotating neutron star. Our approach is based on the previous Newtonian model developed by TBS

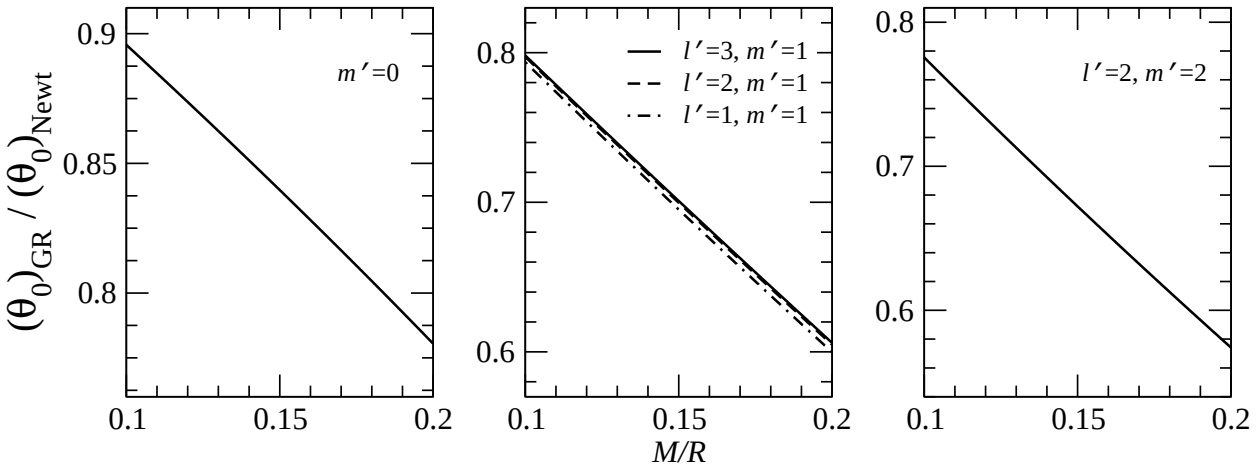

Figure 5.3: The ratio $(\theta_0)_{\rm GR}/(\theta_0)_{\rm Newt}$ is plotted against stellar compactness M/R for some representative toroidal oscillation modes with $m' = 0,\ 1,\ 2$; it asymptotically approaches 1, of course, in the Newtonian limit $M/R \to 0$.

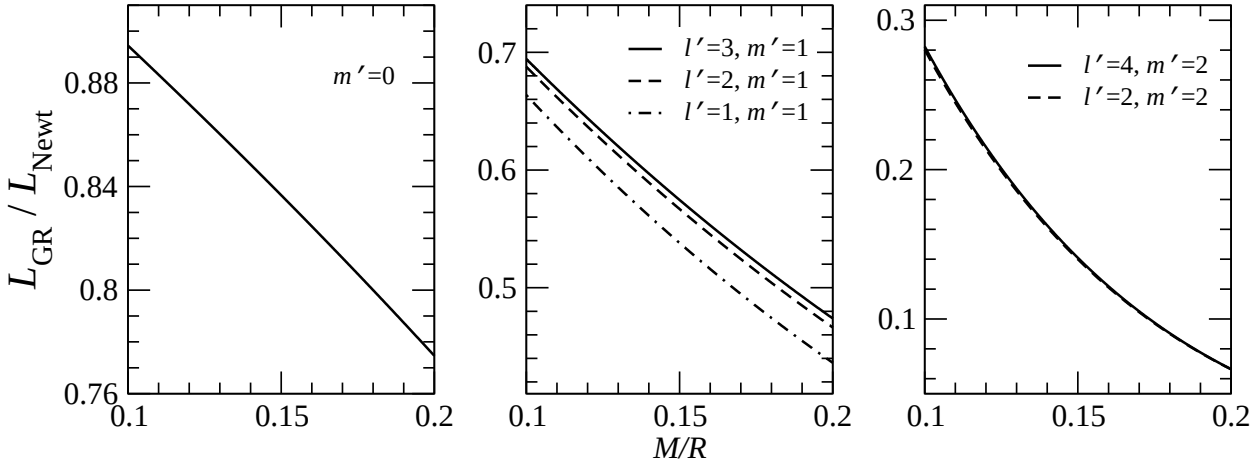

Figure 5.4: The ratio $L_{\rm GR}/L_{\rm Newt}$ is plotted against stellar compactness M/R for toroidal oscillation modes with $m' = 0,\ 1,\ 2$.

and focuses on toroidal modes which are thought to be particularly relevant for magnetar QPO phenomena. We have taken the spacetime geometry to be spherically symmetric and have neglected any modifications of it caused by the electromagnetic fields, the stellar oscillations and the magnetospheric plasma. Within this context, we have derived the general relativistic Maxwell equations for arbitrary small-amplitude oscillations of a neutron star with a generic magnetic field configuration and have shown that, as in the Newtonian case, they can be solved analytically for the force-free configuration of the electromagnetic fields (i.e. $E_{||} \ll B$) under the low current density approximation (LCDA). We have applied our formalism to small-amplitude toroidal oscillations of a neutron star with a dipole magnetic field and have found that the LCDA is valid for at least half of these modes in GR, as in the Newtonian calculations of TBS. We have also discussed the contribution of the GR effects to our solution, finding that they lead to an increase in the absolute values of the electromagnetic fields and the space charge (SC) density near to the stellar surface.

We have calculated the energy losses due to plasma outflow resulting from these oscillations, focusing on cases where the size of the polar cap is small so that one can expand the Maxwell equations as Taylor series in powers of θ, retaining only the two lowest order terms. This approach leads to a great simplification and allowed us to perform a thorough analysis of the solution. We have found that in GR, the polar cap is smaller than in Newtonian theory and have shown that this is due to the change in the geometry of the dipole magnetic field and the gravitational redshift of the energy of the outflowing plasma. Also, we found that the oscillation modes which have small θ_0, all have $m' < 3$ as in the Newtonian case.

The total energy loss resulting from the stellar oscillations causing plasma outflow through the polar cap region, is determined through an integral over the whole polar cap area, and so it depends on both the kinetic energy density of the outflowing plasma and the surface area of the polar cap. Although GR effects lead to some increase in the energy density of the outflowing plasma (due to the increase in the surface magnetic field strength for a given magnetic moment), the area of the polar cap is smaller in GR and we have found that the increase in the energy density of the outflowing plasma cannot compensate for the shrinking in size of the polar cap. Therefore the total energy losses for the toroidal oscillation modes are significantly smaller in GR than in Newtonian theory.

In conclusion, we point out that while our calculations represent an advance with respect to previous ones, they still do not include a number of very important aspects which would be necessary for a realistic description of these phenomena. Most importantly, as noted above, they do not take account of electric currents flowing in the magnetosphere. Inclusion of these in a consistent way would require solving a version of the non-linear "pulsar equation" [266] for oscillating neutron stars, possibly by adopting a numerical approach similar to that of [103] (see also [178, 419]) or performing *time-dependent* simulations of the magnetosphere [385, 211, 261]. This will be the subject of future investigations.

5.7 Appendix A: Calculation of δS

The derivative with respect to ϕ of the right hand side of equation (5.64) must be equal to the derivative with respect to θ of the left-hand side of (5.65). Using this condition and expression (5.49) for S, we obtain

$$\triangle_\Omega(\partial_t \delta S)|_{r=R} = -\Bigg[\left(N\delta v^{\hat{r}}\partial_r \triangle_\Omega S_0 + \frac{\delta v^{\hat{\theta}}}{r}\partial_\theta \triangle_\Omega S_0 + \frac{\delta v^{\hat{\phi}}}{r\sin\theta}\partial_\phi \triangle_\Omega S_0\right)$$

$$+\frac{\triangle_\Omega S_0}{r\sin\theta}\left(\partial_\theta(\sin\theta\delta v^{\hat{\theta}}) + \partial_\phi \delta v^{\hat{\phi}}\right) + N\partial_r\partial_\theta S_0\,\partial_\theta \delta v^{\hat{r}} + \frac{N}{\sin^2\theta}\partial_r\partial_\phi S_0\,\partial_\phi \delta v^{\hat{r}}\Bigg]|_{r=R}. \quad (5.120)$$

We now introduce a new function for shorthand:

$$q_\ell(r) = -M\frac{d}{dr}\left[r\left(1-\frac{2M}{r}\right)\frac{d}{dr}Q_\ell\left(1-\frac{r}{M}\right)\right]\ . \quad (5.121)$$

Using this notation, one can rewrite equations (5.57) and (5.55) in the following way

$$\delta S_{\ell m}(r,t) = \frac{r^2 q_\ell(r)}{M^3}\,\delta s_{\ell m}(t), \tag{5.122}$$

$$\delta S(t,r,\theta,\phi) = \sum_{\ell=0}^{\infty}\sum_{m=-\ell}^{\ell}\frac{r^2 q_\ell(r)}{M^3}\,\delta s_{\ell m}(t) Y_{\ell m}(\theta,\phi). \tag{5.123}$$

Substituting the right hand side of the last equation into the left hand side of (5.120), we get

$$\begin{aligned}&\frac{r^2}{M^3}\sum_{\ell=0}^{\infty}\sum_{m=-\ell}^{\ell} q_\ell(r)\;\partial_t\delta s_{\ell m}(t)\,\ell(\ell+1)Y_{\ell m}|_{r=R} \\ &= \Bigg[\left(N\delta v^{\hat r}\partial_r\triangle_\Omega S_0 + \frac{\delta v^{\hat\theta}}{r}\partial_\theta\triangle_\Omega S_0 + \frac{\delta v^{\hat\phi}}{r\sin\theta}\partial_\phi\triangle_\Omega S_0\right) \\ &+ \frac{\triangle_\Omega S_0}{r\sin\theta}\left(\partial_\theta(\sin\theta\delta v^{\hat\theta}) + \partial_\phi\delta v^{\hat\phi}\right) + N\partial_r\partial_\theta S_0\,\partial_\theta\delta v^{\hat r} + \frac{N}{\sin^2\theta}\partial_r\partial_\phi S_0\,\partial_\phi\delta v^{\hat r}\Bigg]|_{r=R}.\end{aligned} \tag{5.124}$$

Multiplying now both sides of this equation by $Y^*_{\ell' m'}(\theta,\phi)$, integrating it over solid angle 4π and using the orthogonality condition for spherical harmonics $\int Y^*_{\ell' m'} Y_{\ell m} d\Omega = \delta_{\ell'\ell}\delta_{m' m}$, we obtain

$$\begin{aligned}\partial_t\delta s_{\ell m}(t) = \frac{M^3}{\ell'(\ell'+1)\,r^2 q_{\ell'}(r)}\int_{4\pi}\Bigg[&\left(N\delta v^{\hat r}\partial_r\triangle_\Omega S_0 + \frac{\delta v^{\hat\theta}}{r}\partial_\theta\triangle_\Omega S_0 + \frac{\delta v^{\hat\phi}}{r\sin\theta}\partial_\phi\triangle_\Omega S_0\right) \\ &+\frac{\triangle_\Omega S_0}{r\sin\theta}\left(\partial_\theta(\sin\theta\delta v^{\hat\theta}) + \partial_\phi\delta v^{\hat\phi}\right) + N\partial_r\partial_\theta S_0\,\partial_\theta\delta v^{\hat r} + \frac{N}{\sin^2\theta}\partial_r\partial_\phi S_0\,\partial_\phi\delta v^{\hat r}\Bigg] Y^*_{\ell' m'}(\theta,\phi)d\Omega|_{r=R}.\end{aligned} \tag{5.125}$$

In the case of toroidal oscillations of a NS in the mode (ℓ', m'), the oscillation velocity components are given by (5.70). Substituting the right-hand sides of (5.70) and (5.72) into (5.125), we get the following expression for $\partial_t\delta s_{\ell m}(t)$ for a NS with a dipole magnetic field

$$\begin{aligned}\partial_t\delta s_{\ell m}(t) = &\frac{1}{\ell\,(\ell+1)}\frac{B_0 f_{_R} M^3\tilde\eta_{\rm R}}{R\,q_\ell\,(R)} \\ &\times\int_{4\pi}\left[\partial_\theta Y_{\ell m}\left(\sin\theta\cos\chi - e^{i\phi}\cos\theta\sin\chi\right) + ie^{i\phi}\partial_\phi Y_{\ell m}\sin\theta\sin\chi\right]\frac{Y^*_{\ell' m'}(\theta,\phi)}{\sin\theta}d\Omega\,,\end{aligned} \tag{5.126}$$

where $\tilde\eta_{\rm R} = \eta_{_R} e^{-i\omega_{\rm R} t}$. Substituting this into (5.123), we obtain the expression for δS for a toroidal oscillation mode (ℓ', m') of a NS a with dipole magnetic field

$$\begin{aligned}\partial_t\delta S(r,t) = &\sum_{\ell=0}^{\infty}\sum_{m=-\ell}^{\ell}\frac{B_0 R f_{_R}\tilde\eta_{\rm R}}{\ell\,(\ell+1)}\frac{r^2\,q_\ell\,(r)}{R^2\,q_\ell\,(R)} \\ &\times\int_{4\pi}\left[\partial_\theta Y_{\ell m}\left(\sin\theta\cos\chi - e^{i\phi}\cos\theta\sin\chi\right) + ie^{i\phi}\partial_\phi Y_{\ell m}\sin\theta\sin\chi\right]\frac{Y^*_{\ell' m'}(\theta,\phi)}{\sin\theta}d\Omega\,.\end{aligned} \tag{5.127}$$

If the magnetic dipole moment is aligned with the oscillation mode axis ($\chi = 0$), one can easily show that

$$\partial_t\delta s_{\ell m}(t) = \frac{im}{\ell\,(\ell+1)}B_0 R f_{_R} M^3\tilde\eta_{\rm R}\frac{\delta_{\ell'\ell}\delta_{m' m}}{R^2\,q_\ell\,(R)}\,, \tag{5.128}$$

$$\partial_t \delta S = \frac{\imath m'}{\ell'(\ell'+1)} B_0 R f_{_R} \tilde{\eta}_{\rm R} \frac{r^2\, q_{\ell'}(r)}{R^2\, q_{\ell'}(R)}\, Y_{\ell' m'} \ , \tag{5.129}$$

where $\delta_{\ell'\ell}$ is the Kronecker tensor.

5.8 Appendix B: Solution of the $\Psi_{\rm SC}$ Equation for $\chi = 0$

Substituting the right hand side of equation (5.129) and expressions (5.70) into (5.81), we obtain a boundary condition for the function $\Psi_{\rm SC}$ for toroidal oscillations of a NS, for the case $\chi = 0$:

$$\Psi_{\rm SC}|_{r=R} = -B_0 R f_{_R} \tilde{\eta}_{\rm R} \int_0^\theta \left[\cos\vartheta\, \partial_\vartheta Y_{\ell' m'}(\vartheta,\phi) - \frac{m'^2}{\ell'\,(\ell'+1)} \frac{Y_{\ell' m'}(\vartheta,\phi)}{\sin\vartheta} \right] d\vartheta \ , \tag{5.130}$$

where ϑ is the integration variable. Substituting the expression for $\partial_t \delta S$ given by (5.129) into equation (5.80), we obtain an equation for the SC potential, $\Psi_{\rm SC}$, for a toroidal oscillation mode (ℓ', m') of a NS having a dipole magnetic field aligned with the oscillation mode axis

$$\begin{aligned} -2r^2 q_1(r) \cos\theta\, \partial_r(\Psi_{\rm SC}) \quad &+ \quad \partial_r[r^2 q_1(r)] \sin\theta\, \partial_\theta(\Psi_{\rm SC}) \\ &- \quad \frac{m'^2}{\ell'(\ell'+1)} B_0 R f_{_R} \tilde{\eta}_{\rm R} \partial_r[r^2 q_1(r)] \frac{r^2 q_{\ell'}(r)}{R^2 q_{\ell'}(R)}\, Y_{\ell' m'}(\theta,\phi) = 0 \ . \end{aligned} \tag{5.131}$$

This is a first-order partial differential equation. According to a well-known theorem from the theory of such equations, (5.131) is equivalent to the following system of first-order ordinary differential equations (see, for example, Chapter II of Volume II of [108] for a thorough discussion)

$$\begin{aligned} -\frac{dr}{2r^2 q_1(r)\cos\theta} \quad &= \quad \frac{d\theta}{\partial_r[r^2 q_1(r)]\sin\theta} \\ &= \quad \frac{d\Psi_{\rm SC}}{\frac{m'^2}{\ell'(\ell'+1)} B_0 R f_{_R} \tilde{\eta}_{\rm R} \partial_r[r^2 q_1(r)] \frac{r^2 q_{\ell'}(r)}{R^2 q_{\ell'}(R)}\, Y_{\ell' m'}(\theta,\phi)} = \frac{d\phi}{0} = \frac{dt}{0} \ . \end{aligned} \tag{5.132}$$

The characteristics of this system are

$$\varphi_0 = t \ , \tag{5.133}$$

$$\varphi_1 = \phi \ , \tag{5.134}$$

$$\varphi_2 = \sqrt{-r^2 q_1(r)}\, \sin\theta \ , \tag{5.135}$$

$$\varphi_3 = \Psi_{\rm SC} + \frac{1}{2} \frac{m'^2}{\ell(\ell+1)} B_0 R f_{_R} \tilde{\eta}_{_R} \int \frac{\partial_r[r^2 q_1(r)]}{q_1(r)} \frac{q_{\ell'}(r)}{R^2 q_{\ell'}(R)} \frac{Y_{\ell' m'}(\theta(r),\phi)}{\cos\theta(r)}\, dr \ , \tag{5.136}$$

where $\theta(r)$ depends on the variable r due to (5.135):

$$\theta\,(r) = \arcsin\left(\frac{\varphi_2}{\sqrt{-r^2 q_1(r)}} \right) . \tag{5.137}$$

The integral of equation (5.131) is an arbitrary function of φ_0, φ_1, φ_2 and φ_3:

$$\Gamma(\varphi_0, \varphi_1, \varphi_2, \varphi_3) = 0 \ . \tag{5.138}$$

Using this, one can obtain an expression for the general solution of equation (5.131):

$$\Psi_{\rm SC} = -\frac{1}{2}\frac{m'^2}{\ell'(\ell'+1)} B_0 R f_{_R} \tilde{\eta}_{_R} \int \frac{\partial_r[r^2 q_1(r)]}{q_1(r)} \frac{q_{\ell'}(r)}{R^2 q_{\ell'}(R)} \frac{Y_{\ell' m'}(\theta(r),\phi)}{\cos\theta(r)}\, dr \qquad (5.139)$$
$$+\Phi_1\left[\sqrt{-r^2 q_1(r)}\,\sin\theta, \phi, t\right] ,$$

where Φ_1 is an arbitrary function that has to be determined from the boundary condition (5.130). Using (5.130), we can obtain a boundary condition for Φ_1:

$$\Phi_1\left[\sqrt{-r^2 q_1(r)}\,\sin\theta, \phi, t\right]|_{r=R} = \Psi_{\rm SC}|_{r=R} \qquad (5.140)$$
$$+\frac{1}{2}\frac{m'^2}{\ell'(\ell'+1)} B_0 R f_{_R} \tilde{\eta}_{_R} \int \frac{\partial_r[r^2 q_1(r)]}{q_1(r)} \frac{q_{\ell'}(r)}{R^2 q_{\ell'}(R)} \frac{Y_{\ell' m'}(\theta(r),\phi)}{\cos\theta(r)}\, dr|_{r=R} ,$$

where $\Psi_{\rm SC}|_{r=R}$ is given by (5.130). Now using equations (5.139) and (5.140), we can write a final expression for the general solution of equation (5.131) in the following form

$$\Psi_{\rm SC} = -\frac{1}{2}\frac{m'^2}{\ell'(\ell'+1)} B_0 R f_{_R} \tilde{\eta}_{_R} \int_R^r \frac{\partial_{r'}[r'^2 q_1(r')]}{q_1(r')} \frac{q_{\ell'}(r')}{R^2 q_{\ell'}(R)} \frac{Y_{\ell' m'}(\theta(r'),\phi)}{\cos\theta(r')}\, dr' \qquad (5.141)$$
$$+\Phi_2\left[\sqrt{-r^2 q_1(r)}\,\sin\theta, \phi, t\right] ,$$

where r' is the integration variable. The function $\theta(r)$ under this integral must be substituted by (5.137) and, after performing the integration, the function ϕ_2 should be replaced by (5.136). The unknown function $\Phi_2\left[\sqrt{-r^2 q_1(r)}\,\sin\theta, \phi, t\right]$ is determined using boundary condition (5.130):

$$\Phi_2\left[\sqrt{-r^2 q_1(r)}\,\sin\theta, \phi, t\right]|_{r=R} \qquad (5.142)$$
$$= -B_0 R f_{_R} \tilde{\eta}_{_R} \int_0^\theta \left[\cos\vartheta\, \partial_\vartheta Y_{\ell' m'}(\vartheta,\phi) - \frac{m'^2}{\ell'\,(\ell'+1)} \frac{Y_{\ell' m'}(\vartheta,\phi)}{\sin\vartheta}\right] d\vartheta .$$

In order to obtain Φ_2 for arbitrary r, one has to express the right hand side of this equation in terms of $\sin\theta$, and then replace $\sin\theta$ by $\sqrt{[r^2 q_1(r)]/[R^2 q_1(R)]} \times \sin\theta$. We then have our analytical expression for the function $\Psi_{\rm SC}$ for toroidal oscillations of a NS.

5.9 Appendix C: Energy losses for $m' \neq 0$ modes

In this Section we solve equation (5.131) and calculate θ_0 together with the total energy losses for non-axisymmetric toroidal oscillation modes for small θ_0. Taking the limit of small θ in the boundary condition (5.130) for $\Psi_{\rm SC}$, we obtain the following approximate expression for $\Psi_{SC}|_{r=R}$

$$\begin{aligned}\Psi_{SC}|_{r=R} &= -B_0 R f_{_R} \tilde{\eta}_{_R} \Bigg\{ \left[1 - \frac{m'}{\ell'(\ell'+1)}\right] A^{(1)}_{\ell' m'} \theta^{m'} \qquad (5.143)\\ &+ \left[A^{(2)}_{\ell' m'} - \frac{m' A^{(1)}_{\ell' m'}}{2(m'+2)} - \frac{m'^2\left(A^{(1)}_{\ell' m'}/6 + A^{(2)}_{\ell' m'}\right)}{(m'+2)\ell'(\ell'+1)}\right] \theta^{m'+2} \Bigg\}.\end{aligned}$$

Using this result, one can show that the general solution of equation (5.131) for small θ has the following form

$$\begin{aligned}
\Psi &= -B_0 R f_{_R} \tilde{\eta}_{_R} g_1(r)^{m/2} \Bigg\{ \Bigg[\frac{m^2}{\ell'(\ell'+1)} \int_R^r \frac{g_1'(r)}{g_1(r)^{m/2+1}} \frac{g_{\ell'}(r)}{g_{\ell'}(R)} dr \\
&+ \frac{1}{g_1(R)^{m'/2}} \left[1 - \frac{m'}{\ell'(\ell'+1)} \right] \Bigg] A^{(1)}_{\ell' m'} \theta^{m'} + \Bigg[\left[\frac{m'+3}{6} A^{(1)}_{\ell' m'} + A^{(2)}_{\ell' m} \right] g_1(r) \\
&\times \int_R^r \frac{g_1'(r)}{g_1(r)^{m'/2+2}} \frac{g_{\ell'}(r)}{g_{\ell'}(R)} dr - \frac{m' A^{(1)}_{\ell' m}}{6} \int_R^r \frac{g_1'(r)}{g_1(r)^{m'/2+1}} \frac{g_{\ell'}(r)}{g_{\ell'}(R)} dr + \frac{g_1(r)}{g_1(R)^{m'/2+1}} \\
&\times \left[A^{(2)}_{\ell' m'} - \frac{m'}{2(m'+2)} A^{(2)}_{\ell' m'} - \frac{m'^2}{(m'+2)\ell'(\ell'+1)} \left(\frac{1}{6} A^{(1)}_{\ell' m'} + A^{(2)}_{\ell' m'} \right) \right] \\
&+ \frac{m'}{6} \left[1 - \frac{m'}{\ell'(\ell'+1)} \right] \left(\frac{g_1(r)}{g_1(R)} - 1 \right) \Bigg] \theta^{m'+2} \Bigg\} ,
\end{aligned} \tag{5.144}$$

where we have introduced a new function $g_\ell(r) = r^2 q_\ell(r)$ for simplicity of notation. Using (5.44) and (5.98), we obtain an expression for $\Delta\mathcal{E}$:

$$\Delta\mathcal{E} = -B_0 R f_{_R} \tilde{\eta}_{_R} N_{_R} \int_0^\theta \cos\theta \partial_\theta Y_{\ell' m'} d\theta \, . \tag{5.145}$$

Substituting the expansion of $Y_{\ell' m'}$ for small θ given by (5.108) into (5.145), we get the following expression for $\Delta\mathcal{E}$ for small θ

$$\Delta\mathcal{E} = -B_0 R f_{_R} \tilde{\eta}_{_R} N_{_R} \left[A^{(1)}_{\ell' m'} \theta^{m'} + \left(A^{(2)}_{\ell' m'} - \frac{m'}{2(m'+2)} A^{(1)}_{\ell' m'} \right) \theta^{m'+2} \right] . \tag{5.146}$$

Now substituting (5.144) into (5.46), we get an expression for $\rho_{\rm SC}(R,\theta,\phi)$:

$$\rho_{\rm SC}(R,\theta,\phi) = -\frac{B_0 f_{_R} \tilde{\eta}_{_R}}{\pi N_{_R} R} D_{\ell' m'}(R,M) \theta^{m'} \, , \tag{5.147}$$

where we have introduced a new quantity $D_{\ell' m'}(R,M)$ for simplicity of notation:

$$\begin{aligned}
D_{\ell' m'}(R,M) &= \frac{m'}{48} \Bigg\{ 4 A^{(1)}_{\ell' m'} (1+m') \left[1 - \frac{m'}{\ell'(\ell'+l)} \right] \\
&+ \frac{3}{\ell'(\ell'+1)} \Bigg\{ 8m'(1+m') \left[\frac{A^{(1)}_{\ell' m'} m'}{2(2+m')} + \frac{(A^{(1)}_{\ell' m'} + 6A^{(2)}_{\ell' m'}) m'^2}{6(\ell'+\ell'^2)(2+m')} - A^{(2)}_{\ell' m'} \right] \\
&+ \frac{A^{(1)}_{\ell' m'}(2M-R)}{g_1(R)^2 g_{\ell'}(R)} \Big[\partial_r g_1(r) \left(\ell'(\ell'+l)\, g_{\ell'}(R)(4g_1(R) + (m'-2)R\partial_r\, g_1(r) \right. \\
&+ \left. 2mRg_1(R)\partial_r g_{\ell'}(r) \right) + 2\ell'(\ell'+l) R g_1(R) g_{\ell'}(R) \partial^2_{r,r} g_1(r) \Big] \Bigg\} \Bigg\} |_{r=R} \, .
\end{aligned} \tag{5.148}$$

Substituting (5.146) and (5.147) into (5.105), we obtain an algebraic equation for θ_0 for $m \neq 0$ toroidal oscillation modes, which has the solution

$$\theta_0 = \left[\frac{16 N_{_R}\, \tilde{\eta}_{_R}^2 |A^{(1)}_{\ell' m'} D_{\ell' m'}(R,M)|}{f_{_R}^2} \right]^{\frac{1}{6-2m'}} \, . \tag{5.149}$$

We can see from this expression that θ_0 is small for modes with $m' < 3$, in agreement with the estimate of TBS. Remarkably, θ_0 does not depend on B_0 as in the case of $m' = 0$. Substituting (5.146), (5.147) and (5.107) into (5.106) gives

$$L_{\ell' m'} = \frac{2}{(m'+1)\pi} \left(B_0 R f_{_R} \tilde{\eta}_{_R}\right)^2 \; |A^{(1)}_{\ell' m'} \; D_{\ell' m'}(R, M)| \; \theta_0^{2m'+2}. \tag{5.150}$$

Replacing θ_0 in this equation by the right hand side of equation (5.149), we obtain

$$L_{\ell' m'} = \frac{B_0^2 R^2 f_{_R}^4 N_R^{\frac{1+m'}{3-m'}}}{8\pi(m'+1)} \left[\frac{16\tilde{\eta}_{_R}^2 \; |A^{(1)}_{\ell' m'} \; D_{\ell' m'}(R, M)|}{f_{_R}^2}\right]^{\frac{4}{3-m'}} . \tag{5.151}$$

Chapter 6

Future perspectives and concluding remarks

In this thesis, we have presented the results from our study of the dynamics of accretion-induced collapse (AIC) of white dwarfs and phase-transition-induce collapse (PTIC) of neutron stars, as well as the associated gravitational wave emission (Chapters 3-4). As a second topic of this thesis, we have presented a study of the effects of general relativity on the magnetospheres of oscillating neutron stars (Chapter 5). Detailed summaries of the results were presented at the end of the corresponding chapters.

Here we conclude by outlining some future tasks for improving the modelling of both AIC and PTIC, as well as a broader class of stellar core collapse phenomena in the context of GW emission, supernova explosions and long gamma-ray bursts (GRBs).

Our study of the PTIC of neutron stars presented here should be considered as a first step towards a better understanding of the phase-transition-induced dynamics of neutron stars. In the present study, we assumed that the conversion front progates supersonically and used simplified EoS. Due to the presently very limited knowledge about the phase transition, some of the aspects of the physical processes underlying the investigated scenario are necessarily simplified. The treatment of the EoS as a representation of matter in the mixed phase experiencing a phase transition is rather crude, especially when one considers the behaviour of fluid elements undergoing successive stages of compression and decompression, and changing the proportions of the phases. Moreover, our modelling neglects any possible effects from local heating, or from the creation and subsequent emission of neutrinos during the collapse and the subsequent phase of the oscillations. Future studies of the PTIC should improve on this by, in particular, exploiting better and more consistent treatment of the phase-conversion process and the interface between the two phases. The knowledge and experience obtained from the simulations of the thermonuclear combustion in, e.g.,, type Ia supernovae (see, e.g., [451] for a review) could be a useful guide for the future modelling of the phase transformations in neutron stars.

The core temperature in accreting white dwarfs is expected to be of the order of $\sim 10^8$ K [361]. Ignition of the thermonuclear burning of neon and oxygen in the infall phase of AIC rapidly increases the core temperature to $\sim 10^{9.7}$ K. In the simulations presented here, we do not model this initial increase of the temperature, but rather start with a precollapse WD already with core temperature of $\sim 10^{9.7}$ K. In order to model AIC more accurately, one should correctly model this initial thermonuclear heating of the WD core.

At temperatures below $\sim 10^9$ K, nuclear statistical equilibrium does not hold, hence one cannot represent a state of nuclear matter just by three quantities ρ, T and Y_e. Instead, the thermodynamic quantities depend also on the mass fractions of all of the nuclear species. In this case, one has to advect different nuclear fluid components separately as well as to take into account their thermonuclear reactions [207]. Robust techniques for doing this have already been developed in the context of core-collapse supernova simulations

(e.g.,[338, 71, 207]). Another point is that, the tabulated EoSs presently available for numerical simulations are unable to handle temperatures below $\sim 10^9$ [222, 372, 372]. Progress in improving this would be very welcome.

Another shortcoming of our AIC simulations, which is shared also with state-of-the-art multi-dimensional simulations of stellar iron core collapse in general relativity [123, 311, 312, 310], is in the treatment of the postbounce deleptonization and neutrino-cooling. The deleptonization scheme used in our work (and also in [123, 311, 312, 310]), models deleptonization very efficiently only in the collapse phase, while in the postbounce phase, all of the relevant neutrino-processes are completely ignored [229]. Therefore, although the collapse and bounce dynamics is well captured by our current scheme, the late postbounce evolution is poorly described. In fact, the postbounce deleptonization significantly affects the rotational configuration of PNSs: the postbounce cooling and contraction of the latter may lead to increase of its parameter $T/|W|$ by ~ 50 % within ~ 50 ms after bounce (see the discussion in Section 4.5). Contrary to that, in our current approach, $T/|W|$ of the PNS hardly changes in that phase. With such a drawback, it is hard to make accurate predictions about the late postbounce evolution.

In order to make progress with this, it is necessary to combine a multi-dimensional GR hydrodynamics code with a numerical scheme that can treat all of the relevant postbounce neutrino-processes (at least qualitatively correctly). Ideally, such a scheme should be simple to implement and computationally inexpensive in order to enable one to perform extensive parameter studies. One of the schemes that fulfills these requirements is the neutrino-leakage scheme [142, 57, 430, 355, 351, 213]. Original neutrino-leakage scheme ignore the neutrino heating and pressure, but this shortcoming can easily be overcome by using a neutrino-heating prescriptions similar to those suggested by [286, 199] and the neutrino-pressure treatment outlined in [229]. Implementation of the leakage scheme together with the prescriptions for the neutrino-heating and pressure in a multi-dimensional GR hydrodynamics code is currently under developments by the author as well as by other groups (see, e.g., [317] and references therein). In more distant future, GR hydrodynamics codes should incorporate more detailed and accurate neutrino transport schemes.

One of the prime motivation for our GR neutrino-leakage code is the study of the postbounce evolution of the PNSs formed in massive star iron core collapse. Of a particular interest is more accurate estimate of the prospects for the development of the high- and low-$T/|W|$ rotational instabilities in massive star iron core collapse. Extensive parameter studies should establish the dependence on the progenitor mass, rotation, degree of differential rotation, and the details of the EoS of the nuclear matter.

In addition to the more accurate treatment of the deleptonization, future codes should be able to take into account the effects of magnetic fields. This is relevant not only in the context of GW emission, but also in the modelling of the supernova explosions and the long GRBs. Collapse of rapidly rotating magnetized stellar cores has recently received significant attention because of their possible connection with type Ibc SN explosions and long GRBs [449]. In rapidly rotating stellar iron core-collapse, magneto-rotational instability as well as dynamo processes are thought to increase the magnetic field strength up to 10^{15} G near to the protoneutron star in some cases [79]. Such strong magnetic fields are expected to significantly affect the shock propagation and explosion dynamics. Moreover, they would transport angular momentum away from the collapsed core to the postshock region and possibly interact with unstable nonaxisymmetric modes. Investigation of the role of magnetic fields in rapidly rotating stellar collapse will be the subject of future investigations. Solution of the problem of SN explosions and GRBs is likely to be a decade long problem, requiring continuous advances in physics, numerical algorithms and computer science [313].

Bibliography

[1] E. B. Abdikamalov, H. Dimmelmeier, L Rezzolla and J. Miller *Relativistic simulations of the phase-transition-induced collapse of neutron stars.* Mon. Not. Roy. Astron. Soc., 392:52, 2009

[2] E. B. Abdikamalov, B. J. Ahmedov and J. Miller *The magnetosphere of oscillating neutron stars in general relativity*. Mon. Not. Roy. Astron. Soc., 395:443, 2009

[3] E. B. Abdikamalov, C. D. Ott, L Rezzolla, L Dessart, H. Dimmelmeier, A. Marek and H. T. Janka. *Axisymmetric general relativistic simulations of the accretion-induced collapse of white dwarfs.* Phys. Rev. D, submitted. Preprint: arxiv:0910:2703

[4] A. Abrahams and C. Evans. *Reading off gravitational radiation waveforms in numerical relativity calculations: Matching to linearised gravity*. Phys. Rev. D, 37:318, 1988.

[5] A. Abrahams and C. Evans. *Gauge invariant treatment of gravitational radiation near the source: Analysis and numerical simulations*. Phys. Rev. D, 42:2585, 1990.

[6] A. Abrahams, D. Bernstein, D. Hobill, E. Seidel, and L. Smarr. *Numerically generated black hole spacetimes: Interaction with gravitational waves*. Phys. Rev. D, 45:3544, 1992.

[7] URL http://www.ligo.caltech.edu/advLIGO. Advanced LIGO.

[8] C. Alcock and A. Olinto. *Exotic phases of hadronic matter and their astrophysical application*. Annu. Rev. Nucl. Part. Sci., 38:161. 1988.

[9] M. Alcubierre, B. Brgmann, D. Holz, R. Takahashi, S. Brandt, E Seidel, J. Thornburg, A. Ashtekar. *Symmetry Without Symmetry*. Intern. Jour. of Mod. Phys. D, 10:273, 2001.

[10] M. Alcubierre, *Introduction to 3+1 numerical relativity*, Oxform University Press, Oxford, 2008.

[11] M. Alford, D. B. Blaschke, A. Drago, T. Klahn and G. Pagliara *Astrophysics: Quark matter in compact stars?* Nature, 445:E7, 2007.

[12] M. G. Alford and S. Reddy. *Compact stars with color superconducting quark matter*. Phys. Rev. D, 67:074024, 2003

[13] N. Andersson and K. D. Kokkotas. *Towards gravitational wave asteroseismology*. Mon. Not. Roy. Astron. Soc., 299:1059, 1998.

[14] N. Andersson. *TOPICAL REVIEW: Gravitational waves from instabilities in relativistic stars*. Class. Quant. Grav., 20:105, 2003.

[15] A. Arcones, H.-T. Janka, and L. Scheck. *Nucleosynthesis-relevant conditions in neutrino-driven supernova outflows. I. Spherically symmetric hydrodynamic simulations*. Astron. Astrophys., 467:1227, 2007.

[16] D. Arnett. *Supernovae and nucleosynthesis. an investigation of the history of matter, from the Big Bang to the present*. Princeton series in astrophysics, Princeton, NJ: Princeton University Press, 1996.

[17] R. Arnowitt, S. Deser and G. W. Misner. *The dynamics of general relativity*. in Witten L., ed, *Gravitation: An introduction to current research*. Wiley, New York, USA, 1962.

[18] M. Babiuc, B. Szilágyi, I. Hawke, and Y. Zlochower. *Gravitational wave extraction based on Cauchy characteristic extraction and characteristic evolution*. Class. Quant. Grav., 22:5089, 2005.

[19] C. D. Bailyn and J. E. Grindlay. *Neutron stars and millisecond pulsars from accretion-induced collapse in globular clusters*. Astrophys. J., 353:159, 1990.

[20] L. Baiotti *Numerical relativity simulations of non-vacuum spacetimes in three dimension*. PhD Thesis, SISSA – International School for Advanced Studies, Trieste, Italy, 2004

[21] L. Baiotti, I. Hawke, P. J. Montero, F. Loëffler, L. Rezzolla, N. Stergioulas, J. A. Font, E. Seidel *Three-dimensional relativistic simulations of rotating neutron star collapse to a Kerr black hole*. Phys. Rev. D, 71:024035, 2005.

[22] L. Baiotti, R. Di Pietri, G. M. Manca, L. Rezzolla. *Accurate simulations of the dynamical bar-mode instability in full general relativity*. Phys. Rev. D, 75:044023, 2007.

[23] L. Baiotti, S. Bernuzzi, G. Corvino, R. De Pietri, A. Nagar. *Gravitational-Wave Extraction from Neutron Star Oscillations: comparing linear and nonlinear techniques*. Phys. Rev. D, 79:024002, 2009.

[24] E. Balbinski, B. F. Schutz, S. Detweiler and L. Lindblom. *The accuracy of the quadrupole approximation for the gravitational radiation from pulsating stars*. Mon. Not. Roy. Astron. Soc., 213:553, 1985.

[25] S. A. Balbus and J. F. Hawley. *A powerful local shear instability in weakly magnetized disks. I - Linear analysis. II - Nonlinear evolution*. Astrophys. J., 376:214, 1991.

[26] F. Banyuls, J. A. Font, J. M. Ibáñez, J. M. Martí and J. A. Miralles. *Numerical 3+1 General Relativistic Hydrodynamics: A Local Characteristic Approach*. Astrophys. J., 476:221, 1997

[27] Z. Barkat, Y. Reiss and G. Rakavy. *Stars in the mass ratio range from 7 to 10 as candidates for pulsar progenitors*. Astrophys. J. Lett., 193:L21, 1987.

[28] E. Baron, J. Cooperstein and S. Kahana. *Supernovae and the nuclear equation of state at high densities*. Nucl. Phys. A, 440:744, 1985.

[29] E. Baron, J. Cooperstein and S. Kahana. *Collapse of 9 solar mass stars*. Astrophys. J., 320:300, 1987.

[30] E. Baron, J. Cooperstein, S. Kahana and K. Nomoto. *Collapsing white dwarfs*. Astrophys. J., 320:204, 1987.

[31] E. Baron and J. Cooperstein. *The effect of iron core structure on supernovae*. Astrophys. J., 353:597, 1990.

[32] M. Barranco and J.-R.Buchler. *Equation of state of hot, dense stellar matter: Finite temperature nuclear Thomas-Fermi approach]*. Phys. Rev. C, 24:1191, 1981.

[33] T. W. Baumgarte and S. L. Shapiro, *On the numerical integration of Einstein's field equations*. Phys. Rev. D, 59:024007, 1999

[34] T. W. Baumgarter and S. L. Shapiro, *Numerical Relativity and Compact Binaries*, Physics Reports 376, 41-131, 2003

[35] J. P. Boyd, *Chebyshev and Fourier Spectral Methods*, second edition (Dover, New York, 2001).

[36] G. Baym, H. A. Bethe, and C. J. Pethick. *Neutron star matter*. Nucl. Phys. A, 175:225, 1971.

[37] C. Beetle and L. M. Burko. *A Radiation Scalar for Numerical Relativity*. Phys. Rev. Lett., 89(26):A261101, 2002.

[38] M. Beiner, H. Flocard, N. van Giai and P. Quentin. *Nuclear ground-state properties and self-consistent calculations with the skyrme interaction (I). Spherical description*. Nucl. Phys. A, 238:29, 1975.

[39] K. Belczynski, T. Bulik and A. J. Ruiter. *New Constraints on Type Ia Supernova Progenitor Models*. Astrophys. J., 629:915, 2005

[40] O. Benhar, V. Ferrari and L. Gualtieri *Gravitational wave asteroseismology reexamined*. Phys. Rev. D, 70:124015, 2004.

[41] O. Benhar, V. Ferrari, L. Gualtieri and S. Marassi *Quark matter imprint on gravitational waves from oscillating stars*. General Relat. Grav., 39:1323, 2007

[42] M. J. Berger and J. Oliger. *Adaptive mesh refinement for hyperbolic partial differential equations*. Journ. Comput. Phys., 53:484, 1984.

[43] V. S. Beskin. *General Relativity Effects on Electrodynamic Processes in Radio Pulsars*. Soviet Astron. Lett., 16:286, 1990.

[44] V. S. Beskin, A. V. Gurevich and Ya. N. Istomin. *Physics of the Pulsar Magnetosphere*. Cambridge University Press, 1993

[45] V. S. Beskin. *Osesimmetrichnye Stacionarnye Techeniya v Astrofizike (Axisymmetric Stationary Flows in Astrophysics)*. Moscow, Fizmatlit (in Russian), 2005.

[46] H. A. Bethe, G. E. Brown, J. Applegate and J. M. Lattimer. *Equation of state in the gravitational collapse of stars*. Nucl. Phys. A, 324:487, 1979.

[47] H. A. Bethe and J. R. Wilson. *Revival of a stalled supernova shock by neutrino heating*. Astrophys. J., 295:14, 1985.

[48] H. A. Bethe. *Supernova mechanisms*. Rev. Mod. Phys., 62:801, 1990.

[49] A. Bhattacharyya, S. K. Ghosh, P. S. Joarder, R. Mallick and S. Raha. Phys. Rev. C, 74:065804, 2006.

[50] H. Billing, K. Maischberger, A. Ruediger, R. Schilling, L. Schnupp, and W. Winkle *An argon laser interferometer for the detection of gravitational radiation*, J. Phys. E, 12:1043, 1979.

[51] Bisnovatyi-Kogan G. S., *Close Galactic origin of gamma-ray bursts*. Astrophys. J. Supp. Ser. , 97:185, 1995.

[52] L. Blanchet, T. Damour and G. Schäfer, *Post-Newtonian hydrodynamics and post-Newtonian gravitational wave generation for numerical relativity*. Mon. Not. Roy. Astron. Soc., 242:289, 1990.

[53] L. Blanchet, *Gravitational Radiation from Post-Newtonian Sources and Inspiralling Compact Binaries*. Liv. Rev. Rel., 9:4, 2006.

[54] S.I. Blinnikov, N. V. Dunina-Barkovskaya and D. K. Nadyozhin. *Equation of State of a Fermi Gas: Approximation s for Various Degrees of Relativism and Degeneracy*. Astrophys. J. Supp. Ser. , 106:171, 1996.

[55] S. A. Bludman and K. A. van Riper. *Equation of state of an ideal Fermi gas*. Astrophys. J., 212:859, 1977.

[56] S. A. Bludman and K. A. van Riper. *Diffusion approximation to neutrino transport in dense matter*. Astrophys. J., 224:631, 1978.

[57] S. A. Bludman, I Lichtenstadt, G. Hayden. *Homologous collapse and deleptonization of an evolved stellar core*. Astrophys. J., 261:661, 1982.

[58] M. Bocquet, S. Bonazzola, E. Gourgoulhon, J. Novak. *Rotating neutron star models with a magnetic field*. Astron. Astrophys., 301:757, 1995

[59] A. R. Bodmer. *Collapsed Nuclei* Phys. Rev. D4:1601, 1971.

[60] S. Bonazzola, E. Gourgoulhon. *Gravitational waves from pulsars: emission by the magnetic-field-induced distortion*. Astron. Astrophys., 312:675, 1996

[61] S. Bonazzola and J. A. Marck, *Three-dimensional gas dynamics in a sphere*. Journ. Comput. Phys., 87:201, 1990.

[62] S. Bonazzola, E. Gourgoulhon and J.-A. Marck. *Spectral methods in general relativistic astrophysics*. J. Comput. App. Math. 109:433 1999.

[63] S. Bonazzola, E. Gourgoulhon, P. Grandclément and J. Novak, *Constrained scheme for the Einstein equations based on the Dirac gauge and spherical coordinates*. Phys. Rev. D, 70:4007, 2004.

[64] P. Bonche and D. Vautherin. *A mean-field calculation of the equation of state of supernova matter*. Nucl. Phys. A, 372:496, 1981.

[65] P. Bonche and D. Vautherin. *Mean-field calculations of the equation of state of supernova matter II*. Astron. Astrophys., 112:268, 1982.

[66] V. Boriakoff. *Pulsar AP 2016+28 - High-frequency periodicity in the pulse microstructure*. Astrophys. J., 208:L43, 1976.

[67] V. B. Braginskii and K. S. Thorne. *Gravitational-wave bursts with memory and experimental prospects*. Nature, 327:123, 1987.

[68] R. Brockmann and R. Machleidt. *Relativistic nuclear structure. I. Nuclear matter*. Phys. Rev. C, 42:1965, 1990.

[69] S. W. Bruenn. *Stellar core collapse - Numerical model and infall epoch*. Astrophys. J. Supp. Ser. , 58:771, 1985.

[70] R. Buras, M. Rampp, H.-T. Janka and K. Kifonidis. *Improved Models of Stellar Core Collapse and Still No Explosions: What Is Missing?* Phys. Rev. Lett., 90(24):241101, 2003.

[71] R. Buras, M. Rampp, H.-T. Janka and K. Kifonidis. *Two-dimensional hydrodynamic core-collapse supernova simulations with spectral neutrino transport. I. Numerical method and results for a* $15M_{\odot}$ *star*. Astron. Astrophys., 447:1049, 2006.

[72] R. Buras, H.-T. Janka, M. Rampp and K. Kifonidis. *Two-dimensional hydrodynamic core-collapse supernova simulations with spectral neutrino transport. II. Models for different progenitor stars*. Astron. Astrophys., 457:281, 2006.

[73] L. Burderi, A. Possenti, M. Colpi, T. Di Salvo and N. D'Amico. *Neutron Stars with Submillisecond Periods: A Population of High-Mass Objects?* Astrophys. J.519:285, 1999.

[74] A. Burrows and J. M. Lattimer. *The effect of trapped lepton number and entropy on the outcome of stellar collapse*. Astrophys. J., 270, 735, 1983.

[75] A. Burrows and J. M. Lattimer. *The birth of neutron stars*. Astrophys. J., 307:178, 1986.

[76] A. Burrows, E. Livne, L. Dessart, C. D. Ott and J. Murphy. *A New Mechanism for Core-Collapse Supernova Explosions*. Astrophys. J., 640:878, 2006.

[77] A. Burrows, R. Reddy and T. A. Thompson. *Neutrino opacities in nuclear matter*. Nucl. Phys. A, 777:356, 2006.

[78] A. Burrows, L. Dessart, C. D. Ott and E. Livne. *Multi-dimensional explorations in supernova theory*. Phys. Rep., 442, 23, 2007.

[79] A. Burrows, L. Dessart, E. Livne, C. D. Ott and J. Murphy. *Simulations of Magnetically Driven Supernova and Hypernova Explosions in the Context of Rapid Rotation*. Astrophys. J., 664:416, 2007.

[80] A. Burrows, L. Dessart and E. Livne. *The Multi-Dimensional Character and Mechanisms of Core-Collapse Supernovae*. *SUPERNOVA 1987A: 20 YEARS AFTER: Supernovae and Gamma-Ray Bursters*, AIP Conf. Ser., editor S. Immler and R. McCray, 937:370, 2007.

[81] A. Burrows, E. Livne, L. Dessart, C. D. Ott and J. Murphy. *Features of the Acoustic Mechanism of Core-Collapse Supernova Explosions*. Astrophys. J., 655, 416, 2007.

[82] M. Camenzind *Compact Objects in Astrophysics. White Dwarfs, Neutron Stars and Black Holes*. Springer-Verlag Berlin Heidelberg, 2007

[83] R. Canal and E. Schatzman. *Non explosive collapse of white dwarfs*. Astron. Astrophys., 46:229, 1976.

[84] M. Cantiello, S.-C. Yoon, N. Langer, M. Livio. *Binary star progenitors of long gamma-ray bursts*. Astron. Astrophys., 465:L29, 2007

[85] C. Canuto, M. Y. Hussaini, A. Quarteroni and T. A. Zang. *Spectral methods in fluid dynamics* Springer, Berlin, 1988.

[86] E. Cappellaro, R. Evans and M. Turatto *A new determination of supernova rates and a comparison with indicators for gelactic star formation*. Astron. Astrophys., 351:459, 1999

[87] C. Y. Cardall, M. Prakash and J. M. Lattimer. *Effects of Strong Magnetic Fields on Neutron Star Structure*. Astrophys. J., 554:322, 2001

[88] B. Carter. *Killing Horizons and Orthogonally Transitive Groups in Space-Time*. J. Math. Phys., 10:70, 1969.

[89] B. Carter. *The commutation property of a stationary, axisymmetric system*. Commun. Math. Phys., 17:233, 1970.

[90] J. M. Centrella, K. C. B. New, L. L. Lowe and J. D. Brown. *Dynamical Rotational Instability at Low T/W*. Astrophys. J. Lett., 550:L193, 2001.

[91] P. Cerdá-Durán, G. Faye, H. Dimmelmeier, J. A. Font, J. M. Ibáñez, E. Müller and G. Schäfer. *CFC+: improved dynamics and gravitational waveforms from relativistic core collapse simulations*. Astron. Astrophys., 439:1033, 2005.

[92] P. Cerdá-Durán, J. A. Font and H, Dimmelmeier, *General relativistic simulations of passive-magneto-rotational core collapse with microphysics*. Astron. Astrophys., 474:169, 2007.

[93] P. Cerdá-Durán, V. Quilis, J. A. Font. *AMR simulations of the low T/—W— bar-mode instability of neutron stars*. Comp. Phys. Comm., 177:288, 2007

[94] P. Cerdá-Durán, J. A. Font, L Antón, E. Müller. *A new general relativistic magnetohydrodynamics code for dynamical spacetimes*. Astron. Astrophys., 492:937-953, 2008.

[95] S. Chandrasekhar. *Stellar Structure*. 1938, Dover, New York, U.S.A.

[96] S. Chandrasekhar. *Ellipsoidal Figures of Equilibrium* Yale University Press, New Haven, 1969.

[97] S. Chandrasekhar. *The Effect of Gravitational Radiation on the Secular Stability of the Maclaurin Spheroid*. Astrophys. J., 161:561, 1970.

[98] A. Choquet-Bruhat and J. W. york. *The Cuachy Problem*, (In A. Held, editor, *General Relativity and Gravitation*, volume 1, page 99 Plenum, New York, 1980)

[99] A. Choquet-Bruhat and J. W. york. *Geometrical well posed systems for the Einsteins equations*, C. R. Acad. Sc. Paris, 321:1089, 1995

[100] D. D. Clayton *Principles of Stellar Evolution and Nucleosynthesis*. University of Chicago Press. Chicago US, 1983.

[101] A. Colaiuda, V. Ferrari, L. Gualtieri, J. Pons. *Relativistic models of magnetars: structure and deformations*. Mon. Not. Roy. Astron. Soc., 385:2080, 2008.

[102] P. Colella and P. Woodward. *The Piecewise Parabolic Method (PPM) for Gas-Dynamical Simulations*. Journ. Comput. Phys., 54:174, 1984.

[103] I. Contopoulos, D. Kazanas and C. Fendt. *The Axisymmetric Pulsar Magnetosphere*. Astrophys. J., 511, 351, 1999.

[104] G. B. Cook, S. L. Shapiro, and S. A. Teukolsky. *Rapidly rotating polytropes in general relativity*. Astrophys. J., 422:227, 1994.

[105] G. B. Cook, S. L. Shapiro and S. A. Teukolsky, *Testing a simplified version of Einstein's equations for numerical relativity*. Phys. Rev. D, 53:5533, 1996

[106] J. Cooperstein. *The equation of state in supernovae*. Nucl. Phys. A,, 438:722, 1985.

[107] I. Cordero-Carrión, P. Cerdá-Durán, H. Dimmelmeier, J. L. Jaramillo, J. Novek and E. Gourgoulhon. *An improved constrained scheme for the Einstein equations: an approach to the uniqueness isse*. Phys. Rev. D, 79, 024017, 2009

[108] R. Courant and D. Hilbert. *Methods of Mathematical Physics*. John Wiley & Sons, 1962.

[109] M. Dan, S. Rosswog and M. Brüggen *Mass transfer dynamics in double degenerate binary systems*. Journal of Physics: Conference Series, Volume 172, Issue 1, p. 012034, 2009.

[110] T. DeGrand, R. L. Jaffe, K. Johnson and J. Kiskis. *Masses and other parameters of the light hadrons*. Phys. Rev. D, 12:2060, 1975.

[111] L. Dessart, A. Burrows, C. D. Ott, E. Livne, S.-Y. Yoon and N. Langer. *Multidimensional Simulations of the Accretion-induced Collapse of White Dwarfs to Neutron Stars*. Astrophys. J., 644:1063, 2006.

[112] L. Dessart, A. Burrows, E. Livne and C. D. Ott. *Multidimensional Radiation/Hydrodynamic Simulations of Proto-Neutron Star Convection*. Astrophys. J., 645:534, 2006.

[113] L. Dessart, A. Burrows, E. Livne and C. D. Ott. *Magnetically Driven Explosions of Rapidly Rotating White Dwarfs Following Accretion-Induced Collapse*. Astrophys. J., 669, 585, 2007.

[114] L. Dessart, A. Burrows, E. Livne and C. D. Ott. *The Proto-Neutron Star Phase of the Collapsar Model and the Route to Long-Soft Gamma-Ray Bursts and Hypernovae*. Astrophys. J. Lett., 673, L43, 2008.

[115] H. Dimmelmeier, J. A. Font and E. Müller, *Gravitational Waves from Relativistic Rotational Core Collapse*. Astrophys. J. Lett., 560:L163, 2001.

[116] H. Dimmelmeier *General Relativistic Collapse of Rotating Stellar Cores in Axisymmetry*. PhD Thesis, Technische Universität München, 2001.

[117] H. Dimmelmeier, J. A. Font and E. Müller. *Relativistic simulations of rotational core collapse I. Methods, initial models, and code tests*. Astron. Astrophys., 388:917, 2002.

[118] H. Dimmelmeier, J. A. Font and E. Müller. *elativistic simulations of rotational core collapse II. Collapse dynamics and gravitational radiation*. Astron. Astrophys., 393:523, 2002

[119] H. Dimmelmeier, J. Novak, J. A Font, J. M. Ibáñez and E. Müller. *Combining spectral and shock-capturing methods: A new numerical approach for 3D relativistic core collapse simulations*. Phys. Rev. D, 71:064023, 2005

[120] H. Dimmelmeier, N. Stergioulas and J. A. Font, *Non-linear axisymmetric pulsations of rotating relativistic stars in the conformal flatness approximation*. Mon. Not. Roy. Astron. Soc., 368:1609, 2006.

[121] H. Dimmelmeier, P. Cerdá-Durán, A. Marek and G. Faye. *New Methods for Approximating General Relativity in Numerical Simulations of Stellar Core Collapse*. in AIP Conference Series, Vol. 861, Albert Einstein Century International Conference, ed. J.-M. Alimi & A. Füzfa (Melville, USA: American Institute of Physics), 600, 2006

[122] H. Dimmelmeier, C. D. Ott, H.-T. Janka, A. Marek and E. Müller. *Generic Gravitational-Wave Signals from the Collapse of Rotating Stellar Cores*. Phys. Rev. Lett., 98:251101, 2007

[123] H. Dimmelmeier, C. D. Ott, A. Marek and T.-H. Janka *Gravitational wave burst signal from core collapse of rotating stars* Phys. Rev. D, 78:064056, 2008.

[124] H. Dimmelmeier, M. Bejger, P. Haensel and L. Zdunik *Dynamic migration of rotating neutron stars due to a phase transition instability*. Mon. Not. Roy. Astron. Soc., 396:2269, 2009.

[125] K. Y. Ding and K. S. Cheng. *Oscillation-induced gamma-ray emission from dead pulsars: a model for the delayed GeV emission in gamma-ray bursts*. Mon. Not. Roy. Astron. Soc., 287:671, 1997.

[126] R. Donat and A. Marquina. *Capturing Shock Reflections: An Improved Flux Formula*. Journ. Comput. Phys., 125:42, 1996.

[127] R. Donat, J. A. Font, J. M. Ibáñez and A. Marquina. *A flux-split algorithm applied to relativistic flows*. Journ. Comput. Phys., 146:58, 1996

[128] A. Drago, A. Lavagno and I. Parenti. *Burning of a Hadronic Star into a Quark or a Hybrid Star*. Astrophys. J., 659:1519, 2007.

[129] M. C. R. D'Souza, P. M. Motl, J. E. Tohline and J. Frank, *Numerical Simulations of the Onset and Stability of Dynamical Mass Transfer in Binaries*. Astrophys. J., 643:381, 2006.

[130] M. D. Duez, F. Foucart, L. E. Kidder, H. P. Pfeiffer, M. A. Scheel, and S. A. Teukolsky. *Evolving black hole-neutron star binaries in general relativity using pseudospectral and finite difference methods*. Phys. Rev. D, 78:104015, 2008.

[131] R. C. Duncan. *Global Seismic Oscillations in Soft Gamma Repeaters*. Astrophys. J., 498:L45, 1998

[132] D. M. Eardley, *Theoretical models for sources of gravitational waves*. In *Gravitational Radiation*, N. Deruelle, T. Piran editor. Proc. Advanced Study Institute, Les Houches, France. North-Holland Publishing Company, Amsterdam, 1983.

[133] R. S. Eddington *The mathematical theory of relativity*. Cambridge University Press, Cambridge, UK, 1923.

[134] B. Einfeldt *On Godunov-type methods for gas dynamics*. SIAM J. Numer. Anal.,25:294, 1988.

[135] A. Einstein. *Zur Allgemeinen Relativitätstheorie*. Preuss. Akad. Wiss. Berlin, Sitzber., 778, 1915.

[136] A. Einstein. *Die Feldgleichungen der Gravitation*. Preuss. Akad. Wiss. Berlin, Sitzber., 844, 1915.

[137] A. Einstein. *N´aherungsweise Integration der Feldgleichungen der Gravitation*. Preuss. Akad. Wiss. Berlin, Sitzber., 688, 1916.

[138] Einstein Telescope, http://www.et-gw.eu,

[139] M. F. El Eid and W. Hillebrandt. *A new equation of state of supernova matter*. Astron. Astrophys. Suppl., 42:215, 1980.

[140] R. Epstein. *The generation of gravitational radiation by escaping supernova neutrinos*. Astrophys. J., 223:1037, 1978.

[141] R. I. Epstein. *Lepton-driven convection in supernovae*. Mon. Not. Roy. Astron. Soc., 188:305, 1979.

[142] R. I. Epstein and C. J. Pethick. *Lepton loss and entropy generation in stellar collapse*. Astrophys. J., 243:1003, 1981

[143] C. R. Evans *An approach for calculating axisymmetric gravitational collapse*. in *Dynamical space-times and numerical relativity*, Proceedings of the Workshop, Cambridge, Cambridge University Press, UK and New York US, 3, 1986.

[144] É. Flanagan and S. A. Highes. *Measuring gravitational waves from binary black hole coalescences. I. Signal to noise for inspiral, merger, and ringdown*. Phys. Rev. D, 57:4535, 1998

[145] È. Flanagan and S. A. Hughes *The Basics of Gravitational Wave Theory*. New Journ. Phys., 7:204, 2005.

[146] L. S. Finn, in C. R. Evans, S. L. Finn, and D. W. Hobbill, eds., *Frontiers in numerical relativity*, 126, Cambridge University Press, Cambridge, 1989.

[147] L. S. Finn and C. R. Evans. *Determining gravitational radiation from Newtonian self-gravitating systems*. Astrophys. J., 351:588, 1990.

[148] J. A. Font, M. Miller, W. M. Suen and M. Tobias *Three-dimensional numerical general relativistic hydrodynamic: Foudations, methods, and code tests*, Phys. Rev. D, 61:044011, 2000.

[149] J. A. Font, T. Goodale, S. Iyer, M. Miller, L. Rezzolla, E. Seidel, N. Stergioulas, W. M. Suen and M. Tobias *Three-dimensional numerical general relativistic hydrodynamic II: Long-term dynamics of single relativistic stars*, Phys. Rev. D, 65, 084024, 2002.

[150] J. A. Font *Numerical hydrodynamics in general relativity*, Liv. Rev. Rel., 6:4, 2003..

[151] J. Frauendiener, J. Comput. Appl. Math. **109** 475 (1999).

[152] P. C. C. Freire, A. Wolszczan, M. van den Berg and J. W. T. Hessels. *A Massive Neutron Star in the Globular Cluster M5*. Astrophys. J., 679:1433, 2008

[153] . J. L. Friedman and B. F. Schutz *Secular instability of rotating Newtonian stars* Astrophys. J., 222:281, 1978.

[154] J. L. Friedman, L. Parker and J. R. Ipser. *Rapidly rotating neutron star models*. Astrophys. J., 304:115, 1986

[155] H. Friedrich and G. Nagy, *The inial boundary valye problem for Einstein's vacuum field equations*. Commin. Math. Phys., 201:619, 1999.

[156] S. Fritelli, *Note on the propagation of the constraints in standard* $\{3+1\}$ *general relativity*. Phys. Rev. D, 55:5992, 1997

[157] C. Fryer, W. Benz, M. Herant and S. A. Colgate. *What Can the Accretion-induced Collapse of White Dwarfs Really Explain?*. Astrophys. J., 516:892, 1999.

[158] C. L. Fryer. *Mass Limits For Black Hole Formation*. Astrophys. J., 522:413, 1999.

[159] C. Fryer and A. Heger. *Core-Collapse Simulations of Rotating Stars*. Astrophys. J., 541:1033, 2000.

[160] C. L. Fryer, D. E. Holz and S. A. Hughes. *Gravitational Wave Emission from Core Collapse of Massive Stars*. Astrophys. J., 565:430, 2002.

[161] C. Fryer and K. C. B. New. *Gravitational Waves from Gravitational Collapse*. Liv. Rev. Rel., 6:2, 2003.

[162] C. L. Fryer and S. Diehl, *On the Road to Understanding Type Ia Progenitors: Precision Simulations of Double Degenerate Mergers*, in *Hydrogen-Deficient Stars* , editor A. Werner and T. Rauch, ASPC Conf. Ser. 391, 355, 2008.

[163] A. Garat and R. H. Price, *Nonexistence of conformally flat slices of the Kerr spacetime*. Phys. Rev. D, 61:124011, 2000

[164] GEO600, http://geo600.aei.mpg.de

[165] P. Gil-Pons and E. García-Berro. *On the formation of oxygen-neon white dwarfs in close binary systems*. Astron. Astrophys., 375:87, 2001

[166] V. L. Ginzburg and L. M. Ozernoy. Zh. Eksp. Teor. Fiz., 47:1030, 1964,

[167] K. Glampedakis, L. Samuelsson, N. Andersson. *Elastic or magnetic? A toy model for global magnetar oscillations with implications for quasi-periodic oscillations during flares*. Mon. Not. Roy. Astron. Soc., 371:L74, 2006

[168] N. K. Glendenning. *Fast pulsar in SN 1987A - Candidate for strange-quark matter*. Phys. Rev. Lett., 63:2629, 1989.

[169] N. K. Glendenning. *Fast pulsars, variational bounds, other facets of compact stars*. Nucl. Phys. B(Proc. Suppl.), 24B:110, 1991.

[170] N. K. Glendenning *First-order phase transitions with more than one conserved charge: Consequences for neutron stars*. Phys. Rev. D, 46:1274, 1992.

[171] N. K. Glendenning *Compact Stars. Nuclear Physics, Particle Physics, and General Relativity*. Springer, Berlin, 2000.

[172] S. K. Godunov, Mat. Sb., 47:271, 1959. In Russian.

[173] P. Goldreich and W. H. Julian. *Pulsar Electrodynamics* Astrophys. J., 157:869, 1969.

[174] P. Goldreich and S. V. Weber. *Homologously collapsing stellar cores*. Astrophys. J., 238:991, 1980.

[175] D. Gottlieb and S. A. Orszag, *Numerical analysis of spectral methods: theory and applications*. Society of Indust. and Applied Math., Philadelphia, 1977.

[176] P. Grandclément, S. Bonazzola, E. Gourgoulhon and J. A. Marck, *A multi-domain spectral method for scalar and vectorial Poisson equations with non-compact sources*. Journ. Comput. Phys., 170:231, 2001.

[177] P. Gradclèment and J. Novak *Spectral Methods for Numerical Relativity* Liv. Rev. Rel., 12:1, 2009.

[178] A. Gruzinov. *Power of an Axisymmetric Pulsar*. Phys. Rev. Lett., 94:021101, 2005.

[179] J. Gutiérrez, R. Canal and E. García-Berro. *The gravitational collapse of ONe electron-degenerate cores and white dwarfs: The role of ^{24}Mg and ^{12}C revisited*. Astron. Astrophys., 435:231, 2005.

[180] I. Hachisu *A versatile method for obtaining structures of rapidly rotating stars*. Astrophys. J. Supp. Ser. , 61:479, 1986

[181] P. Haensel, A. Y. Potekhin, D. G. Yakovlev. *Neutron Stars I. Equation of State and Structure*. Springer, New York, 2007.

[182] K. Hagiwara et al. (Particle Data Group). Phys. Rev. D, 66:010001, 2002.

[183] B. Haskell, L. Samuelsson, K. Glampedakis, N. Andersson. *Modelling magnetically deformed neutron stars*. Mon. Not. Roy. Astron. Soc., 385, 531, 2008.

[184] S. W. Hawking and G. F. R. Ellis, *The Large Scale Structure of Space-Time*. (Cambridge University Press, Cambridge, 1973).

[185] A. Heger, S. E. Woosley and H. C. Spruit. *Presupernova Evolution of Differentially Rotating Massive Stars Including Magnetic Fields*. Astrophys. J., 626:350, 2005.

[186] M. Herant, W. Benz, W. R. Hix, C. L. Fryer, and S. A. Colgate *Inside the supernova: A powerful convective engine*. Astrophys. J., 435:339, 1994.

[187] F. Herwig. *Evolution of Asymptotic Giant Branch Stars*. Ann. Rev. Astron. Astroph., 43:435, 2005.

[188] W. Hillebrandt, K. Nomoto, R. G. Wolff. *Supernova explosions of massive stars - The mass range 8 to 10 solar masses*. Astron. Astrophys., 133:175, 1984.

[189] W. Hillebrandt and R. G. Wolff. *Models of Type II Supernova Explosions*. In W. D. Arnett and J. W. Truran, editors, *Nucleosynthesis: Challenges and New Developments*, page 131, 1985.

[190] K. Hirata, T. Kajita, M. Koshiba, M. Nakahata and Y. Oyama. *Observation of a neutrino burst from the supernova SN1987A*. Phys. Rev. Lett., 58:1490, 1987.

[191] W. R. Hix, O. E. Messer, A. Mezzacappa, M. Liebendrfer, J. Sampaio, K. Langanke, J. D. Dean, G. Martinez-Pinedo. *Consequences of nuclear electron capture in core collapse supernovae*. Phys. Rev. Lett., 91:201102, 2003.

[192] J. E. Horvath. *The birth of strange stars: kinetics, hydrodynamics and phenomenology of supernovae and GRBs*. 2002. preprint: astro-ph/0703233.

[193] J. Hough and S. Rowan. *Gravitational Wave Detection by Interferometry (Ground and Space)*, Liv. Rev. Rel., 3:3, 2000.

[194] J. M. Ibáñez, J. M. Martí, J. M. Miralles and J. V. Romero, *Godunov-type Methods applied to General Relativistic Stellar Collapse*, In R. D'Inverno, editor *Approaches to Numerical Relativity*, 223, 1992.

[195] I. J. Iben, C. Ritossa and E. Garcia-Berro. *On the Evolution of Stars That Form Electron-degenerate Cores Processed by Carbon Burning. IV. Outward Mixing during the Second Dredge-up Phase and Other Properties of a $10.5 M_{\rm Sun}$ Model Star*. Astrophys. J., 489:772, 1997.

[196] Isenberg J. A., *Waveless approximation theories of gravities,* PhD Thesis. University of Maryland Preprint, 1978, unpublished, gr-qc/0702113

[197] Israel G., et al, *The Discovery of Rapid X-Ray Oscillations in the Tail of the SGR 1806-20 Hyperflare*. Astrophys. J., 628:L53, 2005.

[198] N. Itoh. *Hydrostatic Equilibrium of Hypothetical Quark Stars*. Progr. Theor. Phys., 44:291, 1970.

[199] H.-T. Janka. *Conditions for shock revival by neutrino heating in core-collapse supernovae*. Astron. Astrophys., 368:527, 2001.

[200] H.-T. Janka, R. Buras, F. S. Kitaura, A. Marek, M. Rampp and L Scheck. *Neutrino-driven supernovae: An accretion instability in a nuclear physics controlled environment*. Nucl. Phys. A, 758:19, 2005.

[201] H.-T. Janka, K. Langanke, A. Marek, G. Martínez-Pinedo and B. Müller. *Theory of core-collapse supernovae*. Phys. Rep., 442:38, 2007.

[202] H.-T. Janka, A. Marek and F.-S. Kitaura. *Neutrino-Driven Explosions Twenty Years After SN 1987A*. in *Supernova 1987A: 20 Years After: Supernovae and Gamma-Ray Bursters*, editor S. Immler, K. Weiler, R. McCray., AIP Conf. Ser., 937:144, 2007.

[203] H.-T. Janka, B. Müller, F.-S. Kitaura and R. Buras. *Dynamics of shock propagation and nucleosynthesis conditions in O-Ne-Mg core supernovae*. Astron. Astrophys., 485:199, 2008

[204] V. Kalogera *Compact Binary Mergers and Accretion-Induced Collapse: Event Rates*. in *Gravitational Waves, AIP Conf. Ser.*, editor S. Meshkov, 523:41, 2000.

[205] T. Kellerman, L. Baiotti, B. Giacomazzo and L. Rezzolla. *An improved formulation of the relativistic hydrodynamics equations in 2D Cartesian coordinates*. Class. Quant. Grav., 25:225007, 2008.

[206] R. Kippenhahn and A. Weigert. *Stellar Structure and Evolution*. Springer, Berlin, Germany, 1990.

[207] F. S. Kitaura, H.-T. Janka and W. Hillebrandt. *Explosions of O-Ne-Mg cores, the Crab supernova, and subluminous type II-P supernovae*. Astron. Astrophys., 450:345, 2006.

[208] K. D. Kokkotas, T. A. Apostolatos and N. Andersson *The inverse problem for pulsating neutron stars: a "fingerprint analysis" for the supranuclear equation of state*. Mon. Not. Roy. Astron. Soc., 320:307, 2001

[209] H. Komatsu, Y. Eriguchi and I. Hachisu. *Rapidly rotating general relativistic stars. I - Numerical method and its application to uniformly rotating polytropes*. Mon. Not. Roy. Astron. Soc., 237:355, 1989

[210] H. Komatsu, Y. Eriguchi, I.Hachisu. *Rapidly rotating general relativistic stars. II - Differentially rotating polytropes*. Mon. Not. Roy. Astron. Soc., 239, 153, 1989.

[211] S. S. Komissarov *Simulations of the axisymmetric magnetospheres of neutron stars*. Mon. Not. Roy. Astron. Soc., 267:19, 2006.

[212] K. Kotake, S. Yamada and K. Sato. *Gravitational radiation from axisymmetric rotational core collapse*. Phys. Rev. D, 68:044023, 2003.

[213] K. Kotake, S. Yamada and K. Sato. *Anisotropic Neutrino Radiation in Rotational Core Collapse*. Astrophys. J., 595:304, 2003.

[214] K. Kotake, K. Sato and K. Takahashi. *Explosion mechanism, neutrino burst and gravitational wave in core-collapse supernovae*. Rep. Prog. Phys., 69:971, 2006.

[215] D. Q. Lamb, J. M. Lattimer, C. J. Pethick, and D. G. Ravenhall. *Hot dense matter and stellar collapse*. Phys. Rev. Lett., 41:1623, 1978.

[216] D. Q. Lamb, J. M. Lattimer, C. J. Pethick and D. G. Ravenhall. *Physical properties of hot, dense matter: The bulk equilibrium approximation*. Nucl. Phys. A, 360:459, 1981

[217] Landau L. D. and Lifshitz E. M.,*The Classical Theory of Fields*, 4th ed., Pergamon Press, Oxford, 1987

[218] Landau L. D. and Lifshitz E. M., *Fluid Mechanics*, 4th ed., Pergamon Press, Oxford, 1987

[219] K. Langanke and G. Martinez-Pinedo. *Shell-model calculations of stellar weak interaction rates. II. Weak rates for nuclei in the mass range A = 45 - 65 in supernovae environments.*. Nucl. Phys. A, 673:481, 2000

[220] J. M. Lattimer and T. J. Mazurek. *Leptonic overturn and shocks in collapsing stellar cores*. Astrophys. J., 246:955, 1981.

[221] J. M. Lattimer, C. J. Pethick, D. G. Ravenhall, and D. Q. Lamb. *Physical properties of hot, dense matter: The general case*. Nucl. Phys. A, 432:646, 1985.

[222] J. M. Lattimer and F. D. Swesty. *A Generalized Equation of State for Hot, Dense Matter*. Nucl. Phys. A, 535:331, 1991. URL: http://www.ess.sunysb.edu/dswesty.

[223] L. Lehner, TOPICAL REVIEW: *Numerical relativity: a review* Class. Quant. Grav., 18:R25, 2001.

[224] R. J. Leveque, *Nonlinear conservation laws and finit volume methods*, in O. Steiner and A. Gautschy eds., *Computational methods for astrophysical fluid flow*, Saas-Fee Anvanced Course 27, 1-159, Springer, Berlin, Germany, 1998

[225] R. J. Leveque, *Finite Volume Methods for Fluid Dynamics* Cambridge University Press, Cambridge, UK, 2002

[226] Y. Levin. *On the theory of magnetar QPOs*. Mon. Not. Roy. Astron. Soc., 377:159, 2007

[227] A. Lichnerowicz. *L'intégration des équations de la gravitation relativiste et la probléme des n corps*. J. Math Pures et Appl., 23:37, 1944.

[228] M. Liebendörfer, A. Mezzacappa, F.-K. Thielemann, O. E. Messer, W. R. Hix , S. W. Bruenn. *Probing the gravitational well: No supernova explosion in spherical symmetry with general relativistic Boltzmann neutrino transport*. Phys. Rev. D, 63:103004, 2001.

[229] M. Liebendörfer *A Simple Parameterization of the Consequences of Deleptonization for Simulations of Stellar Core Collapse* Astrophys. J., 633:1042, 2005.

[230] M. Liebendorfer, M. Rampp, H.-T. Janka, and A. Mezzacappa. *Supernova Simulations with Boltzmann Neutrino Transport: A Comparison of Methods*. Astrophys. J., 620:840, 2005.

[231] M. Liebendörfer, S. C. Whitehouse, T. Fischer. *The isotropic diffusion source approximation for supernova neutrino transport* preprint arXiv:0711.2929, 2007.

[232] LIGO, http://ligo.caltech.edu

[233] L. M. Lin, K. S. Cheng, M. C. Chu, W.-M. Suen. *Gravitational Waves from Phase-Transition-Induced Collapse of Neutron Stars*. Astrophys. J., 639:382, 2006.

[234] L. Lindblom, B. J. Owen and D. A. Brown. *Model waveform accuracy standards for gravitational wave data analysis*. Phys. Rev. D78:124020, 2008.

[235] URL http://lisa.jpl.nasa.gov. LISA.

[236] Y. T. Liu and L Lindblom. *Models of rapidly rotating neutron stars: remnants of accretion-induced collapse*. Mon. Not. Roy. Astron. Soc., 324:1063, 2001

[237] Y. T. Liu. *Dynamical instability of new-born neutron stars as sources of gravitational radiation*. Phys. Rev. D, 65:124003, 2002

[238] M. Livio. *The Progenitors of Type Ia Supernovae*. in *Type Ia Supernovae, Theory and Cosmology*, editor J. C Niemeyer and J. W. Truran. 33, 2000

[239] E. Livne. *An implicit method for two-dimensional hydrodynamics*. Astrophys. J., 412:634, 1993.

[240] E. Livne, A. Burrows, R. Walder, I. Lichtenstadt and T. A. Thompson. *Two-dimensional, Time-dependent, Multigroup, Multiangle Radiation Hydrodynamics Test Simulation in the Core-Collapse Supernova Context*. Astrophys. J., 609:277, 2004.

[241] E. Livne, L. Dessart, A. Burrows and C. A. Meakin. *A Two-dimensional Magnetohydrodynamics Scheme for General Unstructured Grids*. Astrophys. J. Supp. Ser. , 170:187, 2007.

[242] `http://www.lorene.obspm.fr`.

[243] G. Lugones, C. R. Ghezzi, E. M. de Gouveia Dal Pino and J. E. Horvath. *Asymmetric Core Combustion in Neutron Stars and a Potential Mechanism for Gamma-Ray Bursts*. Astrophys. J., 581:L101, 2002

[244] M. MacCallum D. Kramer, H. Stephani and E. Herlt. *Exact Solutions of Einstein's Field Equations*. Cambridge University Press, Cambridge, 1980.

[245] A. I. MacFadyen and S. E. Woosley. *Collapsars: Gamma-Ray Bursts and Explosions in "Failed Supernovae"*. Astrophys. J., 524:262, 1999.

[246] A. I. MacFadyen, S. E. Woosley and A. Heger. *Supernovae, Jets, and Collapsars*. Astrophys. J., 550:410, 2001.

[247] P. Madau, M. della Valle and N. Panagia. *On the evolution of the cosmic supernova rates*. Mon. Not. Roy. Astron. Soc., 297:L17, 1998.

[248] J. Madsen. *Probing Strange Stars and Color Superconductivity by r-Mode Instabilities in Millisecond Pulsars*. Phys. Rev. Lett., 85:10, 2000.

[249] M. Maggiore *Gravitational Waves. Vol. 1. Theory and Experiments*. Oxford Univ. Press, Oxford, UK, 2008.

[250] G. M. Manca, L. Baiotti, R. De Pietri and L. Rezzolla. *Dynamical non-axisymmetric instabilities in rotating relativistic stars*. Class. Quant. Grav., 24:S171, 2007.

[251] F. Mannucci, M. della Valle, N. Panagia, E. Cappellaro, G. Cresci, R. Maiolino, A. Petrosian and M. Turatto. *The supernova rate per unit mass*. Astron. Astrophys., 433:807, 2005.

[252] A. Marek, H.-T. Janka, R. Buras, M. Liebendörfer and M. Rampp. *On ion-ion correlation effects during stellar core collapse*. Astron. Astrophys., 443:201, 2005.

[253] A. Marek, T.-H. Janka and E. Müller *Equation-of-state dependent features in shock-oscillation modulated neutrino and gravitational-wave signals from supernovae* Astron. Astrophys., 496:475, 2009.

[254] A. Marek, T.-H. Janka. *Delayed Neutrino-Driven Supernova Explosions Aided by the Standing Accretion-Shock Instability*. Astron. Astrophys., 694:664, 2009.

[255] S. Marcos, M. Barranco and J. R. Buchler. *Low-entropy adiabats for stellar collapse*. Nucl. Phys. A, 381:507, 1982.

[256] G. F. Marranghello, C. A. Vasconcellos, J. A. de Freitas Pacheco. *Phase transitions in neutron stars and gravitational wave emission*. Phys. Rev. D, 66:064027, 2002.

[257] J. M. Martí, J. M. Ibáñez and J. M. Miralles *Numerical relativistic hydrodynamics: Local characteristic approach*, Phys. Rev. D, 43:3794, 1991.

[258] J. M. Martí and E. Müller 2003, *Numerical hydrodynamics in special relativity* Liv. Rev. Rel., 6:7, 2003.

[259] G. Martínez-Pinedo, M. Liebedn'orfer and D. Frekers. *Nuclear Input for Core-collapse Models*. Nucl. Phys. A, 777:395, 2006.

[260] R. Mayle and J. R. Wilson. *Supernovae from collapse of oxygen-magnesium-neon cores*. Astrophys. J., 334:909, 1989.

[261] J. C. McKinney, *Relativistic force-free electrodynamic simulations of neutron star magnetospheres*. Mon. Not. Roy. Astron. Soc., 368:L30, 2006.

[262] P. Mészá ros. *Gamma-ray bursts*. Reports of Prog. in Phys., 69:2259, 2006.

[263] `http://www.luth.obspm.fr/Groupe1.html`.

[264] B. D. Metzger, A. Piro and E. Quataert. *Nickel-Rich Outflows from Accretion Disks Formed by the Accretion-Induced Collapse of White Dwarfs*. Mon. Not. Roy. Astron. Soc., 396:1659, 2009.

[265] B. D. Metzger, A. Piro, E. Quataert, T. A. Thompson *Observable Signatures of the Accretion-Induced Collapse of White Dwarfs*. Preprint:arXiv:0908.1127, 2009.

[266] F. C. Michel. *Rotating Magnetospheres: an Exact 3-D Solution*. Astrophys. J., 180:L133, 1973.

[267] F. C. Michel *Theory of Neutron Star Magnetospheres*. The University of Chicago Press, 1991

[268] D. Mihalas and B. Weibel-Mihalas. *Foundations of Radiation Hydrodynamics*. Dover Publications, Mineola, NY, USA, 1999.

[269] S. Miyaji, K. Nomoto, K. Yokoi and D. Sugimoto. *Supernova Triggered by Electron Captures*. Astron. Soc. Japan Publ., 32:303, 1980.

[270] S. Miyaji and K. Nomoto. *On the collapse of 8-10 solar mass stars due to electron capture*. Astrophys. J., 318:307, 1987.

[271] Miniutti G., Pons J. A., E. Berti, L. Gualtieri and V. Ferrari, 2003 *Non-radial oscillation modes as a probe of density discontinuities in neutron stars*. Mon. Not. Roy. Astron. Soc., 338:389, 2003

[272] C. W. Misner, K. S. Thorne and J. A. Wheeler, *Gravitation*, Freeman, NY, 1974

[273] R. Mochkovitch and M. Livio. *The coalescence of white dwarfs and type I supernovae*. Astron. Astrophys., 209:111, 1989.

[274] R. Mönchmeyer. PhD Thesis, unpublished. PhD thesis, Technische Universität München, 1990.

[275] R. Mönchmeyer, G. Schäfer, E. Müller and R. Kates. *Gravitational waves from the collapse of rotating stellar cores*. Astron. Astrophys., 246:417, 1991.

[276] U. A. Mofiz and B. J. Ahmedov. *Plasma Modes along the Open Field Lines of a Neutron Star*. Astrophys. J., 542:484, 2000.

[277] V. Moncrief. *Gravitational perturbations of spherically symmetric systems. I. the exterior problem*. Annals of Physics, 88:323, 1974.

[278] P. J. Montero, J. A. Font and M. Shibata *NADA: A new code for studying self-gravitating tori around black holes*. Phys. Rev. D, 78:064037, 2008

[279] V. S. Morozova, B. J. Ahmedov, V. G. Kagramanova, 2008, ApJ, in *General Relativistic Effects of Gravitomagnetic Charge on Pulsar Magnetospheres and Particle Acceleration in the Polar Cap*. Astrophys. J., 684: 1359, 2008.

[280] S. M. Morsink, N. Stergioulas and S. R. Blattnig. *Quasi-normal Modes of Rotating Relativistic Stars: Neutral Modes for Realistic Equations of State*. Astrophys. J., 510, 854, 1999.

[281] E. Müller and W. Hillebrandt. *The collapse of rotating stellar cores*. Astron. Astrophys., 103:358, 1981.

[282] E. Müller. *Gravitational radiation from collapsing rotating stellar cores*. Astron. Astrophys., 114:53, 1982.

[283] E. Müller, M. Rampp, R. Buras, H.-T. Janka and D. H. Shoemaker. *Toward Gravitational Wave Signals from Realistic Core-Collapse Supernova Models*. Astrophys. J., 603, 221, 2004.

[284] B. Müller. *Multi-dimensional relativistic simulations of core-collapse supernovae with energy-dependent neutrino transport*. PhD thesis, Technische Universität München, Germany, 2009.

[285] N. O. Murchanha and J. W. York *Gravitational Energy*. Phys. Rev. D, 10:2345-2357, 1974.

[286] J. Murphy and A. Burrows. *Criteria for Core-Collapse Supernova Explosions by the Neutrino Mechanism*. Astrophys. J., 688:1159, 2008

[287] A. G. Muslimov and A. I. Tsygan 1992, *General relativistic electric potential drops above pulsar polar caps*. Mon. Not. Roy. Astron. Soc., 255:61, 1992.

[288] H. Muther, R. Machleidt and R. Brockmann. *Relativistic nuclear structure. II. Finite nuclei*. Phys. Rev. C, 42:1981, 1990.

[289] W. D. Myers and W. J. Swiatecki. *The nuclear thomas-fermi model*. Technical Report LBL-36004, Lawrence Berkeley Laboratory, University of California, 1994.

[290] A. Nagar, O. Zanotti, J. A. Font and L. Rezzolla. *Accretion-induced quasinormal mode excitation of a Schwarzschild black hole*", Phys. Rev. D, 75:044016, 2007

[291] A. Nerozzi, C. Beetle, M. Bruni, L. M. Burko and D. Pollney. *Towards a wave-extraction method for numerical relativity. II. The quasi-Kinnersley frame*. Phys. Rev. D72:024014, 2005

[292] J. Von Newmann and R. D. Richtmyer, *A method for numerical calculation of hydrodynamic shocks*, J. Appl. Physics, 21:232, 1950.

[293] E. Newman and R. Penrose. *An approach to gravitational radiation by a method of spin coefficients*. J. Math. Phys., 3:566, 1962.

[294] K. Nomoto. *Evolution of 8-10 solar mass stars toward electron capture supernovae. I - Formation of electron-degenerate O + NE + MG cores*. Astrophys. J., 277:791, 1984

[295] K. Nomoto. *The fate of accreting white dwarfs: Type I supernovae vs. collapse*. Prog. Part. Nuc. Phys., 17:249, 1986.

[296] K. Nomoto, *Evolution of 8-10 solar mass stars toward electron capture supernovae. II - Collapse of an O + NE + MG core*. Astrophys. J., 322:206, 1987.

[297] K. Nomoto and Y. Kondo. *Conditions for accretion-induced collapse of white dwarfs*. Astrophys. J. Lett., 367:L19, 1991.

[298] K. Nomoto, H. Saio, M. Kato and I. Hachisu, *Thermal Stability of White Dwarfs Accreting Hydrogen-rich Matter and Progenitors of Type Ia Supernovae* Astrophys. J., 663:1269, 2007.

[299] M. L. Norman and K.-H. A. Winkler *Why Ultrarelativistic Numerical Hydrodynamics is Difficult*. in *NATO Advanced Research Workshop on Astrophysical Radiation Hydrodynamics*. Editors K.-H. A. Winkler, L. M. Norman. D. Reidel Publishing Co., Dordrecht, Holland, Boston, MA.

[300] J. Novak and J. M. Ibáñez, *Gravitational Waves from the Collapse and Bounce of a Stellar Core in Tensor-Scalar Gravity*. Astrophys. J., 533:392, 2000.

[301] T. Nozawa, N. Stergioulas, E. Gourgoulhon and Y. Eriguchi. *Construction of highly accurate models of rotating neutron stars - comparison of three different numerical schemes*. Astron. Astrophys. Supp., 132:431, 1998.

[302] M. Obergaulinger, M. A. Aloy and E. Müller. *Axisymmetric simulations of magneto-rotational core collapse: dynamics and gravitational wave signal*. Astron. Astrophys., 450:1107, 2006.

[303] R. Ogasawara and K. Sato. *Nuclei in Neutrino-Degenerate Dense Matter. II Hot Case*. Progr. Theor. Phys., 70:1569, 1983.

[304] J. P. Ostriker and J. W.-K. Mark. *Rapidly rotating stars. I. The self-consistent-field method*. Astrophys. J., 151:1075, 1968

[305] J. O. Ostriker and P. Bodenheimer. *Rapidly Rotating Stars. II. Massive White Dwarfs*. Astrophys. J., 151:1089, 1968.

[306] C. D. Ott, A. Burrows, E. Livne and R. Walder. *Gravitational Waves From Axisymmetric, Rotating Stellar Core Collapse*, Astrophys. J., 600:834, 2004.

[307] C. D. Ott, S. Ou, J. E. Tohline and A. Burrows. *One-armed Spiral Instability in a Low-T/|W| Post-bounce Supernova Core*. Astrophys. J., 625:L119, 2005.

[308] C. D. Ott, A. Burrows, L. Dessart and E. Livne. *A New Mechanism for Gravitational-Wave Emission in Core-Collapse Supernovae*. Phys. Rev. Lett., 96:201102, 2006.

[309] C. D. Ott, A. Burrows, T. A. Thompson, E. Livne and R. Walder. *The Spin Periods and Rotational Profiles of Neutron Stars at Birth*. Astrophys. J. Supp. Ser. , 164:130, 2006

[310] C. D. Ott *Stellar Iron Core Collapse in 3+1 General Relativity and The Gravitational Wave Signature of Core-Collapse Supernovae*. PhD Thesis, Universität Potsdam, Potsdam, Germany, 2006.

[311] C. D. Ott, H. Dimmelmeier, A. Marek, T.-H. Janka, B. Zink, I. Hawke and E. Schnetter *3D Collapse of Rotating Stellar Iron Cores in General Relativity Including Deleptonization and a Nuclear Equation of State*. Phys. Rev. Lett., 98:261101, 2007

[312] C. D. Ott, H. Dimmelmeier, A. Marek, T.-H. Janka, B. Zink, I. Hawke and E. Schnetter *Rotating collapse of stellar iron cores in general relativity*. Class. Quant. Grav., 24:S139, 2007.

[313] C. D. Ott, A. Burrows, L. Dessart and E. Livne. *Two-Dimensional Multiangle, Multigroup Neutrino Radiation-Hydrodynamic Simulations of Postbounce Supernova Cores* Astrophys. J., 685:1069, 2008

[314] C. D. Ott, A. Burrows, L. Dessart and E. Livne. *Two-Dimensional Multiangle, Multigroup Neutrino Radiation-Hydrodynamic Simulations of Postbounce Supernova Cores*. Astrophys. J., 685:1069, 2008.

[315] C. D. Ott, E. Schnetter, G. Allen, E. Seidel, J. Tao, ad B. Zink. *A case study for petascale applications in astrophysics: Simulating Gamma-Ray Bursts*. In Proceedings of the 15th ACM Mardi Gras conference: *From lightweight mash-ups to lambda grids: Understanding the spectrum of distributed computing requirements, applications, tools, infrastructures, interoperability, and the incremental adoption of key capabilities*. ACM International Conference Proceeding Series, 18, Baton Rouge, Louisiana, USA, 2008

[316] C. D. Ott. TOPICAL REVIEW: *The gravitational-wave signature of core-collapse supernovae*. Class. Quant. Grav., 26, 063001, 2009

[317] C. D. Ott, E. Schnetter, A. Burrows, E. Livne, E. O'Connor and F. Löffler. *Computational Models of Stellar Collapse and Core-Collapse Supernovae*. Preprint: arXiv:0907.4043

[318] S. Ou and J. E. Tohline. *Unexpected Dynamical Instabilities in Differentially Rotating Neutron Stars*. Astrophys. J., 651:1068, 2006.

[319] K. Oyamatsu. *Nuclear shapes in the inner crust of a neutron star*. Nucl. Phys. A, 561:431, 1993.

[320] F. Pacini and M. Ruderman *Gamma-ray bursts from neutron star glitches*. Nature, 251:399, 1974.

[321] T. Padmanabhan *Theoretical Astrophysics: Stars and Stellar Systems.*. Cambridge University Press, Cambridge, UK, 2001.

[322] A. Passamonti, M. Bruni, L. Gualtieri, S. F. Sopuerta. *Coupling of radial and nonradial oscillations of relativistic stars: Gauge-invariant formalism*. Phys. Rev. D, 71:024022, 2005.

[323] A. Passamonti, N. Stergioulas, A. Nagar. *Gravitational waves from nonlinear couplings of radial and polar nonradial modes in relativistic stars*. Phys. Rev. D, 75:084038, 2007.

[324] J. Pedlosky, *Geophysical Fluid Dynamics*. 1987, Springer, New York, U.S.A.

[325] H. B. Perets, A. Gal-Yam, P. Mazzali, D. Arnett, D. Kagan, A. V. Filippenko, W. Li, S. B. Cenko, D. B. Fox, D. C. Leonard, D. . Moon, D. J. Sand, A. M. Soderberg, R. J. Foley, M. Ganeshalingam, J. P. Anderson, P. A. James, E. O. Ofek, L. Bildsten, G. Nelemans, K. J. Shen, N. N. Weinberg, B. D. Metzger, A. L. Piro, E. Quataert, M. Kiewe, and D. Poznanski. Preprint: arXiv:0906.2003, submitted to Nature, 2009

[326] S. Perlmutter et al. *Measurements of Omega and Lambda from 42 High-Redshift Supernovae*. Astrophys. J., 517:565, 1999

[327] J. K. Perring and T. H. R. Skyrme. *The Alpha-Particle and Shell Models of the Nucleus*. Proc. Phys. Soc. A, 69:600, 1956.

[328] E. Pfahl, S. Rappaport, P. Podsiadlowski. *The Galactic Population of Low- and Intermediate-Mass X-Ray Binaries*. Astrophys. J., 597:1036, 2003

[329] H. P. Pfeiffer, L. E. Kidder, M. A. Scheel, and S. A. Teukolsky, *A multidomain spectral method for solving elliptic equations*. Comput. Phys. Commun., 152:253, 2003.

[330] L. Piersanti, S. Gagliardi, I. J. Iben and A. Tornambé. *Carbon-Oxygen White Dwarf Accreting CO-Rich Matter. II. Self-Regulating Accretion Process up to the Explosive Stage*. Astrophys. J., 598:1229, 2003.

[331] T. Piran *The physics of gamma-ray bursts*. Rev. of Modern Phys., 76:1143, 2005.

[332] A. Piro. *The internal shear of type Ia supernova progenitors during accretion and simmering*. Astrophys. J., 679:625, 2008.

[333] T. Plewa and E. Muller. *The consistent multi-fluid advection method*. Astron. Astrophys., 342:179, 1999.

[334] A. J. T. Poelarends, F. Herwig, N. Langer and A. Heger. *The Supernova Channel of Super-AGB Stars*. Astrophys. J., 675:614, 2008.

[335] J A. Pons and U. Geppert. *Magnetic field dissipation in neutron star crusts: from magnetars to isolated neutron stars*. Astron. Astrophys., 470:303, 2007.

[336] Y.-Z. Qian and G. J. Wasserburg. *Where, oh where has the r-process gone?* Phys. Rep., 442:237, 2007.

[337] M. Rampp and H.-Th. Janka. *Spherically Symmetric Simulation with Boltzmann Neutrino Transport of Core Collapse and Postbounce Evolution of a 15 Msolar Star*. Astron. Astrophys., 539:L33, 2000.

[338] M. Rampp and H.-T. Janka. *Radiation hydrodynamics with neutrinos. Variable Eddington factor method for core-collapse supernova simulations*. Astron. Astrophys., 396:361, 2002.

[339] P.-G. Reinhard. *The relativistic mean-field description of nuclei and nuclear dynamics*. Rep. Prog. Phys., 52:439, 1989.

[340] M. Rampp, E. Müller and M. Ruffert. *Simulations of non-axisymmetric rotational core collapse*. Astron. Astrophys., 332:969, 1998

[341] D. G. Ravenhall, C. J. Pethick and J. R. Wilson. *Structure of Matter below Nuclear Saturation Density*. Phys. Rev. Lett., 50:2066, 1983.

[342] L. Rezzolla, B. J. Ahmedov and Miller J. C., 2001a, Mon. Not. Roy. Astron. Soc., 322:723, 2001. Erratum 338:816, 2003.

[343] L. Rezzolla *Gravitational Waves from Perturbed Black Holes and Relativistic Stars*. ArXiv:gr-qc/0302025, 2003.

[344] L. Rezzolla and B. J. Ahmedov *Electromagnetic fields in the exterior of an oscillating relativistic star - I. General expressions and application to a rotating magnetic dipole*. Mon. Not. Roy. Astron. Soc., 352:1161, 2004.

[345] P. Rhodes. *Fermi-Dirac function of integral order*. Proc. Royal Soc. Math. Physic. Sci., 204:396, 1950.

[346] A. G. Riess et al. *Observational Evidence from Supernovae for an Accelerating Universe and a Cosmological Constant*. Astron. J, 116:1009, 1998

[347] C. Ritossa, E. Garcia-Berro and I. J. Iben. *On the Evolution of Stars That Form Electron-degenerate Cores Processed by Carbon Burning. II. Isotope Abundances and Thermal Pulses in a* $10M_{\rm sun}$ *Model with an ONe Core and Applications to Long-Period Variables, Classical Novae, and Accretion-induced Collapse*. Astrophys. J., 460:489, 1996.

[348] C. Ritossa, E. García-Berro and I. J. Iben. *On the Evolution of Stars that Form Electron-degenerate Cores Processed by Carbon Burning. V. Shell Convection Sustained by Helium Burning, Transient Neon Burning, Dredge-out, URCA Cooling, and Other Properties of an 11 M_solar Population I Model Star*. Astrophys. J., 515:381, 1999.

[349] P. L. Roe. *Approximate riemann solvers, parameter vectors and difference schemes*. Journ. Comput. Phys., 43:357, 1981.

[350] J. V. Romero, J. M. Ibáñez, J. M. Martí and J. M. Miralles, *A new general relativistic hydrodynamical code*, Astrophys. J., 462:839, 1996.

[351] S. Rosswog and M. Liebendörder *High-resolution calculations of merging neutron stars - II. Neutrino emission* Mon. Not. Roy. Astron. Soc., 342:673, 2003

[352] S. Rosswog *Astrophysical Smooth Particle Hydrodynamics* submitted to New Astronomy Reviews, Preprint arXiv:0903.5075

[353] S. Rosswog, D. Kasen, J. Guillochon and E. Ramirez-Ruiz. *Collisions of white dwarfs as a new progenitor channel for type Ia supernovae*. Preprint: ArXiv:0907.3196

[354] M. Ruderman and P. G. Sutherland *Theory of pulsars - Polar caps, sparks, and coherent microwave radiation*. Astrophys. J., 196:51, 1975

[355] M. Ruffert, T.-H. Janka and G. Schäfer *Coalescing neutron stars - a step towards physical models. I. Hydrodynamic evolution and gravitational-wave emission.* Astron. Astrophys., 311:532, 1996

[356] M. Ruiz, M. Alcubierre and D. Núñez. *Regularization of spherical and axisymmetric evolution codes in numerical relativity*. Gen. Relat. and Grav., 40:159, 2008.

[357] M. Saijo and S. Yoshida. *Low $T/|W|$ dynamical instability in differentially rotating stars: diagnosis with canonical angular momentum*. Mon. Not. Roy. Astron. Soc., 368:1429, 2006.

[358] M. Saijo and Y. Kojima. *Faraday resonance in dynamical bar instability of differentially rotating stars*. Phys. Rev. D, 77:063002, 2008.

[359] H. Saio and K. Nomoto. *Evolution of a merging pair of C + O white dwarfs to form a single neutron star*. Astron. Astrophys., 150:L21, 1985.

[360] H. Saio and K. Nomoto. *Inward Propagation of Nuclear-burning Shells in Merging C-O and He White Dwarfs* Astrophys. J., 500:388, 1998.

[361] H. Saio and K. Nomoto. *Off-Center Carbon Ignition in Rapidly Rotating, Accreting Carbon-Oxygen White Dwarfs*. Astrophys. J., 615:444, 2004.

[362] L. Samuelsson and N. Andersson *Neutron star asteroseismology. Axial crust oscillations in the Cowling approximation*. Mon. Not. Roy. Astron. Soc., 374:256, 2007.

[363] O. Sarbach, G. Calabrese, J. Pullin and M. Tiglio, *Hyperbolicity of the BSSN system of Einstein evolution equations*. Phys. Rev. D, 66:064002, 2002

[364] H. Satz. *Colour deconfinement and bag fusion in SU(2) Yang-Mills matter*. Phys. Lett. B, 113:245, 1982.

[365] E. Scannapieco and L. Bildsten. *The Type Ia Supernova Rate*. Astrophys. J. Lett., 629:L85, 2005

[366] G. Schäfer and A. Gopakumar, *Minimal no-radiation approximation to Einstein's field equations*. Phys. Rev. D, 69:021501, 2004.

[367] S. Scheidegger, T. Fischer, S. C. Whitehouse and M. Liebendörfer, *Gravitational waves from 3D MHD core collapse simulations*. Astron. Astrophys., 490:231, 2008

[368] B. F. Schhutz, *A First Course in General Relativity*, (Cambridge University Press, Cambridge UK, 1985).

[369] S. J. Schwartz and S. Zane and R. J. Wilson et al. *The Gamma-Ray Giant Flare from SGR 1806-20: Evidence of Crustal Cracking via Initial Timescales*. Astrophys. J., 627:L129, 2005.

[370] S. L. Shapiro and S. A. Teukolsky. *Black holes, White Dwarfs and Neutron Stars*. Wiley, New York, 1983

[371] S. L. Shapiro, *Numerical Relativity at the Frontier*, Progress of Theor. Phys. Supp., 163:100, 2006.

[372] H. Shen, H. Toki, K. Oyamatsu and K. Sumiyoshi. *Relativistic equation of state of nuclear matter for supernova and neutron star*. Nucl. Phys. A, 637:435, 1998. URL http://user.numazu-ct.ac.jp/sumi/eos.

[373] H. Shen, H. Toki, K. Oyamatsu, and K. Sumiyoshi. *Relativistic Equation of State of Nuclear Matter for Supernova Explosion. Progress of Theoretical Physics*, Progr. Theor. Phys., 100:1013, 1998.

[374] M. Shibata, *Axisymmetric general relativistic hydrodynamics: Long-term evolution of neutron stars and stellar collapse to neutron stars and black holes*. Phys. Rev. D, 67:024033, 2003.

[375] M. Shibata and Y.-I. Sekiguchi. *Gravitational waves from axisymmetrically oscillating neutron stars in general relativistic simulations*. Phys. Rev. D, 68:104020, 2003.

[376] M. Shibata, and Y.-I. Sekiguchi. *Gravitational waves from axisymmetric rotating stellar core collapse to a neutron star in full general relativity*. Phys. Rev. D, 69:084024, 2004.

[377] M. Shibata, S. Karino and Y. Eriguchi. *Dynamical bar-mode instability of differentially rotating stars: effects of equations of state and velocity profiles*. Mon. Not. Roy. Astron. Soc., 343:619, 2003.

[378] M. Shibata and Y. Sekiguchi. *Three-dimensional simulations of stellar core collapse in full general relativity: Nonaxisymmetric dynamical instabilities*. Phys. Rev. D, 71:0204014, 2005

[379] S. Siegler and H. Riffert, *Smoothed Particle Hydrodynamics Simulations of Ultrarelativistic Shocks with Artificial Viscosity*, Astrophys. J., 531:1053, 2000.

[380] L. Siess. *Evolution of massive AGB stars. I. Carbon burning phase*. Astron. Astrophys., 448:717, 2006.

[381] L. Smarr, A. Čadež, B. DeWitt and K. R. Eppley. *Collision of two black holes: Theoretical framework*. Phys. Rev. D, 14:2443, 1976.

[382] L. Smarr. *Gauge conditions, radiation formulae and the two black hole collision*. In L. Smarr, editor, *Sources of Gravitational Radiation*, page 245. Cambridge University Press, Cambridge, England, 1979.

[383] H. Sotani, K. D. Kokkotas, N. Stergioulas. *Torsional oscillations of relativistic stars with dipole magnetic fields*. Mon. Not. Roy. Astron. Soc., 375:261, 2007.

[384] H. Sotani, K. D. Kokkotas, N. Stergioulas, 2008, MNRAS, 385, L5 *Alfvén quasi-periodic oscillations in magnetars*. Mon. Not. Roy. Astron. Soc., 385:L5, 2008.

[385] A. Spitkovsky. *Time-dependent Force-free Pulsar Magnetospheres: Axisymmetric and Oblique Rotators*. Astrophys. J., 648:L51, 2006.

[386] F. M. Steffens, H: Holtmann, A. W. Thomas. *Mesonic corrections to the shape of quark distributions*. Phys. Lett. B, 358:139, 1995.

[387] AIC $Y_e(\rho)$ Data, http://www.stellarcollapse.org/AIC

[388] Gravitational Waveform Catalog, http://www.stellarcollapse.org/gwcatalog

[389] N. Stergioulas and J. L. Friedman. *Comparing models of rapidly rotating relativistic stars constructed by two numerical methods*. Astrophys. J., 444:306, 1995.

[390] N. Stergioulas. *The Structure and Stability of Rotating Relativistic Stars*. PhD thesis, University of Wisconsin-Milwaukee, Milwaukee, Wisconsin, 1996.

[391] N. Stergioulas. *Rotating stars in relativity*. Liv. Rev. Rel., 6:3, 2003.

[392] N. Stergioulas, T. A. Apostolatos, J. A. Font *Non-linear pulsations in differentially rotating neutron stars: mass-shedding-induced damping and splitting of the fundamental mode*. Mon. Not. Roy. Astron. Soc., 352:1089, 2004.

[393] T. E. Strohmayer. *Fast X-ray Oscillations During Magnetar Flares*. in *ASTROPHYSICS OF COMPACT OBJECTS*: International Conference on Astrophysics of Compact Objects. AIP Conference Proceedings, Volume 968, p. 85, 2008.

[394] T.E. Strohmayer and A. L. Watts *The 2004 Hyperflare from SGR 1806-20: Further Evidence for Global Torsional Vibrations*. Astrophys. J., 653:593, 2006.

[395] P. A. Sturrock. *A Model of Pulsars*. Astrophys. J., 164:529, 1971

[396] Y. Sugahara and H. Toki. *Relativistic mean-field theory for unstable nuclei with non-linear and terms*. Nucl. Phys. A, 579:557, 1994.

[397] E. Suraud and D. Vautherin. *Thomas-Fermi calculations of hot dense matter*. Phys. Lett. B, 138:325, 1984.

[398] K. Sumiyoshi, D. Hirata, H. Toki and H. Sagawa. *Comparison of the relativistic mean-field theory and the Skyrme Hartree-Fock theory for properties of nuclei and nuclear matter*. Nucl. Phys. A, 552:437, 1993.

[399] K. Sumiyoshi and H. Toki. *Relativistic equation of state of nuclear matter for the supernova explosion and the birth of neutron stars.* Astrophys. J.,, 422:700, 1994.

[400] K. Sumiyoshi, H. Kuwabara and H. Toki. *Relativistic mean-field theory with non-linear and terms for neutron stars and supernovae*. Nucl. Phys. A, 581:725, 1995.

[401] K. Sumiyoshi, H. Suzuki, S. Yamada and H. Toki. *Properties of a relativistic equation of state for collapse-driven supernovae*. Nucl. Phys. A, 730:227, 2004.

[402] K. Sumiyoshi, S. Yamada, H. Suzuki, H. Shen, S. Chiba and H. Toki. *Postbounce Evolution of Core-Collapse Supernovae: Long-Term Effects of the Equation of State*. Astrophys. J., 629:922, 2005.

[403] T. Summerscales, A. Burrows, C. D. Ott and L. S. Finn. *Maximum Entropy for Gravitational Wave Data Analysis: Inferring the Physical Parameters of Core-Collapse Supernovae*. Astrophys. J., 678:1142, 2008.

[404] E. Suraud. *A Thomas-Fermi Equation of State of Hot Dense Matter*. In D. Bancel and M. Signore, editors, *Problems of Collapse and Numerical Relativity*, Proceedings of the NATO Advanced Research Workshop held in Toulouse, November 7-11, 1983, Dordrecht: Reidel, 1984, edited by Daniel Bancel and Monique Signore. NATO Advanced Science Institutes (ASI) Series C, Volume 134, page 81, 1984.

[405] D. Swesty. *Thermodynamically Consistent Interpolation of Equation of State Tables*. Journ. Comput. Phys., 127:118, 1996.

[406] F. D. Swesty and E. S. Myra. *A Numerical Algorithm for Modeling Multigroup Neutrino-Radiation Hydrodynamics in Two Spatial Dimensions*. Astrophys. J. Supp. Ser. , 181:1, 2009.

[407] TAMA300, http://tamago.mtk.nao.ac.jp

[408] J.-L. Tassoul. *Theory of Rotating Stars*, 1978, Princeton University Press, Princeton, U.S.A.

[409] J. L. Tassoul *Stellar Rotation*. Cambridge University Press, Cambridge, UK, 2000.

[410] T. A. Thompson, A. Burrows and P. A. Pinto. *Shock Breakout in Core-Collapse Supernovae and Its Neutrino Signature*. Astrophys. J., 592:434, 2003.

[411] C. Thompson and R. C. Duncan. *The soft gamma repeaters as very strongly magnetized neutron stars - I. Radiative mechanism for outbursts*. Mon. Not. Roy. Astron. Soc., 275:255, 1995.

[412] C. Thompson and R. C. Duncan Astrophys. J., 561:980, 2001

[413] Thorne K. S., *Multipole expansions of gravitational radiation* Rev. Mod. Phys., 52:299, 1980

[414] Thorne K. S., 1987, in S. W. Hawking and W. Israel, ed, *300 Years of Gravitation*. Cambridge University Press, Cambridge

[415] F. X. Timmes and S. E. Woosley. *The conductive propagation of nuclear flames. I - Degenerate C + O and O + NE + MG white dwarfs*. Astrophys. J., 396:649, 1992.

[416] F. X. Timmes, S. E. Woosley and R. E. Taam. *The conductive propagation of nuclear flames. 2: Convectively bounded flames in C + O and O + NE + MG cores*. Astrophys. J., 420:348, 1994.

[417] F. X. Timmes and F. D. Swesty. *The Accuracy, Consistency, and Speed of an Electron-Positron Equation of State Based on Table Interpolation of the Helmholtz Free Energy*. Astrophys. J. Supp. Ser. , 126:501, 2000.

[418] A. N. Timokhin, G: S. Bisnovatyi-Kogan, H. C. Spruit. *The magnetosphere of an oscillating neutron star. Non-vacuum treatment*. Mon. Not. Roy. Astron. Soc., 316:734, 2000

[419] A. N: Timokhin *On the force-free magnetosphere of an aligned rotator*. Mon. Not. Roy. Astron. Soc., 368, 1055.

[420] Timokhin A. N., 2007, *Impact of neutron star oscillations on the accelerating electric field in the polar cap of pulsar*. Astrophys. Space Science, 308:345, 2007.

[421] A. N. Timokhin, D. Eichlers and Lyubarsky Y., *On the Nature of Quasi-periodic Oscillations in the Tail of Soft Gamma Repeater Giant Flares*. Astrophys. J., 680:1398, 2007.

[422] J. E. Tohline. *The collapse of rotating stellar cores - Equilibria between white dwarf and neutron star densities*. Astrophys. J., 285:721, 1984.

[423] E. F. Toro, *Riemann Solvers and Numerical Methods for Fluid Dynamics*. Springer-Verlag, 1999.

[424] A. I. Tsygan. *Corequakes of neutron stars and soft gamma-ray bursts*. Astron. Astrophys., 44:21, 1975

[425] T. Uenishi, K. Nomoto and I Hachisu. *Evolution of Rotating Accreting White Dwarfs and the Diversity of Type Ia Supernovae*. Astrophys. J., 595:1094, 2003.

[426] W. Unno, Y. Osaki, H. Ando and H. Satol H. Shibahashi. *Nonradial Oscillations of Stars*, 2nd ed., University of Tokyo Press,1989.

[427] S. van den Bergh and G. A. Tammann. *Galactic and extragalactic supernova rates*. Ann. Rev. Astron. Astroph., 29:363, 1991.

[428] B. J. van Leer. *Towards the ultimate conservative difference scheme: IV. A new approach to numerical convection*. Journ. Comput. Phys., 23:276, 1977.

[429] B. J. van Leer. *Towards the ultimate conservative difference scheme. V - A second-order sequel to Godunovs method* Journ. Comput. Phys., 32:101, 1979.

[430] K. A. van Riper and J. M. Lattimer. *Stellar core collapse. I - Infall epoch*. Astrophys. J., 249:270, 1981.

[431] Van Riper, K. A. and Lattimer, J. M. *Stellar Collapse. II - Inner core bounce and shock propagation*. Astrophys. J., 257:793, 1982

[432] VIRGO, http://www.virgo.infn.it

[433] R. M. Wald, *General Relativity*. The University of Chicago Press, Chicago, 1984.

[434] *R. Walder, A. Burrows, C. D. Ott, E. Livne, I. Lichtenstadt, and M. Jarrah. Anisotropies in the Neutrino Fluxes and Heating Profiles in Two-dimensional, Time-dependent, Multigroup Radiation Hydrodynamics Simulations of Rotating Core-Collapse Supernovae*. Astrophys. J., 626:317, 2005.

[435] A. L. Watts, N. Andersson and D. I. Jones. *The Nature of Low $T/|W|$ Dynamical Instabilities in Differentially Rotating Stars*. Astrophys. J. Lett., 618:L37, 2005.

[436] A. L Watts and T. E. Strohmayer. *Detection with RHESSI of High-Frequency X-Ray Oscillations in the Tailof the 2004 Hyperflare from SGR 1806-20*. Astrophys. J., 637:L117, 2006.

[437] A. L. Watts and T. E. Strohmayer. *Neutron star oscillations and QPOs during magnetar flares*. Adv. Space Research, 40:1446, 2007.

[438] MPA Garching GW Signal Catalog, www.mpa-garching.mpg.de/rel_hydro/wave_catalog.shtml

[439] F. Weber. *Pulsars as Astrophysical Laboratories for Nuclear and Particle Physics*. IoP Publishing, Bristol, 1999

[440] J. M. Weisberg and J. H. Taylor. *The Relativistic Binary Pulsar B1913+16: Thirty Years of Observations and Analysis*. In F. A. Rasio and I. H. Stairs, editors, ASP Conf. Ser. 328: *Binary Radio Pulsars*, page 25, 2005.

[441] J. R. Wilson, G. J. Mathews, P. Marronetti. *Relativistic numerical model for close neutron-star binaries*. Phys. Rev. D, 54:1317, 1996.

[442] S. E. Whitcomb. *Ground-based gravitational-wave detection: now and future*. Class. Quant. Grav., 25:114013, 2008.

[443] E. Witten. *Cosmic separation of phases*. Phys. Rev. D, 30:272, 1984.

[444] P. W. Woods and C. Thompson. *Soft gamma repeaters and anomalous X-ray pulsars: magnetar candidates*. in Lewin W. H. G., van der Klis M., eds, *Compact Stellar X-ray Sources*, Cambridge University Press, 2006.

[445] S. E. Woosley and E. Baron. *The collapse of white dwarfs to neutron stars*. Astrophys. J., 391:228, 1992.

[446] S. E. Woosley *Gamma-ray bursts from stellar mass accretion disks around black holes*. Astrophys. J., 405:273, 1993.

[447] S. E. Woosley and T. A. Weaver. *The Evolution and Explosion of Massive Stars. II. Explosive Hydrodynamics and Nucleosynthesis*. Astrophys. J. Supp. Ser. , 101:181, 1995.

[448] S. E. Woosley, A. Heger and T. A. Weaver. *The evolution and explosion of massive stars*. Rev. Mod. Phys., 74:1015, 2002.

[449] S. E. Woosley and J. S. Bloom. *The Supernova Gamma-Ray Burst Connection*. Ann. Rev. Astron. Astrophys., 44:507, 2006.

[450] S. E. Woosley and A. Heger. *The Progenitor Stars of Gamma-Ray Bursts*. Astrophys. J., 637:914, 2006.

[451] S. E. Woosley, A. Almgren, J. B. Bell, G. Glatzmaier, D. Kasen, A. R. Kerstein, H. Ma, P. Nugent, F. Rpke,V. Sankaran,M. Zingale. *Type Ia supernovae*. Journal of Physics: Conference Series, 78:012081, 2007.

[452] A. Yahil. *Self-similar stellar collapse*. Astrophys. J., 265:1047, 1983.

[453] S. Yamada and K. Sato. *Gravitational Radiation from Rotational Collapse of a Supernova Core*- Astrophys. J., 450:245, 1995.

[454] S.-C. Yoon, P. Podsiadlowski and S. Rosswog. *Remnant evolution after a carbon-oxygen white dwarf merger*. Mon. Not. Roy. Astron. Soc., 380:933, 2007.

[455] S.-C. Yoon and N. Langer. *On the evolution of rapidly rotating massive white dwarfs towards supernovae or collapses*. Astron. Astrophys., 435:967, 2005

[456] S.-C. Yoon and N. Langer. *Presupernova evolution of accreting white dwarfs with rotation*. Astron. Astrophys., 419:623, 2004

[457] J. M. York, *Gravitational degrees of freedom and the initial-value problem*, Phys. Rev. Lett., 26:1656, 1971.

[458] J. M. York, *Kynamatics and Dynamics of General Relativity*, in L. L. Smarr, editor, *Sources of Gravitational Radiation*, page 83, (Cambridge University Press, Cambridge, UK, 1979).

[459] L. R. Yungelson and N. Livio. *Type IA Supernovae: an Examination of Potential Progenitors and the Redshift Distribution*. Astrophys. J., 497:168, 1998.

[460] L. R. Yungelson and M. Livio. *Supernova Rates: A Cosmic History*. Astrophys. J., 528:108, 2000.

[461] F. J. Zerilli. *Effective potential for even-parity Regge-Wheeler gravitational perturbation equations*. Phys. Rev. Lett., 24:737, 1970.

[462] J. L. Zdunik, M: Bejger, P. Haensel, E. Gourgoulhon *Energy release associated with a first-order phase transition in a rotating neutron star core*. Astron. Astrophys., 465:533, 2007.

[463] J. L. Zdunik, M: Bejger, P. Haensel, E. Gourgoulhon *Strong first-order phase transition in a rotating neutron star core and the associated energy release*. Astron. Astrophys., 479:515, 2008

[464] B. Zink, N. Stergioulas, I. Hawke, C. D. Ott, E. Schnetter and E. Müller. *Nonaxisymmetric instability and fragmentation of general relativistic quasitoroidal stars*. Phys. Rev. D, 76:024019

[465] B. Zink, E. Schnetter and M. Tiglio. *Multipatch methods in general relativistic astrophysics: Hydrodynamical flows on fixed backgrounds*. Phys. Rev. D, 77:103015

[466] T. Zwerger and E. Müller. *Dynamics a nd gravitational wave signature of axisymmetric rotational core collapse.*. Astron. Astrophys., 320:209, 1997